Acoustical Studies of Breaking Surface Waves in the Open Ocean

by

Li Ding

B. Sc. , Xiamen University, Xiamen, China, 1983

A Dissertation Submitted in Partial Fulfillment of the
Requirements for the Degree of
DOCTOR OF PHILOSOPHY
in the Department of Electrical and Computer Engineering

We accept this thesis as conforming to the required standard

.....
Dr. D. M. Farmer, Supervisor

.....
Dr. R. L. Kirlin, Co-Supervisor

.....
Dr. R. W. Stewart, Outside Member

.....
Dr. R. M. Clements, Outside Member

.....
Dr. W. K. Melville, External Examiner

Supervisors: Dr. D. M. Farmer and Dr. R. L. Kirlin

Abstract

The work presented in this thesis consists of two parts: development and application of a novel passive acoustical approach for field measurement of breaking surface waves, and interpretation of the resulting observations in terms of wave field information so as to improve the understanding of wave breaking.

The development of the acoustical approach has been motivated by the difficulties inherent in measurement of breaking waves. This approach makes use of an array of four broadband hydrophones which is able to track individual breaking waves by passive detection of the naturally generated sound of wave breaking. The Generalized Cross Correlation method is used to determine time differences of acoustic signals from breaking waves arriving at the array, allowing the breaking waves to be located with the given array geometry.

Observations of breaking waves were made by means of this technique during the Surface Wave Processes Program (SWAPP). The spatial and temporal statistics of breaking waves, including breaking wave density, travel velocity, lifetime of breaking and spacing, are obtained from the observations. Statistical models are developed to assess, and where appropriate, correct for any bias resulting from limitations of the measurement approach. The breaking wave statistics provide important information about the physical process of wave breaking and its distribution in different wave fields. It is found that wave breaking in the open ocean occurs at a scale substantially smaller than the scale associated with the dominant wind wave component in the wave spectrum. Numerical simulation of breaking wave statistics and comparison with the observations demonstrates that the scale of breaking can be predicted from the directional wave spectrum by a linear model with a single breaking threshold. These results will provide input to comprehensive models of wave dissipation.

Acoustical radiation properties of individual breaking waves are a further aspect of wave breaking that has been observed with the aforementioned technique. In-

vestigation of the sound radiated from breaking waves reveals information both on the nature of the sound generation mechanism by breaking and the dimension of breaking waves. Statistical analysis of the acoustic source intensity associated with wave breaking suggests that the source intensity can be related to the breaking scale and wave energy dissipation, thus implying that surface wave dissipation could be remotely measured by using ambient sound.

Examiners:

.....

Dr. D. M. Farmer, Supervisor

.....

Dr. R. L. Kirlin, Co-Supervisor

.....

Dr. R. W. Stewart, Outside Member

.....

Dr. R. M. Clements, Outside Member

.....

Dr. W. K. Melville, External Examiner
(Scripps Institution of Oceanography, University of California, San Diego)

Contents

List of Tables

List of Figures

Acknowledgements

I am indebted to a number of individuals without whose assistance and guidance the successful completion of this thesis would have been impossible. Dr. Farmer introduced me to the field of Acoustical Oceanography during his visit to China, and later provided an opportunity for me to come to this beautiful and peaceful country and start my graduate study in this rapidly growing and exciting area. During the course of the thesis, he has provided me with enormous support and constant inspiration, especially at the difficult initial stage when the research appeared to be heading nowhere. As the supervisor, his frequent sharp questions and constructive suggestions on the research stimulated much of this work and helped ensure that the project was steered to the right direction. The supervisory committee have also been of great help to me. In particular, I have benefited from many valuable discussions with Dr. Stewart who always provided me with excellent physical insight on the problems I ran into.

During my Ph.D program, Dr. Zielinski and later Dr. Kirlin acted as Co-Supervisor and helped handle the administrative affairs with the University. I would also like to thank Ms. Sharon Moulson, Graduate Secretary of the Department, for making sure that the program was going through the right bureaucratic procedure.

Technical support from the staff at the Insitute of Ocean Sciences and from others is greatly appreciated. Ron Teichrob, Craig Elder and Doug Sieberg developed the reliable instrument for this project. Ron Teichrob, Craig Elder and Don Scott (CO-OP student) helped develop the high-speed data processing system. Richard Bennett implemented the pattern recognition algorithm on the computer when he worked here as a CO-OP student. I am particularly indebted to Grace Kamitakahara-King for her generous support in computer programming. Netta Delacretaz and Will Sayers helped with many bureaucratic issues.

The directional wave spectra were kindly provided by Dr. Jerry Smith from the Scripps Institution of Oceangraphy, which is gratefully appreciated.

Financial supports for this project were from the University of Victoria (University Fellowship), the Canadian Panel on Energy Research and Development, and the US Office of Naval Research.

Thanks must also be given to my fellow students: Rex Andrew, Daniela Dilorio, Dimitris Menemenlis, Svein Vagle, Yunbo Xie, and Len Zedel, not only for their sympathy and help when I was in difficult situations, but also for many interesting discussions on my research, science in general, life and many other subjects. I also enjoyed the time I spent with Yunbo Xie and my other Chinese folks, which helped ease my homesickness.

I owe my parents too much ever to pay back for their understanding, encouragement, and most inportantly love, which made it possible for me to persevere through these difficult years of overseas study.

TO MY PARENTS

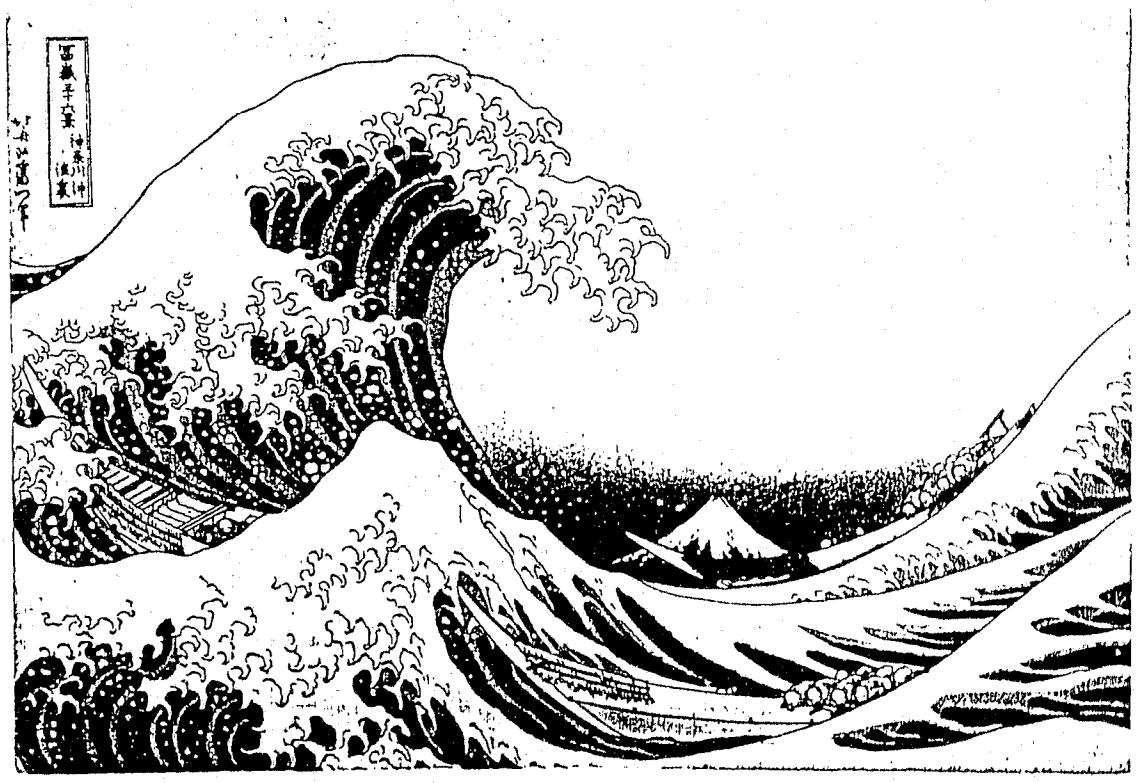

Stormy Sea off Kanagawa: Raging waves and boats being tossed about. From Roni Neuer and Susugu Yoshida: *250 Years of Japanese Art*, Mayflower Books.

Introduction

The ocean surface is the interface where the ocean and atmosphere interact with each other. The study of physical processes occurring at the surface is therefore indispensable to a complete understanding of air-sea interaction. Few ocean surface processes are more apparent than the breaking of surface waves. Breaking surface waves are not only responsible for wave dissipation (Melville and Rapp, 1985; Rapp and Melville, 1990; Agrawal et al., 1992), but have also been recognized as playing a critical role in air-sea interaction (Donelan, 1990) by enhancing the transfer of mass, heat, and gas across the surface (Bortkovskii, 1987; Thorpe, 1992). Yet the detailed mechanism of wave breaking and its spatial and temporal characteristics, still remain poorly understood. Theoretical analysis has so far been limited to the case of single progressive waves , mainly due to nonlinearities inherent in the process. Measurement of breaking waves is made difficult by the rapid and intermittent occurrence of breaking and the hostile near-surface environment. Further progress in the study of wave dissipation and air-sea interaction, however, requires an improved understanding of the physics of wave breaking.

Laboratory studies of breaking waves (Melville and Rapp, 1985; Rapp and Melville, 1990; Hwang et al., 1989) have provided valuable insight and guidance, but field observations are essential to further understanding. Conventional methods such as point measurement (Thorpe and Humpheries, 1980; Longuet-Higgins and Smith, 1983) and photography (Snyder et al., 1983; Monahan and O'Muirheartaigh, 1986) have not been very successful in comprehensive and long-term measurement of this phenomenon in open ocean conditions. Consequently, increasing efforts are

being made to develop and apply new remote sensing techniques that avoid exposing instruments to the violent near surface environment. One of these techniques is passive acoustics that makes use of the sound naturally generated by wave breaking. The work described in this thesis is primarily concerned with the development and application of new passive acoustical methods to improve measurement and understanding of breaking surface waves.

Breaking waves have long been identified as the main source of underwater ambient sound (Knudsen et al., 1948; Wenz, 1962). Ambient sound has previously been observed with a single hydrophone placed close to the surface to extract the temporal properties of breaking waves (Farmer and Vagle, 1988). The present approach involves the use of a broadband (0-5.5 kHz) hydrophone array to include spatial measurement. The array is designed as a self-contained package suspended at a depth of 25 m below the surface, and is able to track individual breaking waves. The instrument was employed during the Surface Wave Processes Program (SWAPP) in February/March 1990. This thesis is based on the data collected in the SWAPP experiment.

The dynamics of ocean surface waves is governed by the energy transfer equation which includes three main source terms: input from the wind, nonlinear wave-wave interaction, and wave dissipation. The least understood aspect so far is probably wave dissipation through breaking. The approach described above allows simultaneous measurement of both spatial and temporal statistics of breaking waves. These statistics provide information on the distributions of wave breaking with respect to its spatial and temporal scales, as well as the frequency of breaking, and are therefore important to modelling wave dissipation. For example, they can be used to estimate the range of scales at which wave breaking occurs in the wave spectrum and thus the rate of energy which is dissipated due to wave breaking (Phillips, 1988).

Breaking waves have been observed extensively during the SWAPP experiment under various wind and wave conditions. Statistical analysis of these results has revealed correlation with wave parameters and provided useful insight. Yet it appears

that the results must also be related to the detailed wave field information. Analytic analysis of breaking wave statistics in a two-dimensional random wave field is not yet available, although some progress has been made in the one-dimensional case. The Monte Carlo experimental approach seems to be the only method that allows computation of breaking wave statistics in the two dimensional wave field. It has therefore been used in this work to simulate breaking wave statistics from simultaneously measured directional wave spectra. The results are compared with the observations, so as to determine how well breaking wave statistics can be predicted from directional wave spectra.

Several theories (e. g. Prosperetti, 1988) have been proposed to address the sound generation mechanism by wave breaking, which is however still not well understood. These theories have mostly been tested in the laboratory due to sparse field data. The aforementioned approach allows us to isolate individual breaking waves and study their sound radiation properties, thus providing an opportunity to examine the sound generation theories in real ocean conditions. In addition, the acoustic power radiated from breaking waves and its statistical distribution can be estimated and related to breaking wave parameters to examine the relation between the acoustic power and wave dissipation obtained in the laboratory (Melville et al., 1988), which implies potential for remote measurement of wave dissipation using ambient sound.

Tracking of breaking surface waves in the complex noisy oceanic environment presents a challenging task in signal processing. The applied tracking technique must be able to tackle the unknown frequency characteristics of the radiated acoustic signal. The algorithm must be robust, and should not require too much computation for the sake of processing a large volume of data. Ambient sound data must be averaged over a sufficiently long period to obtain reliable breaking wave statistics, and these statistics must also be determined in various conditions to reveal any correlation with oceanographic parameters. Consequently, with our ambient sound data sampled at a high rate (88 kHz), processing of these data requires a high-

speed technique and automation of processing. Therefore, much of this work has been devoted to developing an efficient signal processing scheme with some degree of automation, and a fast data processing system.

Prior to this work, we had no information on the spatial coherence of the sound radiated from breaking waves to guide us in the instrument design. Our observations have helped to clarify the nature of this signal and at the same time, revealed certain limitations of the technique when tracking sources of finite dimension in the near field. The finite source dimension effect, together with background noise, is responsible for incomplete measurement of the instrument. In order to investigate these limitations, statistical models have been developed to assess, and where appropriate, correct for any bias resulting from the incomplete measurement. Since the spatial coherence contains information on the spatial dimension of the source, some analysis has also been carried out on this aspect.

This thesis starts in the first chapter with a general description of breaking waves and a review of the necessary physical background for understanding and interpreting our observations. Various techniques for measurement of breaking waves are also described.

Chapter 2 describes the SWAPP experiment, the instrumentation and the data processing system. The underlying technology for tracking breaking waves is discussed in detail in Chapter 3, based on a previously published paper (Ding and Farmer, 1992a).

Acoustical radiation properties of individual breaking waves are discussed in the next chapter (Chapter 4), where we shall examine the nature of sound generation by breaking and the relation between wave-radiated acoustic power and wave dissipation. This part of the work has been published and presented at conferences (Farmer and Ding, 1992; Ding and Farmer, 1992b,c). We shall also review the background knowledge of the ambient sound generation mechanism and the ambient sound field.

Chapter 5 constitutes the most important part of the thesis. In this chapter, we present and discuss our experimental results on breaking wave statistics under

various environmental conditions. Limitations of the measurement approach will also be assessed. In Chapter 6, a numerical model is set up that computes breaking wave statistics from the directional wave spectra measured simultaneously by other participants during the SWAPP experiment. The simulated results are also compared with the acoustical observations.

The work described in this thesis is essentially original, and spans a broad range of both science and engineering. It is therefore unrealistic to expect to solve within a limited time all the problems that have arisen, although some of them are interesting and important enough from either scientific or engineering points of view that it is highly tempting to solve them and include the results in the thesis. Therefore, the thesis ends with a summary of what has been accomplished and recommends future research that would continue and extend this work.

Chapter 1

Background

1.1 Breaking Waves

Surface wave breaking is a commonly observed process at the ocean surface. Breaking surface waves in deep water are visually identified as spilling and plunging breakers (see Fig. 1.1). In a spilling breaker, part of the wave crest spills forward forming a turbulent region on the forward face and leaving behind a less turbulent wake that decays with increasing distance from the crest. At larger scales of breaking, air entrainment may occur and the breaking wave becomes visible. In a plunging breaker, the crest evolves into a forward jet which plunges forwards and downwards into the surface. The jet itself often disintegrates into droplets and spray even before impact. These two types of breakers and the more persistent foam they generate, are usually identified as whitecaps in photographs and video recordings. They also generate sound and are identified as the dominant source of underwater ambient noise (Wenz, 1962; Kerman, 1984). There is also a third type of breaking waves called microbreakers, in which a turbulent patch is generated without clearly visible air entraiment (Weissman et al., 1984). Breaking waves of this type are believed to be important for the generation of ambient noise at very low wind speeds (Updegraff and Anderson, 1991b), which is discussed in Chapter 4.

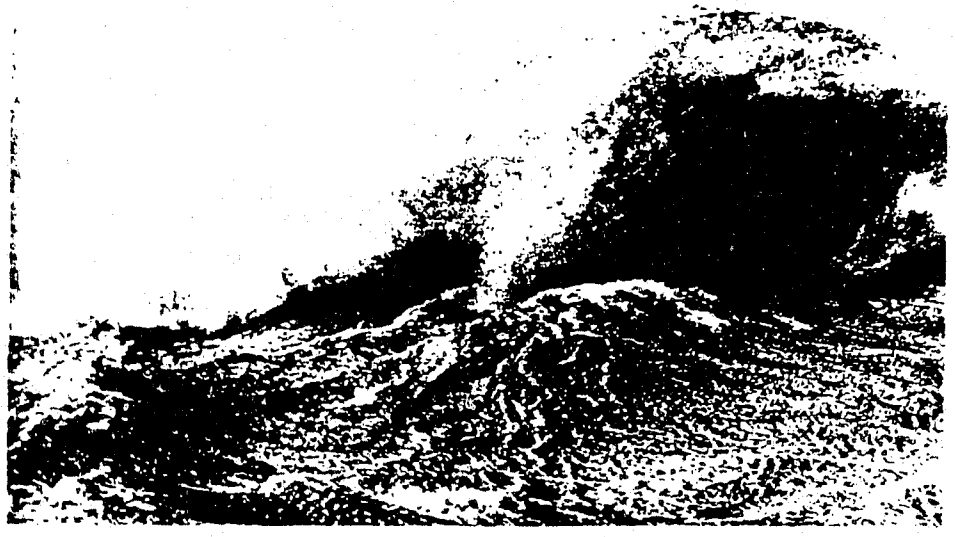

Figure 1.1: (a) Spilling breakers observed during the Surface Wave Processes Program (SWAPP). (b) A plunging breaker in the N. Atlantic (from Longuet-Higgins, 1988).

Because of the significant dynamical processes, breaking waves play an important role in the dynamics of the upper ocean and air-sea interaction. They dissipate momentum and energy in the surface wave field and transfer the momentum and energy to surface currents and near-surface turbulence, and are thus thought to be a primary mechanism of wave dissipation (Mitsuyasu, 1985; Melville and Rapp, 1985; Agrawal et al., 1992) and serve as a dominant source of mixing the upper layers of the ocean. They entrain air bubbles which, being advected by the wave-generated turbulence to considerable depths, are believed to be important in the process of air-sea gas exchange (Thorpe, 1982, 1992; Smith and Jones, 1985). Sea spray is also generated in the process of wave breaking, thus enhancing the transfer of heat and mass across the ocean surface.

Breaking waves exert by far the largest wave-induced force on marine systems, and hence must be considered in coastal engineering design. Uncertainties about important parameters of wave breaking have often led to either failure or expensive overdesign.

Despite the important role played by breaking waves, our understanding of the physics of wave breaking is far from complete. In theoretical studies, the equations of motion can no longer be treated as linear and the nonlinear boundary conditions must be applied at the free surface whose location is unknown yet must be determined as part of the solution. Analytical approaches to such a problem are very limited, and thus far most work has mainly been in the case of single progressive waves, and particularly on the derivation of the breaking criterion from either the kinematics or the dynamics of wave breaking. Most studies of wave breaking in a random wave field, however, have been empirical and experimental. Nevertheless, two recent studies (Snyder and Kennedy, 1983; Ochi and Tsai, 1983) based on the dynamics of wave breaking and the statistics of random waves, have advanced significantly the research in this subject. Both the dynamical and statistical approaches are important in quantifying and modelling the wave breaking process.

Due to lack of analytical tools, numerical modelling has proved useful in evaluat-

ing breaking wave statistics in a random, two dimensional, wave field. Kennedy and Snyder (1983) synthesized surface waves using prescribed directional wave spectra, and calculated breaking wave parameters by applying the dynamical breaking criterion in the wave field. The results compared favourably with their field experiment (Snyder et al., 1983). It is believed that the numerical approach will continue to be important at least until significant progress is made in analytical studies.

1.2 The Breaking Criterion

In order to quantify and model breaking waves, we must first determine the conditions under which waves break, that is, we have to establish a breaking criterion. The breaking criterion for regular gravity waves in deep water has been addressed from various viewpoints, each of which is based on a different parameter. As classified in Hwang et al. (1989), there are three categories of breaking criteria which are most commonly used:

1. Kinematic Criterion: A wave breaks as the velocity of fluid at the wave crest, u, equals or exceeds the phase speed of the wave, c. If $u > c$, the particle at the crest would leave the crest behind and fall on the forward surface, and breaking would ensue. The wave would then lose energy until $u \leq c$ again. This criterion is regarded as the original definition of wave breaking and used to derive other criteria.

2. Geometric Criterion: In steady irrotational flow, the kinematic criterion also defines the limiting form of a wave before it breaks: the crest of the wave contains an angle of 120^0 (Stokes limiting wave). This also implies that the maximum steepness is approximately $1/7$, that is,

$$H_{max} = 0.142\lambda, \tag{1.1}$$

where H is wave height and λ wavelength, or equivalently,

$$(ak)_{max} = 0.142\pi, \tag{1.2}$$

where $a = H/2$ is wave amplitude and $k = 2\pi/\lambda$ is wavenumber. The above criterion can also be expressed in terms of wave period T, that is,

$$H_{max} = 0.027gT^2 \tag{1.3}$$

(Ochi and Tsai, 1983). An alternative geometric description of the limiting form is slope. Longuet-Higgins and Fox (1977) showed that for a regular progressive gravity wave with its height approaching the maximum but the crest still rounded (the so called 'almost-highest wave'), the maximum slope at the free surface is

$$S_{max} = \tan 30.37^o \approx 0.586. \tag{1.4}$$

3. Dynamical Criterion: A wave breaks when the downward particle acceleration at the crest exceeds a portion of the gravitational acceleration, that is

$$a_{max} = \alpha g. \tag{1.5}$$

Longuet-Higgins (1963) showed that for a limiting Stokes wave the particle acceleration near the crest is $0.5g$ and directed radially away from the crest. In a later paper, Longuet-Higgins and Fox (1977), using the theory of the almost-highest wave, showed that the particle acceleration at the crest of a limiting wave is downwards and equal to $0.388g$. More recently, Longuet-Higgins (1985) has pointed out the importance of distinguishing between the particle acceleration (Lagrangian) and the apparent acceleration (Eulerian) in waves of finite amplitude: the apparent acceleration at the crest of a limiting wave tends to be minus infinity whereas the particle acceleration has a limiting value of $-0.388g$. This conclusion is supported by a later experiment by Ewing et al. (1987) who observed that while the particle acceleration seldom exceeded $0.4g$, the apparent downward acceleration reached $1.6g$. This may be a reflection of the above conclusion for regular waves being applied to random waves.

The above breaking criteria were derived assuming that the wave is regular and the flow is steady and irrotational. Theoretical derivations of the criteria for irregular waves are not available yet, and these criteria are usually determined by experiment.

For example, Ochi and Tsai (1983) suggested an empirical criterion for irregular waves

$$H_{max} = 0.020gT^2, \tag{1.6}$$

which would imply that irregular waves break at a lower height than Eq. (1.3) predicts. This criterion does not appear to agree with the data of Holthuijsen and Herbers (1986). Longuet-Higgins (1988) suggests that the discrepancy can be explained by the effects of long waves on short waves as described below.

Extensions of breaking criteria to other more complicated cases include considerations of wind drifts and swells. Banner and Phillips (1974) pointed out that the presence of wind drifts would augment the orbital velocity at the crest and help the particle velocity approach the phase speed at a smaller wave height. This may have an appreciable effect on the limiting form of small-scale waves. They also argued that when long waves move across the surface, the surface drift would be augmented near the long wave crest, and as a result, short waves tend to break preferentially at the long wave crest (Phillips and Banner, 1974). However, Longuet-Higgins (1988) interpreted this as short-long wave interactions: short waves become steeper at the long wave crest and more likely to break due to the orbital motions in the long wave.

1.3 Statistical Approaches

Many statistical investigations of wave breaking in recent years have been on the question of predicting the occurrence of breaking in deep water using the above breaking criteria. Although this problem still remains unsolved, two approaches appear to be promising. In the first approach, Ochi and Tsai (1983) derived the probability of breaking in analytic form by considering the joint distribution of wave height and period and applying the geometric criterion in Eq. (1.6), whereas in the second one, Snyder and Kennedy (1983) applied the acceleration criterion on the water surface and obtained the fraction of the sea surface covered by breaking

water

$$\beta = \frac{1}{2} - \frac{1}{2}\mathrm{erf}\left(\frac{\alpha g}{\sqrt{2m_4}}\right), \tag{1.7}$$

where

$$\mathrm{erf}(x) = \frac{2}{\sqrt{\pi}}\int_0^x e^{-t^2}dt$$

is the error function, m_4 is the fourth spectral moment and α is that used in Eq. (1.5).

Srokosz (1986) however applied the dynamical criterion at the wave crest only, leading to a simpler expression of the probability of wave breaking

$$B = \exp\left(-\frac{\alpha^2 g^2}{2m_4}\right). \tag{1.8}$$

Srokosz also showed that the value of α corresponding to the criterion in Eq. (1.6) is 0.4 in linearized theory, and demonstrated that Eq. (1.8) reproduces the result obtained by Ochi and Tsai if $\alpha = 0.4$.

All the expressions of the probability of breaking include the fourth moment of the wave spectrum m_4 and therefore depend crucially on the behavior of the high frequency tail of the spectrum. For those wave spectra with Phillips' equilibrium range (Phillips, 1985), m_4 does not exist. This difficulty could be overcome by imposing a cutoff on the spectrum at some multiple of the spectral peak frequency as in Snyder and Kennedy (1983). Clearly, the imposition leads to the probability of breaking being dependent on the cutoff frequency and the results are only applicable to wave breaking at length scales larger than the cutoff scale. Nevertheless, all measurements are subject to instrumental cutoff, and also at the scale where surface tension starts to dominate, the physics of wave breaking changes and the same breaking criterion no longer applies.

1.4 Measurement of Breaking Waves

Early observations of breaking waves have been made as whitecap coverage (Monahan and O'Muirheartaigh, 1986), which is an indirect measure and does not lend

itself to interpretation in terms of wave parameters. A more direct approach based on point measurement was first developed by Longuet-Higgins and Smith (1983) who used a jump meter to measure the rise rate of the surface elevation; breaking waves were identified when the rise rate exceeded a certain threshold, and thus the breaking probability was estimated. This approach was later modified and applied in the laboratory by Xu et al. (1986) and Hwang et al. (1989) to include measurements of breaking duration and intensity using different breaking criteria. Measurements made in the laboratory, however, cannot easily be related to the breaking process in the ocean due to a much more complex environment in the field.

Snyder et al. (1983) observed whitecaps in a fetch limited sea by triggering a camera with the sound of breaking waves within and close by its field of view. They were able to measure, in addition to the probability of breaking, the spatial and temporal scales of whitecaps. However, the observation area of the camera was rather limited (10m x 10m), and it was therefore difficult to collect sufficient breaking events for statistical analysis. Another simpler method is visual observation. Holthuijsen and Herbers (1986) observed breaking waves as whitecaps passing under a waverider that also simultaneously monitored the surface elevation. Such an approach relies apparently on subjective impression of wave breaking.

Weissman et al. (1984) detected breaking waves by searching for high frequency energy bursts exceeding a certain critical value, near wave crests in the time history of the surface elevation. It was later realized that this technique was too sensitive to small-scale events. The technique has recently been improved by using a video system to exclude microbreakers from spilling and plunging breakers (Katsaros and Atakturk, 1991), but is still limited to point measurement.

These aforementioned conventional methods have clearly not been able to provide satisfactory measurements of breaking waves. Recent develoments of remote sensing techniques, such as microwave radar (Jessup et al., 1991), active sonar (Thorpe and Hall, 1983) and passive sonar (Farmer and Vagle, 1988), provide an opportunity for improving such measurements. In particular, the sound generated by breaking

waves makes it possible to observe remotely the wave breaking process, and a series of experiments have thus been designed for this purpose. Farmer and Vagle (1988) observed ambient sound with a single hydrophone placed close to the surface and found that the time series of ambient sound spectrum level tends to show a period twice the period of the dominant surface waves. This is consistent with the earlier observation that wave breaking tends to occur in groups at one half the dominant wave frequency (Donelan et al., 1972). More recently, Crowther and Hansla (1990) used an incoherent array of narrow-beam, high-frequency transducers to track sea surface noise and found that the speed of noise was approximately equal to one half the wind speed. In the laboratory, the acoustic power radiated by a breaking wave has been found to be proportional to the dissipated mechanical energy due to breaking (Melville et al., 1988; Loewen and Melville, 1991a), implying that the dynamical properties of breaking waves could also be acoustically probed.

The observations by Farmer and Vagle have demonstrated the feasibility of using passive acoustics to study breaking waves, but have mainly been limited to the study of their temporal properties. The approach described in this thesis has advanced one step further by using a hydrophone array to make simultaneous spatial and temporal measurement of breaking waves and allow estimation of the acoustic power radiated from individual breaking waves, as described in the thesis.

Chapter 2

Experiment and Instrumentation

Field observation and interpretation of the intermittent and rapid wave breaking process still remains a challenging task. The necessary instruments require both a fast response and good areal coverage, and the results must be correlated with the important surface wave field parameters. The Surface Wave Processes Program (SWAPP) described below was the first experiment in which a variety of new observation techniques for measuring surface wave processes were simultaneously employed, allowing intercomparison of results from these techniques and providing more complete measurements of the wave breaking process. As a contribution to SWAPP, a novel acoustical instrument and the related data processing system were developed for measurement of breaking waves, as described in detail subsequently.

2.1 The SWAPP Experiment

SWAPP was a cooperative open ocean experiment carried out during February and March, 1990, 600 miles west-north-west of San Diego (35^0 N, 127^0 W; see also Fig. 2.1). The experiment included the R/P FLIP, the Canadian vessel CSS PARIZEAU, and a drifting acoustic package (A schematic view of the experiment is shown in Fig. 2.2). FLIP was moored at a fixed location and provided a focal point for the experiment. Aboard FLIP were both direct and remote sensing devices for

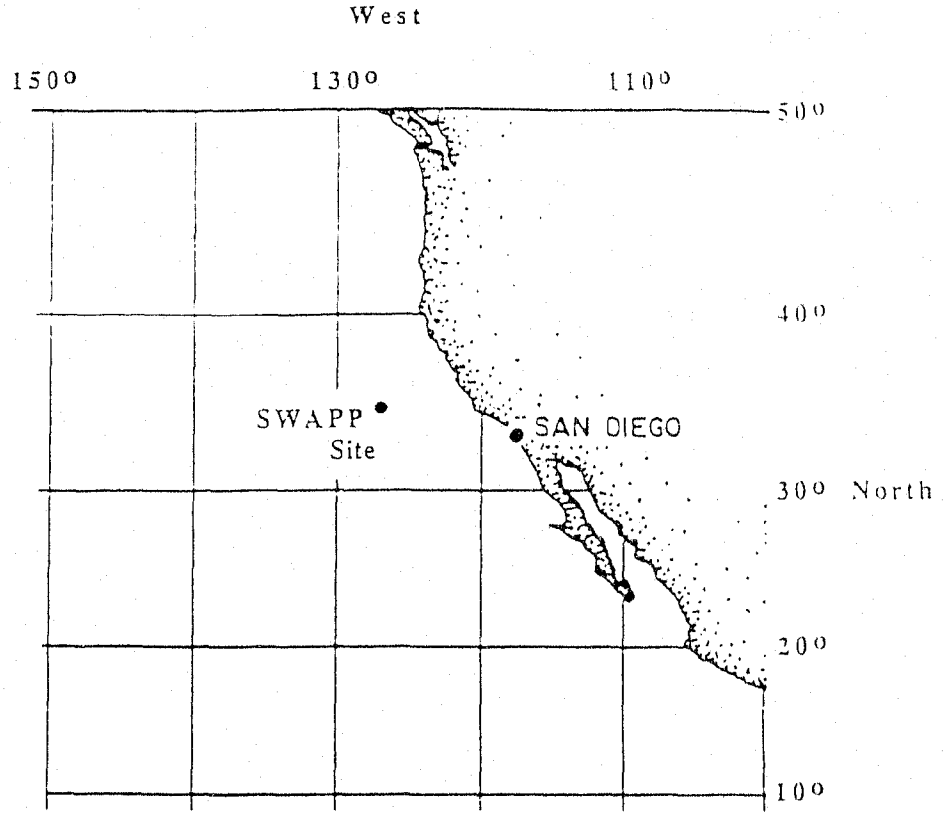

Figure 2.1: The Surface Wave Processes Program experimental site. The experiment was carried out in February/March, 1990.

the measurements of air-sea fluxes, the surface wave field, and the vertical structure of the mixed layer. Standard meteorological and oceanographic measurements were also made from both FLIP and PARIZEAU throughout the whole experiment.

The acoustical instrument described in the next section was used to measure local breaking wave properties, such as breaking duration and velocity. Directional wave spectra were also simultaneously measured with a multi-frequency, multi-beam Doppler sonar array on FLIP. These observations were made under a variety of wind and wave conditions. Comparison between the acoustical observations of breaking wave statistics and the directional wave spectra has been the main theme of this thesis.

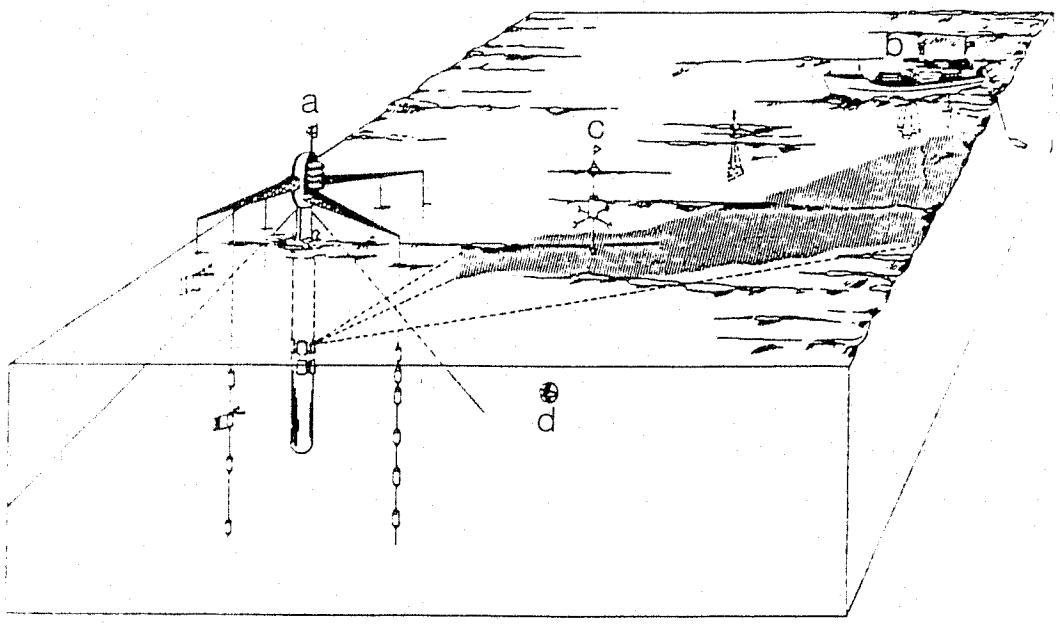

Figure 2.2: Schematic view of SWAPP. (a) Research plotform FLIP. A Doppler sonar system was placed on FLIP for measurement of directional wave spectra; (b) Research vessel CSS Parizeau; (c) Acoustic package for measurement of local breaking waves; (d) Neutrally buoyant float for tracking the motion of subsurface water.

2.2 The Acoustical Instrument

Figure 2.3 shows a diagram of the instrument. (This instrument and the data processing hardware described below were developed by Ron Teichrob, Craig Elder and Doug Sieberg.) The whole system is designed for more comprehensive meaurement of ocean-surface processes. In field experiments, it is suspended from a surface float by a rubber cord, which effectively decouples the instrument from the rapid motion at the ocean surface. A heavy mass is added to the instrument from below to increase its stability. The surface float is covered with thick plastic foam to reduce the sound of wave impact.

The instrument consists of a hydrophone array, four sidescan sonars, six vertically-oriented multifrequency echosounders, and several environmental sensors. Active sonars are used to measure bubble size distributions, two-dimensional bubble cloud distributions, and organized near-surface flows and will not be described here (A more complete description of this system is given in Farmer et al., 1990). A broadband hydrophone is mounted at the ends of four motor-driven arms that are extended when the instrument is at a safe depth and retracted prior to recovery. Opposite arms have a span of 8.5 m when they are fully open. This array is used to track individual breaking waves. The environmental sensors include a pressure sensor, an accelerometer, a magnetic compass, and two tiltmeters. These allow determination of the depth and orientation of the instrument. An additional tiltmeter is mounted on one of the arms for monitoring their deployment status. These sensors are all necessary for the correction of target locations, as discussed in the following chapter.

2.3 Data Recording and Processing

The data collection scheme for the hydrophone channels is show in Fig. 2.4. We have used Met Ocean NH4123 hydrophones with preamplifiers. Signals from the six hydrophones are lowpass filtered at 5.5 kHz and then sampled at 11 kHz by a multiplexer. The sampled signals are then digitized at 16 bit resolution and encoded

in a suitable format for recording with a digital audio PCM (Pulse code Modulation) unit (SONY PCM-501/601); the outputs are recorded onto a VHS video cassette recorder (VCR). (Conversion of PCM numbers to sound pressure is described in Appendix A.) Such a VCR allows a data rate of 176 kbytes per second, and is therefore capable of recording 8 channels of 16 bit digital data at a rate of 11 kHz. Each VCR tape is 8 hours long, providing 5 gigabytes of data storage on the video track. In addition, annotation data are simultaneously stored on the audio track of the tape, allowing accurate time synchronization.

The instrument has four VCRs for the hydrophone channels, allowing 32 hours of continuous recording for each deployment. Analysis of such a huge volume of data places special demands on high speed signal processing techniques. We have therefore developed a real time processing system as shown in Fig. 2.5. Data stored on a VCR tape are played back at the same rate as they were recorded by a digital audio processor (Sony PCM-501/601) which decodes the video signal into a serial digital data stream. The serial data from the PCM are converted to parallel 16-bit words and stored in a hardware Fast Input and Fast Output (FIFO) buffer. A high speed digital signal processing (DSP) board (Motorola 56001 capable of performing a 1024 point complex FFT within 3.39 ms) reads data from the FIFO, performs the first stage of processing, feeds the results to a host HP486 Vectra computer, and then goes back to read data. The host computer can display the outputs on the screen or stores them onto its hard disk for final processing. Simultaneously, annotation data on the VCR audio track are demodulated into a serial digital data stream, converted to parallel and stored in a FIFO buffer. The host computer can take the data as required for adding time and date stamps, as well as applying corrections for tilt and direction.

As described in the next chapter, the tracking of sound sources essentially involves computation of cross correlations. A DSP program has been developed that performs multiple cross correlations of signals from the hydrophone channels using the Fast Fourier Transform (FFT).

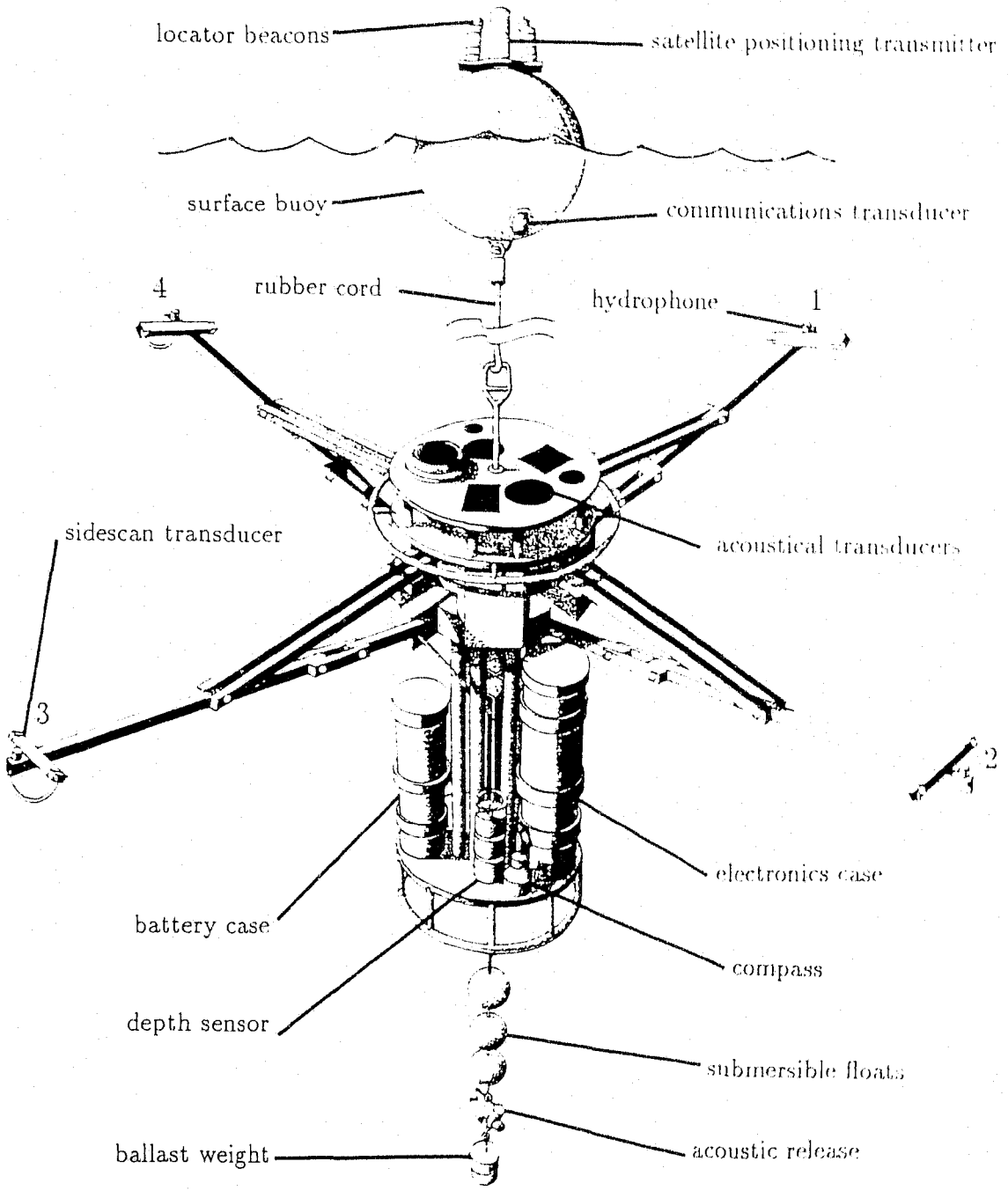

Figure 2.3: Acoustic instrument for passive tracking of breaking waves. The instrument is suspended at a depth of 25 m below the surface. Omnidirectional hydrophones are placed at the ends of the arms (total span 8.5 m). The instrument was deployed in the Surface Wave Processes Program.

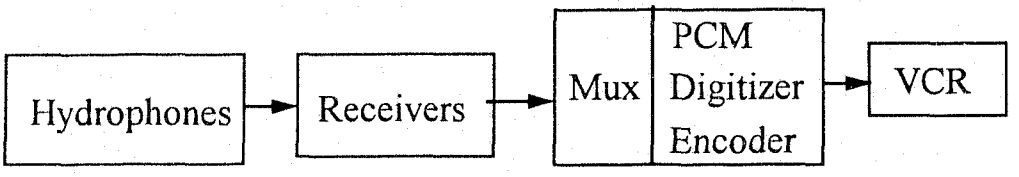

Figure 2.4: Data recording system in the acoustic instrument.

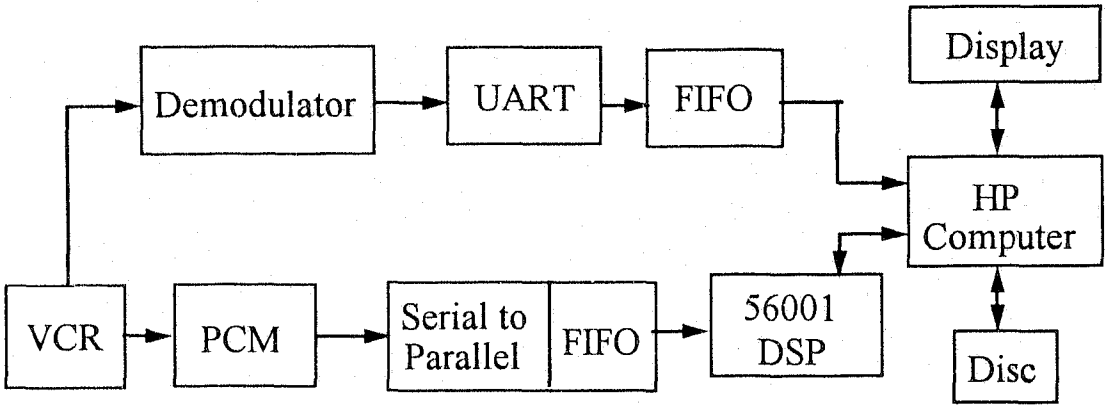

Figure 2.5: Data Processing system.

Chapter 3

Underlying Technology

One of the primary tasks of this work is to track breaking surface waves in a noisy environment. The experimental approach described in the preceding chapter makes use of an array of hydrophones suspended beneath the ocean surface. Sound emanating from an acoustic source arrives at each hydrophone at a time determined by the source position and the hydrophone position, thus allowing the source to be located from the time differences of the arrival of sound at the hydrophones and a knowledge of the array geometry. The choice of Time Delay Estimation (TDE) techniques is critical to success of the scheme, since it determines our ability to locate the source. The importance of this aspect motivates a careful examination of TDE techniques, which are discussed in this chapter and constitute the essential engineering link in the thesis.

The problem of determining target directions or locations has a long history. Numerous methods have been developed, from the delay-and-sum method for a single beam (Clay and Medwin, 1977) to the newly developed matched beam method that is based on the use of even-symmetric and odd-symmetric beam patterns (Henderson, 1985). In many cases of naturally occurring acoustical sources, like the sound generated by wave breaking, signals cover a certain frequency band, but there is no *a priori* knowledge about the frequency characteristics. There is a class of techniques, known as the Generalized Cross Correlation method (Knapp and Carter,

1976), which is particularly useful in broadband time delay estimation. It estimates the time delay between signals at two hydrophones by cross correlating the filtered outputs of the hydrophones and determining the position of the peak in the correlation. The GCC method is robust and has the advantage of simplicity. It serves as the fundamental signal processing technique in our tracking system, and will be reviewed below.

The correlation approach will in principle allow us to locate and track individual breaking waves. However, inasmuch as real data departs from the simplified model of well defined, discrete sound sources, some special techniques are needed to extract useful information from the data. Therefore, after reviewing the GCC method, we shall discuss the use of correlation sequences or images in identifying and tracking sound sources. Then, we shall address the problem of determining source position from the estimated time delays and the array geometry with corrections for the motion of the array. The whole signal processing scheme will be illustrated by analysing a short segment of the SWAPP data. Limitations of the method will also be discussed.

3.1 Generalized Cross Correlator

Consider a signal from a radiating source received at two spatially separated hydrophones in a noisy but homogeneous environment, as shown in Fig. 3.1. The received signals at the hydrophones can be modelled as

$$\begin{aligned} x_1(t) &= s(t) + n_1(t), \\ x_2(t) &= \alpha s(t - D) + n_2(t), \end{aligned} \tag{3.1}$$

where α is the attenuation factor and D is the time delay, both of which will be regarded as constant. It is assumed that $s(t)$, $n_1(t)$, and $n_2(t)$ are jointly stationary random processes. For a simple case where the signal and noise are mutually uncorrelated, we have

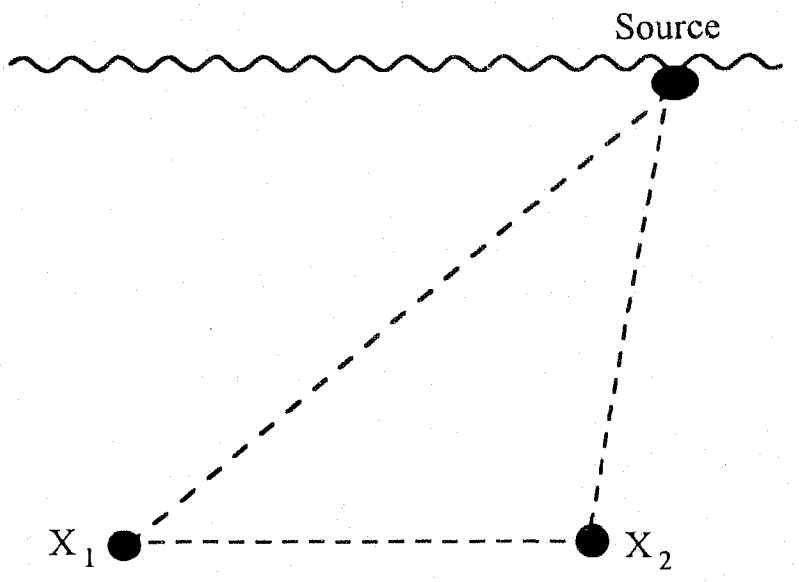

Figure 3.1: Acoustic source and hydrophones for the time delay estimation model. The source is assumed to be at the ocean surface, and the medium homogeneous.

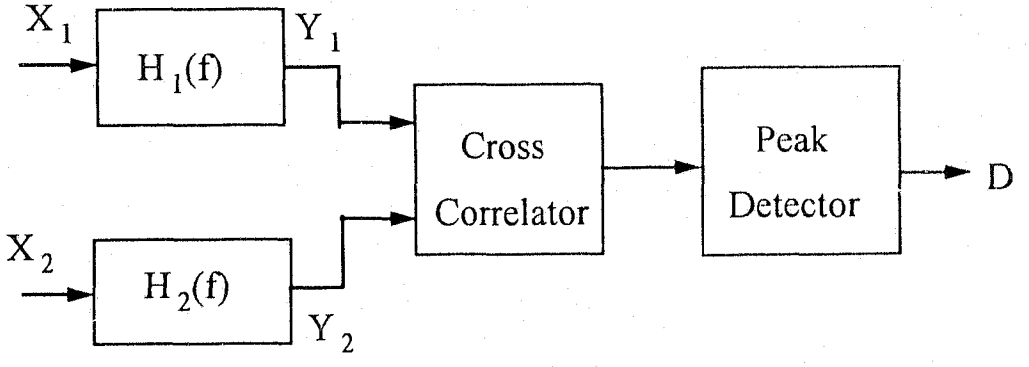

Figure 3.2: Generalized Cross Correlator. Signals received at the hydrophones shown in Fig. 3.1 are filtered by $H_1(f)$ and $H_2(f)$ respectively. Then the filtered outputs are cross-correlated. A peak detector is applied on the correlation output to determine the estimated delay.

$$R_{x_1x_2}(\tau) = E[x_1(t)x_2(t+\tau)] = \alpha R_{ss}(\tau - D).$$

Since $R_{ss}(\tau - D)$ achieves its maximum value at $\tau = D$, the time delay D is given by the argument τ that maximizes $R_{x_1x_2}(\tau)$. By assuming ergodicity, $R_{x_1x_2}(\tau)$ can be obtained with the time-average of one sample function. In reality, the observation time T is always finite, and $R_{x_1x_2}(\tau)$ can only be estimated

$$\hat{R}_{x_1x_2}(\tau) = \frac{1}{T-\tau}\int_0^{T-\tau} x_1(t)x_2(t+\tau)dt.$$

In fact, $\hat{R}_{x_1x_2}(\tau)$ can be computed more efficiently in the frequency domain, that is (omitting the scaling factor $1/(T-\tau)$ for convenience)

$$\hat{R}_{x_1x_2}(\tau) = \frac{1}{2\pi}\int_{-\infty}^{\infty} \phi_{x_1x_2}(\omega)e^{j\omega\tau}d\omega, \tag{3.2}$$

where $\phi_{x_1x_2}(\omega)$ is the estimated cross spectrum of $x_1(t)$ and $x_2(t)$ over the finite observation time T, and the ensemble average of $\phi_{x_1x_2}$ is equal to the true cross spectrum, $\Phi_{x_1x_2}(\omega)$. The direct correlation may not yield good estimates, especially when the signal-to-noise ratio is low or other interference exists. To improve the performance of the estimator, it is desirable to prefilter the received signals before the correlation, as illustrated in Fig. 3.2. This is equivalent to applying a window function to modify $\phi_{x_1x_2}(\omega)$, that is,

$$\hat{R}_{x_1x_2}(\tau) = \frac{1}{2\pi}\int_{-\infty}^{\infty} W(\omega)\phi_{x_1x_2}(\omega)e^{j\omega\tau}d\omega, \tag{3.3}$$

where

$$W(\omega) = H_1^*(\omega)H_2(\omega).$$

Such a correlator is referred to as the generalized cross correlator (GCC). Various prefilters have been suggested to suit the varied situations that can be encountered in practice (Knapp and Carter, 1976; Hassab and Boucher, 1979). We just list some of them here.

Basic Correlator:

$$W(\omega) = 1.$$

Maximum Likelihood (ML) Window:

$$W_{\mathrm{ML}}(\omega) = \frac{1}{|\Phi_{x_1x_2}(\omega)|} \frac{|\gamma_{12}(\omega)|^2}{(1 - |\gamma_{12}(\omega)|^2)}, \tag{3.4}$$

where

$$\gamma_{12}(\omega) = \frac{\Phi_{x_1x_2}(\omega)}{\sqrt{\Phi_{x_1}(\omega)\Phi_{x_2}(\omega)}} \tag{3.5}$$

is the complex coherence function. When the spectra are unknown,the ML window can be approximately obtained using the estimated spectra. Such an estimator is called the Approximate Maximum Likelihood (AML) estimator.

Smoothed Coherence Transform (SCOT) Window:

$$W_{\mathrm{SCOT}}(\omega) = \frac{1}{\sqrt{\Phi_{x_1}(\omega)\Phi_{x_2}(\omega)}}. \tag{3.6}$$

This was originally developed by Carter *et al.* (1973) to counteract the undesirable effects of strong tonals in broadband signals.

Phase Transform (PHAT) window:

$$W_{\mathrm{PHAT}}(\omega) = \frac{1}{|\Phi_{x_1x_2}(\omega)|}. \tag{3.7}$$

This is a pure *ad hoc* window that uses the phase information only. The apparent defect is that if $\Phi_{x_1x_2}(\omega) = 0$ at some frequencies, W_{PHAT} is undefined at these frequencies.

3.2 Performance Evaluations

The variance of the time delay estimate in the neighbourhood of the true delay for a generalized correlator is given by

$$\mathrm{var}(\hat{D}) = \frac{2\pi \int_{-\infty}^{\infty} |W(\omega)|^2 \omega^2 \Phi_{x_1}(\omega)\Phi_{x_2}(\omega)(1 - |\gamma_{12}(\omega)|^2)d\omega}{T\left[\int_{-\infty}^{\infty} \omega^2 |\Phi_{x_1x_2}(\omega)| W(\omega)d\omega\right]^2}. \tag{3.8}$$

It can also be shown that for the ML window, $\mathrm{var}(\hat{D})$ achieves the Cramer-Rao

lower bound (CRLB)

$$\mathrm{var}(\hat{D}) \geq -\left\{ E\left[\frac{\partial^2 \ln p(\mathbf{x}|Q,\tau)}{\partial^2 \tau} \right] \right\}^{-1}_{\tau=D}, \tag{3.9}$$

that is, $\mathrm{var}(\hat{D})_{ML}$ is given by

$$\mathrm{Min\ var}(\hat{D}) = \left\{ \frac{T}{2\pi} \int_{-\infty}^{\infty} \frac{\omega^2 |\gamma_{12}(\omega)|^2}{1 - |\gamma_{12}(\omega)|^2} d\omega \right\}^{-1} \tag{3.10}$$

(Knapp and Carter, 1976). Note that Eq. (3.8) evaluates the local variation of the time-delay estimate; ambiguous peaks are not considered which may result from a relatively short averaging time for the given signal and noise characteristics. However, the ambiguous peaks can be eliminated by selecting persistent patterns in correlation sequences as described below. Eq. (3.8) also assumes that the frequency characteristics of signal and noise are known precisely. Since the spectra can be accurately estimated as T goes to infinity, Eq. (3.8) should be a good performance predictor for a sufficiently large T.

In order to evaluate the performances of various windows in a real environment, we use a short data segment collected during SWAPP. Figure 3.3 shows a comparison among various GCC functions for the data associated with Event 1 in Fig. 3.12. It can be seen from (a)-(d) that AML, SCOT and PHAT tend to sharpen the peak compared with BASIC in (a) at the cost of markedly decreasing its amplitude. AML and SCOT have essentially the same quality. PHAT shows a much higher peak than SCOT and AML, though its background is noisier. A similar comparison made previously using ship noise also indicates that PHAT provides the best performance (Ferguson, 1989).

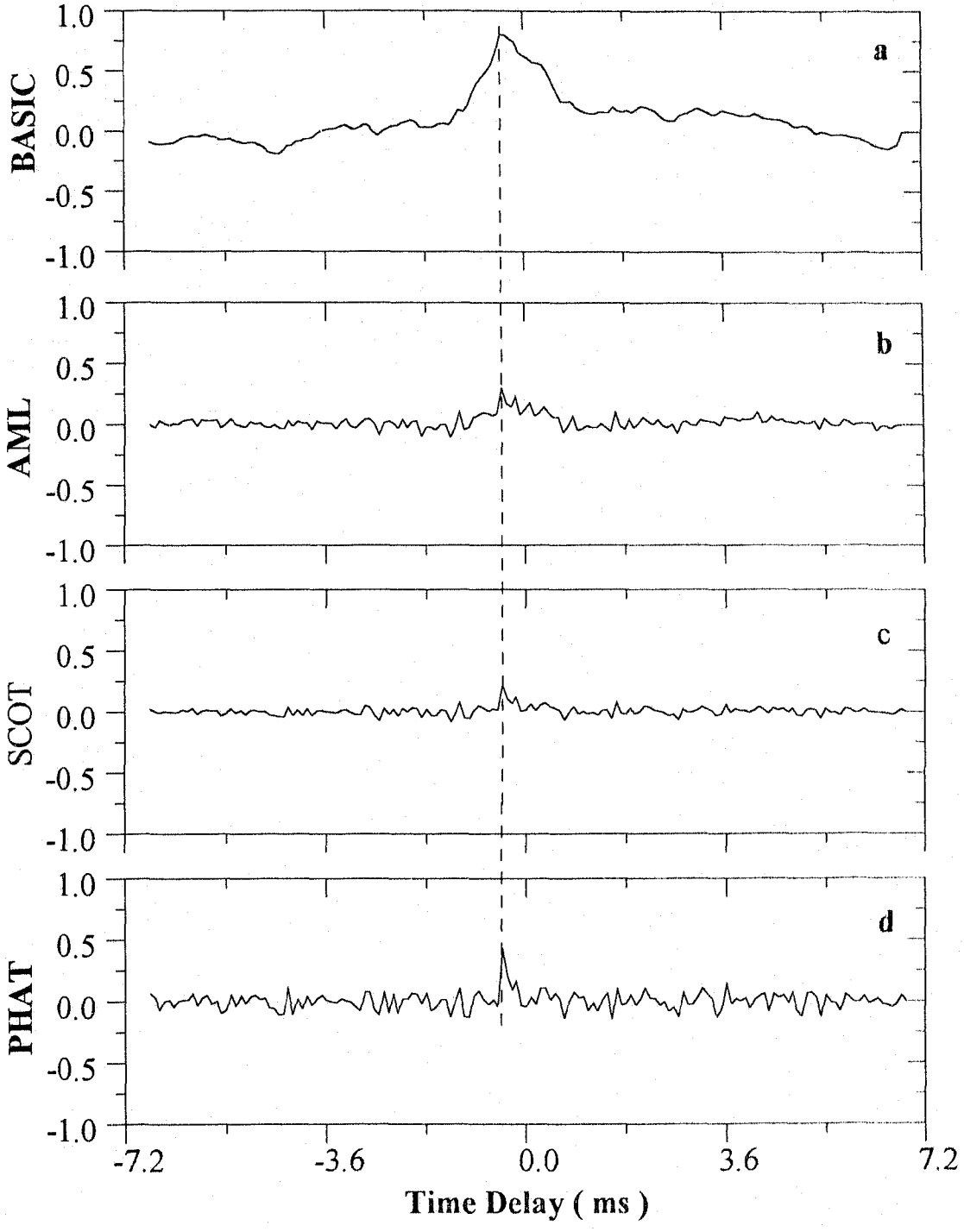

Figure 3.3: A comparison of various GCC windows, as applied to the SWAPP data. (a) BASIC; (b)AML (Approximate Maximum Likelihood); (c) SCOT (Smoothed Coherence Transform); (d) PHAT (Phase Transform).

Window	BASIC	AML	SCOT	PHAT
$\sigma_{\hat{D}}(\mu s)$	4.50	2.76	3.49	9.38

Table 3.1: Deviation of the estimated delay for various windows

The deviation of the estimated delay $\hat{D}$ is also calculated for different windows by estimating spectra and coherence from the data and substituting into Eq. (3.8). The results are given in Table 3.1. As expected, AML gives the least deviation of $\hat{D}$ since the ML estimator achieves the CRLB bound. PHAT has the largest deviation, but as seen from the table, the deviation is still small compared to the sampling period ($T_s = 90.7\mu s$). An error of one sampling period in the estimated time delay may cause an error of ± 1 m at a range of 35 m. From Fig. 3.3 and Table 3.1, it can be seen that PHAT yields a more distinct peak than AML and SCOT, and a sharper peak than BASIC; morever the estimation error it may cause is acceptable. Based on such a practical consideration, we will choose the PHAT window for subsequent data processing.

3.3 Correlation Image

As explained in the preceding section, the time delay of a signal arriving at two hydrophones is determined by the position of the correlation peak. However, it may be difficult to identify the peak from an individual correlation at any instant(i.e. Fig. 3.3). In such a case, we have to resort to additional physical information.

It can be conjectured that if a peak in the correlation is associated with the signal, its position should persist within a certain area from one snapshot to the next. If the peak is due to random noise, then there should be no such spatial and temporal persistence. Therefore our strategy here is to perform cross correlations as a time sequence, with the interval between two consecutive correlations being the averaging time for each correlation, and then to identify the persistence structure. Figures 3.4b and c show an image plot of correlation time sequences for two hydrophone pairs

based on a 45 s segment of the SWAPP data (using the PHAT window). The horizontal axis is time and the vertical axis represents the delay argument in cross correlation. The gray scale denotes correlation level. The temporal persistence structure is clearly revealed in the image as the dark streaks that represent the passage of moving sources. The root-mean- square (rms) sound level is also shown as a time series in Fig. 3.4a. (See also Appendix A for calibration of the pressure level.) It can be seen that the well-defined peaks in the sound level are generally coincident with the dark streaks. Previous observations in which simultaneous video and hydrophne records were acquired show that similar bursts in the sound level are consistent with the occurrence of visible whitecaps (Crowther and Hansla, 1990). This further confirms that the dark streaks in the correlation image are associated with breaking waves.

Figure 3.6 shows a relatively quiet period of data (135 s later than Fig. 3.4) where only a few small events are seen and the rms record does not show as large variability as in Fig. 3.4. Figure 3.7 shows another louder period in which a number of large events occur in groups. These data were acquired in a high sea state (W=11 ms^{-1}, corresponding to dataset 3 in Table 5.1). Figures 3.8- 3.10 show correlation images in a lower sea state (W=6.4 ms^{-1}, corresponding to dataset 22 in Table 5.1), for a period of 135 s. It can be seen that breaking events in a lower sea state occur more frequently. However, their duration is in general shorter, implying that these events have a smaller scale.

It should be pointed out that there are some streaks that appear much more clearly on one hydrophone pair than the other. This would most probably be due to finite dimension of the source and will be discussed later.

Careful thought must be given to the choice of correlation averaging time, T. It should be short enough that a source position does not change significantly during the averaging time and long enough that statistical errors due to finite observation are acceptable. On the basis of these two considerations, T was chosen to be 85.6 ms (944 digital data at a sampling frequency of 11 kHz). As will be seen later, the speed of a breaking event is typically of order 5 ms^{-1}. During the interval T, the event would travel about 0.43 meters, which is small compared with its distance to the hydrophone array (at least 25 meters). As for the statistical errors, we can use Eq.(8.104) in Bendat and Piersol (1986) as a rule of thumb, which gives the normalized rms error of cross correlation. For a cross-correlation peak with a coefficient $\rho(\tau) = 0.4$ (typical in the data, see Fig. 3.3a), the normalized rms error is 8.76%. Therefore we believe that the choice of T is reasonable.

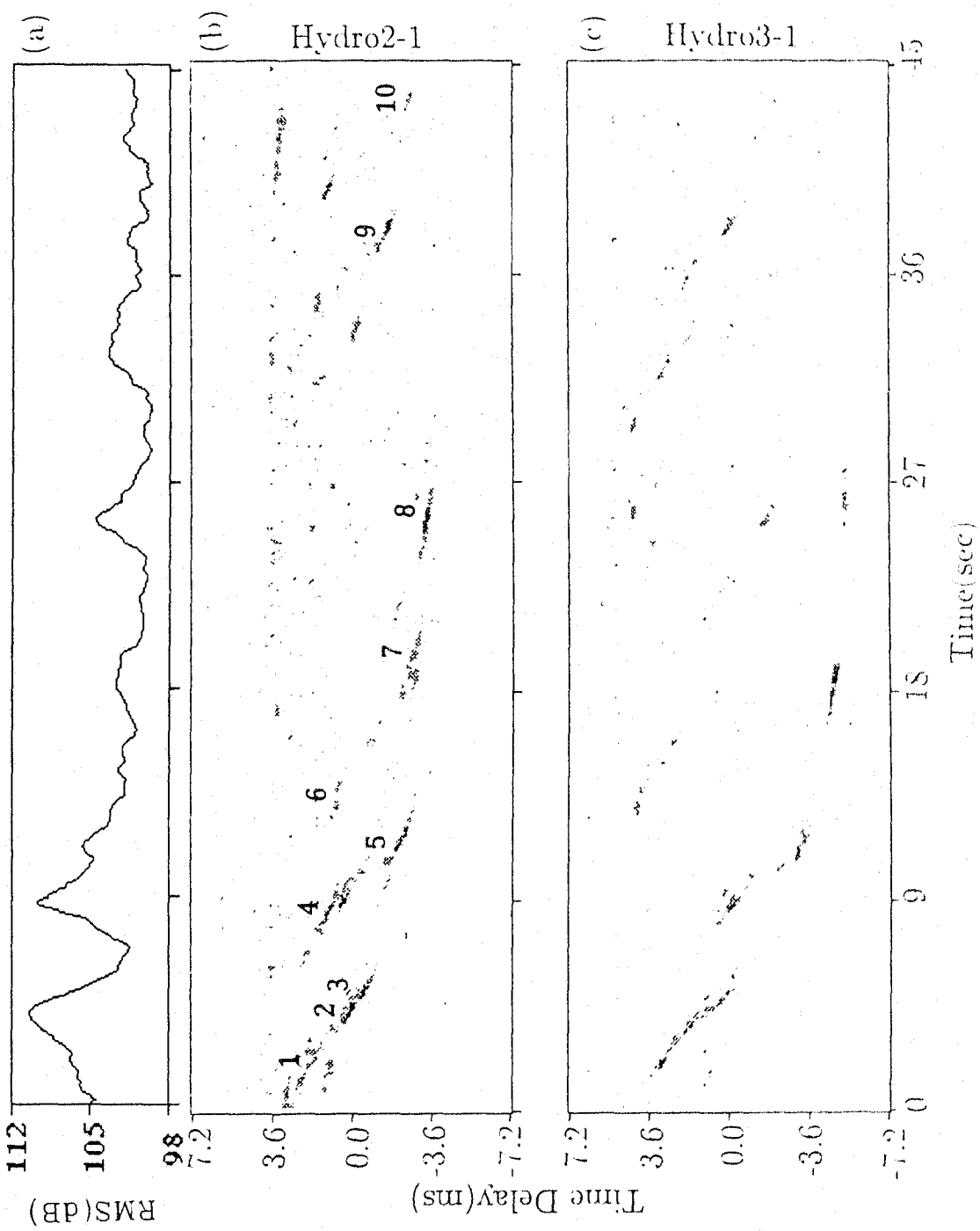

Figure 3.4: RMS sound level and correlation time sequences. Wind speed=11 ms^{-1}. Starting time: 04:56:56, 03/08/90, UTC. (a) RMS sound pressure series (ref: μPa^2); (b) and (c) are correlation sequences for Hydrophone pair 2-1 and 3-1, where the horizontal axis denotes time, the vertical axis time delay, and the gray level correlation levels. The numbered waves are the detected events.

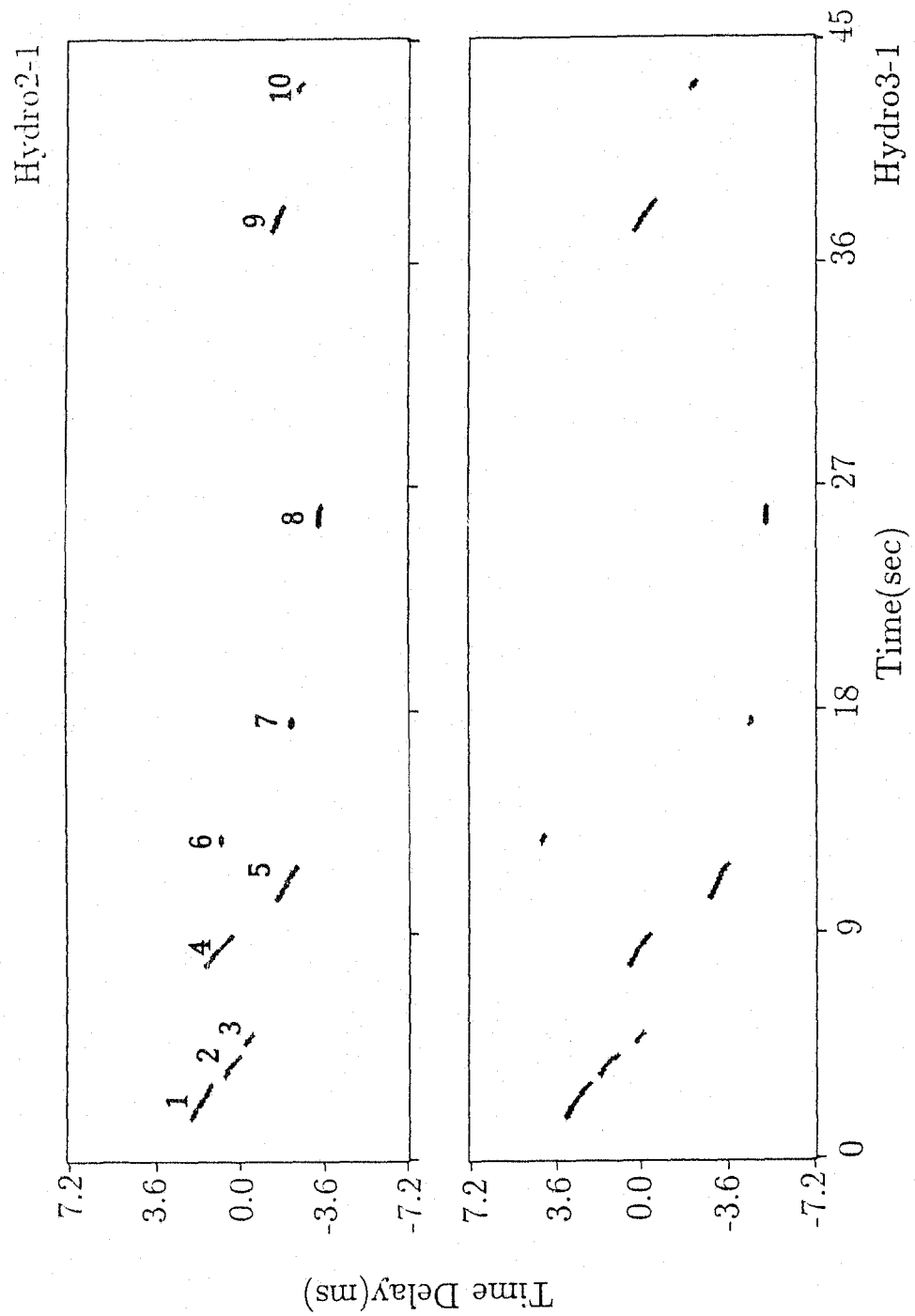

Figure 3.5: Extracted breaking events corresponding to the numbered waves in Fig. 3.4.

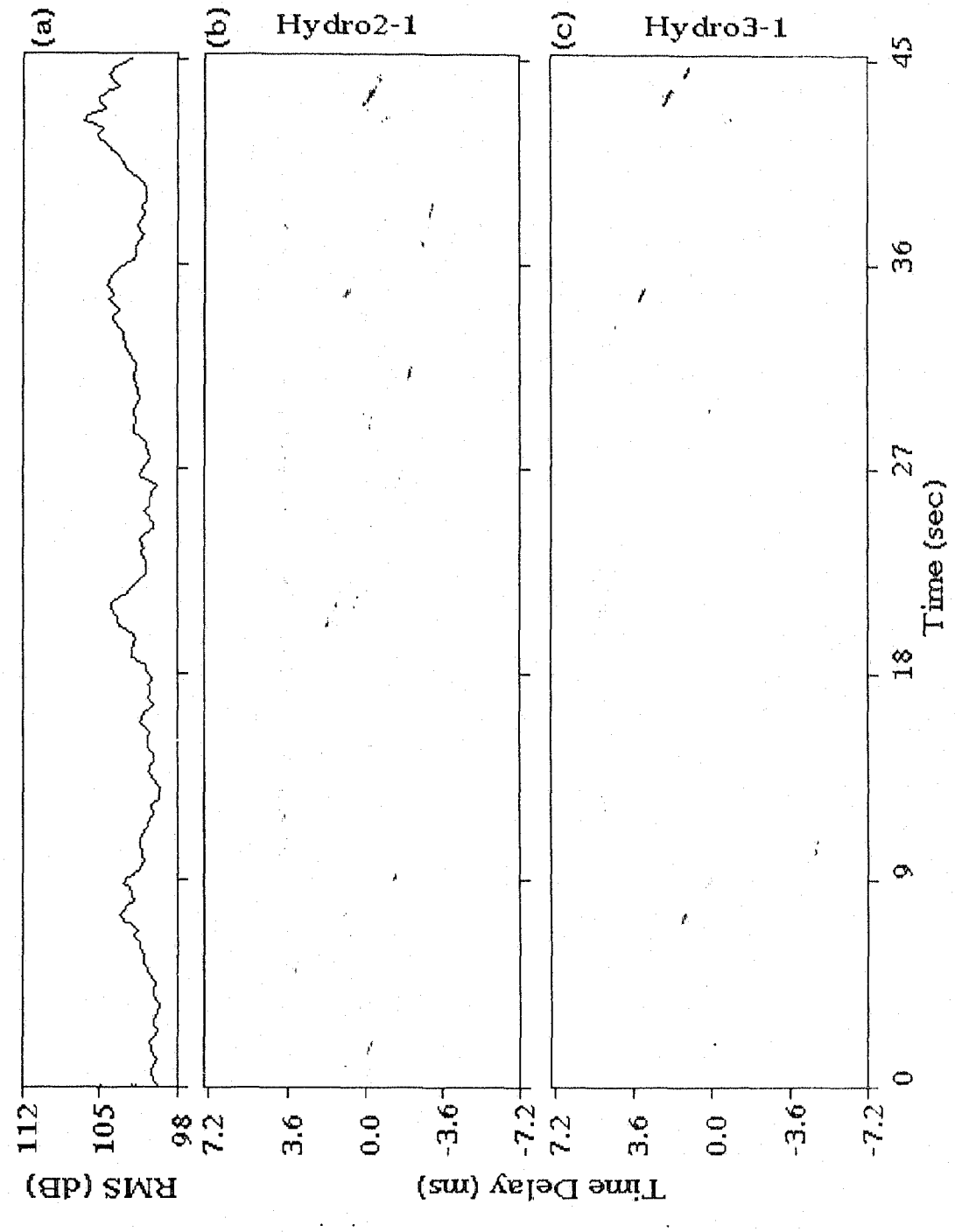

Figure 3.6: RMS sound level and correlation time sequences for a quieter 45 s data segment. Wind speed=11 ms^{-1}. Starting time: 04:59:11, 03/08/90, UTC.

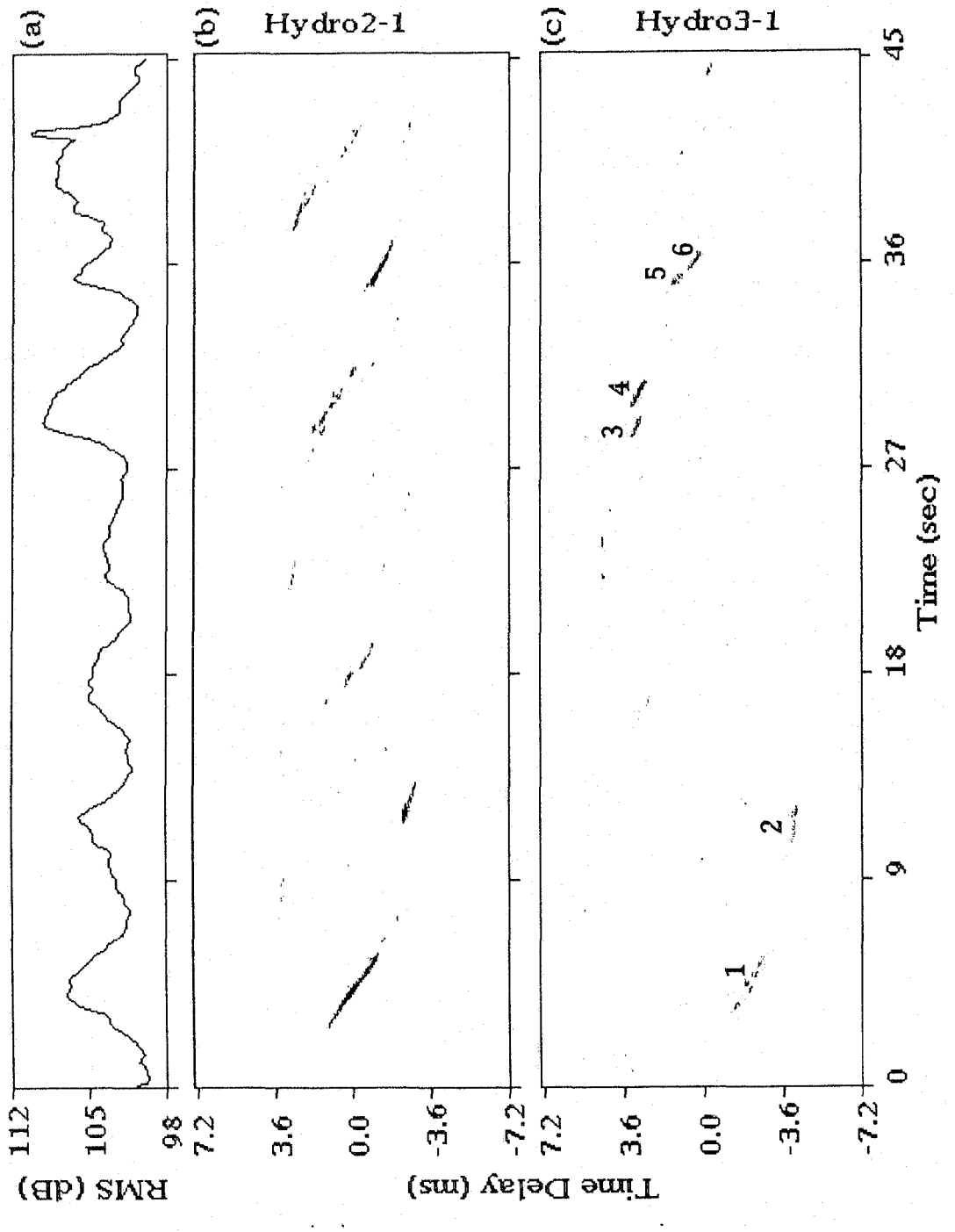

Figure 3.7: RMS sound level and correlation time sequences for another lounder 45 s data segment. Wind speed=11 ms^{-1}. Starting time: 05:17:10, 03/08/90, UTC.

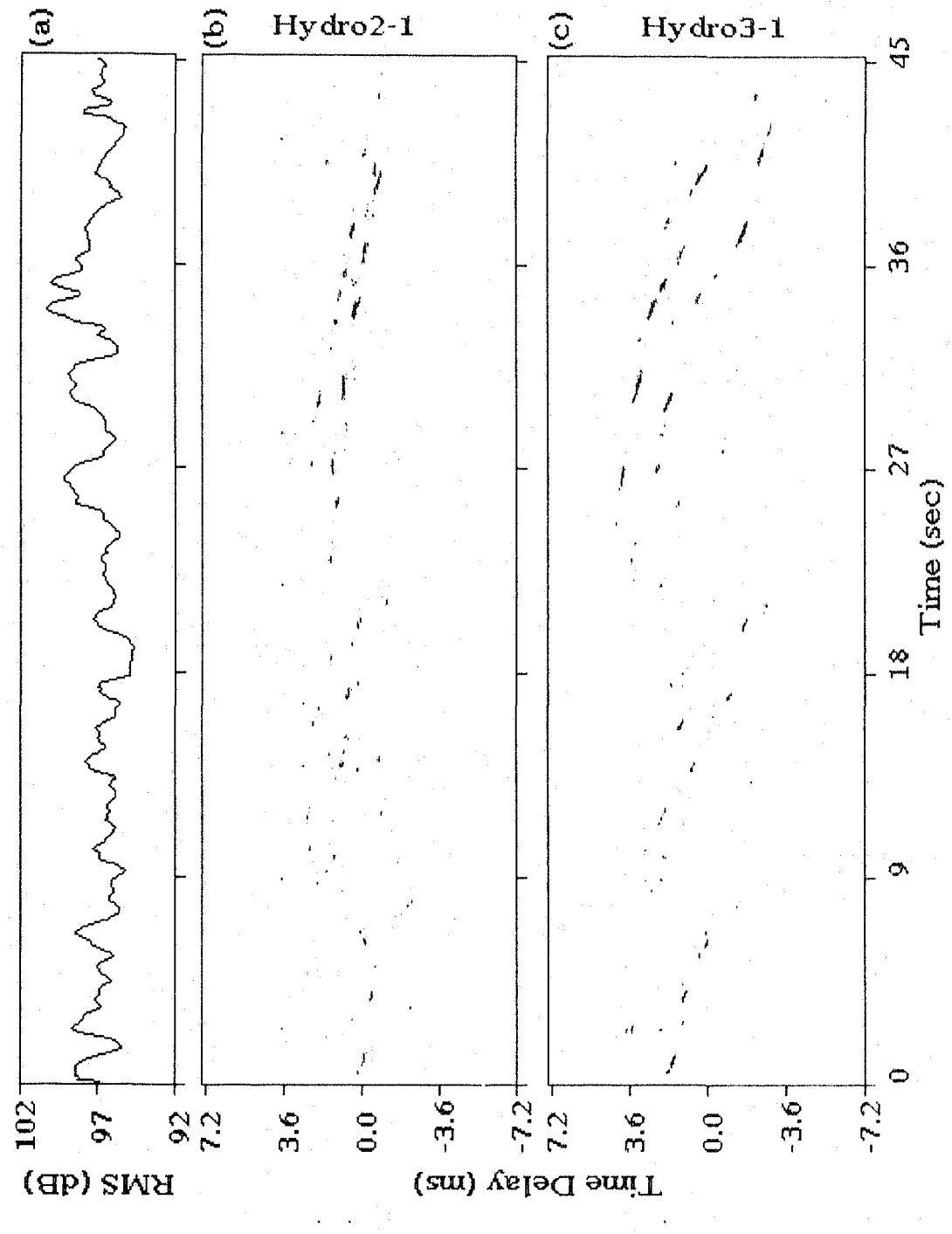

Figure 3.8: RMS sound level and correlation time sequences for a 45 s data segment. Wind speed=6.4 ms^{-1}. Starting time: 10:31:00, 03/14/90, UTC.

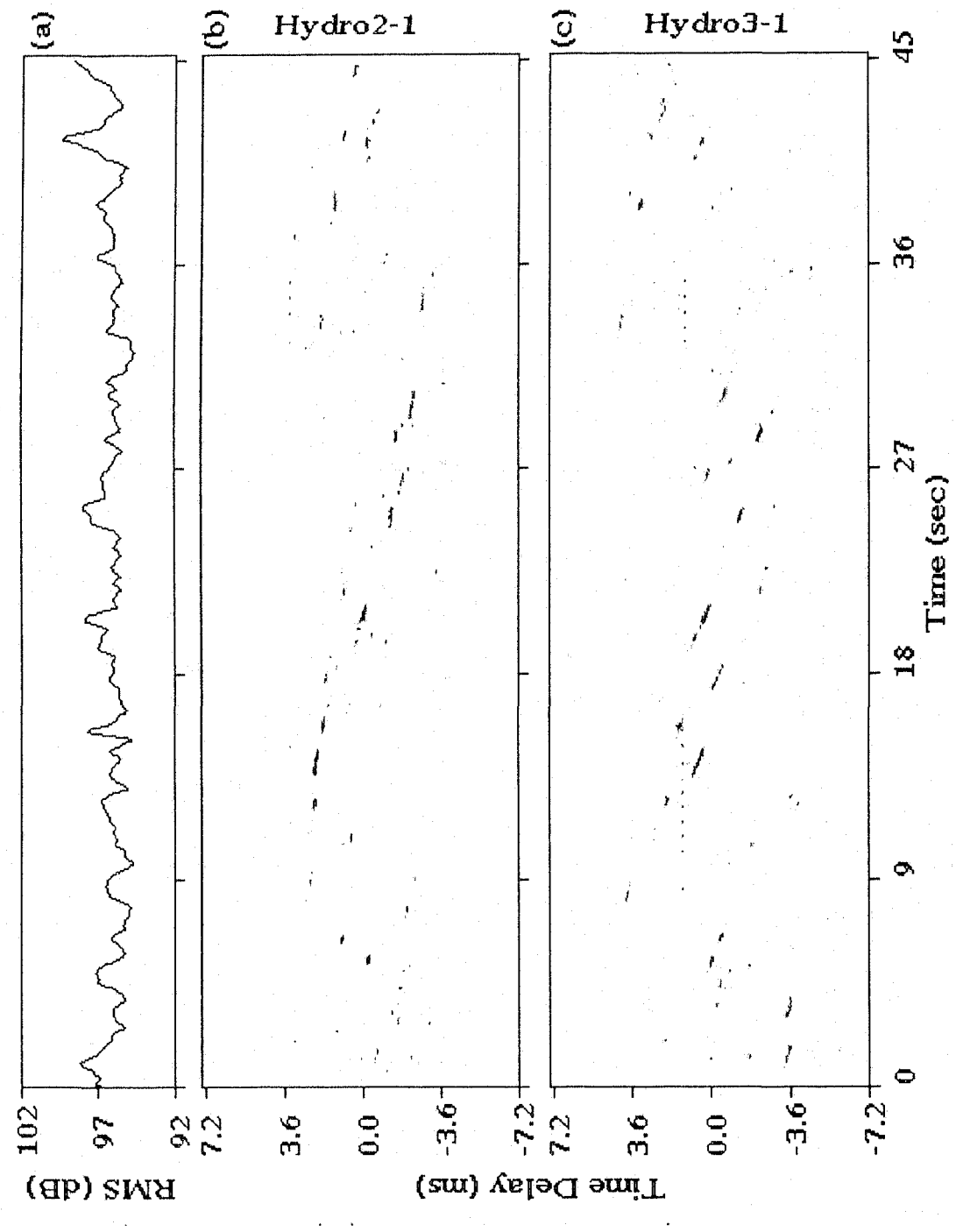

Figure 3.9: RMS sound level and correlation time sequences for a 45 s data segment. Wind speed=6.4 ms^{-1}. Starting time: 10:31:45, 03/14/90, UTC.

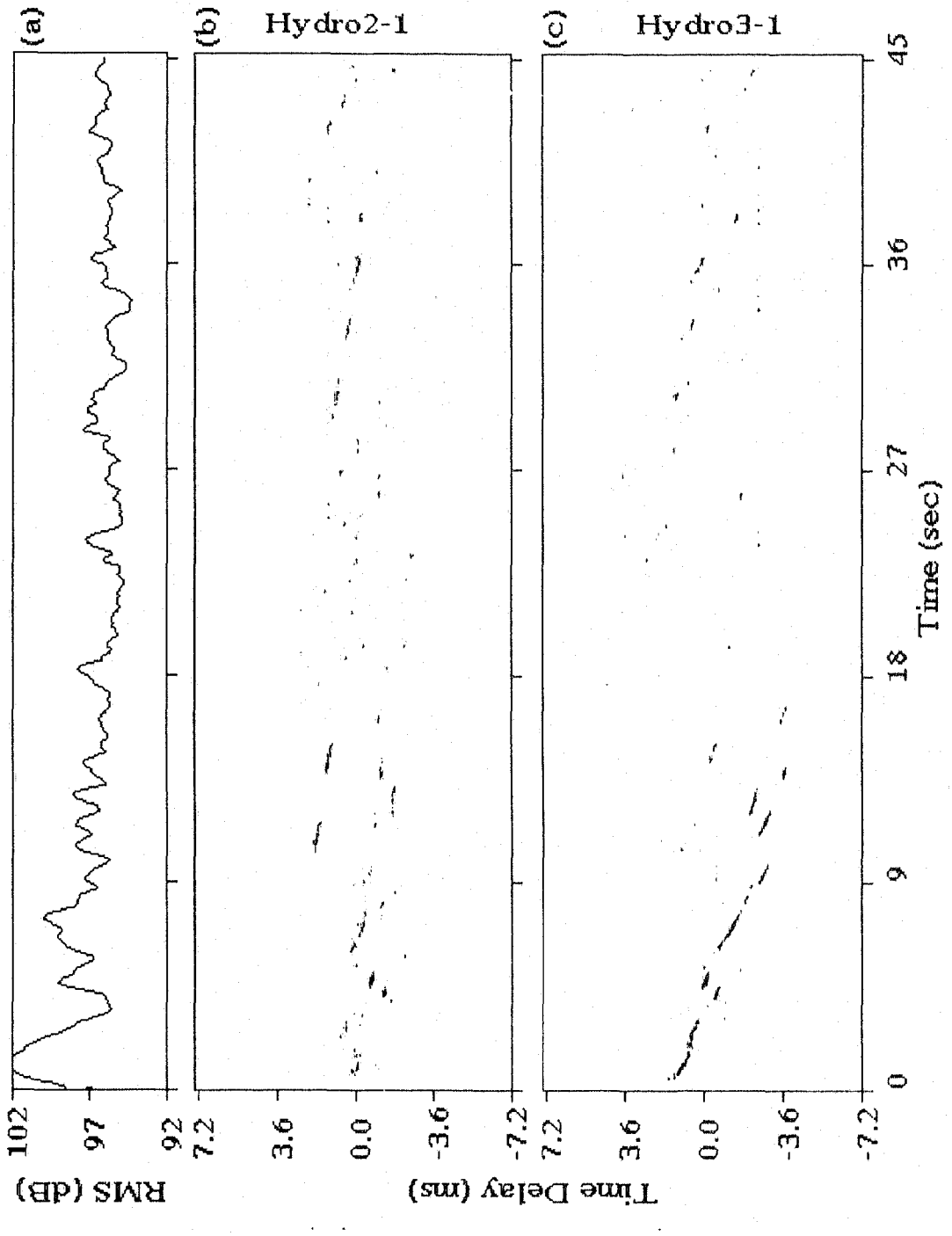

Figure 3.10: RMS sound level and correlation time sequences for a 45 s data segment. Wind speed=6.4 ms^{-1}. Starting time: 10:32:30, 03/14/90, UTC.

3.4 Event Identification

By event identification we mean extraction of the dark streaks from the correlation image. These streaks can, of course, be identified visually, but this is not practical when we have to handle a large amount of data. The capability of automatic identification must be developed. We tackle this problem in the domain of image processing and pattern recognition rather than identification of individual correlation peaks. First, the correlation image is smoothed to suppress the high frequency background noise and enhance the streaks (The correlation images are actually enhanced images after neighborhood averaging using a 3×3 running window). Then, the enhanced image is searched for dark streaks with gray level above some threshold. We notice that these streaks are nearly straight lines, with certain lengths and inclined at certain angles. These features suggest that we should search for the regions with such a pattern. The coordinates of the pixels in these regions are then least-squares fitted to a quadratic curve (or simply a straight line), that is,

$$\tau = at^2 + bt + c, \tag{3.11}$$

where τ is time delay, and t denotes time. The coefficients,a, b, and c are determined from the pixel coordinates. As an example, curves associated with the events extracted from Fig. 3.4 are shown in Fig. 3.5, where we only show those streaks that may be clearly identified on both hydrophone pairs with the identified part longer than a certain threshold.

3.5 Source Location and Correction

Time delays associated with those events that can be identified on both hydrophone pairs can be used to determine the source location given the geometry and depth of the array. The source is considered to be at the surface, and the hydrophone configuration and coordinate system are shown in Fig. 3.11.

Consider the two coordinate systems in Fig. 3.11, where the xyz-system is the

fixed system and $x'y'z'$-system the moving system. In practice, the former can be chosen to be the surface drifting layer, since the motion of waves is with respect to the moving water as well, [1] and the latter is fixed to the instrument itself. We further assume that the sound speed, c, is homogeneous and the surface flat since wave height is small compared to the depth of the instrument. In the moving system, let τ_x be the time delay between the two hydrophones along the x'-axis and assume that τ_x is positive when the source is on the positive x' side of the y'-axis. The same convention also applies to τ_y. Let the coordinates of the hydrophones in the moving system be (-a,0,0), (a,0,0), (0,a,0), and (0,-a,0). Suppose the source position in the moving system is $\mathbf{x}' = [x'\ y'\ z']^T$. We have

$$c\tau_x = \sqrt{(x'+a)^2 + y'^2 + z'^2} - \sqrt{(x'-a)^2 + y'^2 + z'^2} \tag{3.12}$$

$$c\tau_y = \sqrt{x'^2 + (y'+a)^2 + z'^2} - \sqrt{x'^2 + (y'-a)^2 + z'^2}. \tag{3.13}$$

Solving the above nonlinear equations for x' and y', we find

$$\begin{aligned} x' &= \frac{c\tau_x}{2}\sqrt{(1-\frac{c^2\tau_y^2}{d^2})\frac{d^2 - c^2\tau_x^2 + c^2\tau_y^2}{\Delta^2} + \frac{4z'^2}{\Delta^2}} \\ y' &= \frac{c\tau_y}{2}\sqrt{(1-\frac{c^2\tau_x^2}{d^2})\frac{d^2 - c^2\tau_y^2 + c^2\tau_x^2}{\Delta^2} + \frac{4z'^2}{\Delta^2}}, \end{aligned} \tag{3.14}$$

where $d = 2a$ is the spacing between opposite hydrophones, and

$$\Delta^2 = d^2 - c^2\tau_x^2 - c^2\tau_y^2.$$

In practice, τ_x and τ_y are measured with the time delay estimation technique described above. Note that Δ^2 must be positive for any pair τ_x and τ_y. If it is not, the measured delays cannot be due to the same source. This provides an additional means of excluding false peaks in the correlation output.

[1] During the experiment that is described in the following section, the surface mixed layer was 60 m deep whereas the instrument is 25 m deep. Therefore most of the drag was within the layer and the instrument drifted at approximately the same speed as the deeper portion of the mixed layer.

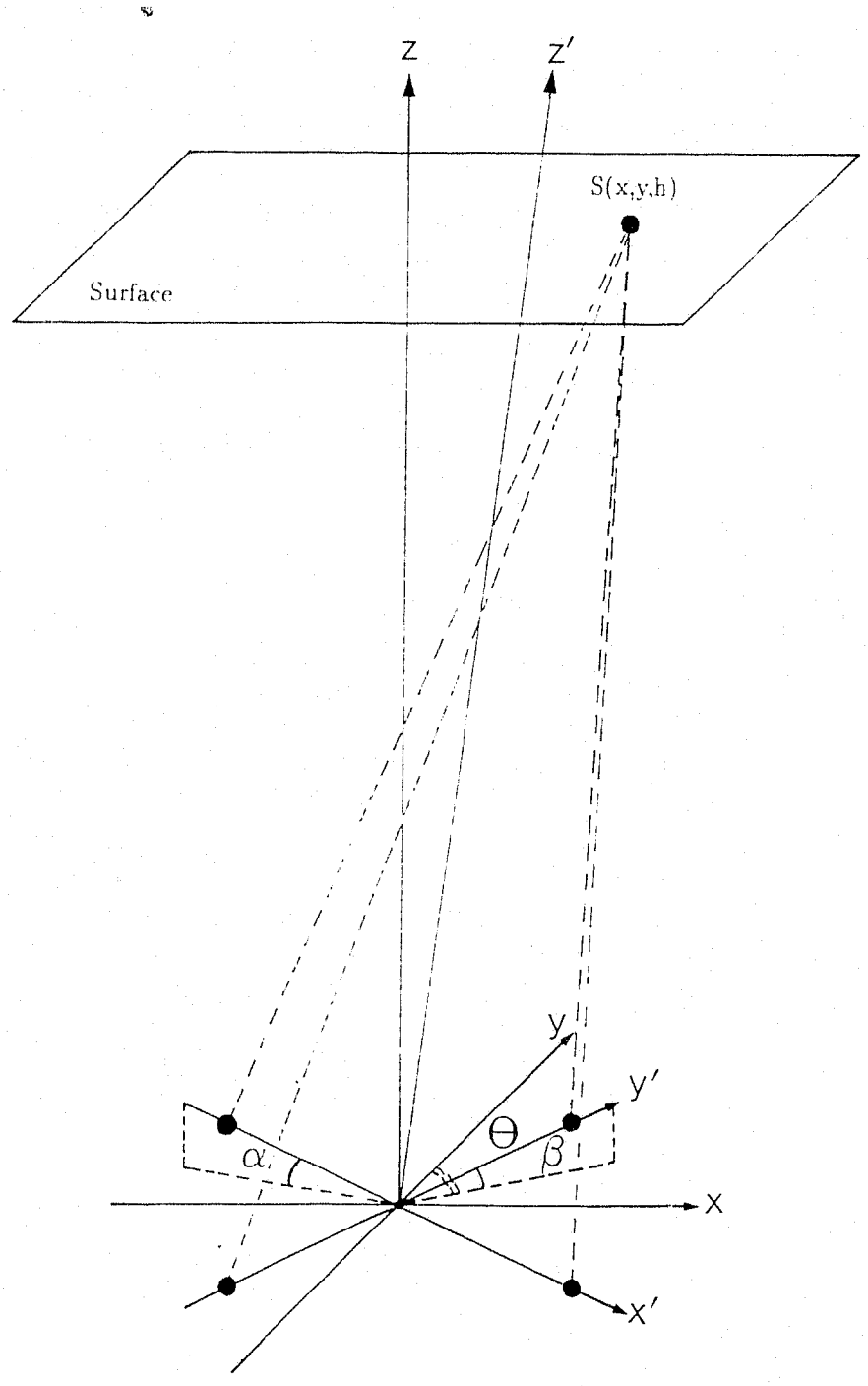

Figure 3.11: Fixed and moving coordinates chosen for the source location and correction problem. The z'-axis is orthogonal to the x'-axis and y'-axis. α and β are positive when the positive x'-axis and y'-axis are tilted up above the xy-plane. It is also assumed that the positive y-axis points to True North.

Now consider the transformation from the moving system to the fixed system. We assume that the short period horizontal motion of the instrument is negligible. This is a reasonable assumption since the vertical motion of the instrument induced by swells is estimated to be within ± 0.5 m (estimated from a vertical accelerometer) and the horizontal motion should be of the same order. This is small compared to the distance a breaking wave may travel during its lifetime (typically 5-10 m). Let the source position in the fixed system be $\mathbf{x} = [x\ y\ z]^T$, and let α and β denote the tilts of the instrument in the positive x'-direction and y'-direction, respectively (measured with the two tiltmeters on the instrument). Suppose that the y'-axis is rotated clockwise with respect to True North (assumed to be the direction of the positive y-axis) by an angle Θ (measured with a compass). Then the transformation matrix from the moving coordinates to the fixed coordinates is found to be

$$\mathbf{T} = \mathbf{H} \cdot \mathbf{T}_0, \tag{3.15}$$

where

$$\mathbf{T}_0 = \begin{bmatrix} \cos\phi\cos\alpha & 0 & \sin\alpha/\cos\beta \\ -\sin\phi\cos\alpha & \cos\beta & \sin\beta\cos\alpha\cos\phi \\ \sin\alpha & \sin\beta & \cos\theta \end{bmatrix},$$

is due to the tilts,

$$\mathbf{H} = \begin{bmatrix} \cos\Theta & \sin\Theta & 0 \\ -\sin\Theta & \cos\Theta & 0 \\ 0 & 0 & 1 \end{bmatrix},$$

is due to the rotation, and

$$\sin\phi = \tan\alpha\tan\beta, \quad \cos\theta = \sqrt{1 - \sin^2\alpha - \sin^2\beta}.$$

The relation between $\mathbf{x}$ and $\mathbf{x}'$ is given by

$$\mathbf{x} = \mathbf{T} \cdot \mathbf{x}'. \tag{3.16}$$

Note that in the fixed coordinate, z equals the depth of the instrument, h, which is estimated from a pressure sensor and an accelerometer, since it is assumed that

the source is at the surface. Solving (3.14) and (3.16), we can obtain the absolute position $\mathbf{x}$ from the measured time delays.

3.6 Example

The time delays associated with each event shown in Fig. 3.5, are then transformed to the xy coordinate system using Eqs. (3.14) and (3.16). Corrections for the motion of the instrument are also applied. The time-varying delays given in Eq. (3.11) yield a two-dimensional map of the horizontal motions of breaking events as shown in Fig. 3.12, where the hydrophone positions at that time are also shown. There are also correlation streaks visible between Events 8 and 9 in Fig. 3.4. These, however, lie below the threshold to which the pattern recognition scheme has been set. Weaker contributions such as these may be included with a more selective scheme using all possible independent hydrophone pairs, but are considered below detection level in the present example. Events 6 and 7 are above the detection threshold, but their range and position with respect to the hydrophone array are such that their velocity is hard to estimate accurately. Finally, Event 8, although distinct in the correlation analysis, lies beyond the range of the map in Fig. 3.12.

The velocity of each event in Fig. 3.5 (except Events 6, 7, and 8) is also determined (Table 3.2). The average speed of these events is about 6.07 ms^{-1}, and the directions of the events appear to be towards the south. The corresponding wind was from the north (Fig. 3.12) with an average speed of 11 ms^{-1}. It is observed that the average event speed is close to one half of the wind speed and the directions (Fig. 3.12) are aligned with the wind direction, which will be discussed in Chapter 5.

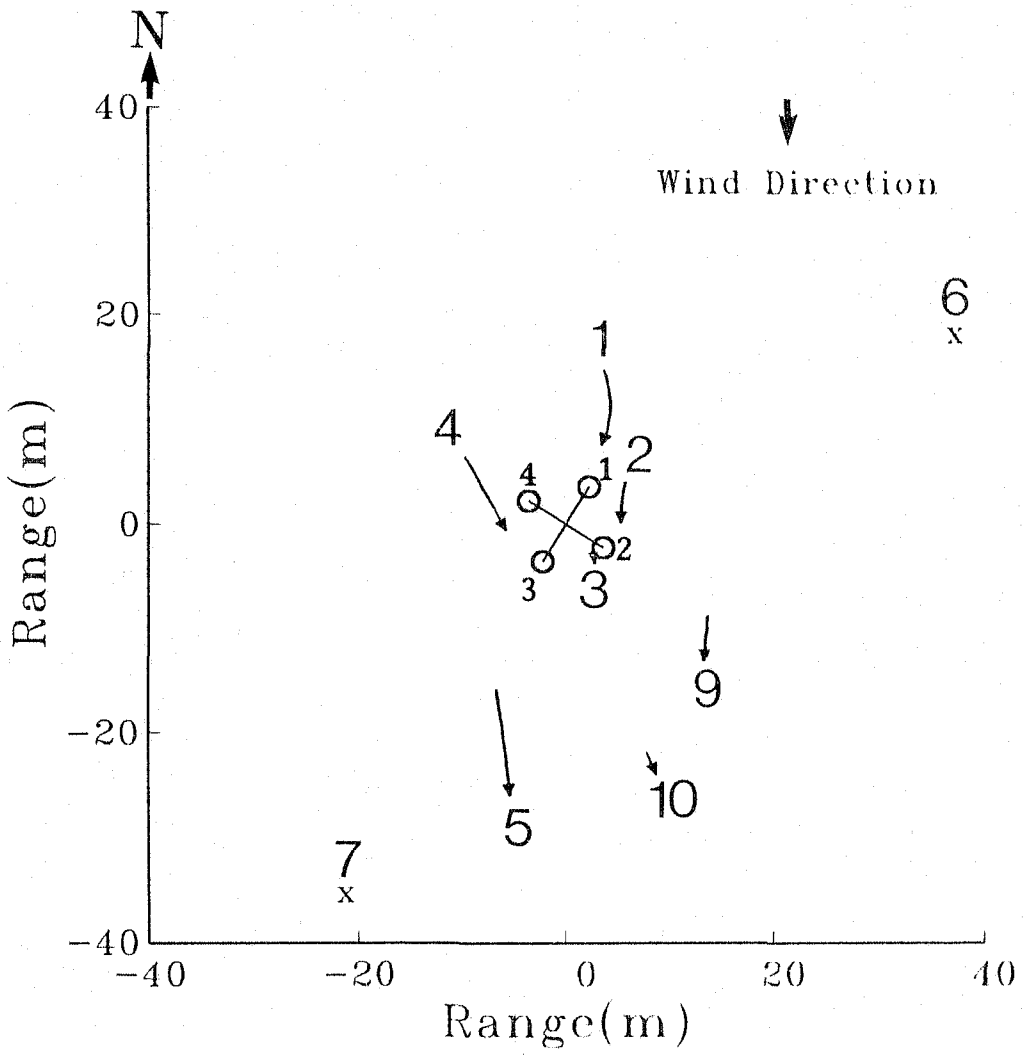

Figure 3.12: 2-D map of source trajectories on the surface. The event numbers (bigger character) correspond to those in Fig. 3.4 and the arrows represent the directions of motion of events. The 'x' sign represents the positions of Events 6 and 7. Event 8 lies beyond the range. The position of each hydrophone (smaller character) and the wind direction are also shown. The wind speed in this example is 12 ms^{-1}.

Event #	1	2	3	4	5	9	10
Speed (m/s)	5.35	5.19	4.02	6.81	7.91	4.14	9.09
Direction(^{0})	182	188	179	151	172	184	157

Table 3.2: Velocities of the observed breaking events. The direction of velocity is given as azimuth, i.e., with respect to True North, from 0^0 to 360^0, increasing clockwise.

3.7 Finite Source Dimension Problem

The anisotropy in the correlation images (e.g. Fig. 3.4) can be attributed to the effect of finite source dimension. As will be discussed in the next chapter, a possible representation of breaking waves would be a line of incoherent acoustic sources along the crest. When the sources are distant from the array compared with the length of the line, the signals from all the sources arrive at nearly the same angle, and thus the correlation will not be affected by the source dimension. However, when the breaking event is not distant, the signal from each source arrives at a different angle and yields a different time delay. Hence in the total correlation output, the superimposed effect of these sources will tend to broaden the peak associated with the signals and reduce the correlation level. Due to the correlation anisotropy, it is natural to choose the two highest correlations for each event from all possible combinations of the four hydrophones to determine the source position. The event statistics presented in Chapter 5 were obtained by selecting event patterns from four independent correlation images. [2] Future work can be conducted to improve on the technique, for example, by replacing the two omnidirectional hydrophones by two subarrays and then filtering and correlating the resulting beam-formed outputs

[2]For each event, we choose from the four independent images two streaks associated with the event that have the longest overlap, to track and determine the event velocity. To determine event duration, we define the length of two streaks associated with the event as the time interval from the earlier starting time to the later ending time. The event duration is the longest length for the streaks in the four images.

(Ferguson, 1989).

The finite source dimension problem can be further investigated by looking at the coherence between hydrophones to infer the evolution of acoustically radiating regions throughout the wave breaking process as described in the next chapter.

In summary, we have described a signal processing scheme for tracking breaking surface waves using ambient sound. This scheme allows us to measure the number of breaking events, as well as their duration and velocity. It starts from the computation of a sequence of cross correlations. Then the correlation sequence is plotted as an image (Fig. 3.4). Subsequent processing involves image enhancement and event identification from the image, during which events are identified. Finally, source positions are determined by the time delays associated with the identified events. Data processing based on this scheme can be highly automatic and conveniently carried out for a long period. However, because of the finite source dimension effect, as well as background noise, the measurement made by the instrument is incomplete. This problem will be addressed in a later chapter (Chapter 5), where we shall perform a careful statistical analysis of the experimental results.

Chapter 4

Acoustical Radiation from Breaking Waves

Since the pioneering work by Knudsen et al. (1948), it has long been recognized that surface winds play a dominant role in the generation of underwater ambient noise. Subsequently, experimental studies have been carried out to obtain empirical relationships between noise and wind speeds for prediction of underwater noise levels and measurement of wind speeds from ambient noise. Although breaking waves have been identified as the main source of wind-generated ambient sound in the ocean (Wenz, 1962; Kerman, 1984), the actual sound generation mechanism still remains unclear. There is however an increasing need to improve our understanding of the mechanism, not only for noise prediction but also for better application of ambient noise in remotely monitoring physical processes associated with wave breaking.

Previous studies of ambient noise have generally been based on the spatial average of contributions from breaking waves uniformly distributed over the infinite surface. Little prior work has thus far been done on the acoustic radiation of individual breaking waves. Characterization of the sound radiated by breaking waves is however critical to understanding the sound generation mechanism. The acoustical instrument described in Chapter 2 tracks individual breaking waves, thus providing an opportunity to investigate the characteristics of the sound radiated from these

waves. In this chapter, we shall focus on both coherent and incoherent acoustical radiation properties of individual breaking waves, including power spectrum, frequency coherence and acoustic intensity, in hopes of providing some insight on the sound radiating process. However, it is necessary to review first the previous knowledge about the ambient sound field and ambient sound generation mechanisms.

4.1 The Ambient Noise Field

Ambient noise arises from a variety of sources: from hydrodynamic sources, oceanic traffic sources, seismic sources and biological sources (Wenz, 1962). Hydrodynamic sources are usually the prevailing source in the open ocean. They may result from bubbles and water sprays caused by surface wave breaking, precipitation and turbulent motion. In this work, we are primarily interested in the sound generated at the ocean surface by wave breaking. The ambient noise field thus formed is the result of the spatial average of sound sources over the entire surface, but its statistical properties are however important for isolating individual sources from the background.

4.1.1 Directivity of Noise Sources

The directivity of noise sources at the ocean surface depends on the generation mechanisms. Ross (1976) describes three basic types of noise sources: monopoles due to volumn or mass fluctuations such as pulsating bubbles, dipoles resulting from fluctuating forces, and quadrupoles caused by turbulent fluid motions without net volume changes or net forces. Quadrupoles rarely exist in the ocean since they require a high Mach number, but turbulence noise may be amplified by bubbles injected by breaking waves and is thus considered by Properetti (1988) an important source for very low frequency ambient noise.

Most previous work has suggested a radiation pattern of the form

$$I(\theta) = I_0 \cos^m \theta, \tag{4.1}$$

for underwater noise sources, where I_0 is acoustic intensity and θ is the angle between the source and receiver, measured from the normal to the surface. (For monopoles, m=0; for dipoles m=2.) It is difficult to measure directly the radiation pattern of individual sources at the surface, but most indirect measurements indicate that a dipole source (m=2) is most consistent with the data (Urick, 1983).

The dipole radiation pattern may be formed by a monopole source (e.g. resonating bubble) and its image in the surface. It is also likely to result from splashing sprays caused by wave breaking (Guo, 1987). In any event, such a pattern seems to be a good assumption and will be used throughout the thesis unless otherwise stated.

4.1.2 Gaussianity and Stationarity of Ambient Noise

In many theoretical models, ambient noise has been assumed to be a Guassian process, and stationary for a short period. This hypothesis has been tested by Arase and Arase (1968) with deep ocean data. It was found that most ambient noise has a Gaussian amplitude distribution in the absence of near field interference. This is consistent with the view that the ambient noise is the sum of a large number of sources, each of which is independent of the others and none of which are dominant, a result of the Central Limit Theorem (Papoulis, 1984). Wenz (1972) presented some ambient noise data that showed that the distributions of noise spectrum levels (in dB) from 10-400 Hz were also approximately Gaussian, at least for probabilities between 5% and 95%.

Arase and Arase (1968) also investigated the stationarity of ambient noise. They found that ambient noise is nonstationary over times as short as a few minutes. Part of the nonGaussianity of ambient noise was found to be due to the nonstationarity.

4.1.3 Spatial Coherence

The spatial coherence in the ambient noise field is important to the design and performance prediction of hydrophone arrays. A number of analytical models have been proposed to describe the spatial coherence. In isotropic noise fields, the coherence is well known to be $\sin kd/kd$ for the three dimensional case and $J_0(kd)$ ($J_0(x)$ is the Bessel function of zeroth order) for the two dimensional case (Cox, 1973), where k is wavenumber and d is the spacing between two hydrophones. However, this isotropic model is apparently inadequate for describing the ambient noise field which is mainly due to contributions from the surface.

Cron and Sherman (1962) were the first to consider directional noise fields. They modelled the ocean surface as a uniform distribution of independent noise sources, each of which radiates sound with a horizontally isotropic and vertically directional pattern. For a source radiation of Eq. (4.1), the coherence can be expressed explicitly. In particular, for a dipole pattern (m=2), the coherence between two horizontally placed hydrophones is given by

$$\rho(k,d) = \frac{2J_1(kd)}{kd}, \tag{4.2}$$

where $J_1(x)$ is the Bessel function of first order.

A more general model was proposed by Cox (1973) who decomposes the directional distribution in spatial harmonics. Such a model yields spatial coherence in good agreement with many experimental data, but the details are beyond the interest of the thesis.

4.2 Mechanisms of Surface-Generated Ambient Sound

Although the strong correlation between ambient noise and wind, discovered by Knudsen et al. (1948), has led to the belief that ambient noise is principally due to

the breaking of wind waves, the physics of sound generation is still poorly understood. However, it appears that the most likely ways for breaking waves to generate high frequency ambient noise (100 Hz to 10 kHz) are the sudden formation of air bubbles and the splashing of spray at the sea surface (Wenz, 1962; Kerman, 1984).

Guo (1987) proposed a model in which the splashing of water spray caused by wave breaking was shown to be the dominant source of surface generated ambient noise. Splashing sprays cause a rapid variation of the density distribution in the airflow, thus inducing acoustic dipole sources. Near surface bubbles were shown by Guo to be a negligible source on the grounds that their monopole field in a turbulent flow would be destroyed by that of their image in the free surface. Recent laboratory and field experiments (Banner and Cato, 1988; Medwin and Beaky, 1989; Pumphrey and Ffowcs Williams, 1990; Updegraff and Anderson, 1991b), however, have demonstrated that bubbles are an efficient source in ambient noise, especially at low wind speeds. Yet the sound generation mechanism by bubbles has not been established conclusively, due to an inadequate knowledge of bubble-related parameters. Prosperetti (1988) set up a general framework for the description of bubble-generated noise in different frequency ranges. Very low frequency noise from a few Hz to 100-200 Hz was suggested to be due to the amplification of turbulence noise by bubbles. In the range from 1 to 10 kHz, noise was assumed to be produced by freely oscillating individual bubbles. In the intermediate range from a few hundred Hz to 1 kHz, the noise was attributed to collective oscillations of bubble clouds which emit sound at substantially lower frequencies than single oscillations. However, Loewen and Melville (1991b) argued that lower frequency sound (down to 500 Hz) can be generated by a distribution of single bubbles that do not necessarily collectively oscillate.

Single bubble oscillations have been confirmed by experiment to be the dominant source of high frequency (1-20 kHz and perhaps a wider range) ambient noise. Medwin and Beaky (1989) studied the sound of spilling breaking waves generated by a plunger in the laboratory and suggested that oceanic noise in this frequency range is

generated by freely oscillating bubbles entrained by spilling breakers. Pumphrey and Ffowcs Williams (1990) have also suggested, on the basis of their laboratory work, that the free oscillation of newly created bubbles is responsible for the Knudsen spectrum.

In very low wind conditions (as low as 1 ms^{-1}) when there are no obvious whitecaps, ambient noise is still wind dependent. Shang and Anderson (1986) suggest two mechanisms for noise generation at low wind speeds. One is bubble cavitation caused by turbulent pressure fluctuations, and the other is the rupture or bursting of bubbles at the ocean surface. Both have however been shown to be physically implausible by Prosperetti and Lu (1988). One of the most likely mechanisms for sound generation at low winds seems to be 'microbreaking', in which case air entrainment can only be observed at a very close distance. This phenomenon has been studied in detail by Updegraff and Anderson (1991a, b), who used a hydrophone array and a video camera at 1 m depth to observe ambient noise and small breakers simultaneously. They concluded that wind-dependent ambient noise at low winds is caused by small wavelet spills. The acoustical signatures they observed strikingly resembled those obtained in the laboratory by Medwin and Beaky, thus implying that the free oscillation plays a key role in this case.

Collective oscillations of bubbles within a cylindrical column have been confirmed in a laboratory experiment (Yoon et al., 1991), although the choice of the particular bubble cloud shape may not be relevant to real situations in the ocean. Later laboratory observations of the sound and void fraction beneath breaking waves have further supported the collective oscillation hypothesis (Loewen and Melville, 1992; Lamarre and Melville, 1992). Our own field observations of the sound radiated by individual breaking waves at high wind speeds (11 ms^{-1}) have also revealed a low frequency peak around 250 Hz in the spectrum, which can be well accounted for by collective bubble oscillations (Farmer and Ding, 1992). We shall discuss this issue in the next section.

An alternative theory of sound generation by bubbles has also been proposed by

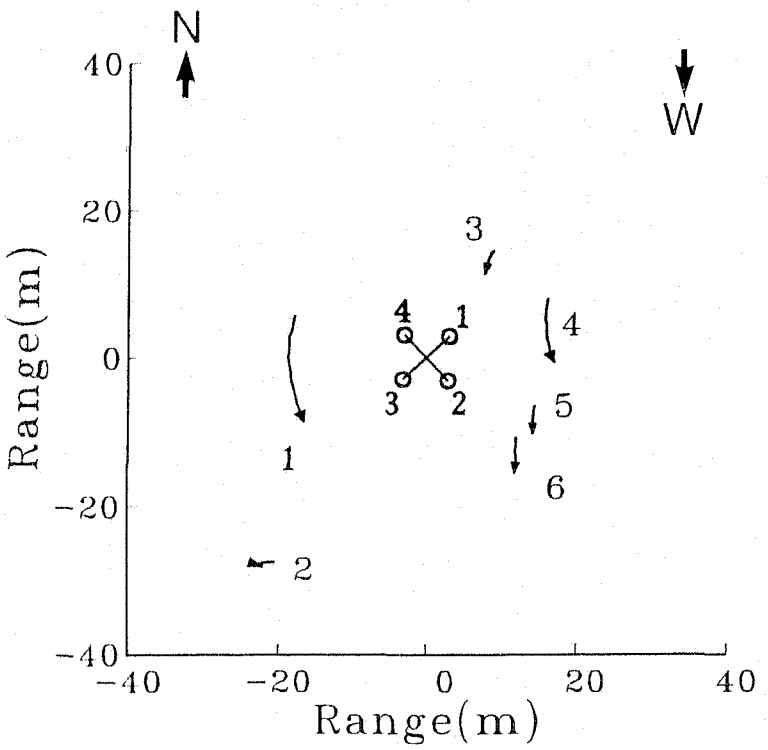

Figure 4.1: Trajectories of breaking waves in a 45 s period of data, where Events 1, 3, 4 were analyzed. The numbers correspond to those in Fig. 3.7. W=11 ms^{-1}.

Longuet-Higgins (1989) who noticed that an asymmetric, normal-mode bubble oscillation, though a negligible emission of sound in linear theory, will emit monopole radiation at second order in nonlinear theory. It has also been shown that any broadband sound generated by bubbles may show spectral peaks at the corresponding resonance frequencies (Longuet-Higgins, 1990), but more convincing evidence is needed to verify this theory.

4.3 Coherent Radiation from Breaking Waves

In this section, we shall examine in detail the frequency characteristics of the acoustic signal from individual breaking waves. Simultaneous observations of the power spectrum and coherence of the signal reveal a strong, coherent low frequency com-

ponent and provide information on the source dimension.

4.3.1 Observation

Figure 4.1 shows the trajectories of breaking waves in a 45 s period of data, during which time the wind was blowing at 11 ms^{-1} from the North. These breaking waves were obtained from the correlation image in Fig. 3.7, and have an average speed of 5 ms^{-1}. Event 1 is chosen for subsequent analysis. The acoustic power series for Event 1 is shown in Fig. 4.2a. The corresponding sequence of power spectral density (PSD) functions is shown in Fig. 4.2b, where the signal is broken into 0.7 s segments for analysis. The PSD is shown relative to the background noise field measured just prior to the breaking event. The vertical scale is linear in an arbitrary unit and shows the departure from the background spectrum as the breaking event evolves. Significant departures occur for the third PSD in the form of a sharp peak at 250 Hz which subsequently rises in frequency and broadens. Later laboratory work (Melville, 1992, personal communication) suggested that the shift of the peak towards higher frequencies is due to the outgassing of trapped air under the breaking event as the breaking evolves.

The corresponding coherence (we use Magnitude-Squared Coherence in the present analysis) plots for hydrophones 2-1 (orthogonal to the wave crest) are shown in Fig. 4.2c, and for hydrophones 4-1 (aligned with the crest), in Fig. 4.2d. The coherence is in general greater for the orthogonal pair, and extends over a greater frequency range. For example, the coherence in plot 4 for the orthogonal pair (Fig. 4.2c) extends up to 1.4 kHz, whereas for the aligned pair the upper limit is 0.6 kHz. Note that there is a low frequency minimum typically around 150 Hz in the coherence plots, which apparently results from the spatial coherence of the background noise as modelled in Eq. (4.2), though the predicted value is significantly lower (100 Hz) for the given hydrophone spacing (6.0 m). One explanation for this difference is that the Cron and Sherman model is based on the far field assumption and does not account for the observation made at a relatively shallow depth (25 m).

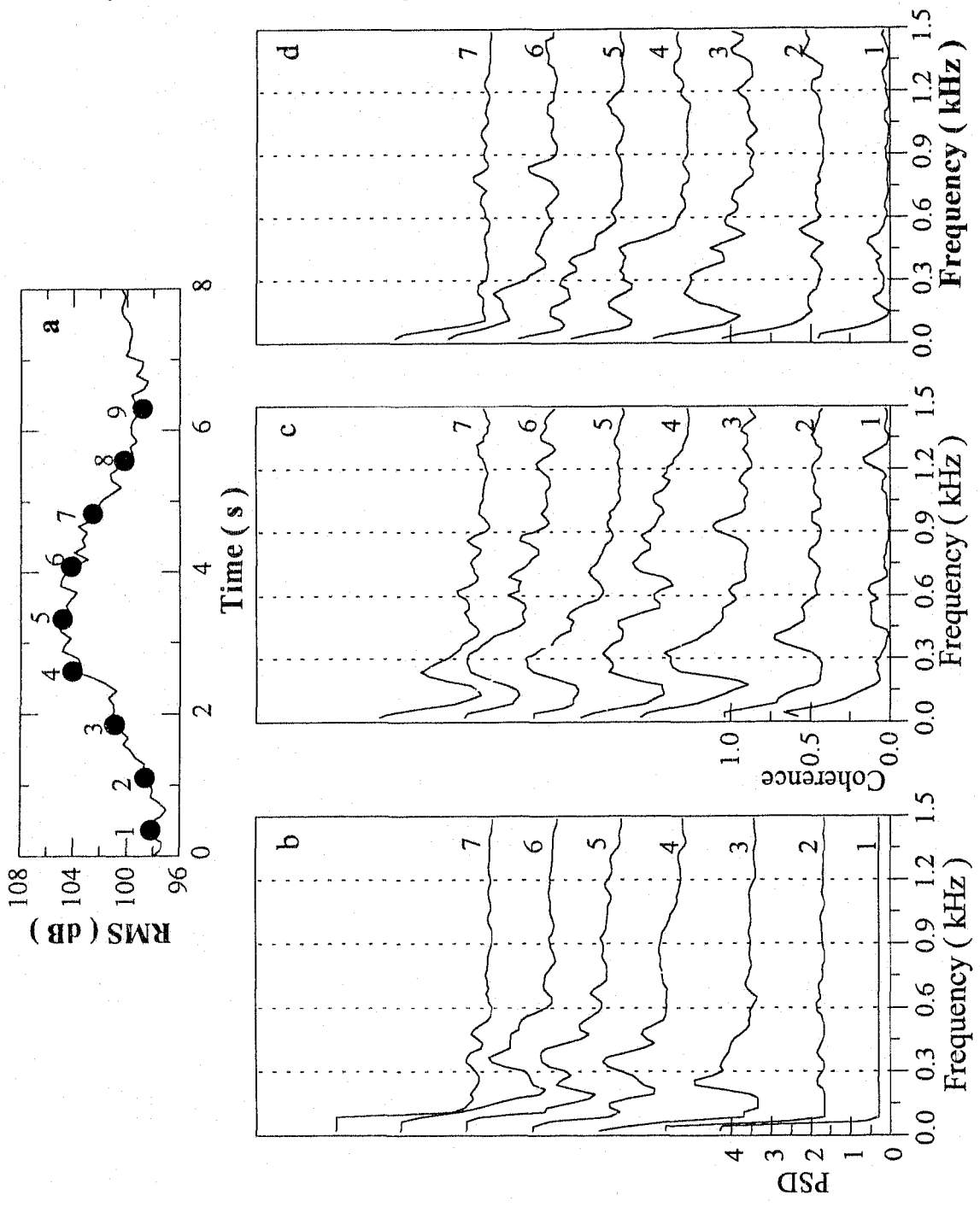

Figure 4.2: (a) RMS sound level (ref: μPa^2) for event 1 in Fig. 4.1. Numbered dark circles indicate successive data segments used for subsequent analysis; (b) Power spectral density difference from background level for each successive data segment; (c) Magnitude-Squared Coherence (MSC) between hydrophones 2-1, aligned orthogonal to the wave crest; (d) MSC for hydrophones 4-1, aligned with the wave crest.

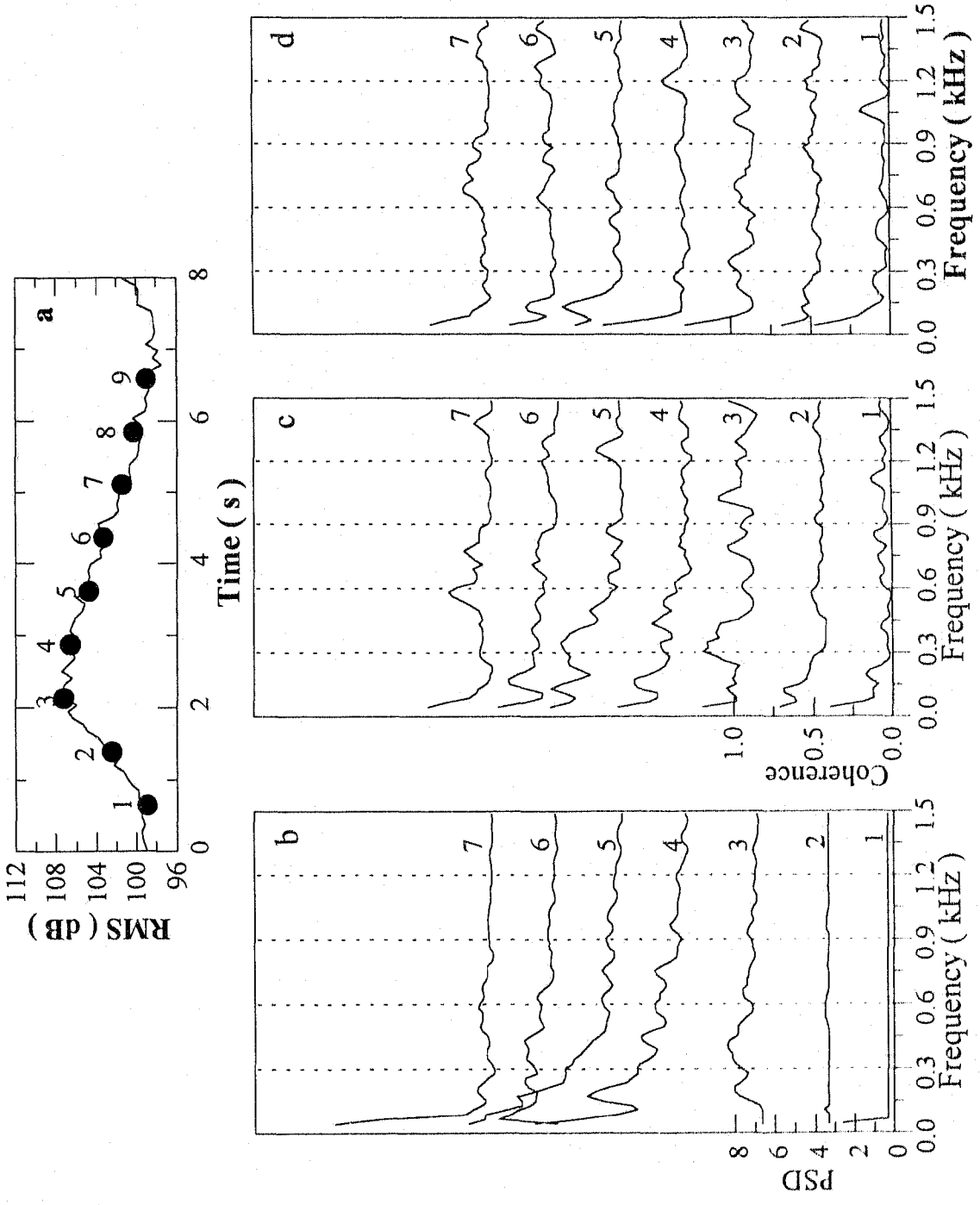

Figure 4.3: (a) RMS sound level (ref: μPa^2) for events 3 and 4 in Fig. 4.1. Numbered dark circles indicate successive data segments used for subsequent analysis; (b) Power spectral density difference from background level for each successive data segment; (c) Magnitude-Squared Coherence (MSC) between hydrophones 3-1, aligned orthogonal to the wave crest; (d) MSC for hydrophones 4-2, aligned with the wave crest.

Similar analysis was also performed for Events 3 and 4, and the results are shown in Fig. 4.3. These two events last for a shorter period than Event 1, and thus their evolution process is not as clearly seen as in Fig. 4.2. Referring to Fig. 3.7, plots 1-3 are associated with Event 3. The PSD departs from the the background noise in plot 3, showing a broader, but less significant, frequency peak between 300-600 Hz. Event 4 follows immediately, starting from plot 4 with a sharp peak below 300 Hz. This peak appears to broaden towards lower frequencies before it diminishes. The coherence is also generally greater in the direction orthogonal to the wave crest (Fig. 4.3c) than aligned with the wave crest (Fig. 4.3d).

It is clear from these observations that breaking waves radiate a significant portion of sound over the range of 100-500 Hz and that the coherence of the radiated sound is spatially anisotropic, depending on the orientation of the receiving hydrophone pair. This phenomenon may be explained as follows in terms of the nature of the sound generation mechanism and the finite source dimension effect.

4.3.2 Discussion

Consider first the low frequency component in the PSD. Two limiting possibilities exist. Either the sound is generated by entrainment of individual bubbles resonant at that frequency, or there is a collective oscillation of the bubbles, each of which might individually have much a higher resonant frequency. A single bubble oscillating in the breathing mode with resonant frequency 250 Hz would have a radius of 1.4 cm. Medwin and Daniel (1990) observed bubbles of radius up to 7.4 mm under spilling breakers in the laboratory. Bubbles of radius 1.4 cm could probably be formed under larger breaking waves in the ocean such as observed here, but they would be unlikely to be created in a significant number and last very long. Loewen and Melville (1991b) used Medwin and Daniel's laboratory measurements of bubble size distributions under a spilling breaker to model the sound radiated from the breaker, and found that the modelled sound spectrum is consistent with the observation. Their modelling therefore implies that it does not require too many large

bubbles resonant at their lowest mode to generate low frequency sound (down to 500 Hz). This model, however, assumes a constant depth for bubbles of any size (thus their dipole strength is constant) and ignores their motion; in the real situation, larger bubbles return to the surface more quickly and thus their contribution to low frequency sound would not be as significant as the model would imply. Therefore, the strong low frequency peak in our data may hardly be explained by this model.

An alternative explanation is that bubbles in the breaking wave oscillate collectively. If the bubble cloud is of linear dimension L, the lowest eigenfrequency must in the simplest approximation be of order c_m/L, that is,

$$f_{min} = \frac{c_m}{L}, \tag{4.3}$$

where c_m is the effective speed of sound in the bubble mixture. The sound speed depends upon the void fraction β:

$$c_m^2 \approx \frac{p}{\rho\beta}, \tag{4.4}$$

where p is the ambient pressure and ρ the ambient water density (Prosperetti, 1988). The correct eigenfrequencies depend on boundary conditions, bubble sizes, void fractions and bubble cloud shapes. The problem can only be solved explicitly in a limited number of cases. However, it has been found that the eigenfrequencies predicted by Eq. (4.3) are in good agreement with the correct solution in an infinite bubble layer model for $\beta > 3\%$ (Lu and Prosperetti, 1990). Recent laboratory studies found that the void fraction in a plunging breaker is typically 5-20% (Lamarre and Melville, 1991).

We use Eq. (4.3) to obtain a first order estimate of bubble cloud dimension. If we take the higher value of void fraction found in the tank experiments for a plunging breaker ($\beta = 20\%$), the dimension is 9 cm for $f_{min} = 250$ Hz. If we accept the lower value of 5% the dimension is 18 cm at $f_{min} = 250$ Hz. In general, for $f_{min} = 250$ Hz, L is less than 30 cm for $\beta > 3\%$. This result is consistent with a layer of entrained bubbles oscillating collectively at the leading edge of the wave.

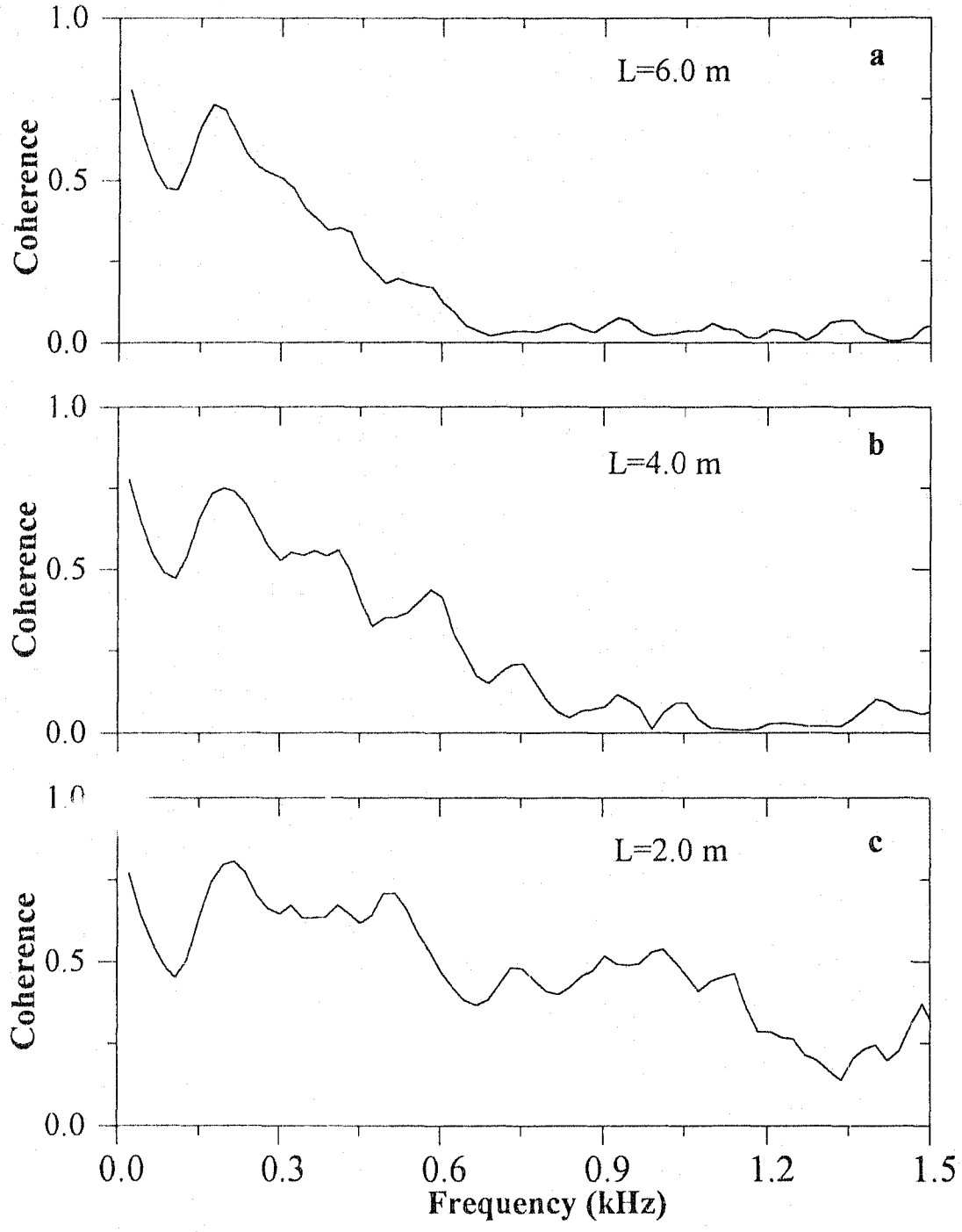

Figure 4.4: Model simulations of magnitude-squared coherence for a breaking wave at location of event 1 (Fig. 4.1), for a wave width of 6 m, 4 m and 2 m. The wave is assumed long relative to its width, and coherence is for hydrophones aligned orthogonal to the wave crest.

If the sound were merely radiated by a compact source (point source) as resulting from collective oscillations, it would be coherent between any two receiving hydrophones (the coherence would be unity independent of frequency if the noise were absent). The observed coherence is however much more complicated, showing a decaying tendency with increasing frequency. This is a significant feature of the coherence in the presence of finite dimension sources (Bendat and Piersol, 1980),suggesting that breaking waves cannot be described as a compact source in this case. Other factors such as shadowing and surface scattering may also affect the coherence, but they are beyond the scope of this discussion.

We therefore believe that the sound source in a breaking wave must be of finite dimension. It may consist of a distribution of incoherent sources, for example randomly phased bubbles or perhaps randomly phased groups of bubbles in collective oscillation. In Section 4.2, we conclude that the most likely mechanism for sound generation by wave breaking would be the sudden formation of bubbles and their subsequent oscillations. This suggests that the most effective acoustically radiating regions in a breaking wave are near the wave crest where bubbles are entrained. Therefore we can model the acoustic sources in a breaking wave as a rectangular matrix of incoherent sources with the longer side aligned with the wave crest. For such a source to be compact over a bandwidth the least wavelength of which is λ, and thus to provide coherence between separated hydrophones of the array, the difference in path length from a radiating point to each hydrophone must be independent of the location of that point in the source, to within a fraction of λ. In this sense a source may be compact in one direction but not in another, depending or its geometry. The upper frequency coherence bound will be determined by the effective width of the incoherent source as viewed by a given hydrophone pair. We can incorporate this concept in model simulations so as to better understand a finite dimension source.

In Fig. 4.4 we simulate a breaking wave at the position of Event 1 in Fig. 4.1, using a linear matrix of incoherent sources each of which radiates sound with the

observed PSD. Since the direction of travel of the event can be determined, the width (downwind dimension) of the simulated event is set aligned with the direction of travel. Background noise with coherence of the form of Eq. (4.2) is also generated and added to the signal from the matrix source with the SNR equal to the observed one (The algorithm that generates the signal and noise is described in Appendix B). Previous observation (Bortkovskii 1987) indicates that the length (crosswind dimension) of a breaking wave is typically twice its width. Therefore the length of the simulated wave is set about twice the width, but the choice does not affect the basic results. As the width changes from 2 m to 6 m, the high frequency coherence cut-off drops from about 1.5 kHz to about 600 Hz. Figure 4.2c shows an observed high frequency cut-off with a maximum value of 1.3 kHz (plot 4), declining to about 500 Hz by plots 6 and 7. Referring to Fig. 4.2a, we see that plot 4 corresponds to the time of rapid rise in rms sound pressure level. The simulation results would suggest that at this point the breaking event is compact, of width approximately 2 m, but that it increases in width with time (i.e. to 4 m by plots 5 and 6).

A coherence peak at about 600 Hz can be seen in the simulation (especially for L=2.0 m and 4.0 m) although there is no obvious peak at this frequency in the data; this peak is due to the use of discrete sources in the simulation, resulting in some discrete frequency bands. The simulation cannot reconstruct the detailed features of the observed coherence. It does, however, explain a dominant feature: the higher frequency coherence is gradually eroded as the source dimension increases.

These results do not explain the well defined coherence peak at 250 Hz in Fig. 4.2c, plots 2 and 3, since it is highly unlikely that in the initial stages of development the breaking wave is large (i.e. 6 m wide to be consistent with the simulation in Fig. 4.4c). An alternative explanation applicable to this initial phase of breaking is that the source is relatively compact, but that the reduced signal to noise ratio eliminates contributions to the coherence except in the neighbourhood of the strong spectral peak. It is also noticed that plot 3 of Fig. 4.2c and 4.2d appears to be more isotropic than later plots, possibly due to the compactness at this stage.

As pointed out above, a spectral peak at 250 Hz would be consistent with collective bubble oscillations having a thickness of 10-20 cm. A collective oscillation would also account for the coherence peak observed at the same frequency.

4.4 Acoustic Intensity of Breaking Waves

In the preceding section, we have investigated the detailed frequency characteristics of the sound radiated by individual breaking events. In this section, we ignore the details of the sound but focus on its intensity which is related to the radiated power. Our approach is to track individual events, calculate the intensity received from these events, and determine the source intensity from the tracked position by using a dipole radiation pattern. It requires a longer observation period to collect sufficient events for analysis and obtain statistics of the source intensity. The resulting statistics may be related to important kinematic and dynamical parameters of surface waves. They are also important to the analysis of breaking wave statistics described in the next chapter.

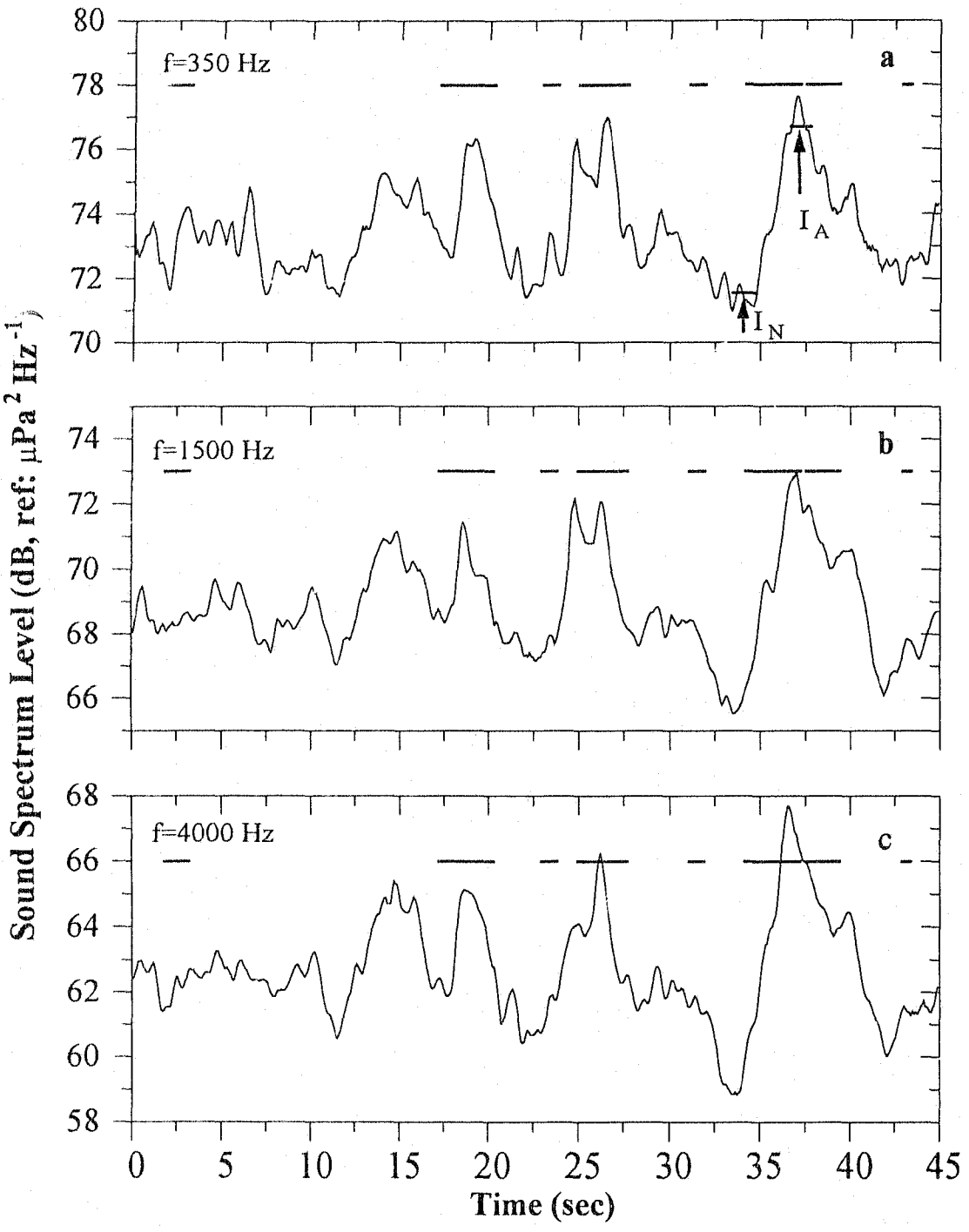

Figure 4.5: Sound spectrum level time series at three frequencies for a 45 s data segment, at a wind speed of 11 ms^{-1}. Starting time: 04:46:00, 03/08/90, UTC. The horizontal bars indicate the occurrences of tracked breaking waves. I_A denotes the total received level and I_N the background noise level.

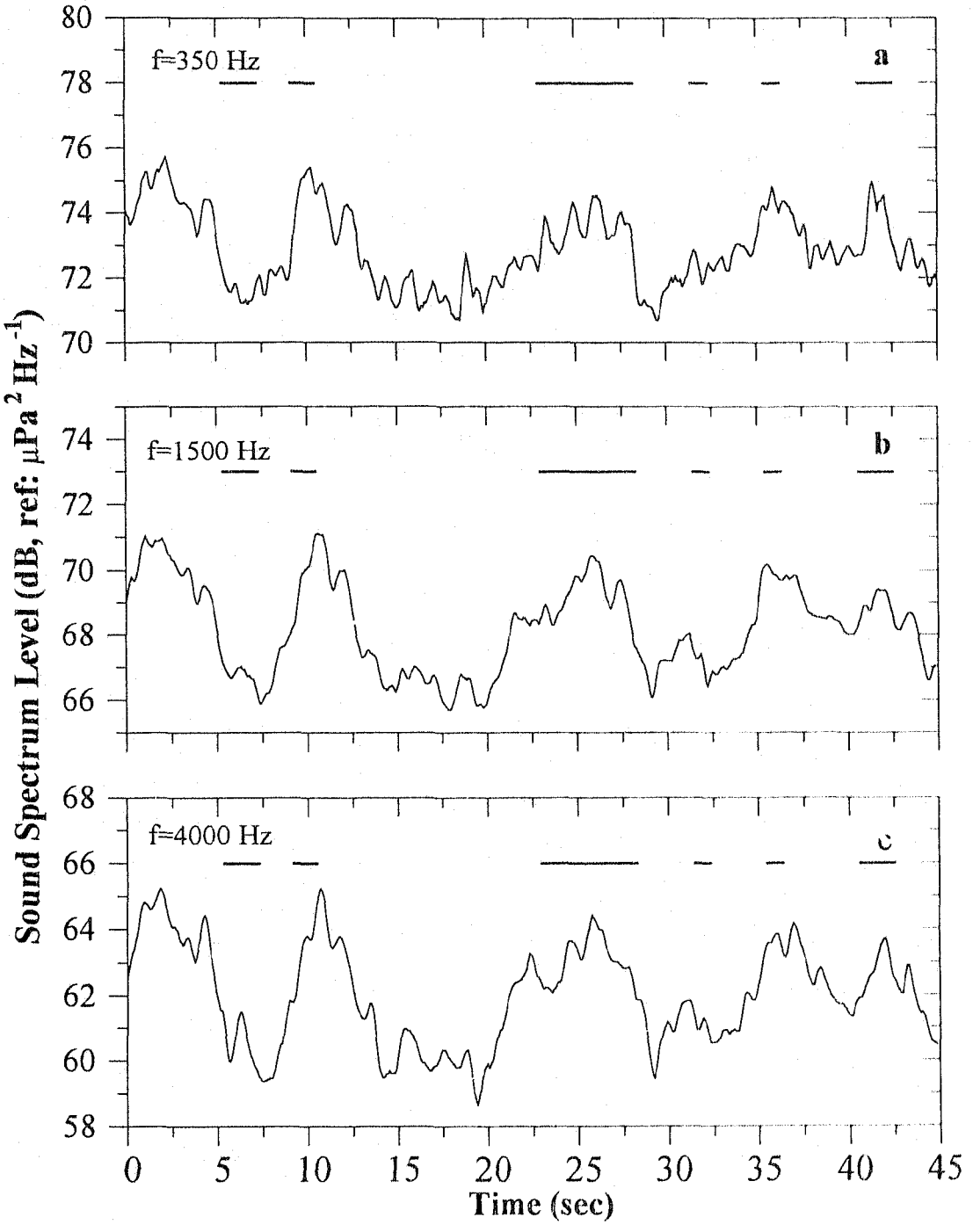

Figure 4.6: Sound spectrum level time series at three frequencies for a 45 s data segment, immediately after Fig. 4.5. Starting time: 04:46:45, 03/08/90, UTC.

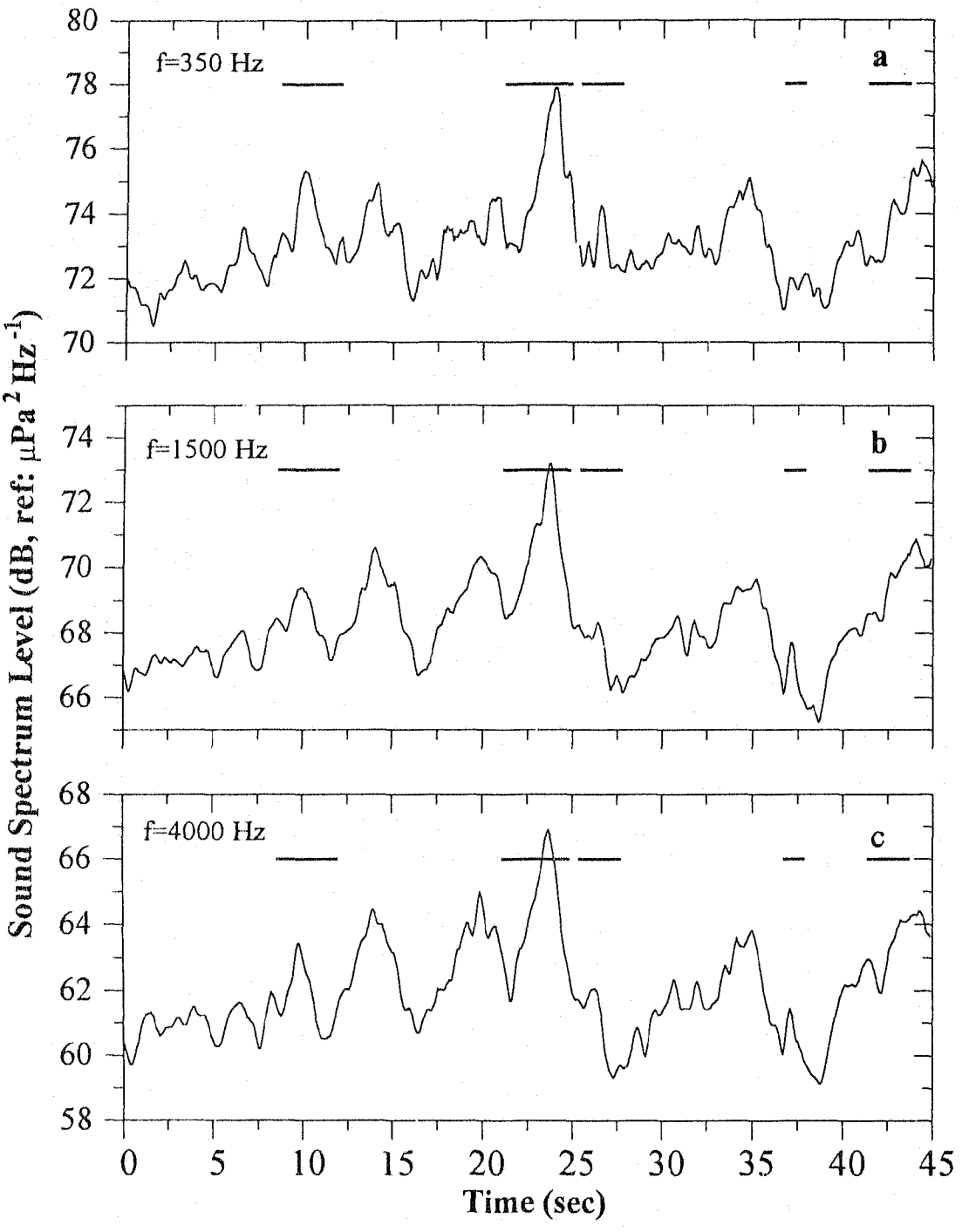

Figure 4.7: Sound spectrum level time series at three frequencies for a 45 s data segment, immediately after Fig. 4.6. Starting time: 04:47:30, 03/08/90, UTC.

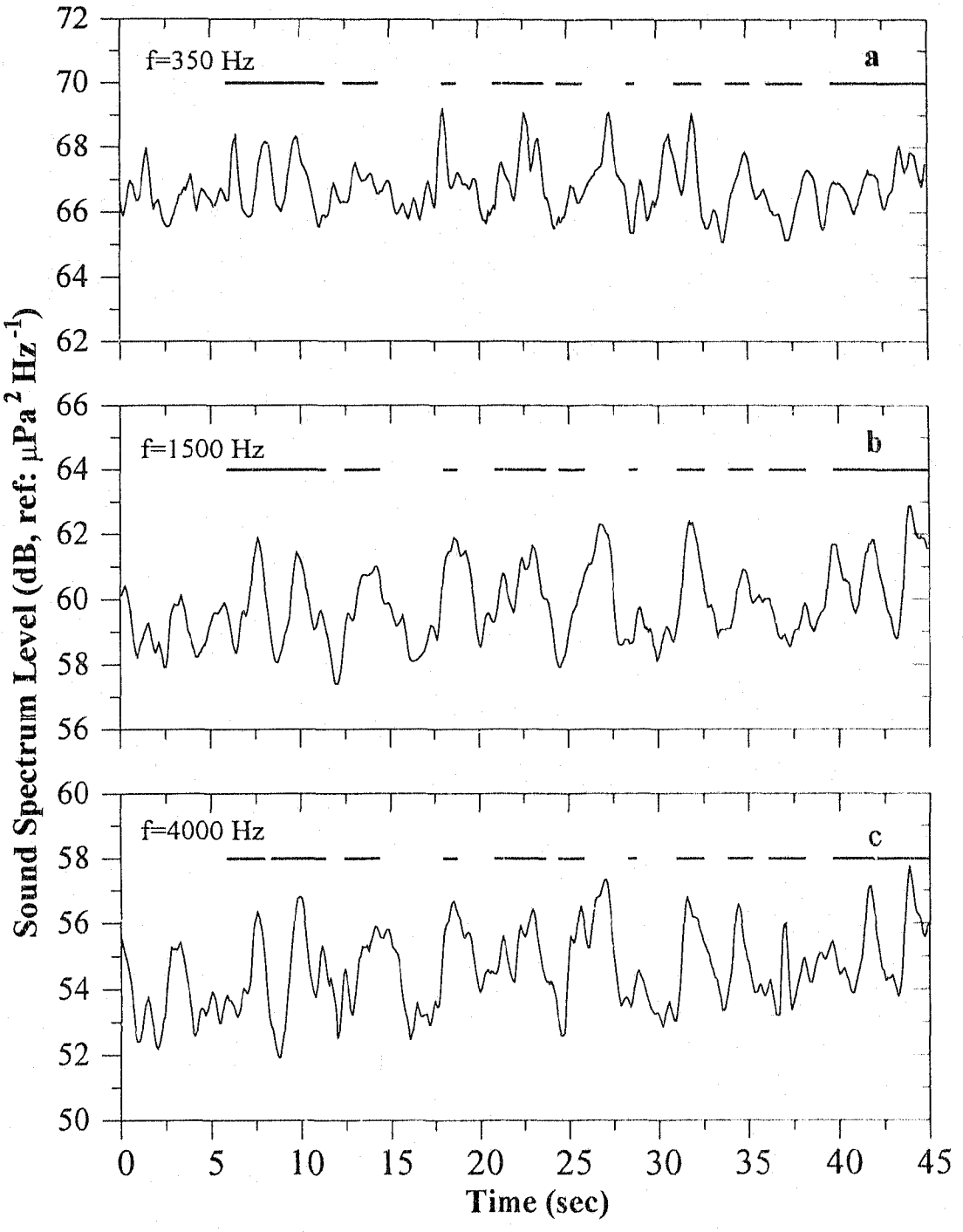

Figure 4.8: Sound spectrum level time series at three frequencies for a 45 s data segment, at a wind speed of 6.4 ms^{-1}. Starting time: 10:34:45, 03/14/90, UTC.

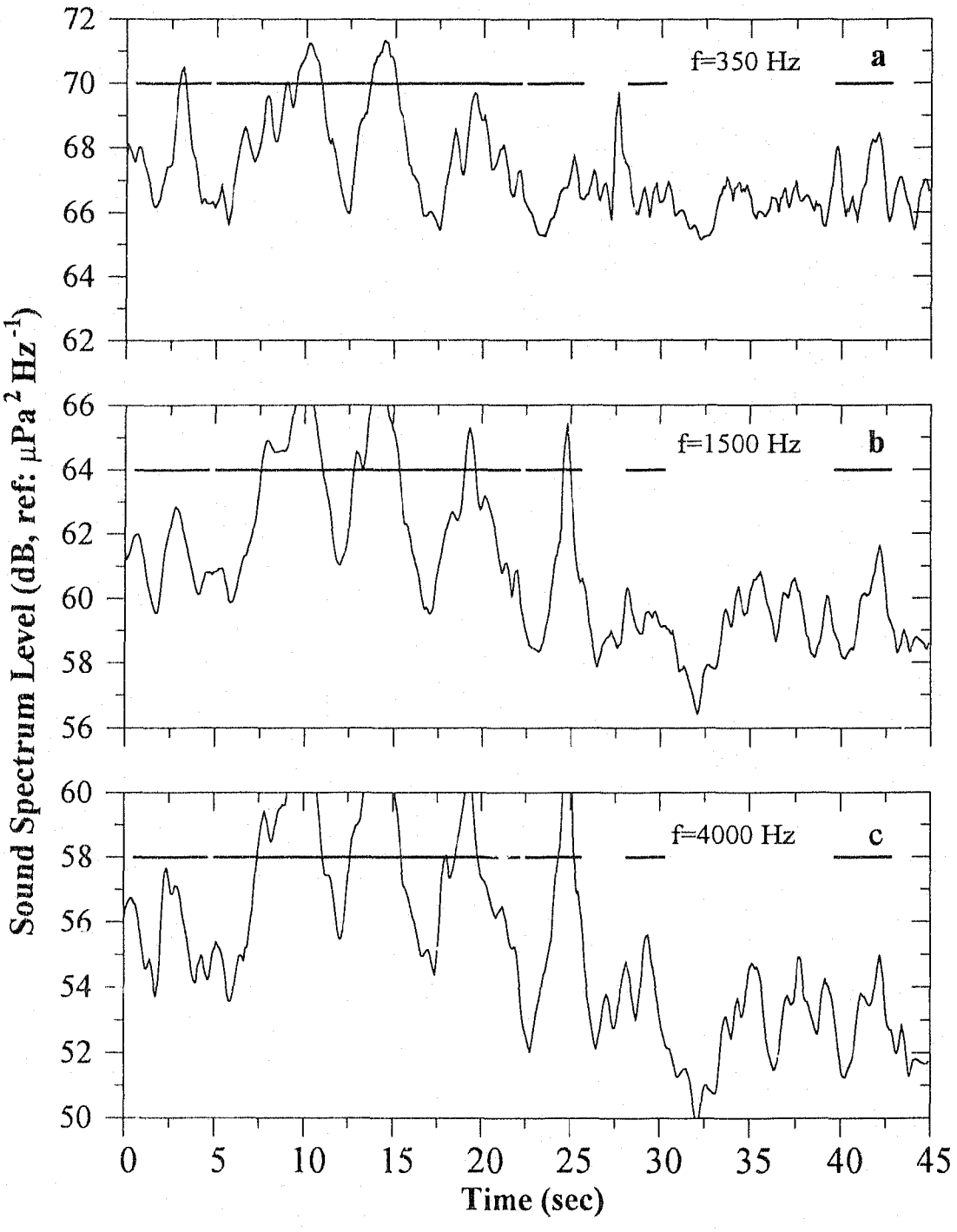

Figure 4.9: Sound spectrum level time series at three frequencies for a 45 s data segment, immediately after Fig. 4.8. Starting time: 10:35:30, 03/14/90, UTC.

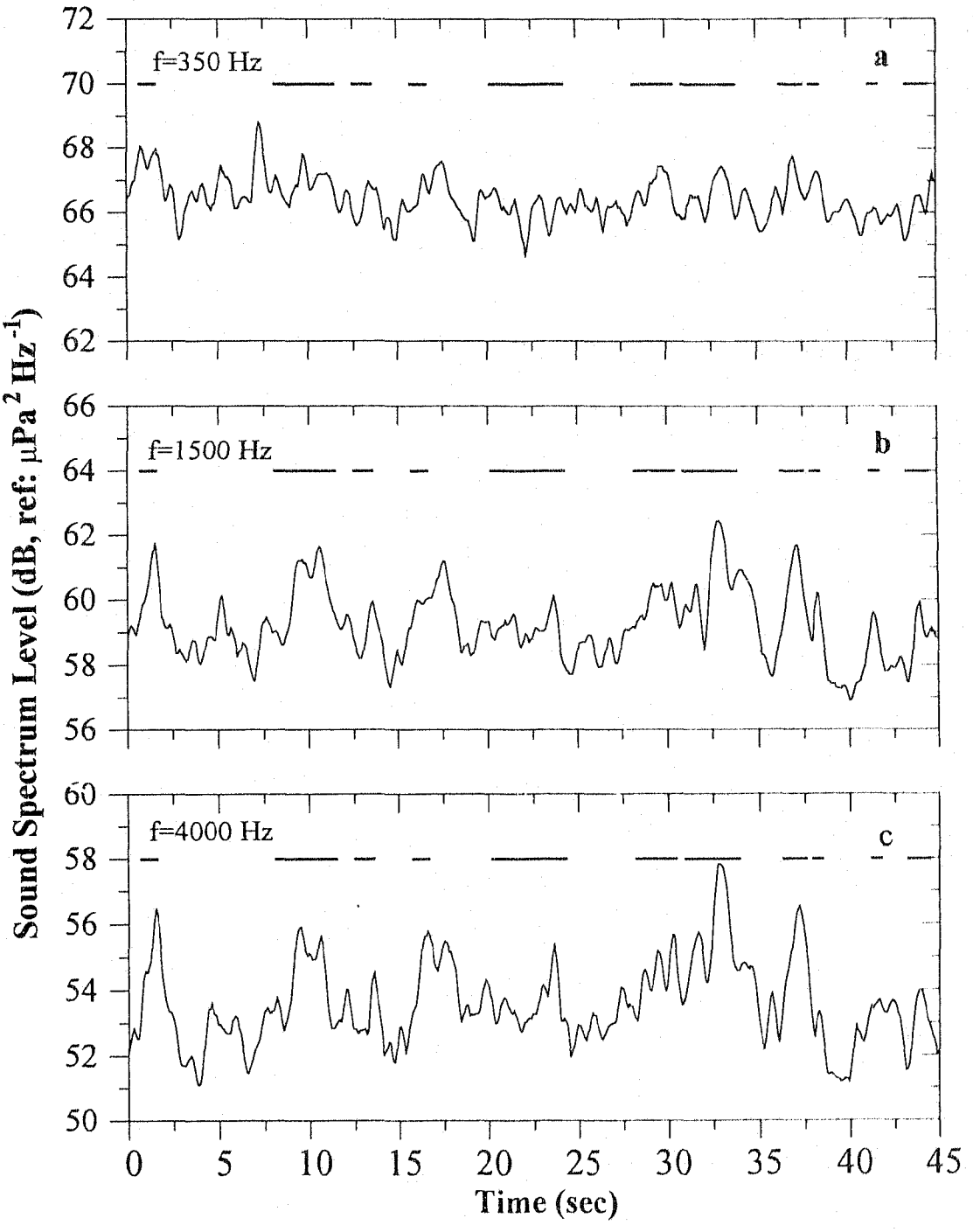

Figure 4.10: Sound spectrum level time series at three frequencies for a 45 s data segment, immediately after Fig. 4.9. Starting time: 10:36:15, 03/14/90, UTC.

4.4.1 Observation

Sound Spectrum Level Series

Let us look first at the sound spectrum level (SSL) received at one single hydrophone. The ambient sound data from Hydrophone 1 were bandpassed at three frequencies (f=350, 1500, and 4000 Hz). The spectrum level was then calculated as a time series. (See Appendix A for calibration of sound level.) Figures 4.5- 4.7 show SSL time series for a continuous period of 135 s, at the three frequencies. The wind speed for these data is 11 ms^{-1}, corresponding to dataset 3 in Table 5.1. (A median filter was applied to remove spikes in the series caused by interference and the resulting series was smoothed with a moving averaging filter). Occurrences, locations, and travel speeds of breaking waves during this period were simultaneously tracked using the technique described in the preceding chapter. The horizontal bars on the top of the figures indicate the period of each tracked event. The larger bursts in the SSL series are seen to be generally associated with the occurrence of breaking events, although for some bursts no events were tracked due to the finite source dimension effect described earlier. SSL time series in a lower sea state (wind speed=6.4 ms^{-1}, corresponding to dataset 22) are also shown in Figs. 4.8- 4.10 for comparison. It can be seen that the energy bursts generally last for a shorter period in the lower sea state than in the higher sea state. In addition, breaking occurs more frequently in the lower sea state as seen in the correlation images in Chapter 3.

Distributions of Acoustic Intensity

Given the instant of occurrence, the received sound level from each individual event can be found in the SSL time series by averaging over the breaking period. However, the background noise level should be subtracted from the total level to obtain the actual received level from the event. Due to the nonstationarity of ambient noise over a longer period, the noise level must be estimated locally. The longest bursts last typically for 8-10 s in Figs. 4.5- 4.7, and for 5-7 s in Figs. 4.8- 4.10. Therefore

for each event, we search for a local minimum within the neighbourhood of the event ($\pm$9 s around its instant of occurrence for dataset 3; $\pm$6 s for dataset 22). Then the corresponding local noise level I_N is estimated at the location of the minimum. The actual sound level received from the event is given by $I_R = I_A - I_N$ (see Fig. 4.5a).

Figure 4.11a shows the distribution of I_R at f=350 Hz over a period of 30 min in an area of radius 40 m, for the data in Figs. 4.5- 4.7. The background noise level (I_N) obtained during the same period is given in Fig. 4.11b. Note that in both distributions the horizontal axis is in the logarithm scale (dB). It is seen that the distribution of I_N is highly concentrated compared to the distribution of I_R. (In other words, the deviation of I_N is much smaller than that of I_R). This implies that I_N, although random by nature, has little variability compared to I_R. In view of this observation, I_N can be assumed constant rather than random. The statistical analysis of breaking waves in the following chapter will benefit greatly from this assumption, since it simplifies the derivation appreciably.

Assume that the acoustic radiation pattern of breaking waves is dipole. Then the received level at depth h from a breaking wave located at horizontal range r, is given by

$$I_R(r,h) = \frac{I_0 h^2}{(r^2+h^2)^2} \tag{4.5}$$

if absorption is neglected, where I_0 is the equivalent source level at 1 m distance on the beam axis (that is, at $r = 0$ and $h = 1m$). Given the received level and the position of the breaking wave, the source level can be determined from Eq. (4.5). Thus the distribution of the received level such as shown in Fig. 4.11a can be converted to the distribution of I_0. Figures 4.12 and 4.13 show the probability distributions of source level I_0 at the three frequencies, for datasets 3 and 22 respectively. These source level distributions will be discussed later.

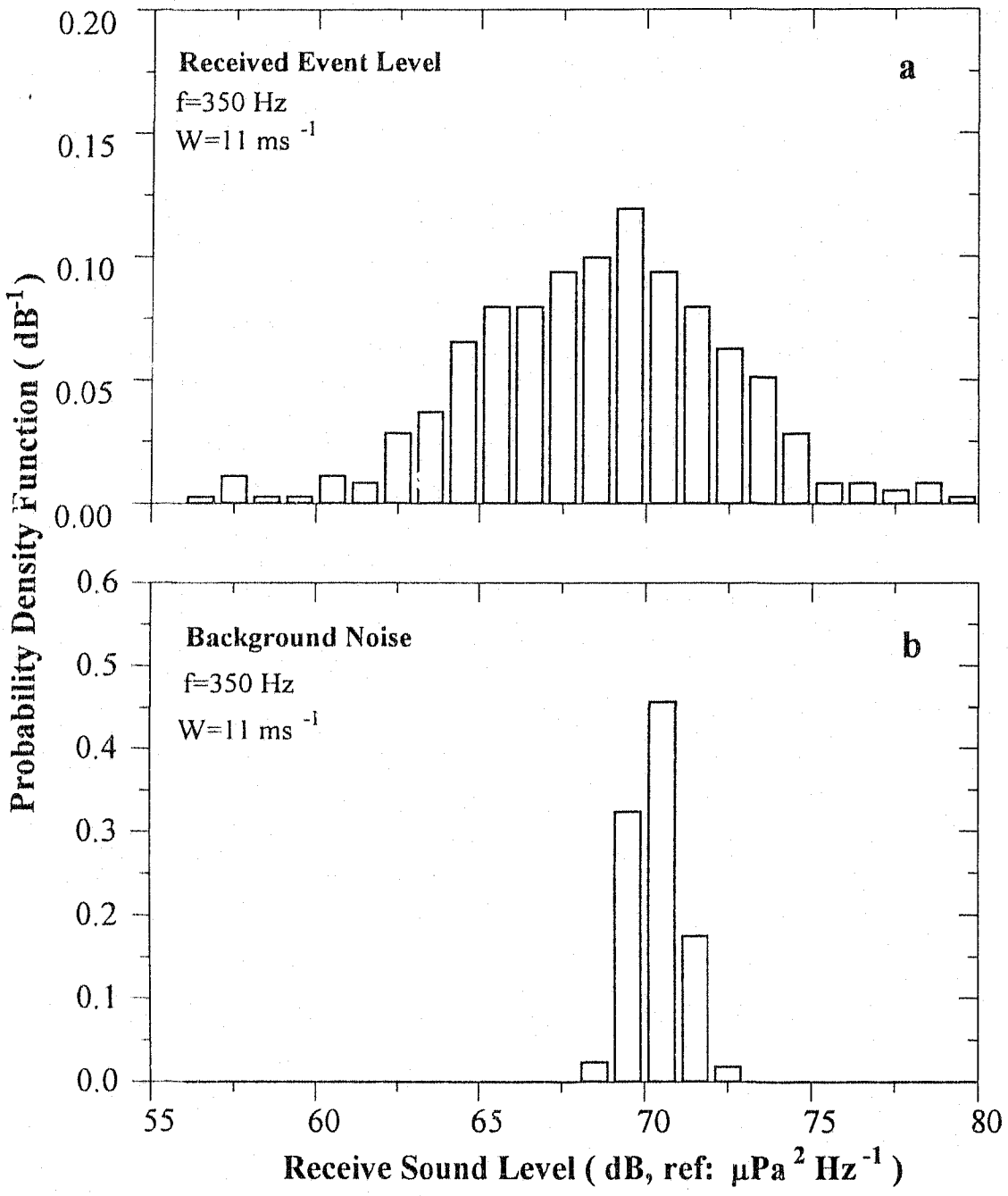

Figure 4.11: (a) Probability distribution of event acoustic level at frequency 350 Hz received at the array. (b) Probability distribution of the background noise level at f=350 Hz. Wind speed=11 ms^{-1}.

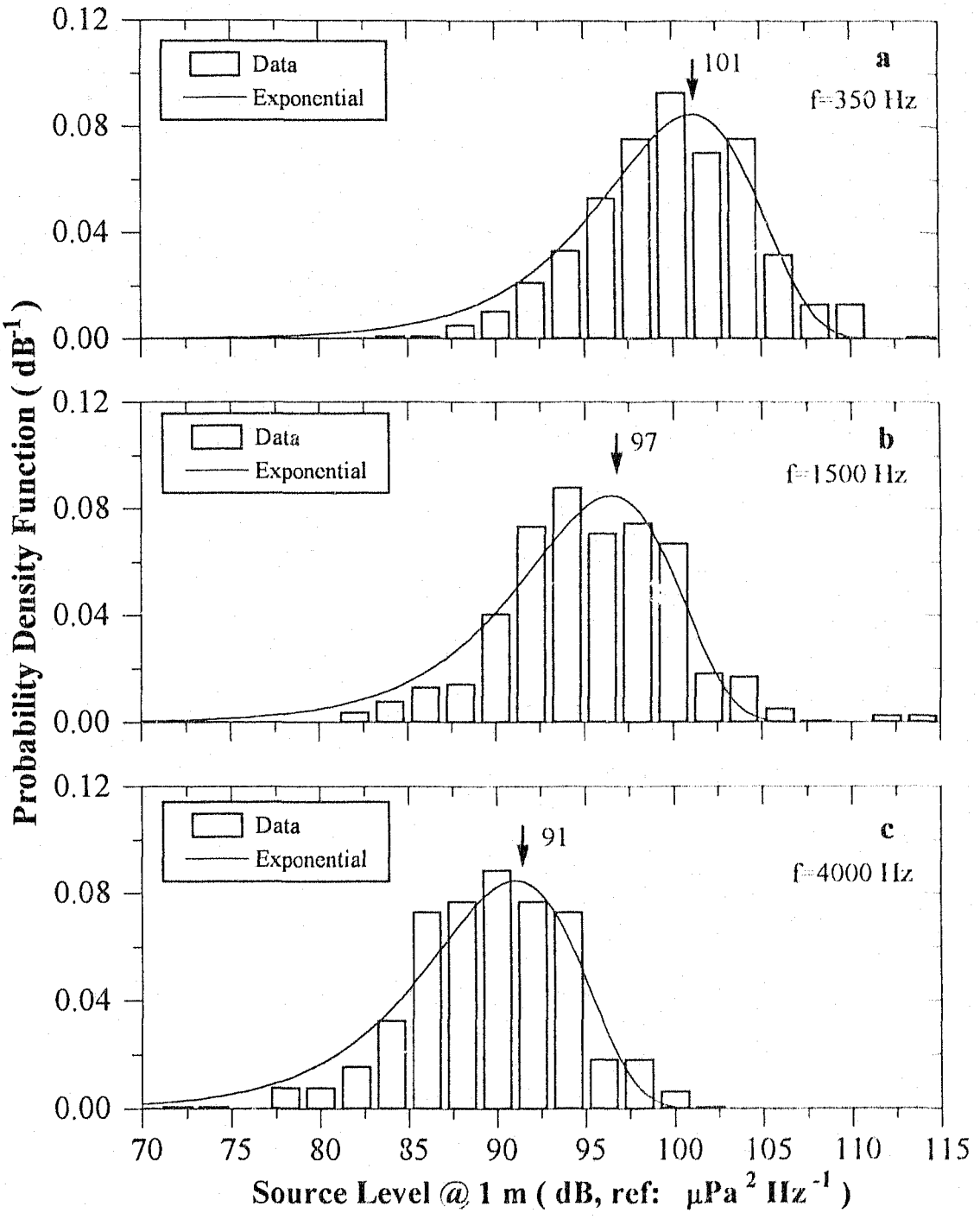

Figure 4.12: Probability distribution of acoustic source level of breaking events at three frequencies. Wind speed= 11 ms^{-1}. The curve is Eq. (4.12) with β (indicated by the arrow) obtained using the least squares fit.

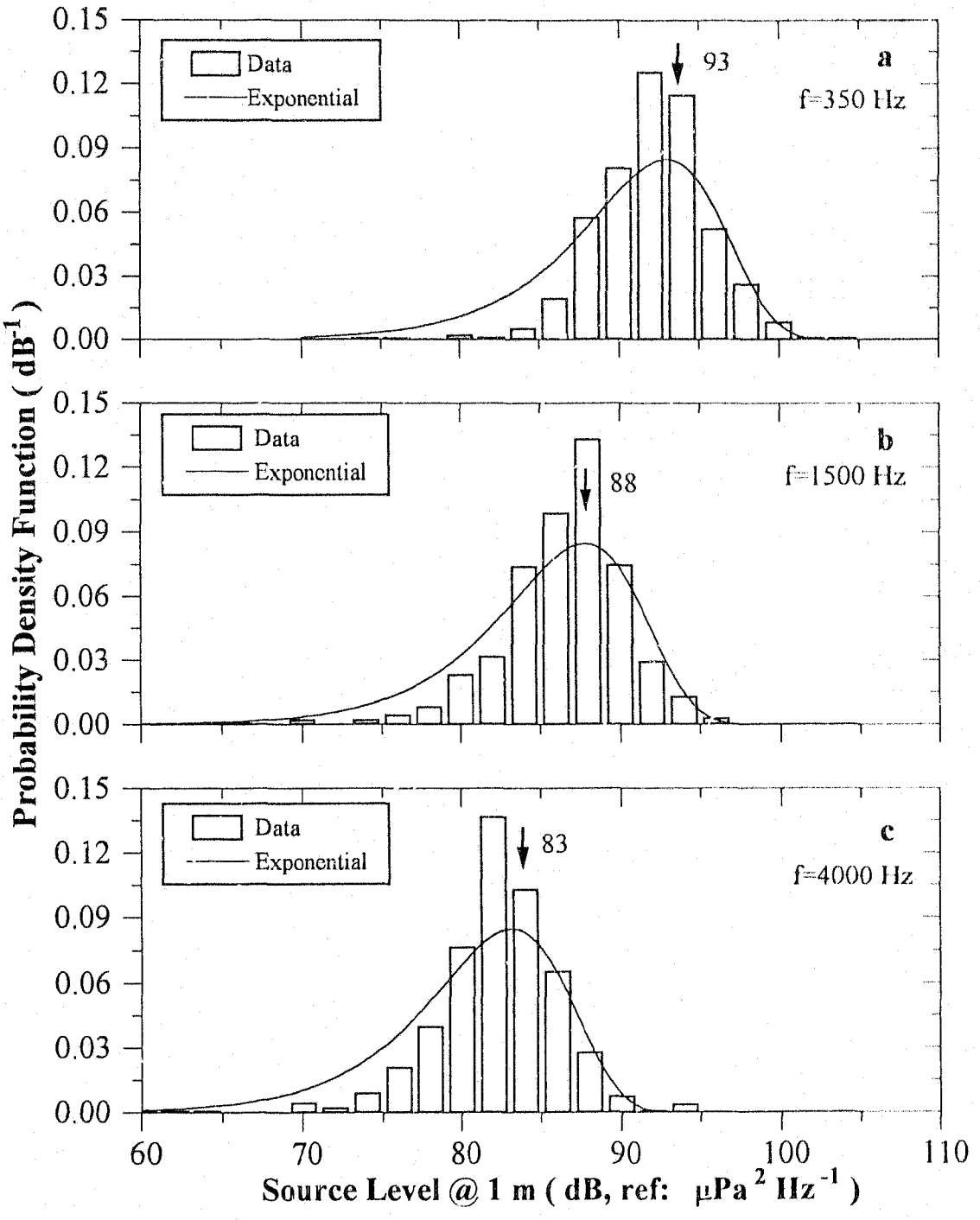

Figure 4.13: Probability distribution of acoustic source level of breaking events at three frequencies. Wind speed= 6.4 ms^{-1}. The curve is Eq. (4.12) with β (indicated by the arrow) obtained using the least squares fit.

Dependence on the Breaking Scale

As discussed in the following chapter, breaking event speed represents the scale of breaking. It is therefore of interest to examine the dependence of source level on event speed. Figure 4.14a [1] shows the source level at frequency 350, plotted against event speed (dataset 3), where a low speed cutoff (1.5 ms^{-1}) is imposed to remove a few (about 4%) rather scattered points which are believed to be due to noise interference. There is still considerable scatter in the data (correlation coefficient r=0.38). The source level is also shown against the event duration (with the range correction as described in Chapter 5) in Fig. 4.14b, which has a correlation coefficient of 0.48. The results for the other two frequencies show similar features, but have a lower correlation coefficient (e.g. r=0.21 and 0.26 at f=1500 and 4000 Hz for event speed) and thus are not shown. Figure 4.15 shows the source level at frequency 4000 Hz against the breaking event parameters for dataset 22 (a low speed cutoff of 1.0 ms^{-1} was used in Fig. 4.15a). The correlation coefficient is 0.21 for event speed and 0.39 for event duration. The results for the other two frequencies are not shown either, due to the lower correlation (e.g. r=0.14 and 0.17 at f=350 and 1500 Hz for event speed).

The least squares fit is difficult to apply to these scattered data, and we therefore resort to the principal component analysis (Preisendorfer, 1988). The two eigenvalues of the scatter matrix for the data in Fig. 4.14a are found to be $\lambda_1 = 1.38$ and $\lambda_2 = 0.62$, and for the data in Fig. 4.14b, they are $\lambda_1 = 1.48$ and $\lambda_2 = 0.52$ (see Appendix C for details). In the principal directions of the higher eigenvalues as shown in the figures (in the directions of the longer arrows), the sound level is found

[1] Although we use the notation for acoustic intensity I in the text, the sound level in these figures has a reference unit of $\mu Pa^2 Hz^{-1}$, which is for acoustic pressure. Note that acoustic intensity is related to rms pressure through $I = \bar{p}^2_{rms}/\rho c$, where ρ is water density and c sound speed. Therefore the magitude in terms of dB is the same for I and p^2_{rms} except that the reference is changed.

to have the following relation with the event speed and duration for Fig. 4.15:

$$I_0 = 10^{8.4} V_e^{2.30} \tag{4.6}$$

$$I_0 = 10^{9.7} D_e^{2.01}, \tag{4.7}$$

where V_e and D_e are the travel speed and duration of breaking events respectively. Similarly, for the data in Fig. 4.15, λ_1 and λ_2 are found to be 0.79 and 1.21 for the event speed, and 0.61 and 1.39 for the event duration. The source level, at a lower correlation level, appears to have the following relation with the event speed and duration:

$$I_0 = 10^{7.2} V_e^{1.93} \tag{4.8}$$

$$I_0 = 10^{8.0} D_e^{1.75}. \tag{4.9}$$

4.4.2 Discussion

The low correlation between the source level and the breaking scale suggests that the radiated acoustic power does not only depend on the breaking scale. The acoustic power radiated from breaking waves is intrinsically related to the energy dissipated through breaking. This was studied in recent laboratory experiments using colliding plane waves, which demonstrated that the acoustic power radiated by a breaking wave is proportional to the energy dissipated by breaking (Melville et al., 1988; Loewen and Melville, 1991a). We shall discuss possible connection of this laboratory observation with our measurements of the acoustic source level distribution.

The dissipated energy due to a two-dimensional breaking wave is proportional to the difference of the upstream and downstream surface displacement variances (a_1^2 and a_2^2 respectively) of the wave. The acoustic power radiated from a source is proportional to the source level, I_0. Therefore, the laboratory observation implies

$$I_0 \sim E_{dis} \sim a_1^2 - a_2^2. \tag{4.10}$$

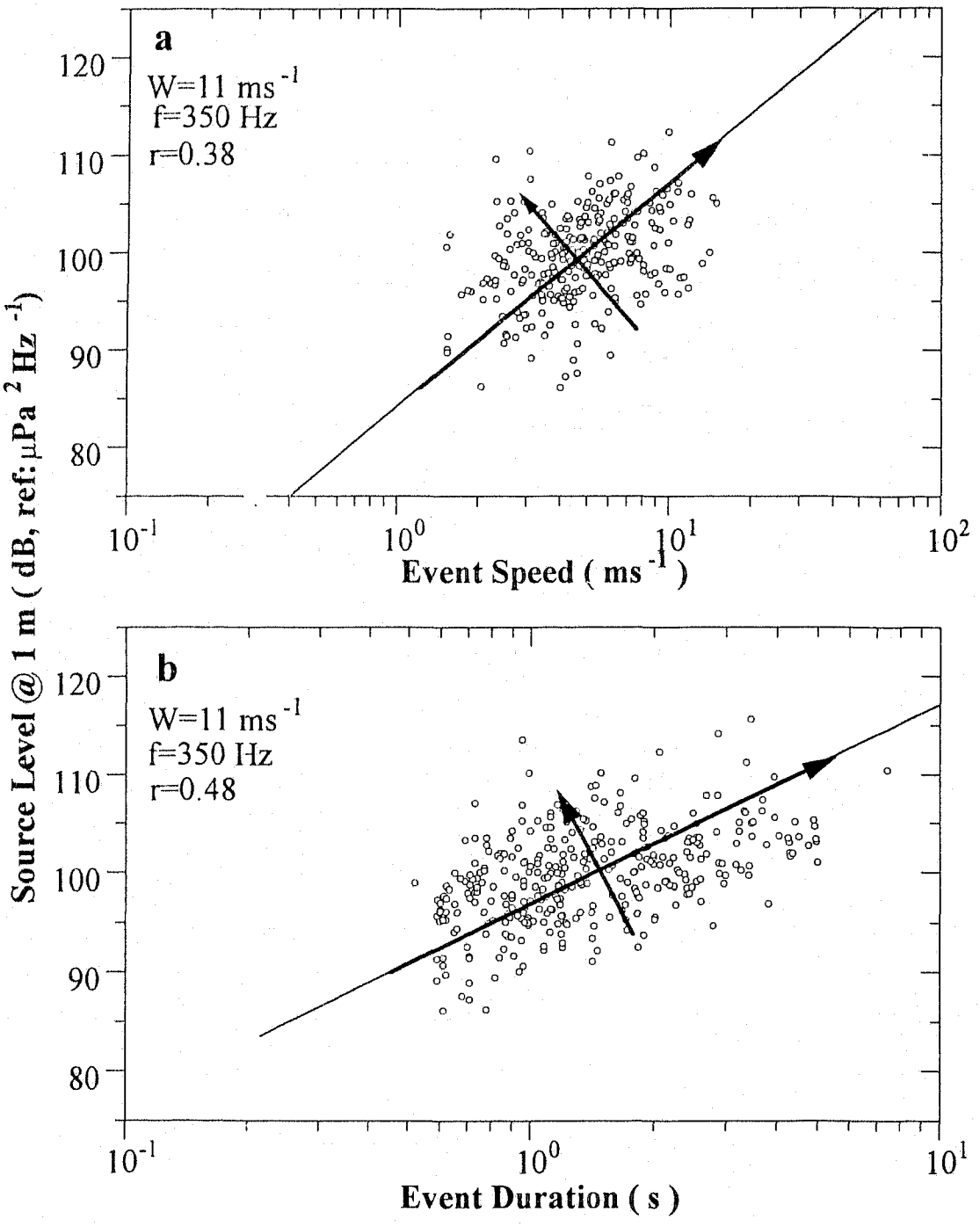

Figure 4.14: Acoustic source level of breaking events against (a) event speed, and (b) event duration. Wind speed=11 ms^{-1}. The straight lines are in the principal direction corresponding to the higher eigenvalues. Also shown are the axes of the data ellipse, with the lengths proportional to the eigenvalues.

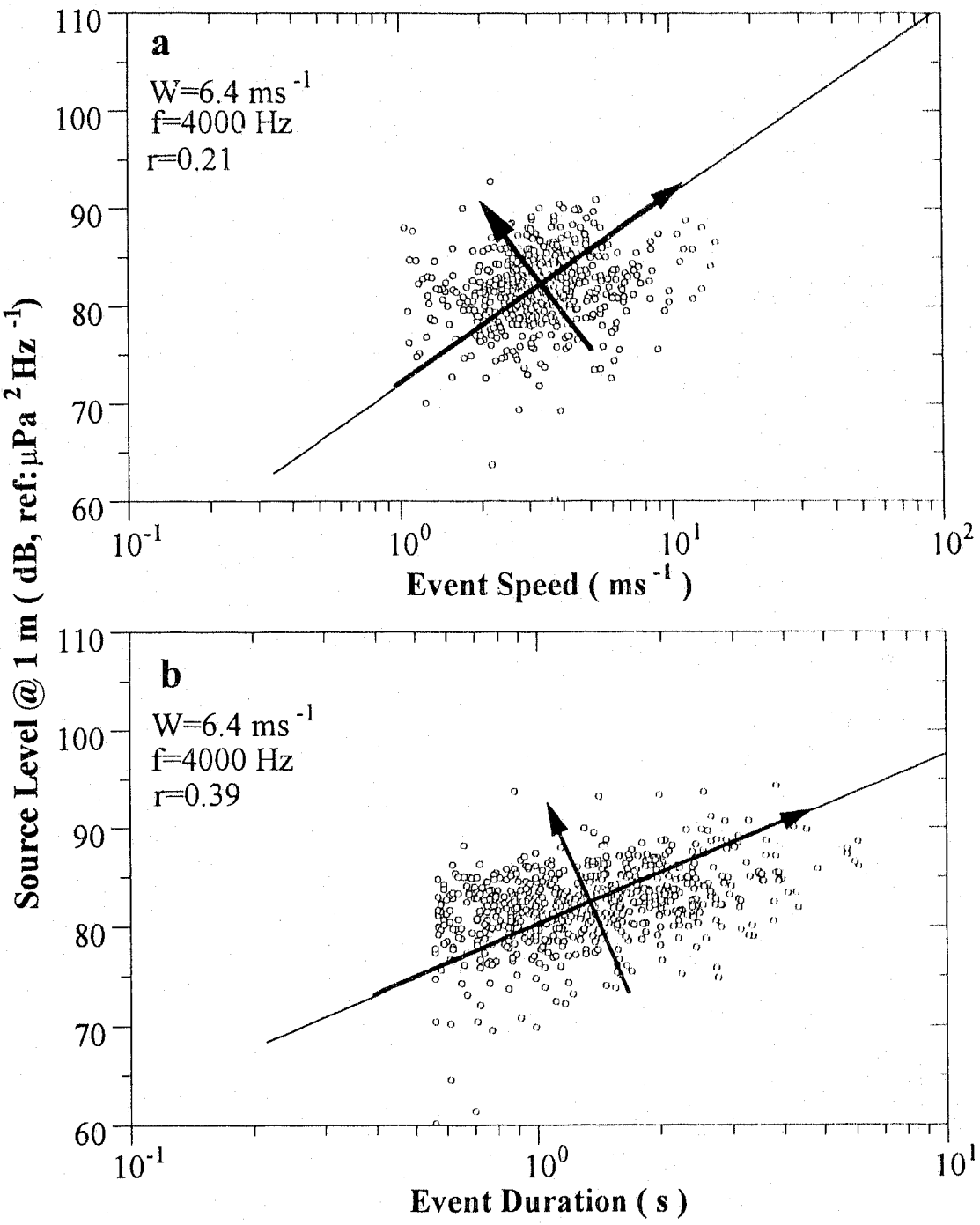

Figure 4.15: Acoustic source level of breaking events against (a) event speed, and (b) event duration. Wind speed=6.4 ms^{-1}. The straight lines are in the principal direction corresponding to the higher eigenvalues. Also shown are the axes of the data ellipse, with the lengths proportional to the eigenvalues.

Unlike laboratory experiments, a_1^2 and a_2^2 are not practically measurable in the ocean. Conceptually, they represent a space-time statistic in the wave field, with a temporal span of D and a spatial span of vD, where v and D are respectively the speed and duration of a breaking event. Here we use this concept to discuss the implications of the laboratory relation for our field observations. However, in the real ocean the surface has a three-dimensional structure. The concept really applies to larger waves for which the elevations at the beginning and ending of the breaking event are only modified by dissipation. Clearly, this would not apply to the case of short waves breaking due to their modulation by long waves. Therefore, the following discussion is only applicable to larger breaking waves, for which most of the wave energy is concentrated in the wind direction.

Assume that this relation also holds for breaking waves in a random sea. It is well known that for wind waves the distribution of wave amplitude a with a finite bandwidth is closely Rayleigh (Longuet-Higgins, 1980), and hence a^2 is found to be exponentially distributed. If it is assumed that the wave field is stationary and homogenous for a given observation period and area, then a_1^2 and a_2^2 have the same exponential distribution. As for the independence, we can examine the space-time correlation function of the wave field, which can be computed from the directional wave spectrum (Longuet-Higgins, 1957). For these datasets, the correlation coefficient for the given temporal and spatial span is found to be of order 0.1-0.2, on the basis of simultaneously observed directional wave spectra described in the next chapter. Therefore, the upstream and downstream surface elevation, ξ_1 and ξ_2, can approximately be assumed independent, because they are essentially gaussian (Longuet-Higgins, 1980). Since a_1^2 and a_2^2 are derived from ξ_1 and ξ_2 separately, they can also be assumed independent.

If a_1^2 and a_2^2 are independent and have the same exponential distribution, then it can be shown that the magnitude of the difference, $z = (a_1^2 - a_2^2) \geq 0$, is also exponentially distributed (see Appendix D). Therefore Eq. (4.10) implies that I_0

(and also E_{dis}) has an exponential distribution:

$$f_{I_0}(I_0) = \frac{1}{\bar{I}_0} e^{-I_0/\bar{I}_0}. \tag{4.11}$$

The measured distributions of the source intensity of breaking waves shown in Figures 4.12-4.13 are compared with the distribution in Eq. (4.11). In order to facilitate comparison between the data and Eq. (4.11), we make a transformation $x = 10\log_{10} I_0$ to reduce the dynamic range of I_0. The resulting distribution of x is found to be

$$f_x(x) = \alpha e^{-\alpha\beta} \exp\{\alpha x - e^{\alpha(x-\beta)}\} \tag{4.12}$$

where $\alpha = \ln 10/10$ and $\beta = 10\log_{10} \bar{I}_0$.

Equation (4.12) is then fitted to the data in Figs. 4.12 and 4.13 by selecting β such that the cost function

$$cost = \sum_i [f(x_i) - \hat{f}(x_i)]^2 \tag{4.13}$$

is minimized, where $\hat{f}(x_i)$ is the estimated distribution from the data. The resulting curve is also plotted in Figs. 4.12 and 4.13. It can be seen that the fit in Fig. 4.12 is fairly good at frequency 350 Hz, although deviations from the curve due to statistical errors must exist. (The deviations are also possibly caused by lack of dipole radiation from a rough surface, or at least, tilting of dipole sources.) The fit at the higher frequencies (f=1500 and 4000 Hz) is less satisfactory, possibly because the signal-noise ratio is lower at the higher frequencies. In the lower sea state (Fig. 4.13), however, the distribution deviates from the exponential distribution considerably at lower intensities, for all the three frequencies (the fit appears slightly better at f=1500 and 4000 Hz than at f=350 Hz). This can be explained on the basis that more small events occur in a lower sea state and these events tend to be masked by the background noise. Nevertheless, the fact that the source level follows the exponential distribution for larger breaking events appears to support the hypothesis that the acoustic power released by breaking waves is proportional to the dissipated wave energy. Additional supporting evidence, though indirect, is recent work by

Kennedy (1992), which suggested that the surface source spectrum level, if the source is assumed dipole, is proportional to the total rate of energy input caused by wave breaking in the gravity wave equilibrium range.

4.5 Summary

In this chapter, we have addressed the problem of acoustical radiation from individual breaking waves. Detailed investigation of the sound from single breaking events suggests a dual nature of the source including both coherent and incoherent components. As the wave evolves the areal spreading of the incoherent sources serves to limit the frequency below which the received signal at two hydrophones is coherent. The spatial anisotropy of the source therefore imposes a corresponding anisotropy on the coherence, with the greatest coherence occurring between hydrophone pairs orthogonal to the wave crest. There is also some evidence of a coherent low frequency source within the breaking wave which would be consistent with collective bubble oscillations at least at the beginning of the breaking. Observations of the acoustic intensity distribution of breaking waves in the open ocean appear to be consistent with the dependence of the radiated acoustic power on the dissipated wave energy obtained for the special case of colliding plane waves in the laboratory. The acoustic intensity, within the limits of the low correlation, shows a generally increasing trend as the breaking scale increases (event speed and duration). These observations suggest that the sound radiated by breaking waves may prove useful not only in determining the kinematic properties of wave breaking as will be discussed in the following chapter, but also in probing the dynamical aspects such as surface wave energy dissipation by breaking.

Chapter 5

Statistics of Breaking Surface Waves

In this chapter, we shall present the statistics of breaking surface waves in the open ocean obtained from the SWAPP data. These statistics, including breaking event density, duration and velocity, represent some fundamental spatial and temporal characteristics of breaking waves. We shall first examine the problem of incomplete measurement and where appropriate, correct for any bias that may arise from the instrumental limitations. Breaking wave statistics are then obtained under various meteorological conditions, and also compared with the simultaneously measured directional wave spectra. Conclusions are drawn from these observations concerning the scale of breaking and its relationship with the wave field parameters.

5.1 Statistical Analysis

Our statistical analysis in this section involves two aspects: the determination of thresholds used to separate breaking events from background noise and statistical corrections for incomplete measurement by the instrument.

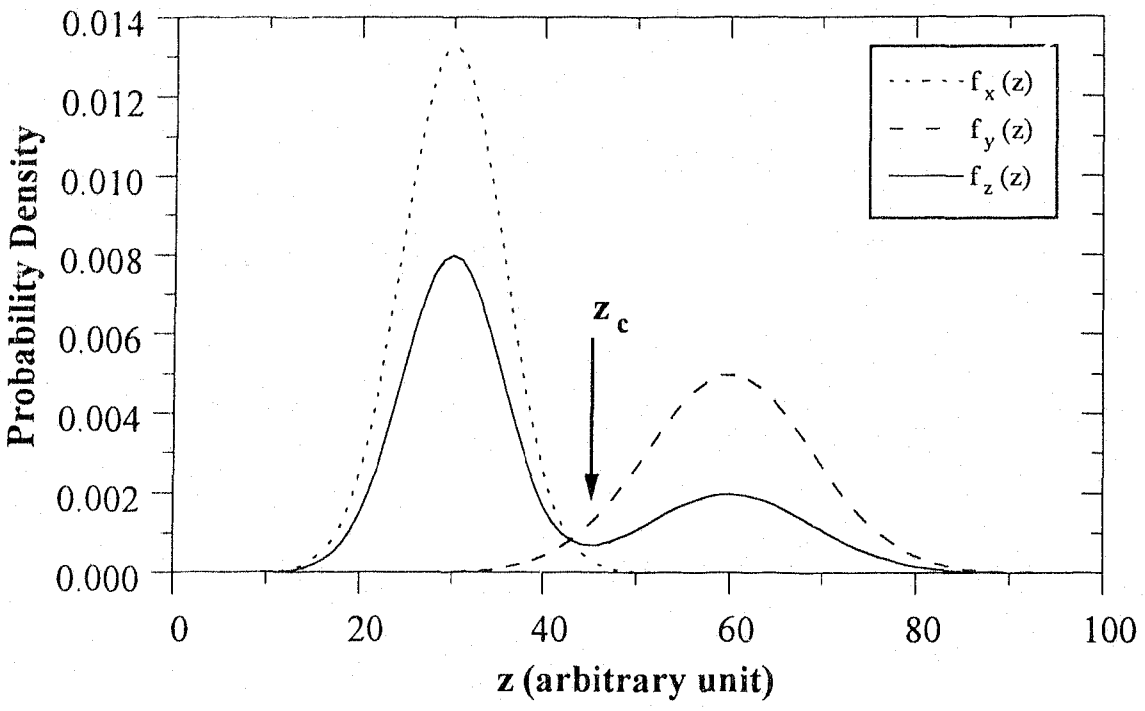

Figure 5.1: Illustrative sketch of the probability distribution (in arbitrary unit) in a two-mode model, where z_c is the selected threshold. $f_z(z)$ is shown as the solid line.

5.1.1 Determination of Thresholds

The event identification scheme described in Chapter 3 selects from the correlation images those events with gray level over a threshold, G. The determination of G is important to the later statistical analysis, since too high a value leads to needless elimination of events whereas too low a value introduces too much noise. Therefore we must choose this threshold optimally in some statistical sense.

If events are well separated from background, then their statistical properties, such as their probability distributions of gray level, should be sufficiently different. Let x be a random variable representing the gray level of events and y be that of background noise. Assume that the probability of selecting events is p. Then the

selected gray level, z, is given by

$$z = \begin{cases} x & \text{with probability } p \\ y & \text{with probability } 1-p \end{cases}.$$

This yields a distribution of z

$$f_z(z) = pf_x(z) + (1-p)f_y(z)$$

where $f_x(x)$ and $f_y(y)$ are the probability density functions of x and y respectively (see Papoulis, 1984, p84). Figure 5.1 shows a sketch of $f_x(z)$, $f_y(z)$, and $f_z(z)$. It can be seen that $f_z(z)$ has two modes, with one corresponding to $f_x(z)$ and the other to $f_y(z)$. We need to choose a threshold to separate these two modes. The optimal choice of the threshold should be the local minimum (z_c) between them. This local minimum corresponds to a plateau in the cumulative function, which can also be used to choose the threshold (Longuet-Higgins and Smith,1983; Weissman et al., 1984).

The correlation image is digitized to 16 gray levels, and searched for event patterns with gray level over a threshold. The density distribution of events is accordingly obtained. Figure 5.2a shows the number of identified events at different gray levels (from the SWAPP data). There is a minimum at gray level 3 that is chosen to be the threshold. Throughout all the datasets we have analysed, $G = 3$ is typical at high winds ($> 7\text{ms}^{-1}$) while $G = 4$ is selected at lower winds ($< 7\text{ms}^{-1}$).

In addition to the gray level threshold, it is also necessary to determine the minimum size of breaking waves. One apparent parameter is duration. In other words, we need to impose a short duration cutoff to reduce further noise and interference that are still above the gray level threshold. The same procedure can also be applied to choose this duration threshold. Figure 5.2b shows the number of events at different durations with gray level over the selected threshold, where it can be seen that $D = 4$ (samples) is the optimal choice for the duration threshold, since it appears to separate a smoothly varying distribution from a much larger number of shorter events which are identified as noise. This choice is typical of the datasets, though for some datasets D=5 was chosen.

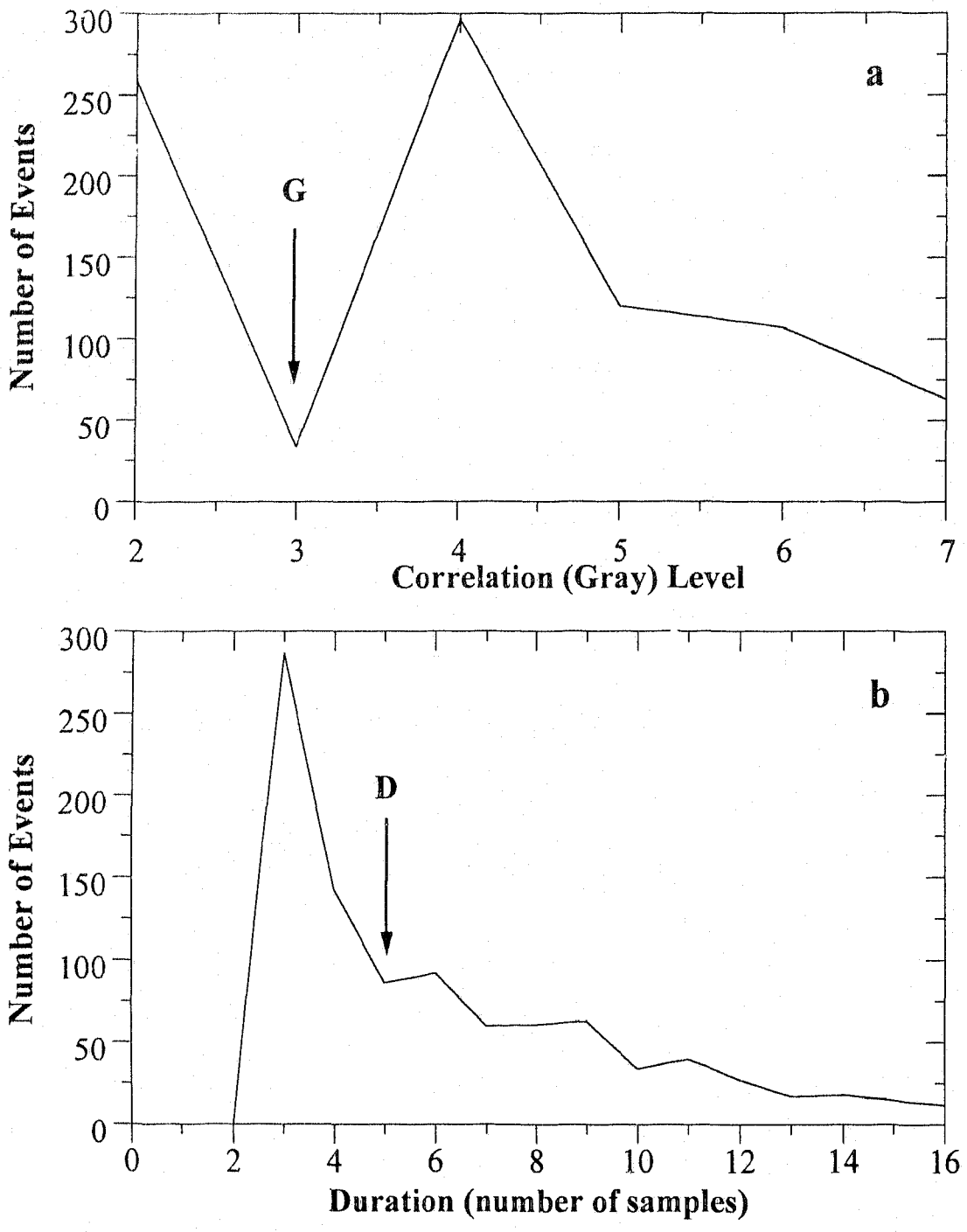

Figure 5.2: Determination of correlation (gray) level and duration thresholds. (a) Density distribution of events with respect to gray level, where the gray level threshold is chosen at $G = 3$. (b) Density distribution with respect to duration for events with gray level above the selected threshold. The duration threshold is at $D = 4$ samples (one sampling interval is 0.0856 s).

5.1.2 Incomplete Measurement and Correction

By incomplete measurement, we mean that the instrument cannot measure all the events that actually occur. Incomplete measurement of our instrument is caused by two factors. One is background noise; weak events cannot be detected if their signal to noise ratios (SNR) are below a certain threshold. This also results in a position dependence of the measured breaking duration. The second factor is the finite source dimension effect that limits our ability to locate breaking waves as mentioned earlier. Incomplete measurement biases the resulting statistics, and thus must be corrected to some extent. In order to explain the problem conveniently, we define the following concepts:

Detectability: An event is detectable if it can be seen on any hydrophone pair.

Locatability: An event is locatable if it can be seen on more than one hydrophone pair.

Trackability: An event is trackable if it can be seen on more than one hydrophone pair and its duration is longer than a threshold so that it can be tracked.

In the following analysis of detectability and breaking duration, the intensity of background noise will for simplicity be considered to be an ordinary rather than a random variable. This is based on the observation that the variability of noise intensity is much smaller than that of breaking event intensity received at the array as shown in Fig. 4.11. Therefore, when both are involved in the same problem, the randomness of noise intensity can be ignored. Treating background noise intensity as constant does not allow false alarm. Although false alarm may actually exist, it does not introduce events at larger scales, since the noise is unlikely to have long persistent patterns in the correlation image due to its little coherence over the hydrophone spacing, as discussed in Chapters 3 and 4. Shorter events that may be introduced by noise have been reduced by using a duration cutoff described earlier.

Detectability

Detectability is determined by received signal intensity, background noise and the required SNR. Received intensity depends on the acoustic strength of a breaking wave and the distance from the wave to the array. Background noise depends on the environment and the required SNR is fixed once the event detection algorithm is chosen. One parameter that describes detectability is the detection probability of events, which can be derived by assuming a certain probability distribution of source intensity and an acoustic radiation pattern.

The radiation pattern is assumed to be a dipole as in Eq. (4.5), and it has also been suggested in Chapter 4 that source intensity I_0 can be assumed to be exponentially distributed (Eq. (4.11)). As a result, the distribution of received intensity $I(r,h)$, is found from Eqs. (4.5) and (4.11) to be

$$f_I(I|r) = \frac{h^2}{\bar{I}_0}(1+\eta^2)^2 \exp\left\{-\frac{Ih^2}{\bar{I}_0}(1+\eta^2)^2\right\}, \tag{5.1}$$

where $\eta = r/h$. Consequently, the detection probability of a breaking event at horizontal range r, is given by

$$p_D(z_d|r) = \int_{I_d}^{\infty} f_I(I|r)dI = \exp\left\{-z_d^2(1+\eta^2)^2\right\}, \tag{5.2}$$

where

$$z_d = \sqrt{\frac{I_d}{\bar{I}_0}}h$$

and I_d is the required detection intensity.

If it is assumed that the background noise results mainly from a distribution of breaking waves with mean intensity $\bar{I}_0$ and density Q, then the total received noise intensity is given by

$$I_N = \int_0^{\infty}\int_0^{2\pi} \frac{Q\bar{I}_0 h^2}{(r^2+h^2)^2} r dr d\theta = \pi Q \bar{I}_0. \tag{5.3}$$

That is, I_0 is proportional to the received noise intensity and, therefore, z_d can be interpreted as the required SNR for an event to be detected.

One of the important breaking wave parameters is event density, that is the number of events in a given area. In the next section, we shall show that the number of events in a selected area can be derived from the number of detectable events in the area and the detection probability, and discuss how to estimate z_d from the data.

Correction of Duration

Because of the background noise, the breaking duration measured from the correlation image is dependent on the event position. That is, a distant event 'looks' shorter than a local one even if they have equal durations, because the received intensity from the distant event is weaker. In order to make correction for this range dependence, it is necessary to assume an acoustical radiation process of the breaking wave, that is, the received intensity should be expressed as a time dependent function:

$$I(t) = Ip(t) = \frac{I_0 h^2}{(r^2 + h^2)^2} p(t). \tag{5.4}$$

The choice of $p(t)$ is rather arbitrary due to lack of *a priori* information. We choose $p(t)$ to be a Hamming function for simplicity,

$$p(t) = \cos^2(\frac{\pi t}{T}) \quad -\frac{T}{2} \le t \le \frac{T}{2},$$

where T is the true duration of a breaking event. Under the circumstances, this choice appears reasonable while proving mathematically tractable.

Let I_d be the detection threshold. Then the measured duration $\hat{D} = 2t_d$ satisfies the relation

$$I_d = I\cos^2(\frac{\pi t_d}{T}),$$

from which we can find the distribution of t_d

$$f_d(t_d) = f_I\left(I_d \sec^2(\frac{\pi t_d}{T})\right)\frac{dI}{dt_d}, \tag{5.5}$$

where $f_I()$ is given in Eq. (5.1). The ML estimate of T can be found by choosing T to maximize $f_d(t_d)$, the solution of which is the root of

$$2\alpha^2 x \tan^2 x \sec^2 x - x(3\tan^2 x + 1) - \tan x = 0, \tag{5.6}$$

where

$$\alpha = z_d(1 + r^2/h^2), \quad x = \frac{\pi t_d}{T}.$$

Then

$$\hat{T}_{ML} = \frac{\pi \hat{D}}{2\hat{x}_{ML}}.$$

Locatability and Trackability

Determination of event density requires determination of the number of detectable events in an 'observation' area. However, due to the finite source dimension effect, we can only obtain the number of locatable events in the area. Nevertheless, from the correlation images, we can determine the ratio of the number of locatable events to that of detectable events within the detection range of the instrument, which will be called the 'locatability ratio'. This ratio however will still be used in the observation area which is enclosed by the detection area, since most of the lost events due to the finite source dimension effect are expected to be relatively close to the hydrophone array. More distant events would subtend a smaller angle and thus be more readily locatable if they rise above the background noise. The locatability ratio obtained in an observation area can thus be considered to be approximately equal to the ratio obtained in the detection area. Therefore, the number of detectable events in the observation area can be obtained from that of locatable events and the locatability ratio.

Trackability is equivalent to locatability except that it requires a longer duration for tracking. Therefore, events with observed durations shorter than a threshold can not be tracked. In addition, if the event is too far away, then it may not be possible to track it due to larger tracking errors occurring at greater distance. The proportion of trackable events is normally 80% of locatable events.

5.1.3 Effects of Incomplete Measurement on the Distribution of breaking parameters

Incomplete measurement not only leads to an underestimate of the total number of events but may also affect the overall distribution of breaking parameters. Here we discuss the possible effects of incomplete measurement on the distribution of two parameters, i.e., event speed and duration.

Background Noise

Consider first the effect of background noise, which results in an underestimate of the number of events at smaller scales. In order to model the effect of noise, we assume the noise is due mainly to the contributions of breaking waves randomly distributed at the ocean surface. It is further assumed that the position of breaking events (x, y) is uniformly distributed in an area of radius R, that is,

$$f(x,y) = \begin{cases} 1/\pi R^2 & x^2+y^2 \le R^2 \\ 0 & \text{otherwise} \end{cases} . \tag{5.7}$$

Following the approach used to derive Eq. (5.2), the distribution of the received intensity from an event with intensity I_0 located in this area is found to be

$$f_I(I|I_0) = \begin{cases} \frac{\sqrt{I_0}h}{2R^2} I^{-3/2} & \frac{I_0 h^2}{(R^2+h^2)^2} \le I \le \frac{I_0}{h^2} \\ 0 & \text{otherwise} \end{cases} .$$

Therefore the detection probability is given by

$$p_D(I_0) = \int_{I_d}^{\infty} f_I(I|I_0)dI = \begin{cases} 0 & I^* \le z_d^2 \\ (h/R)^2(\sqrt{I^*}/z_d - 1) & z_d^2 \le I^* \le z_d^2(1+(R/h)^2)^2, \\ 1 & I^* \ge z_d^2(1+(R/h)^2)^2 \end{cases} \tag{5.8}$$

where $I^* = I_0/\bar{I}_0$. z_d and $\bar{I}_0$ are the same as defined above. The resulting I_0 distribution for detectable events in this area is, according to Bayers' theorem (Papoulis, 1984, p85), given by

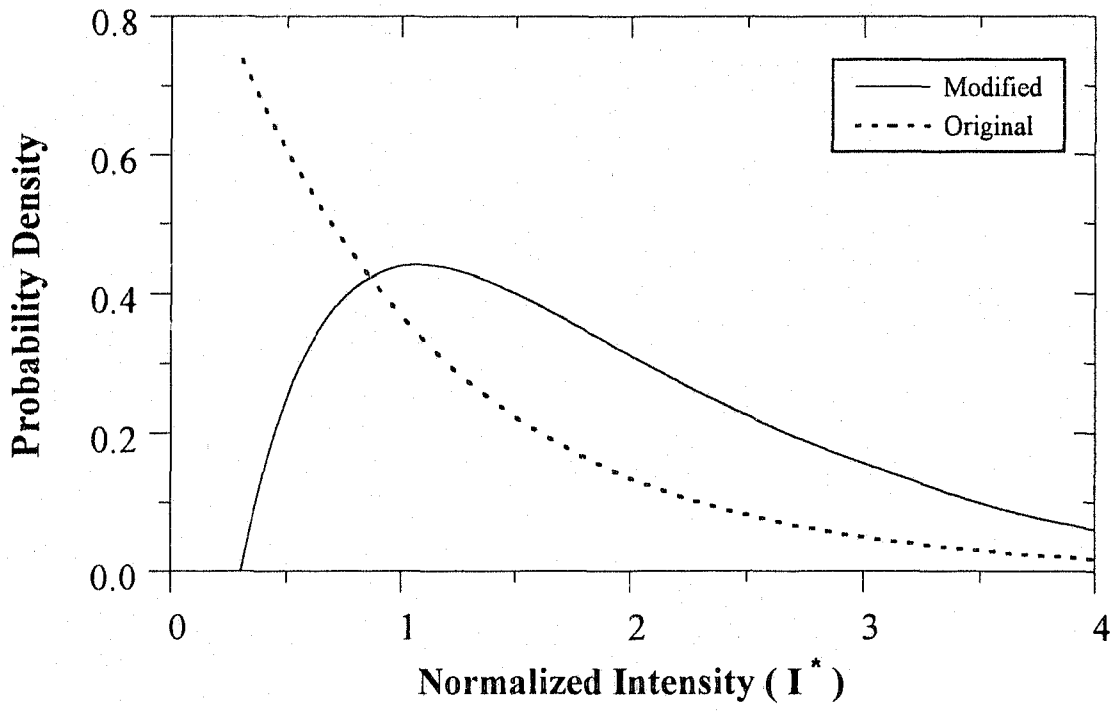

Figure 5.3: Distribution of acoustic source intensity for detectable events. The horizontal axis is the normalized intensity I^*. The solid line is the modified distribution ($f_D(I_0)$) while the dashed line is the original (exponential) distribution for comparison (based on dataset 3 in the table). Note that the vertical axis is scaled by I_0.

$$f_D(I_0) = \frac{p_D(I_0)}{P_D} f_{I_0}(I_0), \tag{5.9}$$

where $f_{I_0}(I_0)$ is the exponential distribution as given in Eq. (4.11), and P_D is the total event detection probability:

$$P_D = \int_0^\infty p_D(I_0) f_{I_0}(I_0) dI_0.$$

Take dataset 3 in Table 5.1 as an example. The modified I_0 distribution is shown against the normalized intensity, I^*, in Fig. 5.3, together with the original distribution. While the original distribution decreases monotonically with I^*, the modified distribution shows a sharp increase at the beginning due to the background

noise and starts to decrease monotonically at $I^* = 1$, which serves as a cutoff scale; thus the correction for low SNR ratios is only reliable above this value. The event duration and speed corresponding to this intensity scale depend on the relation between these parameters and the acoustic intensity. Eqs. (4.6) and (4.7) give the dependences of I_0 on the event duration and speed for locatable and trackable events. Although these empirical relations are obtained for larger scales of breaking, we may assume that they can be extrapolated down to smaller scales, and then use them to estimate the corresponding scales of duration and speed. In order to do so, we must first estimate the mean intensity $\bar{I}_0$. From Eq. (5.8), the minimum required intensity for a breaking event to be detected is $I_0 \geq z_d^2 \bar{I}_0$. It is seen from Fig. 4.14 that the hydrophone array detects events with source intensity as low as 86 dB for this dataset. z_d determined using the approach described in the following section, is 0.552. Therefore $\bar{I}_0$ is approximately 91 dB for this dataset. Now using the relations in Eqs. (4.6) and (4.7), the corresponding scales of duration and speed are estimated to be of order 0.5 s and 1.8 ms^{-1}, respectively. These scales would probably be the cutoff of our instrument for this dataset. Above these scales, the measured distribution still deviates from the true distribution, but the deviation is relatively small. [1] Note that these estimates are based on the empirical relations derived from larger scale breaking waves, and only provide a rule of thumb for assessing the effect of background noise.

Finite Source Dimension

Finite source dimension may also affect the distribution of breaking parameters. Figure 5.4 shows the locatability ratio as a function of the duration measured at the hydrophone array (without the ML correction). The ratio increases rapidly from 10% to 70% as the duration increases from 0.2 s to 0.6 s. For $D > 0.6$ s, the ratio

[1] The mean intensity of the detectable events for $I^* > 1$ (conditional mean) is about 14% greater than that of the total events for the same scale. Thus the corresponding mean event speed and duration of the detectable events are estimated to be approximately 6% greater than the true scales, based on Eqs. (4.6) and (4.7).

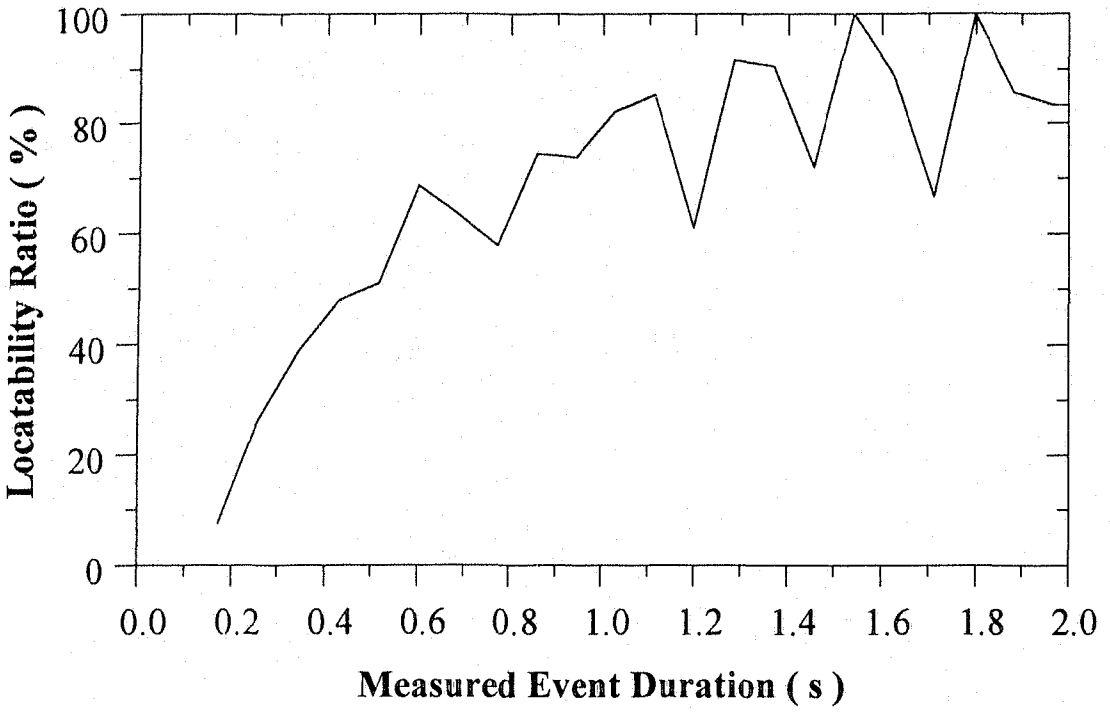

Figure 5.4: Locatability ratio v. s. the measured duration at the hydrophone array (based on dataset 3 in the table).

fluctuates between 60% and 100% with a mean value of 70%, and also shows a slowly increasing trend as D increases. Note that this does not mean that the locatability increases with the true duration, or the scale of breaking, since D is the measured duration. It is possible that a shorter measured duration corresponds to a longer true duration, since a larger event may be farther away, or it may have shorter coherent acoustical signals; a smaller event is more compact and its coherent signal may last for a longer period.

The low locatability for $D < 0.6$ s can be explained as follows: the detected events below this scale contain a considerable amount of noise because of low source intensities so that the number of detected events is larger than it should be. The noise is filtered out by using two hydrophone pairs. Thus the resulting locatability ratio is reduced. We therefore determine the bounds of the ML corrected duration corresponding to $D = 0.6$ s. For an event at range $r = 0$, the lower bound is 0.82

s. For $r = 35$ which is a typical observation radius, the upper bound is 1.7 s. For a uniform position distribution of events as in Eq. (5.7), the mean horizontal range of event position is $\bar{r} = 2/3R = 23$ m for R=35 m. The ML corrected duration corresponding to $D = 0.6$ s is 1.15 s for this mean range. The duration distribution is not severely affected by finite source dimension for duration larger than this scale. Below this scale, the locatability ratio is contaminated by noise, which is difficult to evaluate. Nevertheless, our primary concern is the mean scale of breaking which is better represented by event speed.

The effect of finite source dimension on the speed distribution can only be addressed indirectly, due to the inability to obtain the speed of non-locatable events. The only information available for such analysis is the time delay of events on one hydrophone pair, from which we can calculate the rate of change of the time delay. This rate depends on the velocity and position of the breaking event. Assuming the position of a breaking event is uniformly distributed, the probability distribution of the rate of change can be found given the velocity, and has a sharp peak corresponding to the speed of the event. (Derivation of this distribution is tedious but straightforward. Details are not given here however.) That is, the location of the peak represents the speed. Therefore, we calculate the rate of change for non-locatable events on the hydrophone pair in the downwind direction, which usually has most of the non-locatable events (using dataset 3 in Table 5.1). The apparent speed distribution is shown in Fig. 5.5a, compared with the distribution for the tracked events with respect to the same hydrophone pair (Fig. 5.5b). Although the details of these distributions are different, the dominant peaks are located in the same region. Therefore, on the basis of this limited information, we conclude that the finite source dimension effect does not selectively eliminate breaking events at a particular speed and that the speed distribution is not significantly modified. The reason for this is that breaking waves are randomly distributed in space. Thus larger scale waves can be farther away from the array and easier to locate as mentioned earlier.

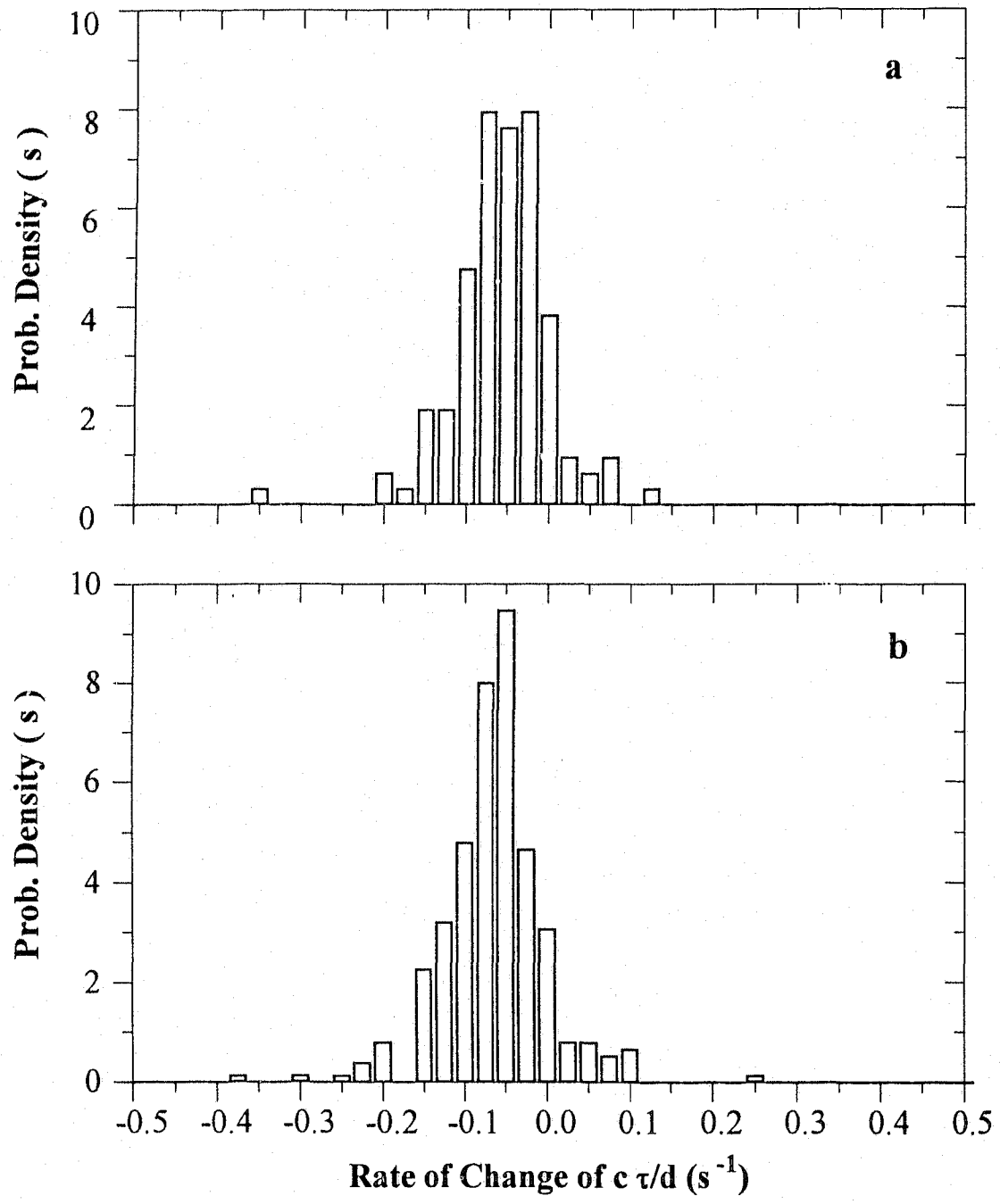

Figure 5.5: Distribution of the rate of change of $c\tau/d$, where τ is the time delay of signals arriving at the hydrophone pair in the downwind direction. c is sound speed and d is the spacing between the hydrophones. (a) For non-locatable events; (b) For tracked events. (Based on dataset 3 in the table.)

In summary, background noise masks small scale breaking events and therefore affects the distributions at lower values. Finite source dimension eliminates some of the detectable events, but does not appear to affect the overall distribution of either event speed or event duration at higher values. The dataset used in the example was acquired at a relatively steady and high sea state. Although only this single dataset was presented, for those datasets at lower sea states, the incomplete measurement is not expected to affect the distributions in the range above the scale described here.

5.2 Determination of Event Statistics

The acoustic instrument measures the spatial position, duration, and velocity of individual events. From these event parameters, we can determine the spatial and temporal statistics of breaking events, such as event density, duration, velocity, spacing, active acoustic coverage, and breaking probability. Of these, event density, duration, and velocity are the basic statistics. Other statistics can also be derived as long as they are defined appropriately. This section focuses on the definition and determination of breaking wave statistics from the event parameters.

5.2.1 Event Density

Event density ($\hat{Q}$) is defined as the number of events per unit area per unit time. It can be determined by the number of detectable events in a selected area and the detection probability of events. The number of detectable events is obtained by dividing the number of locatable events by the locatability ratio. This ratio ranges from 65% at higher winds (14 ms^{-1}) up to 85% at lower winds (6 ms^{-1}). The detection probability depends on the required SNR, which can be estimated from the data.

We notice that the detection probability in Eq. (5.2) is dependent on z_d and the horizontal range, r. The range distribution of detected events will be determined only by z_d. Let $m(r)$ be the number of detected events in unit range interval at

range r, and Q be the number of events per unit area. Then

$$m(r)dr = 2\pi r dr Q p_D(z_d|r),$$

that is

$$m(r) = 2\pi r Q p_D(z_d|r),$$

where $p_D(z_d|r)$ is given in Eq. (5.2). The number of total received events is given by

$$N = \int_0^\infty m(r)dr = \frac{\sqrt{\pi}}{2}\pi Q h^2 \frac{1 - \mathrm{erf}(z_d)}{z_d},$$

where

$$\mathrm{erf}(x) = \frac{2}{\sqrt{\pi}} \int_0^x e^{-t^2} dt$$

is the error function. Then we obtain a normalized range distribution

$$n(r) = \frac{m(r)}{N}, \tag{5.10}$$

which depends on z_d only.

Figure 5.6a shows a normalized range distribution from the acoustical observation for locatable events. Although this distribution deviates from the distribution for detectable events, it preserves a general feature of $n(r)$: the number of detectable events increases initially with range r since the observation area $2\pi r dr$ increases with r, but decreases at greater range because the detection probability drops rapidly. The finite source dimension effect may modify the range distribution of detectable events by reducing the number of events at shorter range, since a local event 'looks' larger than a distant one. Generally speaking, the probability of loss due to finite source dimension decreases with increasing range. Nevertheless, the use of four independent hydrophone pairs improves the locatability of near events to an extent that depends on the event orientation (this factor is less important for more distant events). Hence the distribution is not expected to be severely modified. [2] Therefore,

[2] Morever, z_d determined from the data using the following optimization scheme seems to be relatively insensitive to slight variations in $\hat{n}(r)$.

we can choose z_d by best fitting $n(r)$ to the data, that is, by minimizing the cost function

$$cost = \sum_i [n(r_i) - \hat{n}(r_i)]^2. \tag{5.11}$$

Once z_d is chosen, event density can be estimated from

$$\hat{Q} = \frac{\hat{N}(R_1, R_2)}{A_{eff} T_o}, \tag{5.12}$$

where $\hat{N}(R_1, R_2)$ is the number of detectable events located between horizontal range R_1 and R_2 during the period of T_0. A_{eff} is referred to as the 'effective' observation area defined as

$$A_{eff} = \int_{R_1}^{R_2} 2\pi r p_D(z_d|r) dr = \frac{\pi\sqrt{\pi}h^2}{2z_d}[\Phi(z_d(1+\eta_2^2)) - \Phi(z_d(1+\eta_1^2))], \tag{5.13}$$

where $\eta_1 = R_1/h$ and $\eta_2 = R_2/h$.

The curve in Fig. 5.6a gives the model distribution $n(r)$ in Eq. (5.10), with z_d derived from the least squares fit. It can be seen from Fig. 5.6a that the model fits the data well at closer range ($r \leq 15$ m) but that the distribution of data extends farther than the model, implying that the array detects more distant events than the model predicts. Figure 5.6b shows the estimated density from Eq. (5.12) as a function of R_1 and R_2. The flat region of Fig. 5.6b (0-35 m) is chosen to be the effective observation area. Event density is then averaged over this area by substituting $R_1 = 0$ and $R_2 = 35$ into Eqs. (5.13) and (5.12).

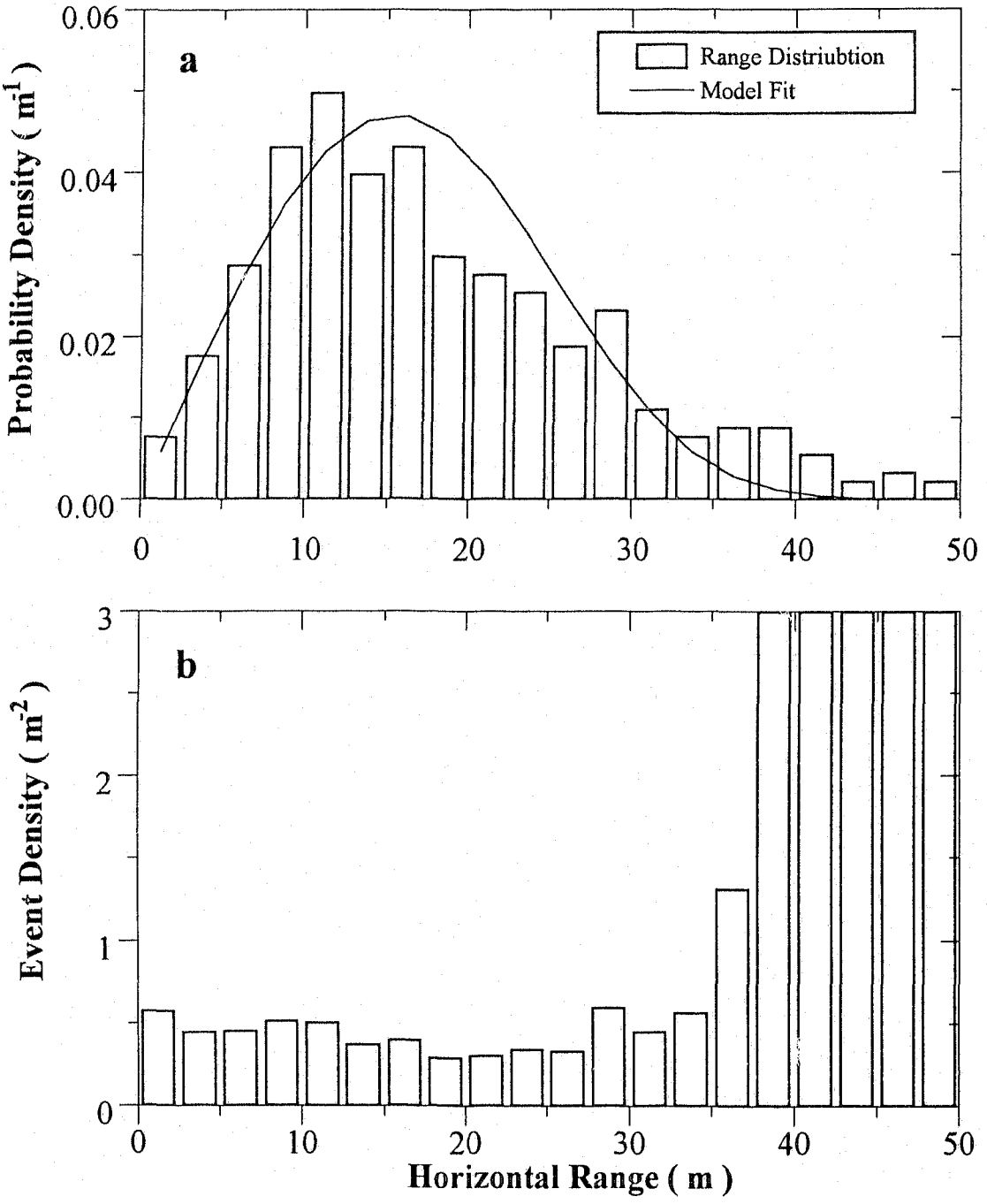

Figure 5.6: Determination of event density, based on dataset 14 in the table. (a) Horizontal range distribution of events where the curve is the least squares fit of the distribution; (b) Corrected event density in range from R_1 to $R_2 = R_1 + 2.5$ m. The flat region (0-35 m) is chosen to be the observation area, where event statistics are obtained.

5.2.2 Duration, Velocity, Downwind Dimension

Event duration is obtained, by comparing the measured durations in the correlation images from all possible hydrophone pairs and choosing the longest; this value is corrected with the maximum likelihood estimator. The corrected duration is also affected by finite source dimension but this effect is not expected to be severe, as discussed earlier. Velocity however is directly measured without necessity of correction. Downwind dimension L_D defined as the distance a breaking event travels, is given by the product of event speed and duration, i. e., $L_D = vD$. The duration distribution of locatable events and the velocity distribution of trackable events can also be obtained in the same observation area as above.

5.2.3 Mean Spacing and Active Acoustic Coverage

From these statistics, we also evaluate the mean spacing between breaking waves. Consider an observation area S where there are N breaking events with mean spacing $\bar{l}_s$. Then $S \approx N\bar{l}_s^2$ when N is large and the area of breaking events is small compared to $\bar{l}_s^2$. Given breaking density $\hat{Q}$ as defined above, the number of events occurring in S and during the mean lifetime $\bar{D}$, is $N = \hat{Q}\bar{D}S$. Therefore the mean spacing can be estimated by

$$\bar{l}_s = \frac{1}{\sqrt{\hat{Q}\bar{D}}}. \tag{5.14}$$

It is also of interest to calculate a statistic that is an acoustic analog of whitecap coverage. We define 'active acoustic coverage' as the fraction of the sea surface swept by active acoustic events during their mean lifetime. The mean area swept by each individual event during its lifetime is given by $\epsilon = \overline{L_D L_c}$, where L_c is the cross dimension. Bortkovskii's data (1987) show that the correlation coefficient between the downwind dimension and crosswind dimension of whitecaps varies from 0.15 to 0.78 in the Southern Ocean and from 0.28 to 0.85 in the tropics, but that the correlation is rather scattered, showing no clear dependence on the wind speed and the whitecap size. Due to scarce information about the correlation, we assume

for this calculation that the crosswind dimension is independent of the downwind dimension; better estimation of ϵ could be achieved with further developments of the measurement technique. The mean cross-wind dimension of a breaking wave is estimated by Bortkovskii to be twice the mean downwind dimension, that is, $\epsilon = \bar{L}_D \bar{L}_c = 2\bar{L}_D^2$. Then acoustic coverage as a fraction of the sea surface is given by

$$AC = \frac{N\epsilon}{S} = \frac{\epsilon}{\bar{l}_s^2} = \frac{2\bar{L}_D^2}{\bar{l}_s^2}. \tag{5.15}$$

5.3 Results

In this section, we present statistical results from the SWAPP data in a variety of wind and wave conditions, over the period of 7-14 March, 1990 (Fig. 5.7). The data were separated into groups corresponding to different wind speeds. At each wind speed, breaking event statistics were obtained in an area of radius 30-40 m and over a period of 30 min (there are two 15 min datasets), and the number of events is normally between 350-700, depending on the sea state. Two types of wave data were acquired from RP FLIP and kindly made available to us by J. Smith (Scripps Institution of Oceanography). These included one-dimensional wave spectra measured with a capacitance wave gauge (with a cutoff at 2.5 Hz), and directional wave spectra inferred from nearly horizontally oriented Doppler sonars (with a cutoff at 0.5 Hz). The wind and wave conditions under which the acoustical measurements were made, are summarized in Table 5.1. The corresponding breaking wave statistics are given in Table 5.2. Error analysis of the statistical results is given in Appendix E.

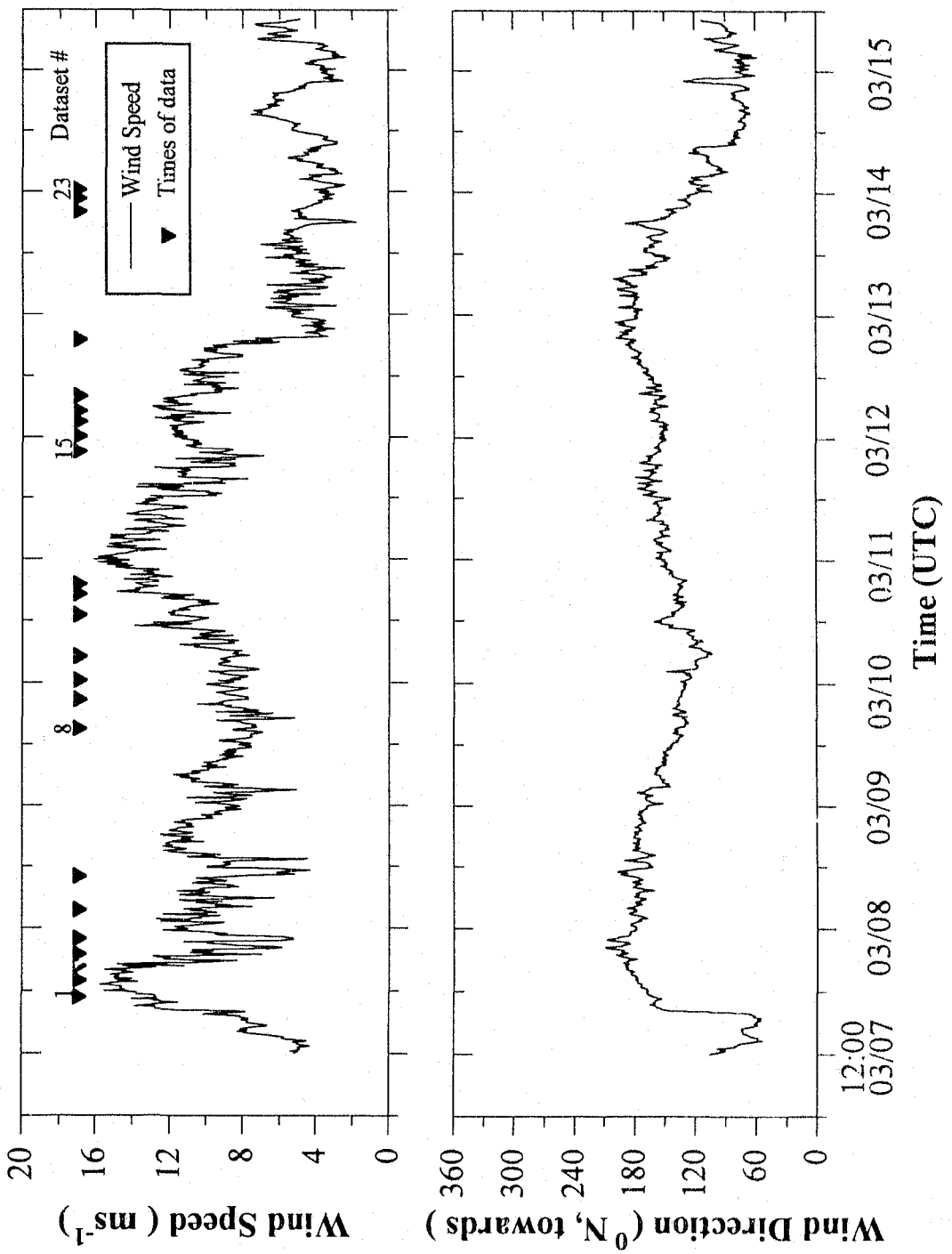

Figure 5.7: Time history of the wind velocity during part of the SWAPP experiment. Raw wind data (provided by A. Plueddemann, WHOI) were averaged over a period of 9.375 minutes and plotted in this figure. The periods during which the acoustical data presented in this paper were acquired are marked by dark downward triangles.

Data set #	Date	Time UTC	W ms^{-1}	θ_w °N	T_s s	θ_s °N	T_p s	θ_p °N	s	t_w °C	t_a °C
1	03/07	22:46	14.6	170	10.7	129	4.92	125	-5.72	13.02	11.38
2	03/08	02:01	14.3	186	9.1	134	8.00	40	-5.43	12.94	10.27
3	03/08	04:46	10.4	191	10.7	131	7.68	146	-5.17	12.94	9.48
4	03/08	07:01	8.0	191	10.7	133	6.40	154	-5.28	12.93	9.48
5	03/08	10:01	10.7	178	10.7	135	5.49	164	-5.56	12.85	9.67
6	03/08	15:31	10.7	176	12.0	136	5.19	176	-5.16	12.80	9.33
7	03/08	22:01	11.0	172	10.1	142	4.00	176	-4.89	12.84	9.79
8	03/10	03:01	8.9	131	12.8	149	3.62	120	-5.08	12.83	13.13
9	03/10	08:46	8.9	117	12.8	144	4.47	117	-4.85	12.80	13.13
10	03/10	12:31	9.6	119	11.3	145	3.92	104	-4.33	12.95	13.07
11	03/10	17:01	10.7	136	12.8	139	4.47	126	-5.34	13.10	12.98
12	03/11	01:01	14.7	149	12.0	132	6.62	116	-4.82	13.87	11.92
13	03/11	05:01	14.3	155	12.8	130	6.40	136	-5.22	13.87	10.96
14	03/11	07:01	13.0	151	10.1	135	7.11	136	-5.22	13.80	10.17
15	03/12	09:01	10.0	159	10.7	134	5.05	154	-4.98	13.18	10.65
16	03/12	12:01	10.4	170	8.7	128	4.80	154	-5.54	13.17	11.03
17	03/12	15:01	9.6	178	13.7	141	5.19	152	-4.93	12.88	11.03
18	03/12	17:01	6.9	181	13.7	141	5.19	152	-4.93	12.87	11.16
19	03/12	20:01	4.6	183	12.8	138	6.40	154	-5.05	12.92	11.00
20	03/13	07:01	5.1	155	12.0	142	4.27	169	-4.73	12.77	10.83
21	03/14	08:01	6.2	73	10.7	129	2.74	66	-5.31	12.80	12.20
22	03/14	10:31	6.4	70	10.1	129	2.95	58	-6.65	12.75	12.38
23	03/14	12:15	6.1	80	10.1	126	3.20	65	-6.14	12.75	12.70

Table 5.1: Wind and wave conditions for the SWAPP data. W and θ_w –wind speed and direction; T_s and θ_s – period and direction of swell; T_p and θ_p – period and direction of the peak wind wave; s – slope of the spectrum; t_w and t_a – water and air temperature; Starting times and dates of the datasets are also given in UTC (Universal Time Clock).

Data set #	$\hat{Q}(\times 10^{-3})$ $m^{-2}s^{-1}$	$\bar{D}_e$ s	$\bar{V}_e$ ms^{-1}	$\bar{\theta}_e$ °N	$\bar{L}_D$ m	$\bar{c}_{br}$ ms^{-1}	$\bar{\theta}_{br}$ °N	m_4 $(ms^{-2})^2$
1	0.551	1.71	4.67	162	9.61	5.38	136	0.501
2	0.311	1.71	5.48	181	11.49	6.99	152	0.699
3	0.246	1.61	5.39	170	11.41	6.55	163	0.606
4	0.422	1.64	4.98	192	10.63	6.22	172	0.572
5	0.378	1.55	5.06	183	10.67	5.84	170	0.539
6	0.426	1.41	4.65	183	8.31	5.56	174	0.445
7	0.429	1.70	4.63	176	9.79	4.72	171	0.311
8	0.643	1.51	3.81	125	7.36	4.37	116	0.295
9	0.553	1.40	4.25	92	8.09	4.80	105	0.391
10	0.516	1.44	4.43	107	8.32	4.49	102	0.313
11	0.382	1.56	4.59	134	8.30	4.93	123	0.424
12	0.289	1.78	5.46	137	11.54	5.97	127	0.569
13	0.303	1.61	5.39	150	11.17	6.26	139	0.630
14	0.337	1.79	5.31	144	12.00	6.39	137	0.635
15	0.818	1.49	4.58	160	8.83	5.31	149	0.447
16	0.381	1.44	4.46	157	7.87	5.19	150	0.432
17	0.678	1.37	4.40	177	7.57	5.30	162	0.397
18	0.529	1.40	3.88	182	6.53	5.30	162	0.397
19	0.656	1.42	3.74	181	6.17	5.86	168	0.410
20	0.720	1.18	3.34	167	4.68	4.75	168	0.233
21	1.063	1.29	3.18	61	4.44	3.75	62	0.186
22	0.770	1.40	3.30	55	5.54	3.90	58	0.231
23	0.688	1.30	3.32	64	5.10	4.08	61	0.245

Table 5.2: Breaking wave statistics from the SWAPP data. $\hat{Q}$–event density; D_e event duration; $\bar{V}_e$–event speed; $\bar{\theta}_e$–event direction of motion; $\bar{L}_D$–downwind dimension; $\bar{c}_{br}$–mean breaking wave speed; $\bar{\theta}_{br}$–mean breaking wave direction; m_4–the fourth moment of the spectrum.

5.3.1 Wave Spectra

Directional wave spectra are in the form of the velocity spectrum $V(\omega, \theta)$, but can be transformed to the elevation spectrum or acceleration spectrum by multiplying $V(\omega, \theta)$ by ω^{-2} or ω^2. The frequency spectrum can be obtained by integrating the directional spectrum with respect to the angle:

$$V(\omega) = \int_0^{2\pi} V(\omega, \theta) d\theta.$$

For a directional spectrum, the direction of waves at frequency ω is defined as:

$$\theta(\omega) = \tan^{-1} \frac{a(\omega)}{b(\omega)}, \tag{5.16}$$

where

$$\begin{aligned} a(\omega) &= \int_0^{2\pi} V(\omega, \theta) \sin\theta d\theta \\ b(\omega) &= \int_0^{2\pi} V(\omega, \theta) \cos\theta d\theta, \end{aligned}$$

and θ is with respect to True North. From the elevation spectrum, we identify the swell component and find the corresponding direction using Eq. (5.16). For all the datasets we analyzed, the swell has a period of 10-13 s between 120^0N and 150^0N. Figure 5.8a gives an example of the elevation spectrum (Dataset 3 in Table 5.1), showing a swell at 10 s. The entire wind wave portion of the spectrum is of fairly uniform slope, which is typical of most of these datasets. A second peak at 8.0 s after the swell can be identified, but is barely distinguishable.

As will be explained in the next section, we have decided that the dominant wind wave peak in the elevation spectrum is less important to the statistics of breaking waves. Thus we identify instead the dominant peak in the acceleration spectrum and determine its direction. The acceleration spectrum corresponding to Fig. 5.8a is shown in Fig. 5.8b, where the peak next to the swell peak is at 7.68 s. The peak period and direction from the acceleration spectrum are given for each dataset in Table 5.1.

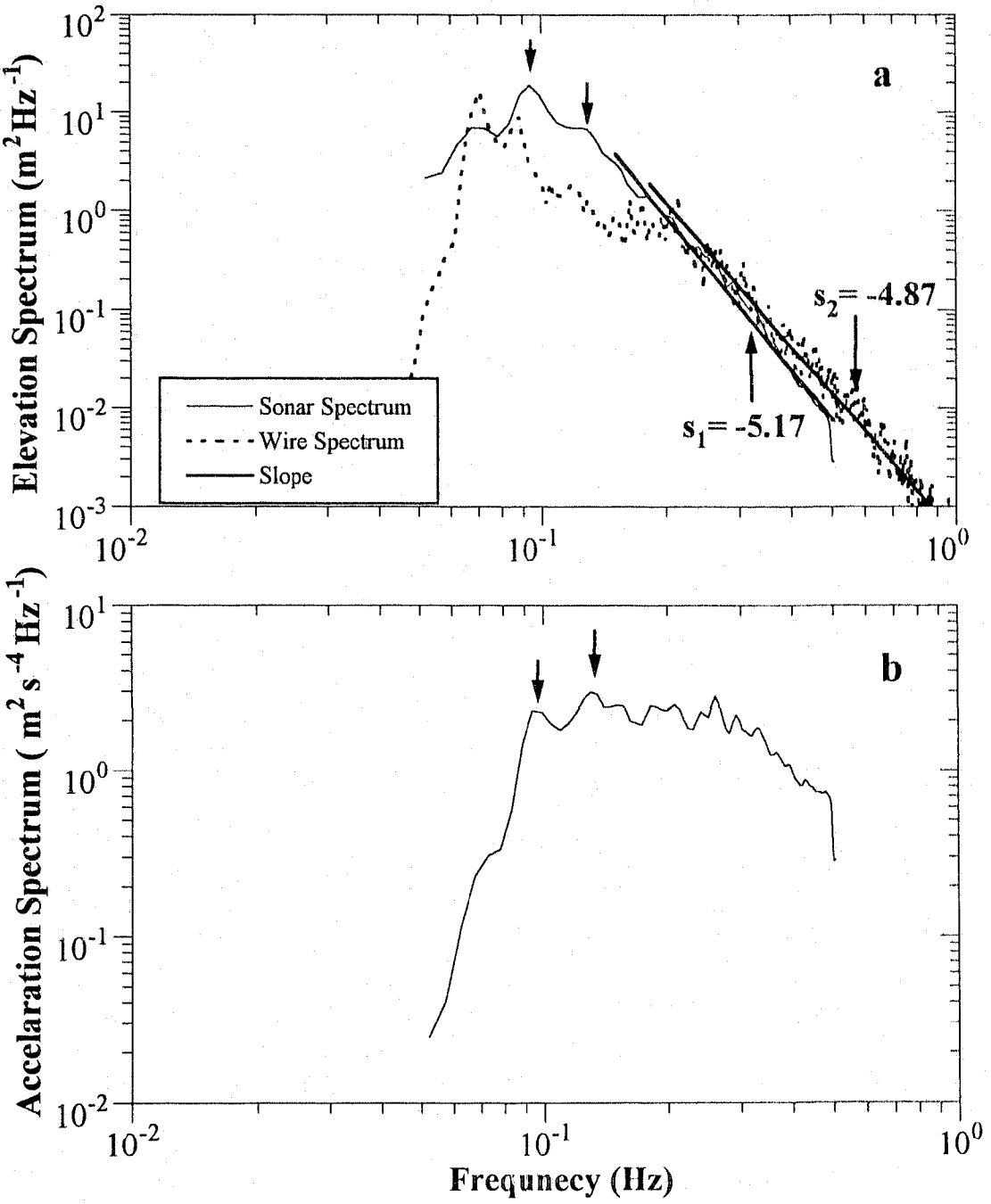

Figure 5.8: Frequency spectrum for dataset 3 in the table. (a) Elevation spectrum. The wind wave region has a slope of $s_1 = -5.17$ as shown by the straight line. The corresponding wire spectrum is also shown as the dotted line, with a less steep slope of $s_2 = -4.87$. (b) Acceleration spectrum (sonar spectrum). Arrows indicate the swell and the peak wind wave component.

The slope of the spectrum for wind waves, s, is defined by

$$F(\omega) \sim \omega^s$$

where $F(\omega)$ is the elevation spectrum. This was calculated for each spectrum with linear regression, using the spectrum (in the logarithm scale) in the wind wave region (starting from the second peak to the cutoff frequency), and the result is also given in the table. The slope values in the table generally show a steeper slope than the Phillips spectrum ($s = -4$). One explanation is that the sonar measurement at higher frequencies has lower sensitivity. For illustration, the wire gauge spectrum corresponding to the sonar spectrum is also shown in Fig. 5.8a. It can be seen that the wire spectrum shows somewhat higher spectrum levels for frequencies greater than 0.2 Hz, and a less steep slope ($s = -4.87$ for the wire spectrum, compared with -5.17 for the sonar spectrum). The behaviour of the directional wave spectrum at higher frequencies affects calculation of the fourth spectral moment and the breaking probability, as described later.

5.3.2 Breaking Event Density

Previous results on breaking wave properties such as whitecap coverage are generally expressed in the form of a power law. In the following presentations of our results, we use a log-log display in order to facilitate comparison. Fig. 5.9a shows breaking event density as a function of wind speed from the SWAPP data (solid circles). The event density lies in the range of $0.2 - 1.1 \times 10^{-3}$ m^{-2} s^{-1} for these data. It is interesting to see that, although scattered, the density actually decreases with increasing wind. A possible factor is that more small breaking waves are masked by large ones at higher winds. This effect is however not expected to be severe, since large waves appear less often than small waves and as a result, small waves should be seen for most of the observation time. A more likely explanation would be that the dominant wave frequency decreases with increasing wind, resulting in a decrease in the total number of wave crests per unit observation area.

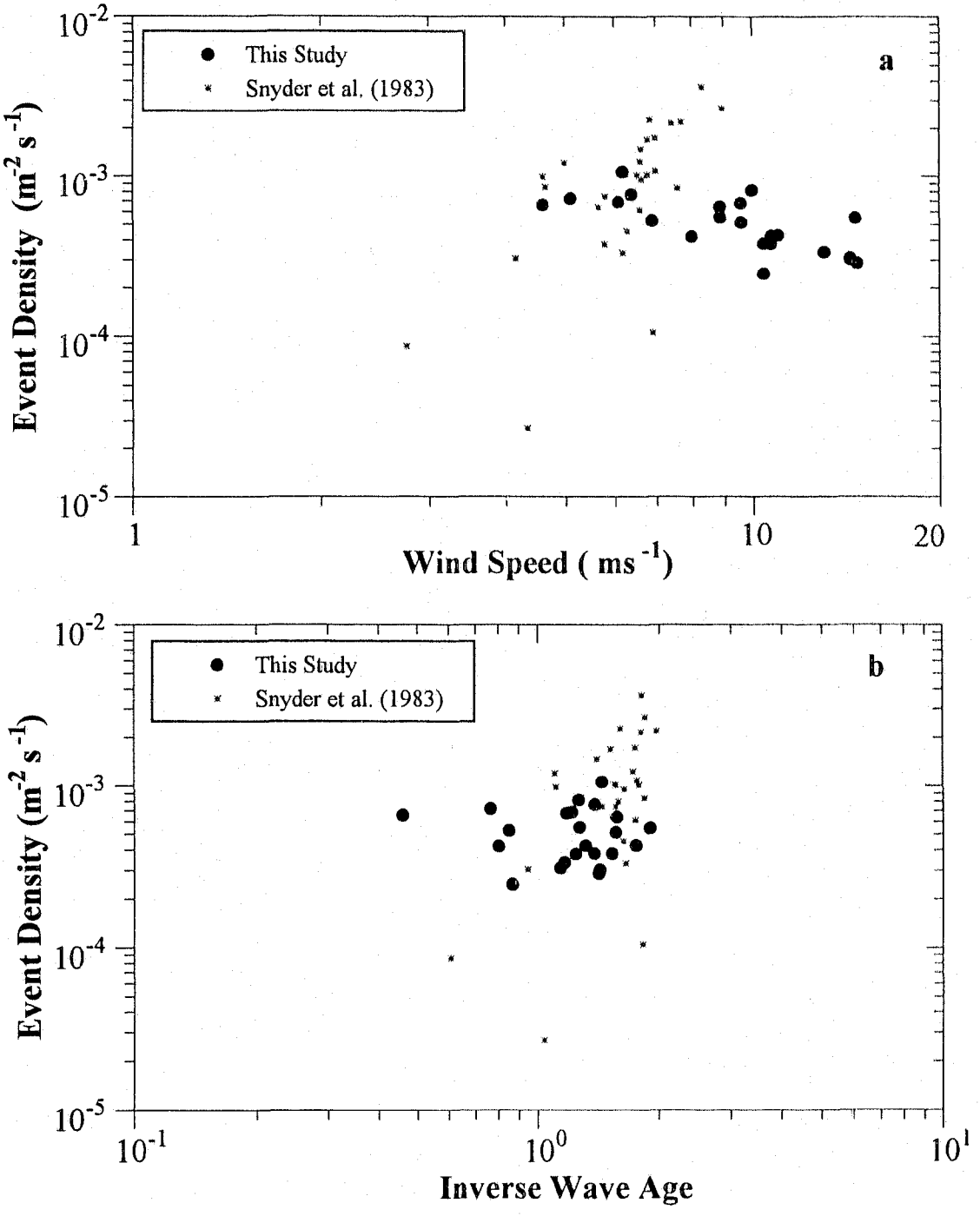

Figure 5.9: Breaking event density versus (a) wind speed, and (b) inverse wave age. The solid circle represents the SWAPP data and the star is from the data of Snyder et al. These data are plotted in the log-log scale.

Snyder et al. (1983) measured breaking wave density with a camera over the wind speed range 2 to 8 ms^{-1}. We plot their results (stars) together with our results for comparison. It can be seen that their data are considerably more scattered, especially at winds between 6-7 ms^{-1}, possibly because they were collected in a fetch limited sea where waves were still developing or there were fewer events collected for statistical analysis. Nevertheless, there is overlap between these two data sets at winds between 4-7 ms^{-1}, although they were acquired with different techniques. The event density is also plotted in Fig. 5.9b against the inverse wave age, W/C_p, where W is the wind speed and C_p the dominant wave phase speed obtained from T_p in Table 5.1. Our data show no significant dependence on the wave age, possibly because the sea states were essentially fully developed. The data of Snyder et al. have a tendency towards increased density with inverse wave age apparently due to the fact that their data were acquired in a fetch limited sea.

5.3.3 Event Velocity and Duration

Figures 5.10a-c show the speed distribution of trackable events at wind speeds of 6.4, 10.7 and 13.0 ms^{-1} (datasets 22, 11, 14), where the arrow indicates the mean speed, which increases with the wind but is substantially less than the wind speed. It can be seen that the distribution is more concentrated at lower wind speeds, and gradually spreads as the wind increases. As discussed in Section 5.1.3, the incomplete measurement of the instrument has no significant effect on the speed distribution at scales above 1.8 ms^{-1} for high sea states (Fig. 5.10c). For a lower sea state as in Figs. 5.10a (dataset 22), this scale decreases to 1.1 ms^{-1} (estimated using Eqs.(4.8) and (4.9)).

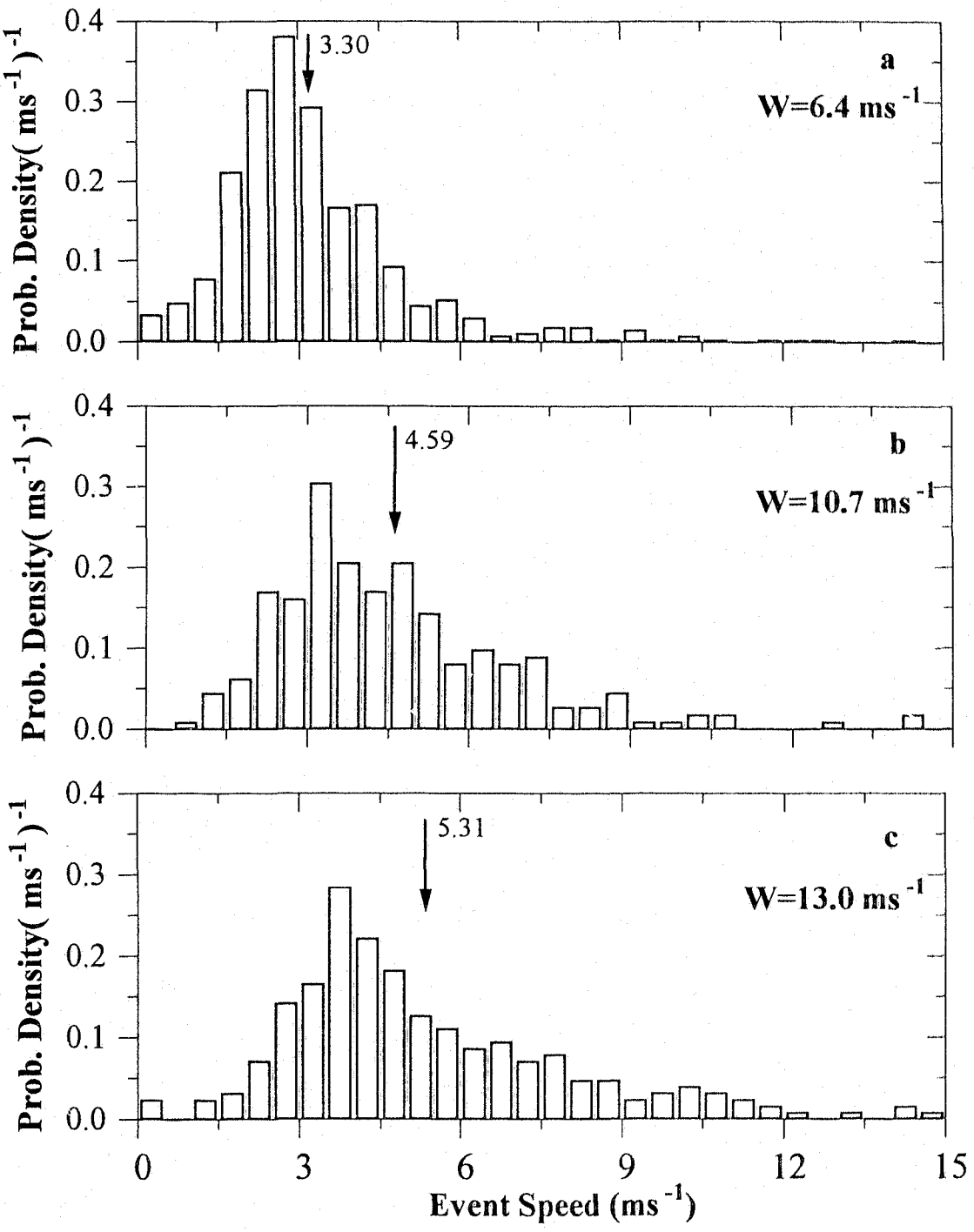

Figure 5.10: Event speed distribution at three wind speeds. The arrow indicates the mean event speed. (a) W=6.4 ms^{-1}.(b) W=10.7 ms^{-1}. (c) W=13.0 ms^{-1}, corresponding to datasets 22, 11, and 14 in the table.

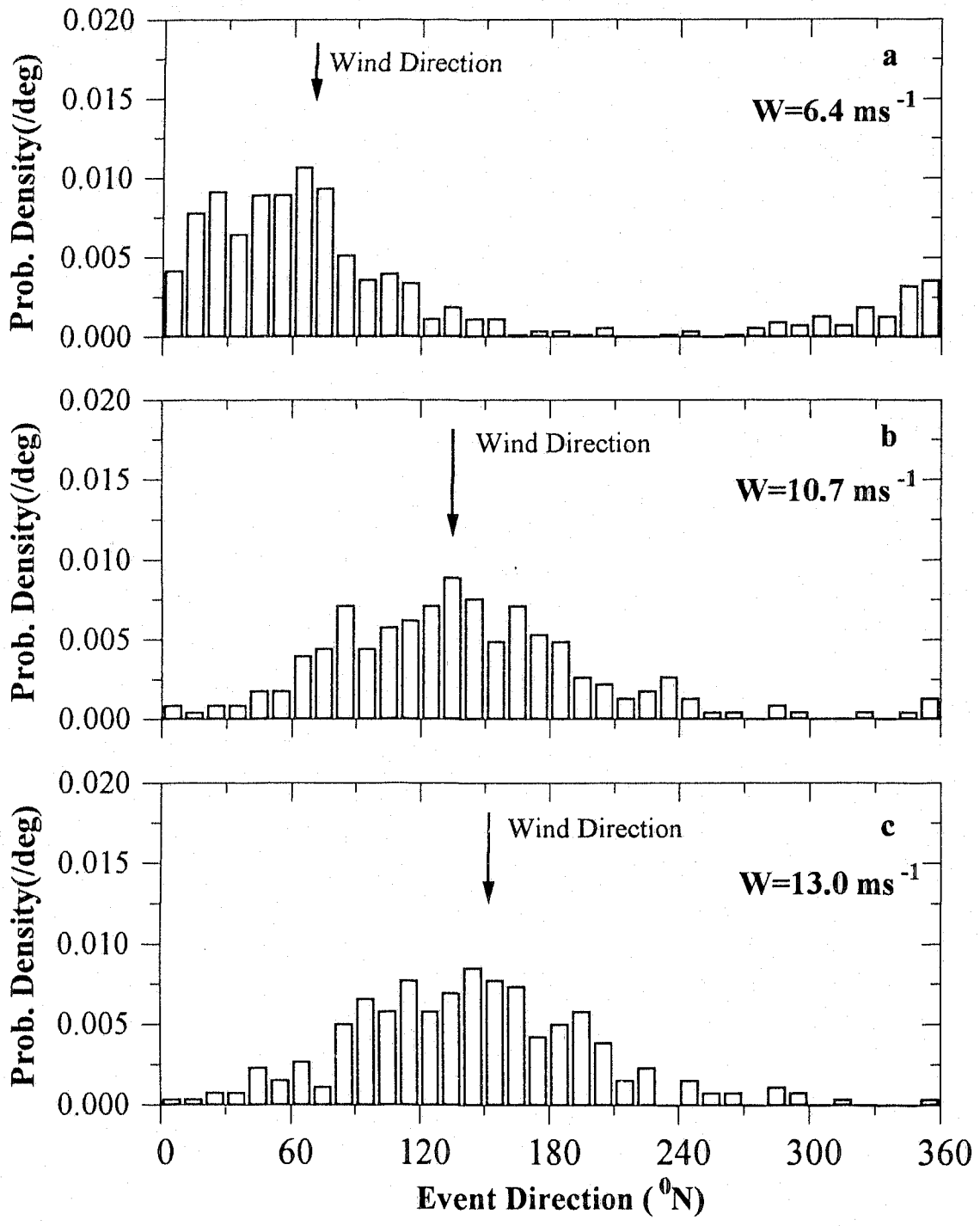

Figure 5.11: Event direction distribution for the same data as in Fig. 5.10. The wind direction indicated by the arrow is towards (a) 70°, (b) 136°, and (c) 151°, with respect to True North.

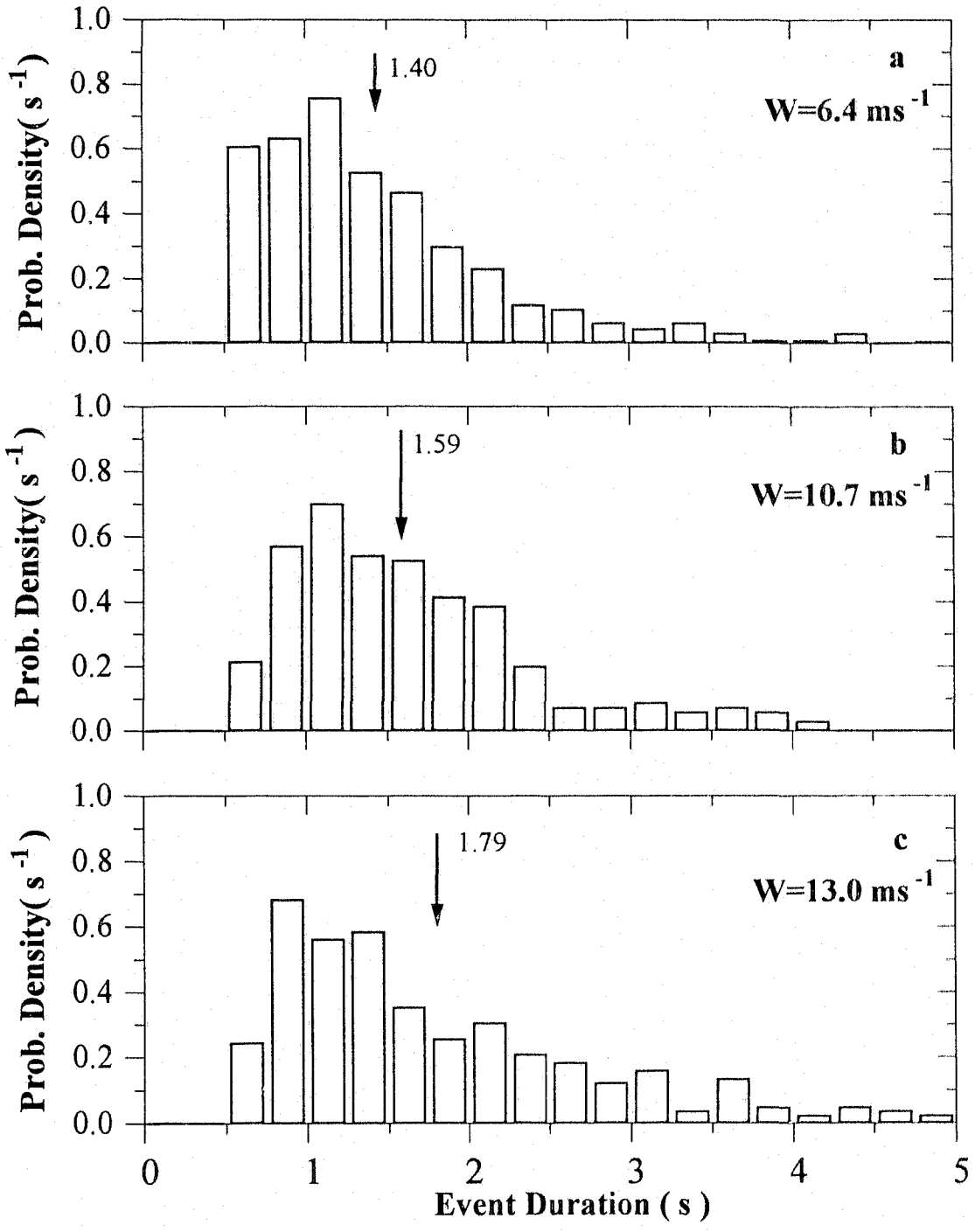

Figure 5.12: Event duration distribution for the same data as in Fig. 5.10. The arrow indicates the mean duration.

Figures 5.11a-c show the corresponding distributions of event direction of motion, which are seen to be generally aligned with the wind direction. The mean event direction is defined as

$$\bar{\theta}_e = \tan^{-1} \frac{\bar{v}_y}{\bar{v}_x}, \tag{5.17}$$

where $\bar{v}_y$ and $\bar{v}_x$ are the mean x and y components of the event velocity. This value is 55^0, 134^0 and 144^0 for these examples. Their corresponding wind directions are 70^0, 136^0 and 151^0, respectively.

Figures 5.12a-c show the duration distribution of locatable events for the same data as above. Comparing with Fig. 5.10, we can see that the duration distribution is more asymmetric, showing higher densities on the left and a longer tail on the right. Similar to Fig. 5.10, the duration distribution is broader as the wind increases. In Section 5.1.3, it is estimated that the duration is not severely affected by incomplete measurement for scales above 1.15 s.

Figure 5.13a shows mean event speed against wind speed. The mean event speed is approximately 0.7 of the wind speed at 5.0 ms^{-1} and drops to 0.4 at 14.0 ms^{-1}. There will be more discussion on this issue in the next section.

In Fig. 5.13b, we show the dependence of mean duration on wind speed. The mean duration ranges from 1.2 s at 5.0 ms^{-1} to 1.7 s at 14 ms^{-1}, and increases with the wind speed. Snyder et al. (1983) observed that the duration of whitecaps was of order 0.5 s for wind speeds from 2 to 8 ms^{-1}. Wu (1992) has suggested that this lack of wind dependence may arise because their measurements were made in a fetch limited sea; normalization of their data by the dominant wave period shows a dependence on the wave period (Wu, 1992).

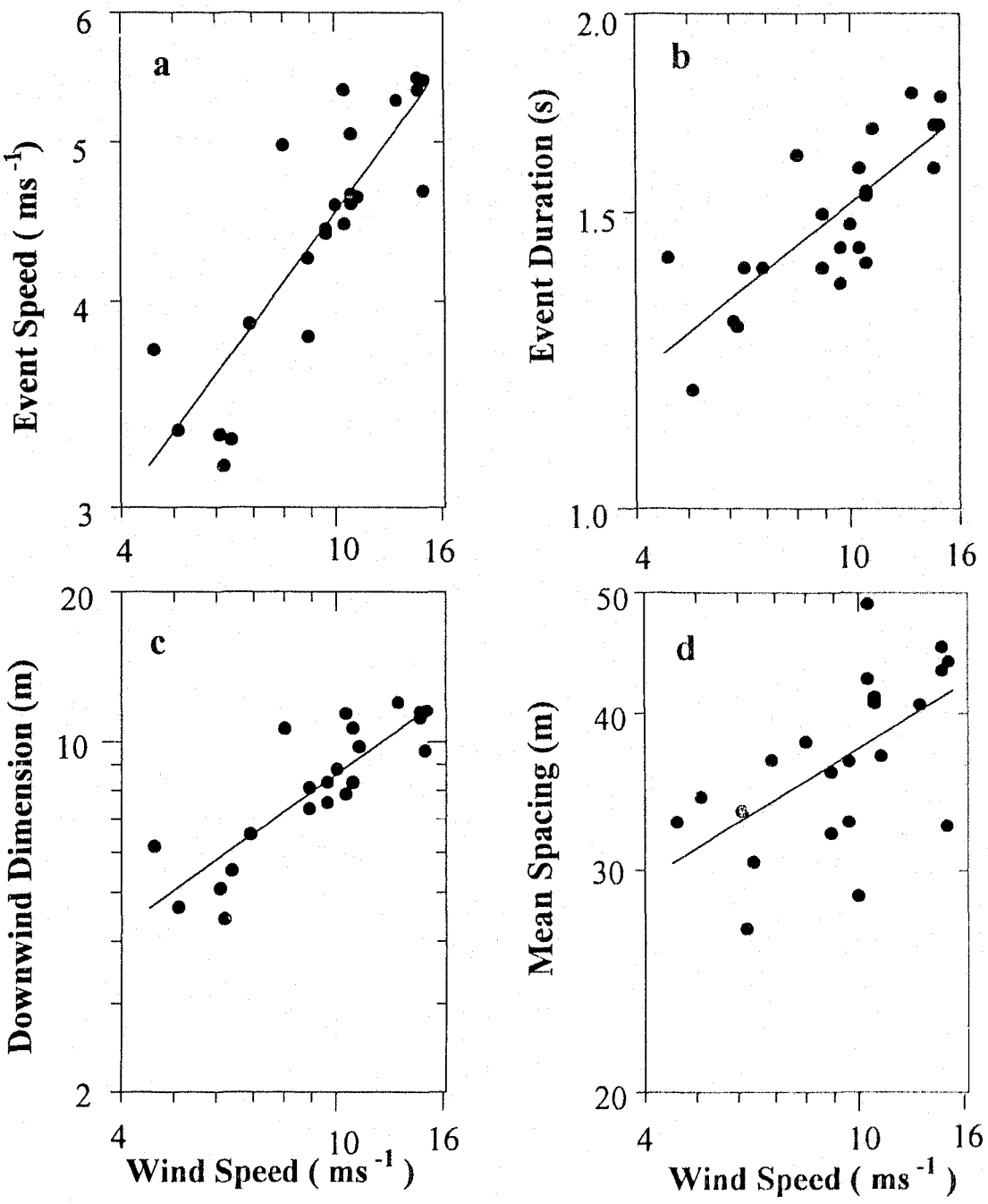

Figure 5.13: Event statistics versus wind. Data are plotted in the log-log scale. The straight lines are the linear regression of the data. (a) Mean event speed. Slope=0.44; (b) Mean duration. Slope=0.26; (c) Mean downwind length. Slope=0.77; (d) Mean spacing. Slope=0.27.

5.3.4 Downwind Dimension

Figure 5.13c shows the dependence of mean downwind dimension on wind speed. Although there is considerable scatter, these data appear to fit a power of 0.77 dependence on the wind speed. Previous observations of the downwind and cross-wind dimensions of whitecaps in the Southern Ocean and Tropical Ocean are given in Bortkovskii (1987). Although the data are scattered, the characteristic length, defined as $s = \sqrt{\bar{L}_D \bar{L}_c}$, appears to be well approximated by a power of 0.75 dependence on the wind speed (Wu, 1992), which is comparable to our present result in Fig. 5.13c. However, the dimension determined from our data is considerably larger (2-4 times) than that given by Bortkovskii. This is discussed in the next section.

5.3.5 Mean Spacing and Active Acoustic Coverage

The dependence of mean spacing and of active acoustic coverage on wind speed are shown in Figs. 5.13d and 5.14 respectively. The mean spacing has an increasing trend as the wind increases, varying from about 30 m at a wind speed of 4 ms^{-1} to about 45 m at 14 ms^{-1}. The active acoustic coverage, varying from 4% to 14% for the same wind speeds, shows a nearly linear dependence on the wind speed. This is unlike the 3.75 power relation between whitecap coverage and wind previously obtained by Wu (1979), but consistent with the observations of active whitecap coverage by Bortkovskii (1987), who distinguished between the active breaking crest of waves and the foam produced by the breaking crest. The explanation is that previous whitecap observations usually include both active whitecaps and foam, thus resulting in a much more rapid increase with wind. Our acoustic observation is derived from the sound radiated primarily by active breaking crests where bubbles are injected, and is therefore more consistent with Bortkovskii's measurements of active whitecap coverage. Note that our acoustic coverage is significantly larger than his whitecap coverage (below 5% for the same wind speeds), apparently due to the different observation techniques, as discussed in the next section. Nevertheless, the absolute magnitude is not what we are seeking here. It is the dependence on the

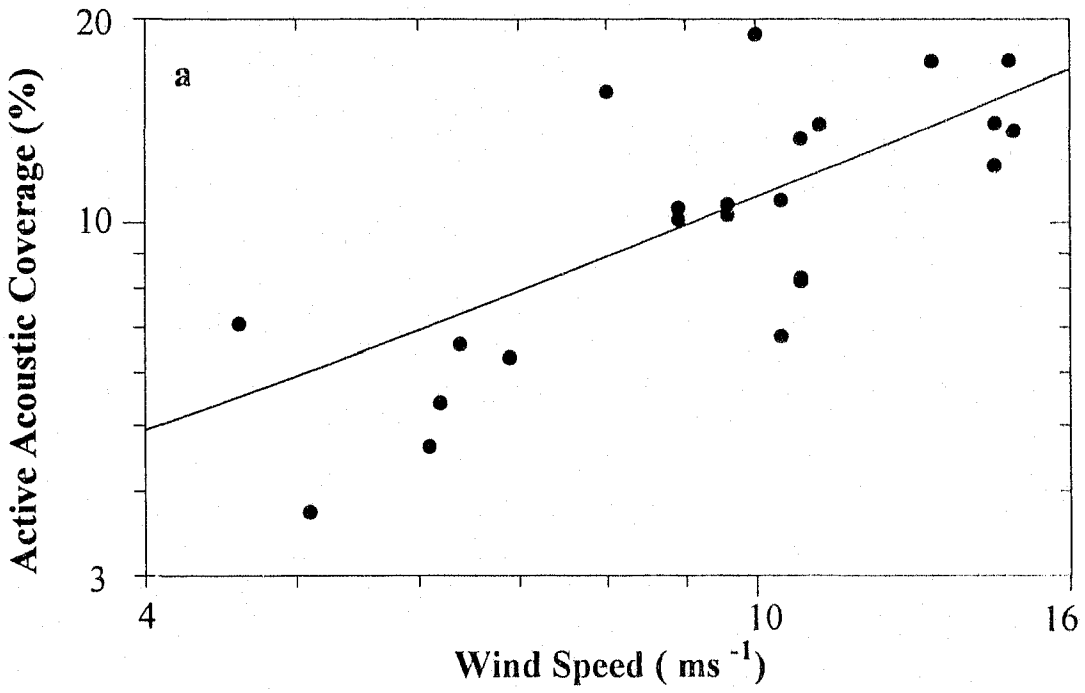

Figure 5.14: Dependence of active acoustic coverage on wind speed. Data are plotted in the log-log scale. The straight line is the linear regression of the data. Slope=1.03.

wind speed that is of interest.

Wu (1992) derived a dependence of mean spacing between whitecaps on wind, which is nearly inverse

$$\bar{l}_s \sim U_{10}^{-1.07},$$

instead of an increasing dependence as in our data. The power dependence of whitecap dimension on wind used by Wu was 0.8, close to that in Fig. 5.13c. Thus the difference in the wind dependence of mean spacing is clearly caused by the use of the higher power (3.75) dependence of whitecap coverage on wind.

The dependence of the mean spacing and of the acoustic coverage on the inverse wave age is shown in Figs. 5.15a and b. Similar to Fig. 5.9b, both the mean spacing and the acoustic coverage have no clear dependence on the wave age.

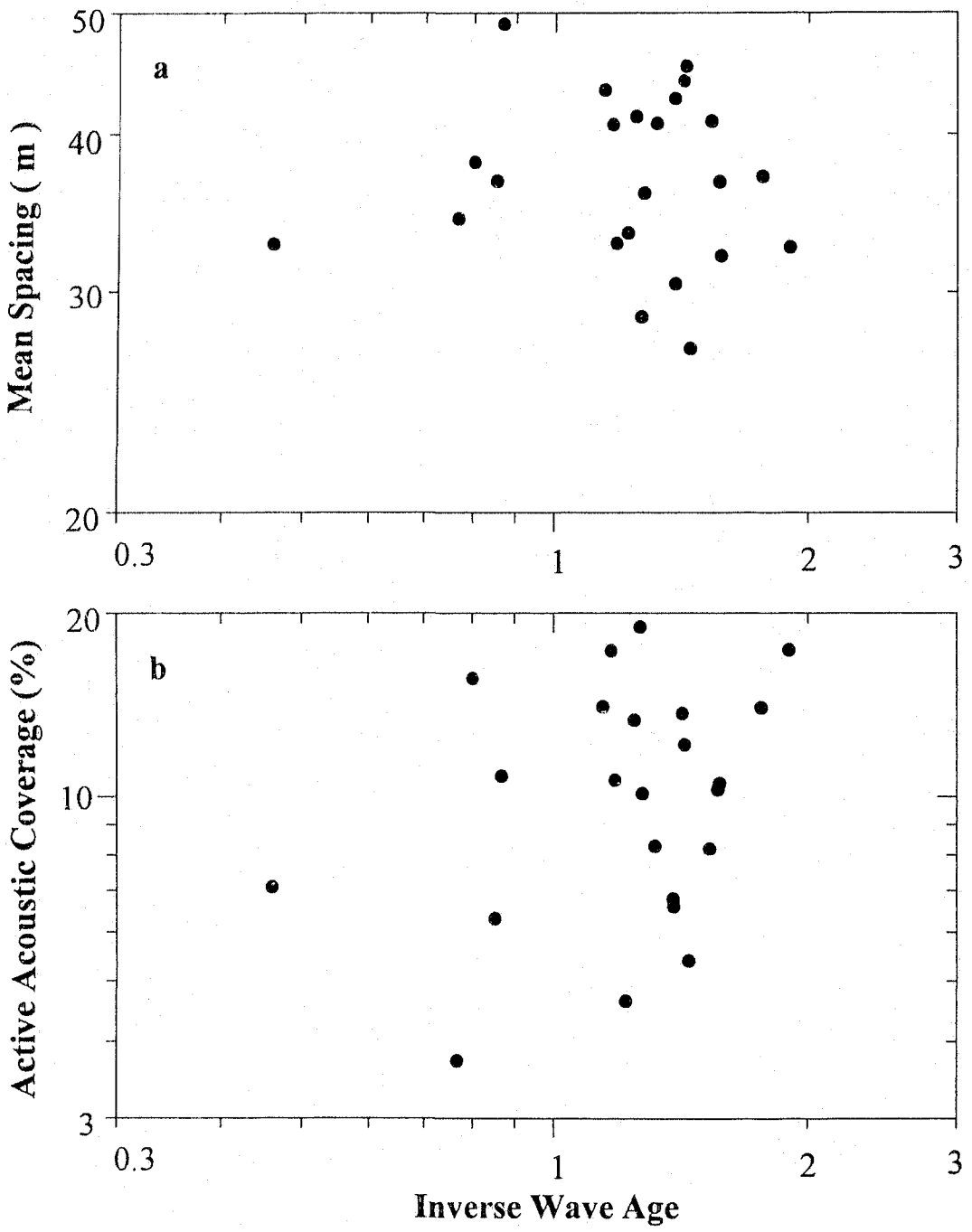

Figure 5.15: Dependence of (a) mean spacing and (b) active acoustic coverage on inverse wave age. Data are plotted in the log-log scale.

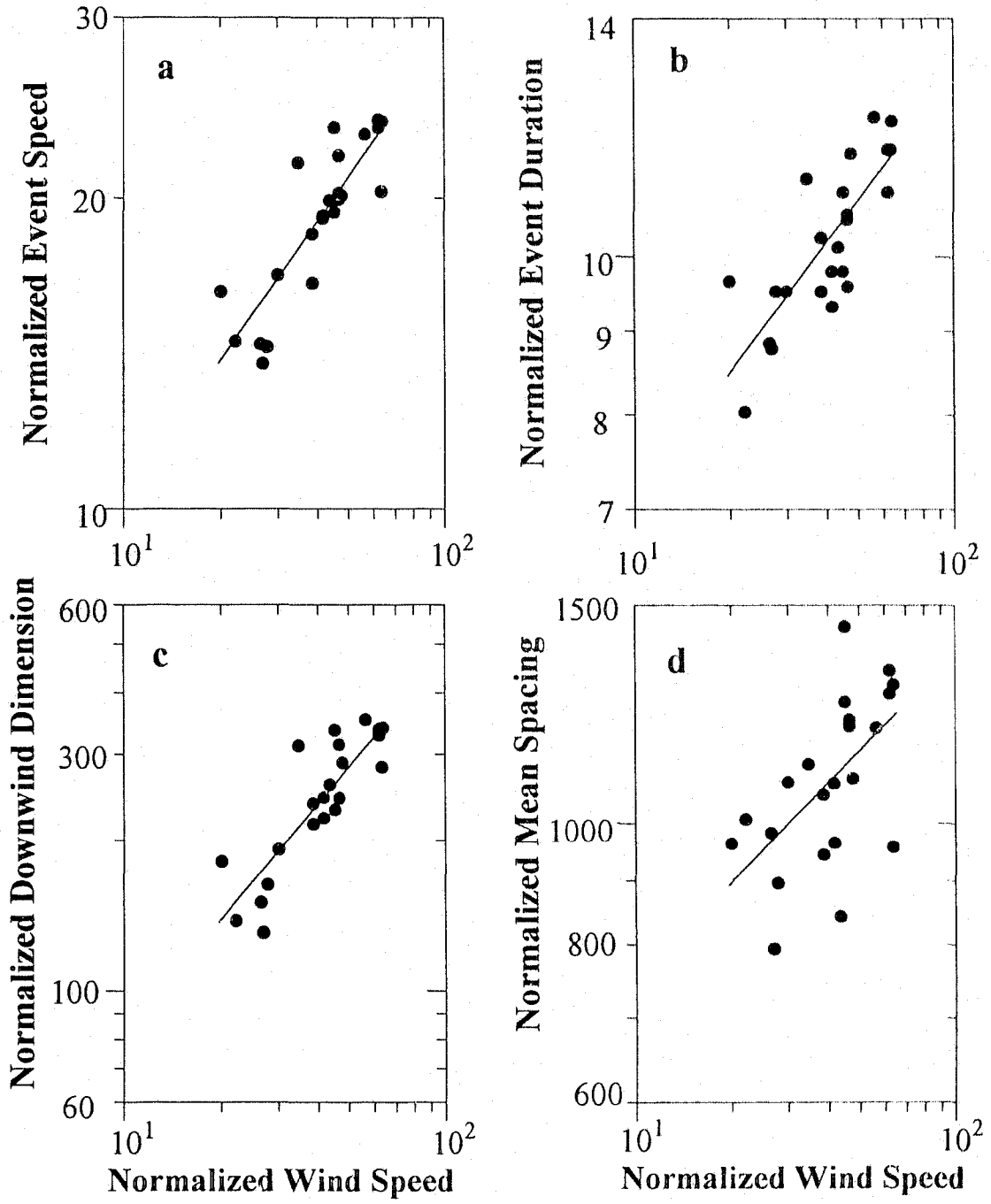

Figure 5.16: Event statistics (from Fig. 5.13) normalized by the minimum phase speed for gravity-capillary waves and its corresponding wave period and wavelength, against wind speed normalized by the phase speed. (a) Event speed normalized by phase speed; (b) event duration normalized by wave period; (c) Downwind length normalized by wavelength; (d) Mean spacing normalized by wavelength.

The results in Fig. 5.13 are normalized by the minimum phase speed C_{min} for gravity-capillary waves, and its corresponding wave period and wavelength. The normalized results are shown in Fig. 5.16. The minimum phase speed at a sea surface temperature of 10^0C is 0.23 ms^{-1}, with the corresponding wave period and wavelength being 0.15 s and 0.034 m respectively. In Fig. 5.16, the wind speed is also normalized by C_{min}.

5.4 Discussion

5.4.1 The Scale of Breaking

In the ocean, breaking may occur at a wide range of scales, and there should be some measure of breaking scale. Phillips (1985) suggested the use of the velocity of breaking waves as a measure of the breaking scale, since it is a well defined parameter; it is often difficult to define an unambiguous parameter from the local surface configuration at one given instant or from the time history at one given location. Our observations provide direct measurement of this velocity, which will therefore be used as a measure of the breaking scale in the subsequent discussion.

It has been observed in the preceding section that the measured speed of breaking events is 0.4-0.7 of the wind speed. This appears to be associated with the corresponding group speed for a fully developed sea. However, there is no apparent physical association of the event speed with the group speed. When waves break, the particle velocity at the crest is close to the phase velocity. Bubbles injected by the breaking waves are therefore advected at the phase velocity. This has been observed in a narrow band wave field by detecting bubbles generated by wave breaking with active sonar (Thorpe and Hall, 1983). Since sound is believed to be generated by bubble formation, acoustic sources associated with breaking waves at some frequency should travel at a speed close to the phase speed, at least at the stage of active breaking. The fact that the mean event speed in a broadband wave field is considerably smaller than the dominant phase speed C_p implies the importance of

higher frequency components, since breaking waves with higher frequencies travel at smaller speeds than the dominant wave.

Let us assume that the travel velocity of breaking waves at some frequency, is equal to the corresponding phase velocity. It is desirable to derive from the wave spectrum some mean velocity comparable to the mean event velocity. The probability of wave breaking (see Eq.(1.7)) derived by Snyder and Kennedy (1983) depends on the fourth spectral moment, which is physically the variance of downward acceleration. Therefore, it is not unreasonable at this stage to weight the contribution from each component with the acceleration spectrum to derive the mean velocity; this yields reasonable results as seen below, although further theoretical work is needed to develop a more realistic weighting function.

In the linear approximation, the Lagrangian and Eulerian accelerations are equivalent. We can therefore derive the acceleration spectrum from the velocity spectrum using

$$A(\omega,\theta) = \omega^2 V(\omega,\theta).$$

The mean speed of breaking waves is defined as

$$\bar{c}_{br} = \frac{1}{m_4}\int_{\omega_1}^{\omega_2} c(\omega)A(\omega)d\omega, \tag{5.18}$$

where

$$m_4 = \int_{\omega_1}^{\omega_2} A(\omega)d\omega \tag{5.19}$$

is the fourth moment of the elevation spectrum or the variance of acceleration between ω_1 and ω_2, and $c(\omega)$ is the phase speed at frequency ω. The mean direction of motion is defined as

$$\bar{\theta}_{br} = \tan^{-1}\frac{a}{b}, \tag{5.20}$$

where

$$\begin{aligned} a &= \int_{\omega_1}^{\omega_2} c(\omega)\int_0^{2\pi} A(\omega,\theta)\sin\theta d\theta d\omega, \\ b &= \int_{\omega_1}^{\omega_2} c(\omega)\int_0^{2\pi} A(\omega,\theta)\cos\theta d\theta d\omega, \end{aligned}$$

and θ is with respect to True North. Each of the parameters m_4, $\bar{c}_{br}$ and $\bar{\theta}_{br}$, is obtained by integrating the acceleration spectrum from the dominant frequency peak in the acceleration spectrum to the high frequency cutoff of the Doppler sonar (0.5 Hz). The results are included in Table 5.2 for comparison, where it can be seen that $\bar{V}_e$ is close to, but slightly smaller than $\bar{c}_{br}$ (75% -95% of $\bar{c}_{br}$). [3] The difference can be explained in part by the fact that our instrument is able to measure breaking events with speeds down to 1.5 ms^{-1} (Fig. 5.10), much smaller than the high frequency cutoff of the Doppler sonar (0.5 Hz corresponds to a phase speed of 3.12 ms^{-1}).

It is therefore concluded that the observed mean event speed is an average result of the contributions from different wave components in the spectrum. It is of interest to compare the mean breaking scale ($\bar{V}_e$) with the dominant wave scale. Figure 5.17a shows the mean event speed normalized by the dominant wave phase speed C_p (obtained from T_p in Table 5.1). It is seen that $\bar{V}_e$ is about 75% of C_p at lower C_p (4 ms^{-1}) and decreases down to 45% as C_p increases to 12 ms^{-1}. The decreasing trend of the normalized mean event speed with increasing C_p can be explained as follows: since the instrumental cutoff for measurement of event speeds is fixed (of order 1.5 ms^{-1}), as the dominant wave phase speed C_p decreases, the frequency range over which the wave components are averaged (as in Eq. (5.18)) becomes smaller, and thus the resulting mean event speed is closer to C_p.

[3]Long wave advection should be examined here, since the measured velocity is relative to the stationary frame whereas $\bar{c}_{br}$ is the phase speed in the moving medium (in this case, the medium is the current induced by swell). Swell has typically a period of 10 s for these datasets (Table 5.1), and the amplitude is estimated from the pressure sensor and accelerometer on the instrument to be of order of 1.35 m. This yields a particle velocity $u_0 = 0.85$ ms^{-1}. Consider dataset 21 in Table 5.1, for which the mean event speed is the smallest (3.18 ms^{-1}) and the angle between the event velocity and swell is 68^0. The event speed relative to the moving medium is therefore

$$V_e' = V_e - u_0 \cos\theta = 2.85 \text{ ms}^{-1}$$

at most, some 10% smaller than the absolute speed.

5.4.2 Normalization by the Breaking Scale

As discussed above, the mean event speed represents the mean scale of breaking. Therefore from this speed, we can derive the mean breaking period $\bar{T}_{br}$ and wavelength $\bar{\lambda}_{br}$ using the dispersion relation for surface gravity waves; we may then use these to normalize the observed breaking wave statistics.

Figure 5.17b shows the ratio of the mean breaking duration to the mean breaking period $\bar{T}_{br}$. The mean duration is 45%-65% of $\bar{T}_{br}$. Wu (1992) normalized the results of Snyder et al. on the whitecap duration by the dominant wave period, resulting in a ratio generally below 25%, which is much smaller than our data. Thorpe and Hall (1983) used active sonar to observe echoes from bubbles produced by breaking waves and found that bubbles produced near the crests of individual breaking waves last for 30-50% of the wave period. Since the sound from breaking waves is generated mainly by the entrained bubbles, our results are closer to Thorpe and Hall's results than to the results of Snyder et al. As mentioned in the preceding section, the downwind length and coverage of whitecaps observed from aircraft or shipboard are significantly smaller than our acoustical observations. We attribute the difference between the acoustical and optical results to the different measurement techniques; it is possible that the weaker stage of air entrainment that cannot be observed at a distance with photographic techniques, is nevertheless acoustically detected with hydrophones. In the laboratory, the durations of active whitecapping and sound were observed to be essentially the same (Melville, personal communication). Field experiments by Updegraff and Anderson (1991a, b) using a video camera and a hydrophone array placed very close to the sea surface (1 m) showed that microbreakers, although difficult to see at a greater distance, can actually generate detectable sound even at very low wind speeds. Since the acoustical radiation is intrinsic to the breaking process, we consider it a more reliable signal of wave breaking in the ocean than the visible manifestations such as whitecaps identified in photographic observations.

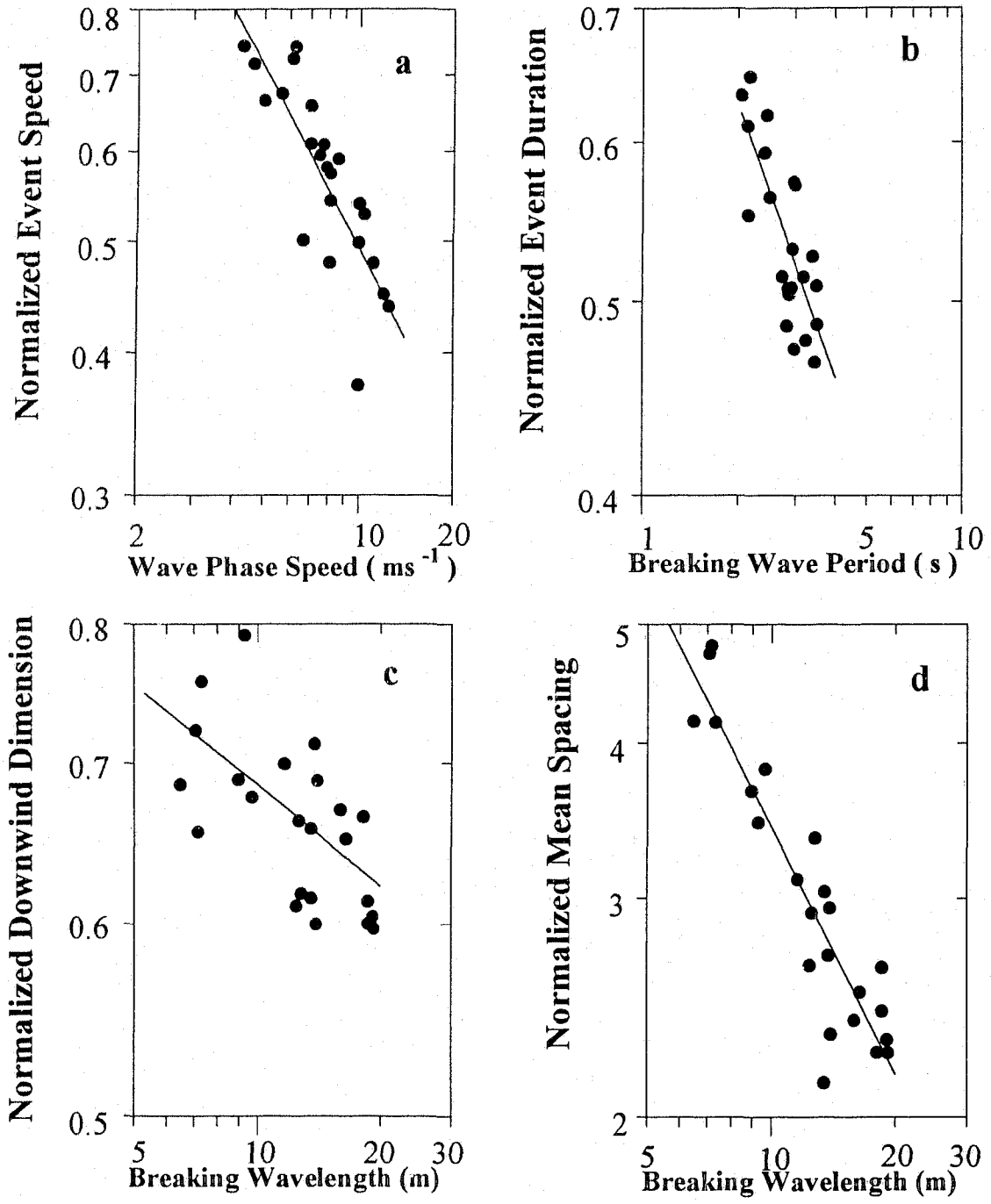

Figure 5.17: Event statistics normalized by the corresponding abcissa variable. Data are plotted in the log-log scale. The straight lines are the linear regression of the data. (a) Normalized event speed. Slope=-0.53; (b) Normalized breaking duration. Slope=-0.45; (c) Normalized downwind length. Slope=-0.14; (d) Normalized mean spacing. Slope=-0.66.

Figures 5.17c-d show downwind dimension and spacing normalized by the mean wavelength. The normalized downwind dimension is more scattered than the normalized duration, varying between 60% and 75% of the breaking wavelength. The mean spacing is seen to drop from 5 to 2 times the breaking wavelength as the wavelength increases from 10 m to 25 m. The decrease of normalized spacing with increasing wavelength indicates an increase of the breaking probability with the breaking scale as discussed below.

5.4.3 Direction of Motion of Breaking Events

The event direction of motion in Table 5.2 is scattered in relation to the mean breaking wave direction and wind direction. There are in general however three cases in which these three directions are related, as sketched in Fig. 5.18. The first is where these three directions are close (within $\pm 10^{o}$; Fig. 5.18a). The small difference in the wave and event directions is likely due to the fact that the sonar cutoff is not high enough to include the smallest waves observed by the hydrophone array. In the second case, the wave and event directions are close but the wind direction is significantly different (e. g. dataset 3; see Fig. 5.18b). This behavior may be caused by the delay of waves in response to the change in wind direction. There is however a third case in which although the wave direction falls behind the wind direction, the event direction appears to follow the wind direction (e. g. datasets 1, 2, 4, 17, 19; see Fig. 5.18c). This phenomenon implies that wind action may affect the direction of motion of breaking events but this effect depends also on the history of wind and waves. A better understanding of this phenomenon would require a careful examination of the time history of wind, surface waves and breaking event statistics, which is beyond the scope of this paper. For all these datasets, swell is seen to have no clear impact on the event direction, since, as we discuss above, the breaking scale is not small enough that advection by swell has a significant effect.

The direction of events at different scales provides more details of the directivity of breaking waves. Figure 5.19 shows the mean direction of breaking events as a

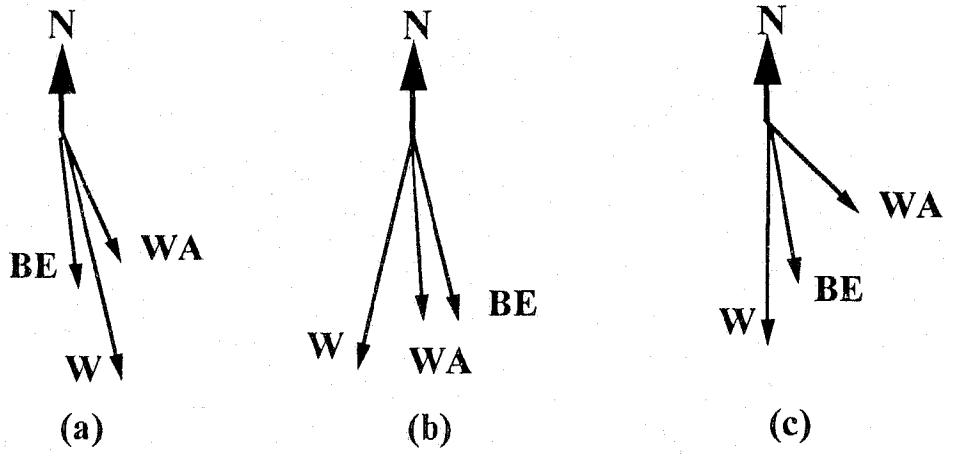

Figure 5.18: Interrelation between the mean direction of motion of events, the wave direction and the wind direction in three cases: (a) the three directions are basically aligned; (b) the wave and breaking event directions are close, but the wind direction is different; (c) the event direction and wind direction are close but the wave direction is different. BE–breaking event direction. WA–wave direction. W–wind direction.

function of event speed for dataset 1, together with the corresponding wave direction as a function of phase speed, as given in Eq. (5.16). The horizontal line is the wind direction. The event direction for speeds between 3-6 ms^{-1} is seen to follow the dependence of the wave direction on phase speed, but has an offset from the wave direction possibly due to the effect of wind action. The event direction at high speeds appears more uncertain, because the number of events is smaller resulting in more statistical fluctuations.

5.4.4 Breaking Probability

Previous statistical studies of wave breaking have focused on the probability of breaking given a certain breaking criterion, either the steepness criterion (Ochi and Tsai,1983) or the acceleration criterion (Snyder and Kennedy, 1983). Laboratory

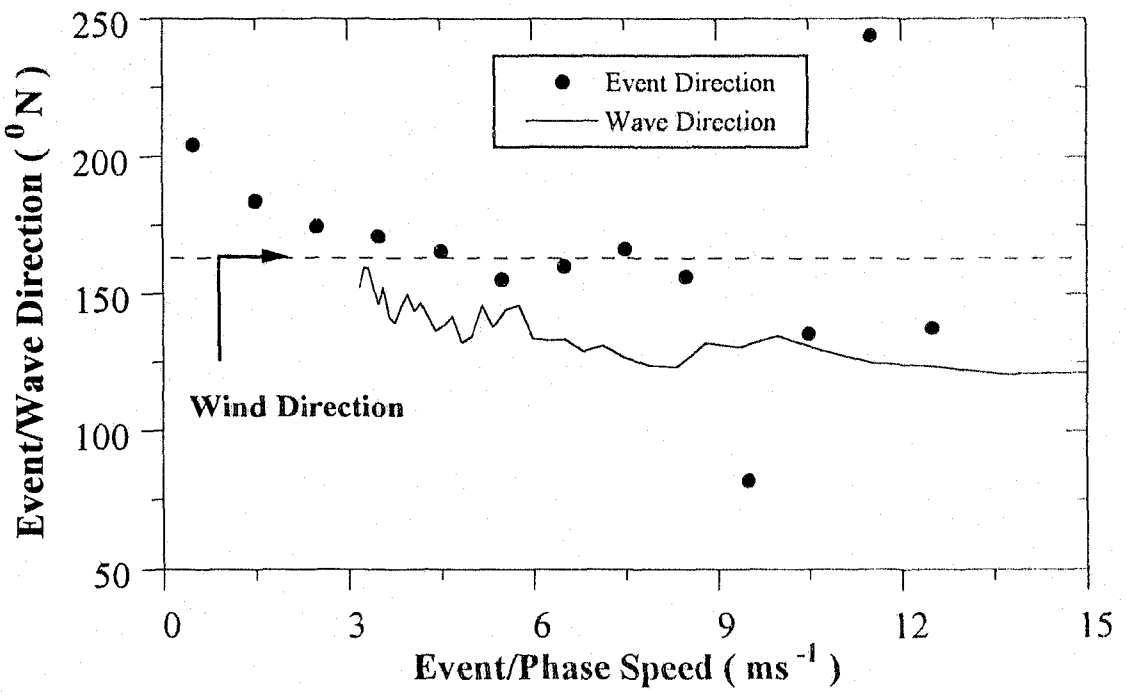

Figure 5.19: Mean direction of motion for events against the event speed. The solid line is the wave direction as a function of phase speed, calculated using Eq.(5.16) and plotted in the same scale as the event speed for comparison. The horizontal line is the wind direction.

experiments (Ochi and Tsai, 1983; Hwang et al., 1989) have also been carried out to test these theoretical models. It was found that by choosing an appropriate breaking threshold, the models generally agree with the experiments.

Snyder and Kennedy's model gives an expression for the breaking probability at any point on the surface (Eq. (1.7)). This probability is equivalent to the fraction of the sea surface covered by breaking water. Figure 5.20 shows the active acoustic coverage (from Fig. 5.14) as a function of m_4^{-1}, where m_4 is calculated from the directional wave spectra using Eq. (5.19). Equation (1.7) is fitted by least squares to these data to choose α, which was found to be 0.082. This value is extremely low compared with the one found in the laboratory by Ochi and Tsai (0.40) and that found by Snyder et al. (1983) in a fetch limited sea (0.25-0.4). The low value

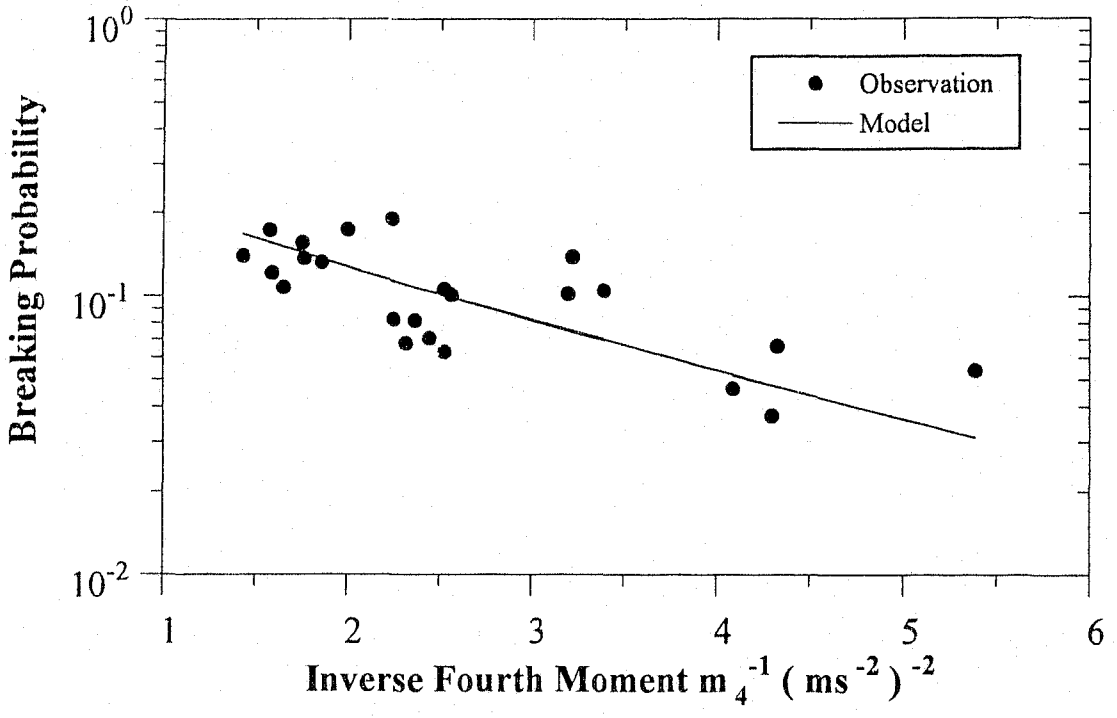

Figure 5.20: Breaking Probability measured as active acoustic coverage (as in Fig. 5.14) versus the inverse fourth moment of the wave spectra simultaneously measured from FLIP. The solid line is the breaking probability predicted by Snyder and Kennedy's model (1983), given the same fourth moment and $\alpha = 0.082$. This value of α is obtained by least-squares fitting the model to the data.

of α partly reflects the sensitivity of the acoustic system to detection of breaking processes that do not show up for the same duration, or as often, as in other types of data. An additional factor is that m_4 is underestimated. As mentioned earlier, our instrument observes event speeds down to 1.5 ms^{-1}, corresponding to a frequency of 1 Hz, while the sonar spectra have a cutoff at 0.5 Hz. In addition, as shown in Fig. 5.8a, the sonar measurement is less sensitive to higher frequency components. Since m_4 is very sensitive to higher frequency energy and depends crucially on the high frequency cutoff, the real m_4 values for waves with scales down to 1 Hz can be appreciably larger than those estimated from the sonar spectra. Therefore the α value determined from the sonar spectra is further underestimated.

With the chosen α and estimated m_4^{-1}, the predicted probability can be found from Eq. (1.7) which is also shown in Fig. 5.20 as the solid line. It can be seen that the observed probability generally agrees well with the predicted probability, with the standard deviation of the data from the curve being 0.007, which is small compared to the observed probabilities.

5.5 Summary

Our acoustical observation has for the first time provided comprehensive measurements of the spatial and temporal statistics of breaking surface waves in the open ocean. Despite the limitations of the instrument, it has been possible to obtain the empirical dependence of breaking wave statistics on wind conditions. Comparison between the statistics and the simultaneously measured directional wave spectra has also led us to the following observations:

1. Wave breaking occurs at multiple scales in the ocean. Since the breaking wave travels at a speed close to the phase speed of the wave, the observed breaking event speed can be used as a measure of the breaking scale. It is due to the effects of higher frequency components that the mean breaking event speed is found to be considerably smaller than the phase speed of the dominant wind wave, implying that breaking occurs at a mean scale significantly smaller than that associated with the dominant wind wave.

2. The directions of wind, waves and breaking events are generally aligned. However, when the wind direction is significantly different from the wave direction, there is some evidence that the event direction lies closer to the wind direction, depending on the history of wind and waves.

3. It was found that the breaking threshold α determined from our field data using Snyder and Kennedy's model and the directional wave spectra is appreciably smaller than found by other investigators. This is partly attributed to

the increased sensitivity of the acoustic method and partly to an underestimate of m_4 using the sonar data. Incomplete measurement of m_4, in which contributions from higher frequency components are ignored, is an inevitable consequence of using a high frequency cutoff determined by the available directional wave spectra, and has no intrinsic significance. Use of the wire gauge data would result in a higher calculated breaking threshold. More significant is the predicted dependence of the breaking probability on m_4 using Snyder and Kennedy's model which appears to agree closely with our observations. It should be emphasized that the effects of the nonlinearity of wave breaking have not been considered in the present model. We speculate that the nonlinearity would affect the choice of α in the breaking criterion.

The wind dependence of breaking wave properties (Fig. 5.13) is generally quite scattered. Normalization by the breaking scale yields only a moderate reduction in scatter (Figs. 5.17a and d). The implication is that the observed breaking wave properties depend on more than just one or two parameters. We anticipate that greater insight may be derived by exploiting the detailed wave field information. In the following chapter, we shall use the observed directional wave spectra to simulate breaking waves with a Monte-Carlo approach, and compare the resulting breaking wave statistics with the acoustical observations, so as to relate our observations to the wave field information.

Chapter 6

Numerical Modelling

The acoustical observations presented in the preceding chapter suggest that it is not sufficient to relate the results only to local wind conditions and the dominant wind wave component, especially in the case of three-dimensional waves; the results should also be related to the details of the wave field (e.g. directional wave spectra). It is however analytically difficult to evaluate the spatial and temporal statistics of breaking waves in a two-dimensional, broadband, random wave field. In this respect, the Monte Carlo experimental approach proves particularly useful (Kennedy and Snyder, 1983), since it allows numerical evaluation of these statistics from directional wave spectra. In this chapter, we describe the use of this approach to simulate breaking wave statistics from field observed directional wave spectra, and compare the results with the acoustical observations so as to determine how well breaking wave statistics can be predicted from directional wave spectra.

The approach for determining breaking wave statistics is to synthesize a wave field with observed wave spectra and to use a breaking criterion to identify breaking events. These breaking events are then tracked over time to determine their spatial and temporal parameters. By allowing the model to run until sufficient events are collected, the statistics of these parameters can be obtained. With the development of powerful digital computers, such numerical simulations have been becoming less expensive, making this approach more efficient.

6.1 Synthesis of the Surface Wave Field

Synthesis of linear surface waves has previously been performed by Kennedy and Snyder (1983). Their approach calculates surface elevation as a time series using the Fast Fourier Transform (FFT), for every point in a two dimensional spatial aperture (24×24 points). In this study, we choose a different approach taking advantage of recent developments of digital computers: we perform a two-dimensional FFT on time-dependent, randomly phased directional wave spectra to construct a spatial wave field and by incrementing successive time steps, generate a sequence of frames of the wave field. Our approach allows a much larger spatial aperture (128×128 points).

It is important to emphasise the limitations of this linear approach. Wave breaking is an inherently nonlinear process which also involves dissipation. A linear model will not faithfully reproduce the steep slopes near a crest which precede breaking. Morever, the absence of dissipation in the model described below eliminates an important consequence of breaking. Nevertheless, a linear model does provide a useful first-order representation of the wave field. It appears that linear computation can provide useful insight on some important properties of wave breaking in a variety of wave conditions. The time-dependent three-dimensional topography of the ocean surface is a challenging environment to study and it seems wise to approach it first using the simplest possible representation that will capture the essential directionality and scale implied by the observed wave field. Nonlinear models built on a linear representation such as developed by Creamer et al. (1989), can be incorporated into our approach. The implementation of more accurate schemes is currently under investigation.

The first-order surface elevation can be represented as (Kennedy and Snyder, 1983)

$$\xi(\mathbf{x},t) = \sum_{\mathbf{k}} \{Z_+(\mathbf{k}) \exp[j(\mathbf{k}\cdot\mathbf{x} - \omega t)] + Z_-(\mathbf{k}) \exp[j(\mathbf{k}\cdot\mathbf{x} + \omega t)]\}, \qquad (6.1)$$

where the complex Fourier amplitudes are independent random variables satisfying

the orthogonality conditions:

$$< Z_{\pm}(\mathbf{k}')Z_{\pm}^{*}(\mathbf{k}) >= \frac{1}{2}\Psi(\mathbf{k})\delta(\mathbf{k}-\mathbf{k}')dk_x dk_y,$$

$$< Z_{\pm}(\mathbf{k}')Z_{\pm}(\mathbf{k}) >= 0,$$

$$< Z_{\mp}(\mathbf{k}')Z_{\pm}(\mathbf{k}) >= 0,$$

where $\Psi(\mathbf{k})$ is the spectral density function (i.e. directional wave spectrum). Since $\xi(\mathbf{x}, t)$ is real, we have

$$Z_{+}(\mathbf{k}) = Z_{-}^{*}(-\mathbf{k}). \tag{6.2}$$

One approach for constructing $Z_{\pm}(\mathbf{k})$ is to create a sequence of Gaussian random numbers with $\mu = 0$ and $\sigma = 1$ for both the real part and imaginary part of $Z_{\pm}(\mathbf{k})$. It is however more convenient, in the case of a large number of frequency components, to set the amplitude of $Z_{\pm}(\mathbf{k})$ constant and use only the random phase part. That is,

$$Z_{+}(\mathbf{k}) = B(\mathbf{k})\exp[j\phi(\mathbf{k})],$$

where $\phi(\mathbf{k})$ is uniformly distributed over $[0, 2\pi]$, and

$$B(\mathbf{k}) = \sqrt{\Psi(\mathbf{k})dk_x dk_y}.$$

The output resulting from the sum of many random components (Eq. (6.1)) will show approximately Gaussian behaviour by the central limit theorem.

The input to this model is the observed directional wave spectra described in Chapter 5, which are given in the form of the frequency-angle spectrum $F(\omega, \theta)$. By using the dispersive relation for linear surface gravity waves, we can convert $F(\omega, \theta)$ to $\Psi(\mathbf{k})$ with

$$\Psi(\mathbf{k}) = \frac{g^2}{2\omega^3}F(\omega, \theta)\Bigg|_{\omega^2 = gk} \tag{6.3}$$

(Phillips, 1977). A 2-D random process such as $\xi(\mathbf{x}, t)$ in Eq. (6.1) can be easily synthesized on a computer by applying a 2-D FFT. In order to do so, we rewrite Eq. (6.1) as

$$\xi(\mathbf{x}, t) = \sum_{\mathbf{k}} \xi(\mathbf{k}, t)\exp(j\mathbf{k}\cdot\mathbf{x}), \tag{6.4}$$

where

$$\xi(\mathbf{k},t) = Z_+(\mathbf{k})e^{-j\omega t} + Z_-(\mathbf{k})e^{j\omega t}.$$

Then $\Phi(\mathbf{k})$ is sampled in the wavenumber domain:

$$k_x = k_1 dk_x \quad k_1 = 0, 1, ..., N_1 - 1$$

$$k_y = k_2 dk_y \quad k_2 = 0, 1, ..., N_2 - 1,$$

and $\xi(\mathbf{x},t)$ is evaluated at

$$x = n_1 dx \quad n_1 = 0, 1, ..., N_1 - 1$$

$$y = n_2 dy \quad n_2 = 0, 1, ..., N_2 - 1,$$

where

$$dk_x dx = \frac{2\pi}{N_1} \qquad dk_y dy = \frac{2\pi}{N_2}.$$

Therefore Eq. (6.4) can be written in a digital form

$$\xi(n_1, n_2, t) = \sum_{k_1=0}^{N_1-1} \sum_{k_2=0}^{N_2-1} \xi(k_1, k_2, t) W_{N_1}^{-n_1 k_1} W_{N_2}^{-n_2 k_2}, \tag{6.5}$$

which is a standard form of the 2-D FFT, where $W_N = e^{-j2\pi/N}$. By changing t in $\xi(k_1, k_2, t)$, we can easily create a time series of frames of the suface. This model has been implemented with the 2-D FFT performed by a Digital Signal Processor (Motorola 56000 DSP; See also Chapter 2). The software is highly efficient and synthesizes a 128×128 point surface within 500 ms.

In this model, we choose the acceleration criterion to determine the occurrence of breaking. The slope criterion in Eq. (1.4) may also be used but is computationally more complicated. Other criteria are not suitable for the present setup of the model. To generate a linear acceleration field, the model transforms the elevation spectrum to the acceleration spectrum using

$$a(\mathbf{k},t) = \frac{\partial^2 \xi(\mathbf{k},t)}{\partial^2 t} = -\omega^2 \xi(\mathbf{k},t)$$

and substitutes $a(\mathbf{k},t)$ into Eq. (6.4).

6.2 Design of the Monte-Carlo Experiment

Before the model can be run, the temporal and spatial resolutions must be determined. The temporal resolution, i.e. time step δt, determines the smallest scale of waves that can be tracked. This is equivalent to imposing a short duration cutoff on the output; events shorter than δt cannot be tracked. It is therefore necessary to keep this cutoff constant, since this will facilitate the comparison of event statistics in different wave conditions. The instrumental cutoff for the wave spectrum is 2.0 sec, and laboratory work by Hwang et al. (1989) indicates that the breaking duration determined by measuring breaking threshold variables, both the geometric and kinematic variables, is approximately 4-6% of the wave period. [1] Although our model uses the dynamical criterion, this ratio should not vary significantly. Hence we choose 5% so that $\delta t = 0.1$ sec.

The spatial resolution ds is determined by the size of the FFT (N) the model uses, and the wavenumber resolution dk. For the instrumental cutoff, the directional wave spectrum has a highest wavenumber of $K_{max} = 0.707m^{-1}$, in each of the x and y directions. Let M be the number of samples in the k-domain. Then the wavenumber resolution is $dk = K_{max}/M$. Since the spatial and wavenumber resolutions satisfy

$$dsdk = \frac{2\pi}{N},$$

the spatial resolution is determined by

$$ds = \frac{2\pi}{Ndk} = \frac{2\pi}{K_{max}}\frac{M}{N}.$$

[1] The duration measured by Hwang, et al. appears to be much smaller than other results, such as those of Snyder et al. (1983). Hwang et al. offered two possible explanations: one is that the wave in the laboratory is younger than in the field, and the second is that the data of Snyder et al. were collected in sea water in which bubbles stay longer than in fresh water. Another explanation would be that Hwang et al. measured breaking variables (slope or particle velocity) in the wave field; the occurrence of these variables exceeding a threhold is not necessarily coincident with the occurrence of whitecaps. Since in the model we also evaluate a breaking variable, we use the results of Hwang et al.

The current computer setup accommodates 128 × 128 FFTs. Therefore ds is dependent only on M. It is desirable to reduce ds to a size such that small scale waves can be tracked with good accuracy. There is however a tradeoff, since a small value of M reduces the wavenumber resolution. In addition, a few preliminary runs of the model showed that an increase of M tends to reduce the duration of waves. The explanation would be that an increase in the number of random wave components makes the superimposed waves less regular, causing individual waves to last for a shorter period. Our solution to this problem is by trial and error: we search for a range of M in which the resulting mean event speed and duration from the model are relatively stable. The mean value in this range is chosen. This value is 13 and fixed for all the spectra.

The choice of different seeds for generating random phases has little impact on the resulting event statistics (changed by less than 5%) when the results are averaged over a sufficiently long period. Therefore, the event statistics presented below were obtained for only one realization, but in a long enough period that sufficient events (order of 500) were collected.

6.3 Clustering and Tracking

The output from the wave field model at each time step is the vertical acceleration field in a finite spatial aperture. A breaking threshold is applied to select those points with acceleration above the threshold. These selected points are concentrated in a number of regions referred to as breaking events. Breaking events are usually randomly distributed in space as shown in Fig. 6.1, and the number and spatial distribution pattern of breaking events change from time to time. For this reason, a technique is needed to group automatically the breaking points in each frame into their corresponding regions (breaking events). This is apparently a problem of clustering in the context of pattern recongition.

The clustering algorithm we used is a modified version of Batchelor and Wilkins'

original algorithm (Bow, 1984), the details of which are given in Appendix F. For each cluster (breaking event), we determine its center using

$$\mathbf{r}_c = \frac{\sum_{m=1}^{M} a_m \mathbf{r}_m}{M \bar{a}_c}, \tag{6.6}$$

where $\mathbf{r}_m$ and a_m are respectively the position and acceleration of each point in the cluster, and

$$\bar{a}_c = \frac{\sum_{m=1}^{M} a_m}{M}$$

is the mean acceleration of the cluster. M is the total number of points in the cluster.

The wave model is run with time incrementing, generating a series of frames. In each frame, the clustering algorithm is applied and the center and mean acceleration of each cluster are recorded. These cluster centers are tracked over time to determine their speed, direction and duration. The tracking algorithm is described as follows:

At each time step, compare the location of each cluster center in the present frame to the location of each center in the previous frame. For each center in the previous frame, the closest center in the present frame is chosen to represent a possible continuation of the previous center.

In order to represent the same event as the old center, the new one must be within a predefined distance from the old one. If the new center lies within the predefined distance, then test the acceleration of the old center. If the acceleration is decreasing, then the acceleration of the new center should be smaller than the old acceleration. If it is greater, then the new center represents the start of a new event.

If no corresponding new center can be found for an old center, the event is assumed to have ended. Its speed, direction, and duration are recorded in a file, and the total number of events is incremented.

If no corresponding old center can be found for a new center, the new center is assumed to represent the start of a new event.

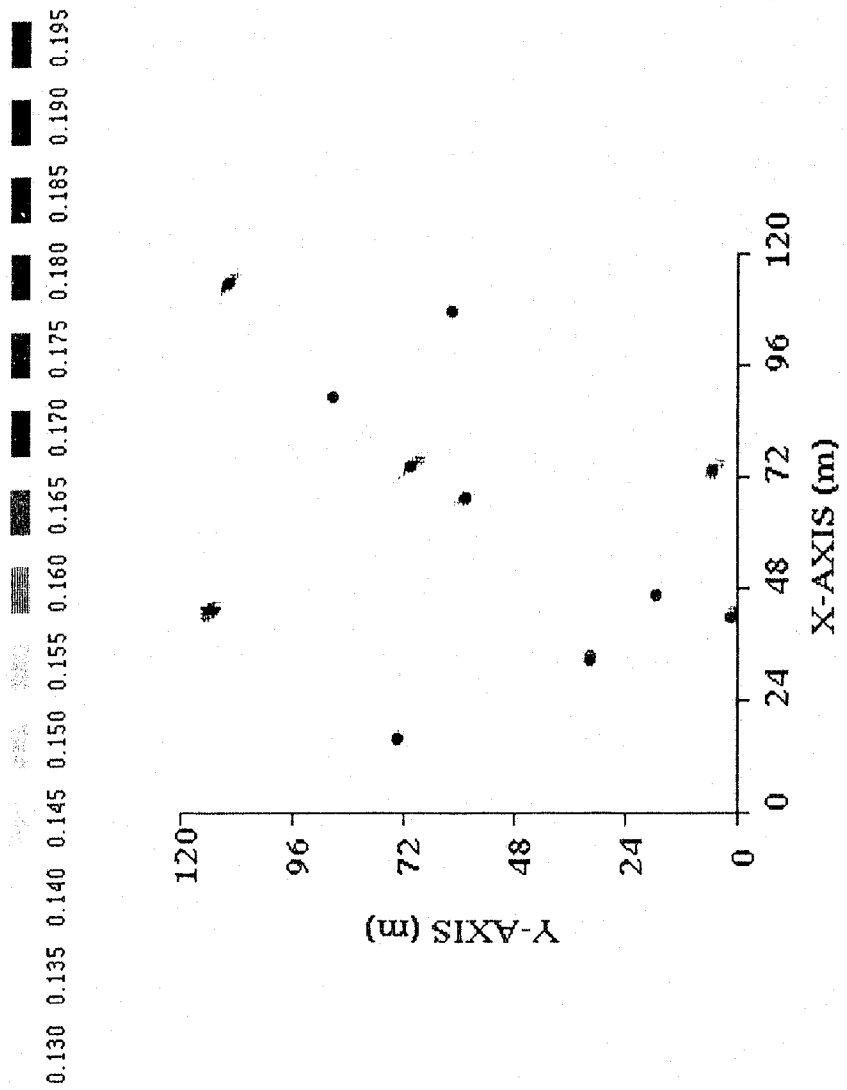

Figure 6.1: Distribution of simulated breaking waves. The gray level represents the downwards vertical acceleration (fraction of the gravitational acceleration) at the surface. The center of each cluster determined with the clustering algorithm described in the text is also shown (filled circle). Some weak events are below the breaking threshold and are not identified by the algorithm.

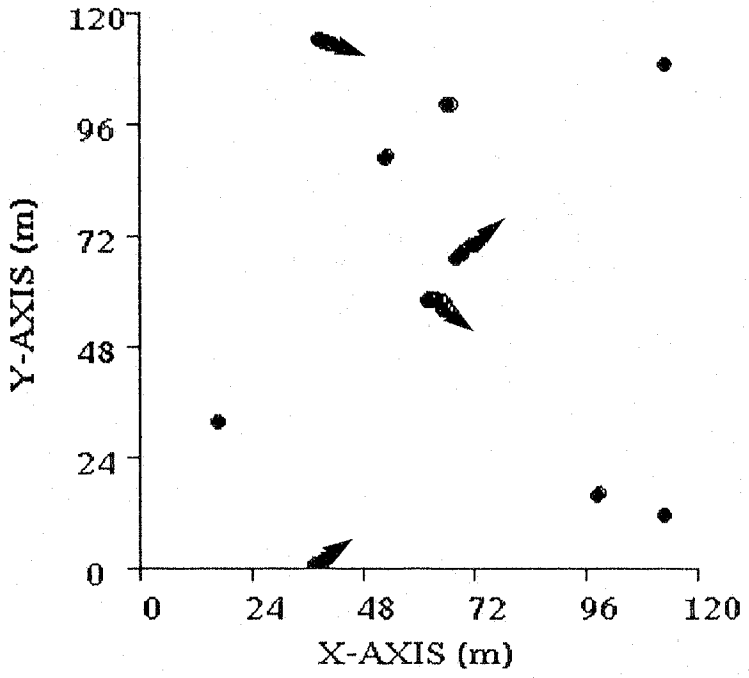

Figure 6.2: Trajectories of cluster centers tracked with the tracking algorithm described in the text, for a period of 1 s. Arrows indicate the direction of motion of the centers (breaking events). Some events stay for only one or two snapshots and thus their direction is not shown.

The use of the acceleration criterion helps to distinguish a new event which is too close to an old one and would be identified as part of the old event without this acceleration criterion. Because of the use of the acceleration criterion, the choice of the distance criterion is relatively unimportant. A small value of the distance threshold tends to increase the number of tracked events since it may break an event into multiple events. However, if the threshold is above a certain value, the number of events becomes stable. This value is usually 2.0-2.5 times the spatial resolution. A larger value results in a higher mean event speed, but the increase is negligible.

For illustration of the clustering-tracking algorithm, the centers of the clusters in Fig. 6.1 determined with the clustering algorithm are shown as the filled circles. These centers are tracked with the tracking algorithm as time increments, and the trajectories of the cluster centers are shown in Fig. 6.2, for a period of 1 s. Some events last for a longer period while some stay only for one or two snapshots. The trajectory for each center is recorded, from which the travel velocity and duration of the cluster center are determined. By averaging over a longer period, event statistics are obtained.

6.4 Results and Discussions

In the following presentations, event statistics are all shown against the fourth moment of the spectrum, m_4, rather than wind speed, since wind conditions are not taken into account in the model. Physically m_4 is the variance of acceleration and is the most relevant parameter to the simulated event statistics. However, m_4 is crucially dependent on the behavior of the high frequency tail of the spectrum. As mentioned in Chapter 5, the directional wave spectra appear to be less sensitive at higher frequencies than the wire gauge wave spectra. The behaviour of the directional wave spectra at higher frequencies affects calculation of m_4 and contributes to discrepancies between the model results and the acoustical observations, as will be seen below.

6.4.1 Determination of the Breaking Threshold

Before calculating event statistics, the breaking threshold α in Eq. (1.5) must first be determined. Although for single progressive waves, α is found to be 0.388 (Longuet-Higgins and Fox, 1977), in the case of irregular, three-dimensional waves, this value must be determined experimentally. In the present case, the breaking threshold can be determined by adjusting α such that the model event density is closest to the observed density in Chapter 5. Due to the limited upper frequency cutoff of the

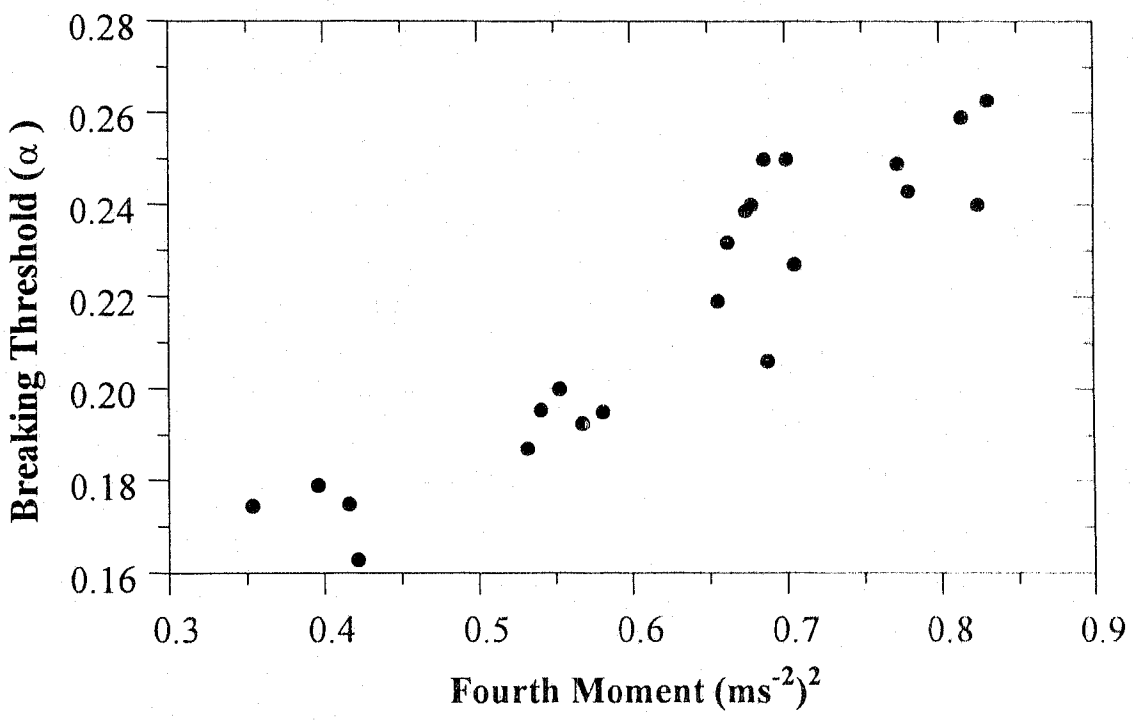

Figure 6.3: Dependence of the chosen breaking threshold α on the fourth moment of the spectrum.

Doppler sonar, we must determine the corresponding cutoff scale in the observation. Loewen and Melville's (1991a) laboratory experiment suggests that the acoustical duration of a breaking event is at least 0.48 of the wave period, and our own field observation shows this ratio is 0.45-0.65 (Fig. 5.17b). This ratio was thus chosen to be 0.5. The wave spectrum cutoff (2.0 sec) therefore corresponds to a duration cutoff of 1.0 s in the acoustically derived data. The observed event density is determined for events above this scale.

Figure 6.3 shows the dependence of the selected breaking threshold (α) on the fourth moment of the spectrum (m_4), where the breaking threshold is seen to range from 0.17 to 0.26. The α value (0.082) in the preceding chapter is much smaller, possibly because for the given observed event density, the use of the acoustic coverage data leads to a higher value of the breaking probability. There is also a general trend in Fig. 6.3 that α increases with increasing m_4. If a constant α is used, then at low

m_4 values, the model would produce fewer events than the acoustic instrument would observe, whereas at high m_4 values, the model would produce more. This partly reflects the low sensitivity of the directional wave spectra at higher frequencies: At lower m_4 values, the dominant scale of breaking is smaller. Since the directional wave spectra are not sensitive enough at higher frequencies, the model cannot produce as many small events as the hydrophone array can detect.

6.4.2 Event Statistics

Given the chosen α values, event statistics including event density, whitecap coverage, velocity, duration and downwind length (defined as the distance an event travels during its lifetime), were obtained for each directional wave spectrum. Slight variations in α may change the event density and whitecap coverage appreciably, but do not affect the other statistics significantly. The results, together with the chosen α values and m_4, are summarized in Table 6.1, where the datasets denoted by the numbers are in the same period as those with the same numbers in Tables 5.1 and 5.2. In the table, m_4 was obtained by integrating from the lowest frequency of the spectrum to the cutoff frequency.

Whitecap Coverage

Whitecap coverage was obtained by dividing the number of points with acceleration above the breaking threshold, by the total number of points (128×128). Referring to Eq. (1.7), the probability of breaking depends only on the rms of acceleration $\sqrt{m_4}$, normalized by the threshold acceleration αg. Therefore the results (filled circles) are plotted in Fig. 6.4a against the normalized rms acceleration $a_{rms} = \sqrt{m_4}/\alpha g$, where it is seen that the whitecap coverage increases slightly with a_{rms}. The open circle is the whitecap coverage predicted by Eq. (1.7). It is seen that Eq. (1.7) predicts a much more rapidly increasing rate of whitecap coverage with a_{rms} than the simulation. This can at least partly be attributed to the choice of larger α values at larger m_4, since whitecap coverage from the simulation is very sensitive to the

variations of α. To demonstrate this, we chose α to be constant at the mean of the values in Fig. 6.3 (0.21) and repeated the calculation of whitecap coverage. The results together with the prediction are shown in Fig. 6.4b. It is obvious that the simulation in Fig. 6.4b agrees better with the theoretical prediction , although the predicted values are still generally higher than the simulation. The difference in Figs. 6.4a and 6.4b is clearly due to the high sensitivity of the simulated whitecap coverage to the variations of α. For example, those simulated whitecap coverage values with a_{rms} around 0.4 in Fig. 6.4a are below 0.3%. These values were obtained for α around 0.24. However, when α is reduced to 0.21, these values jump to 0.6-0.8% as shown in Fig. 6.4b, and are able to follow the predicted values at a_{rms} values between 0.43 and 0.45. The minor difference between the Snyder and Kennedy model and the simulation in Fig. 6.4b can be attributed to the fact that their model is based on point analysis and the simulation on spatial average; conversion from point measurement to spatial measurement can only be approximate. It also appears that the use of analytical directional wave spectra (e. g. JONSWAP) produces simulation results in better agreement with the model (Kennedy and Snyder, 1983).

Event Speed, Duration, Downwind Length

Figures 6.5a-c show the m_4-dependences of event speed, duration and downwind length. The event speed shows an increasing dependence on m_4, ranging from 4.5 ms^{-1} to 5.5 ms^{-1}. The event duration, however, has a very weak dependence on m_4, varying only by 0.06 s. The downwind length also shows an increasing trend due to the increase of event speed, and varies from 1.7 m to 2.5 m. There will be more discussion on these event statistics in the next section.

Data set #	m_4 $m^{-2}s^{-4}$	α	WC %	$\hat{Q}(\times 10^{-3})$ $m^{-2}s^{-1}$	$\bar{D}_m$ s	$\bar{V}_m$ ms^{-1}	$\bar{\theta}_m$ °N	$\bar{L}_D$ m
1	0.680	0.2400	0.303	0.384	0.467	5.22	133	2.25
2	0.772	0.2490	0.126	0.219	0.471	5.32	157	2.40
3	0.701	0.2500	0.125	0.181	0.470	5.48	167	2.46
4	0.800	0.2430	0.222	0.302	0.457	5.47	173	2.39
5	0.825	0.2400	0.161	0.249	0.461	5.42	166	2.41
6	0.706	0.2270	0.217	0.274	0.455	5.19	170	2.29
7	0.656	0.2190	0.201	0.317	0.448	5.09	162	2.25
8	0.541	0.1954	0.253	0.454	0.459	4.86	125	2.09
9	0.567	0.1925	0.197	0.341	0.437	4.95	113	2.09
10	0.553	0.2000	0.155	0.367	0.448	4.61	102	1.76
11	0.674	0.2387	0.175	0.335	0.473	4.95	126	2.08
12	0.686	0.2500	0.143	0.235	0.460	5.20	132	2.33
13	0.831	0.2627	0.148	0.221	0.460	5.42	140	2.41
14	0.814	0.2590	0.174	0.252	0.473	5.38	140	2.42
15	0.688	0.2061	0.385	0.589	0.454	5.24	149	2.28
16	0.663	0.2318	0.158	0.270	0.470	5.03	150	2.33
17	0.581	0.1950	0.247	0.426	0.464	5.00	163	2.20
18	0.581	0.1950	0.247	0.426	0.464	5.00	163	2.20
19	0.532	0.1870	0.189	0.375	0.435	5.11	166	2.15
20	0.421	0.1629	0.220	0.399	0.448	5.14	164	2.17
21	0.353	0.1745	0.289	0.671	0.411	4.58	79	1.82
22	0.416	0.1749	0.191	0.510	0.431	4.64	65	1.79
23	0.396	0.1790	0.189	0.428	0.442	4.60	68	1.84

Table 6.1: Event statistics from the numerical simulation. where $\bar{D}_m$, $\bar{V}_m$, $\bar{\theta}_m$ and L_D denote the event duration, travel speed and direction, and downwind dimension from the model. The numbers correspond to those in Tables 5.1 and 5.2

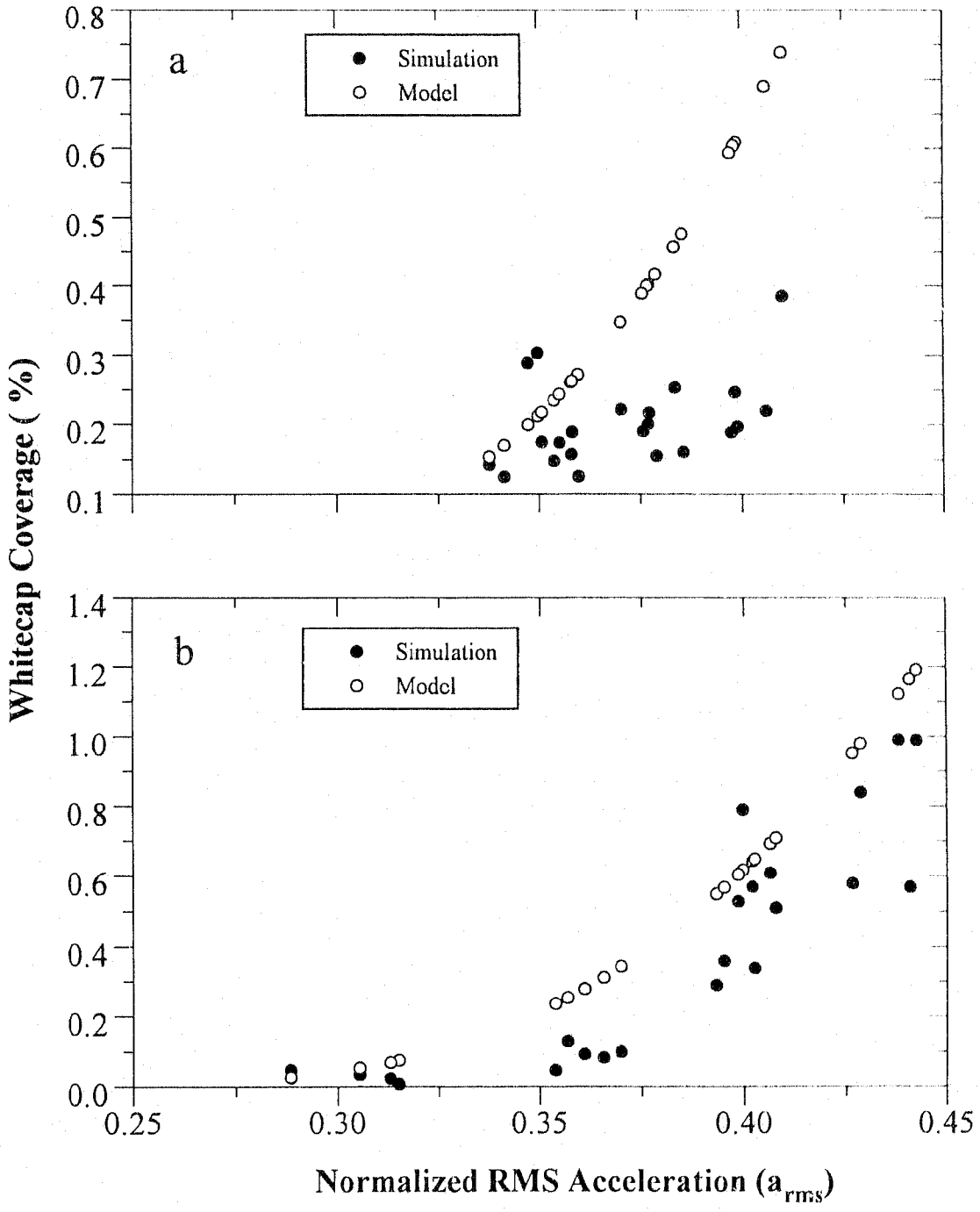

Figure 6.4: Dependence of whitecap coverage (percentage) on a_{rms}. The filled circle represents the simulation outputs and the open circle is the predicted value using Snyder and Kennedy's model. (a) The threshold α varies for different datasets as given in Table 6.1; (b) α is fixed at 0.21.

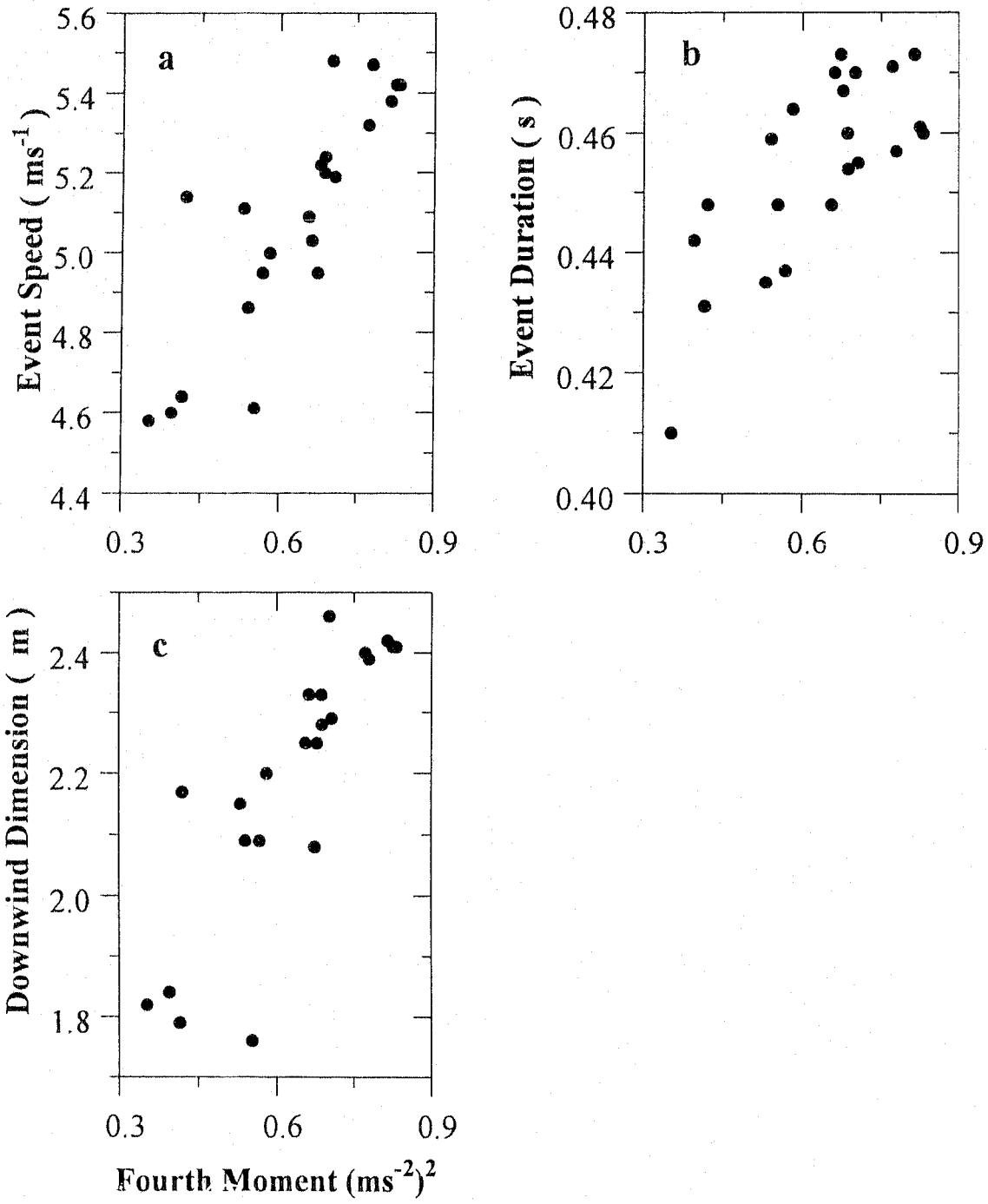

Figure 6.5: Dependences of simulated event statistics on m_4. (a) Event speed; (b)Event duration; (c) Downwind length.

6.4.3 Comparison with Acoustical Observation

Event Speed

Since breaking wave velocity represents the scale of breaking, we start from comparison of breaking event speed to examine the model results. Figure 6.6a shows the distribution of event speed from the model for dataset 14 in Table 6.1, with the acoustically observed distribution during the same period shown in Fig. 6.6b (replotted from Fig. 5.10c). Both distributions are concentrated at some speed, with the observed distribution concentrated at a lower speed than the model distribution. This is possibly because the directional wave spectra have a relatively low sensitivity at higher frequencies and are limited to a cutoff speed of 3.0 ms^{-1} as mentioned earlier; the low sensitivity tends to suppress small simulated events and thus the distribution shifts to larger scales (higher speeds). There is a longer tail at higher speeds on the observed distribution. It is believed that this tail results from the uncertainty in estimating the speeds of distant events. Except for the tail, the general features of these two distributions are similar. Therefore, it is observed that finite source dimension has little effect on the observed speed distribution, as discussed in Chapter 5.

In Fig. 6.7, the mean event speeds from the model v_m and from the observation $\bar{v}_e$ are plotted together against m_4. It can be seen that they are very close at higher values of m_4 (> 0.75), but gradually deviate as m_4 decreases, with v_m being above $\bar{v}_e$. This is clearly due to the limit of the the directional wave spectra: At low m_4 values, the breaking scale is smaller, and the model based on the directional wave spectra tends to produce fewer small events, resulting in a larger mean speed.

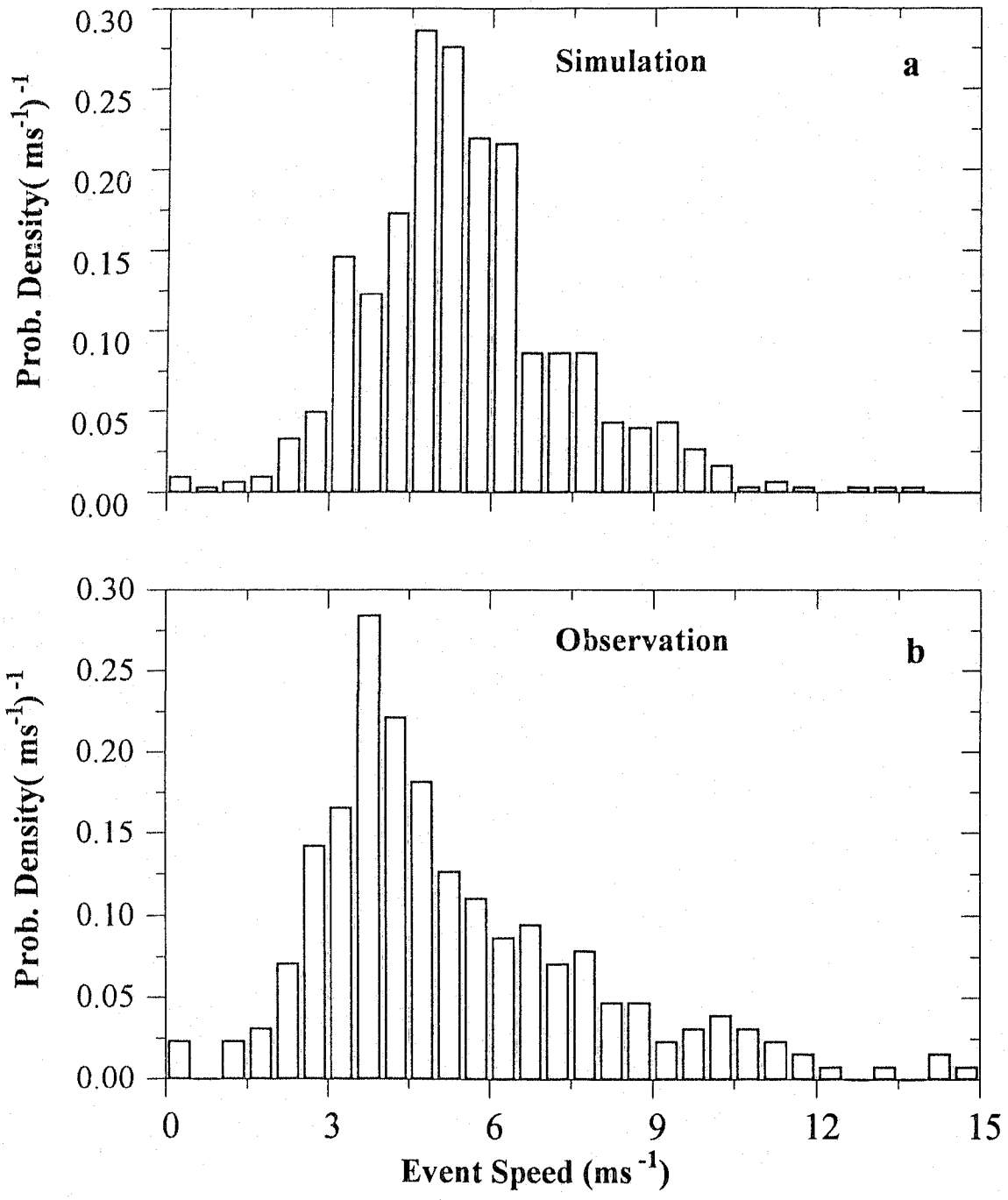

Figure 6.6: Distribution of event speed. (a) From the numerical simulation; (b) From the acoustical observation, based on dataset 14 in the table.

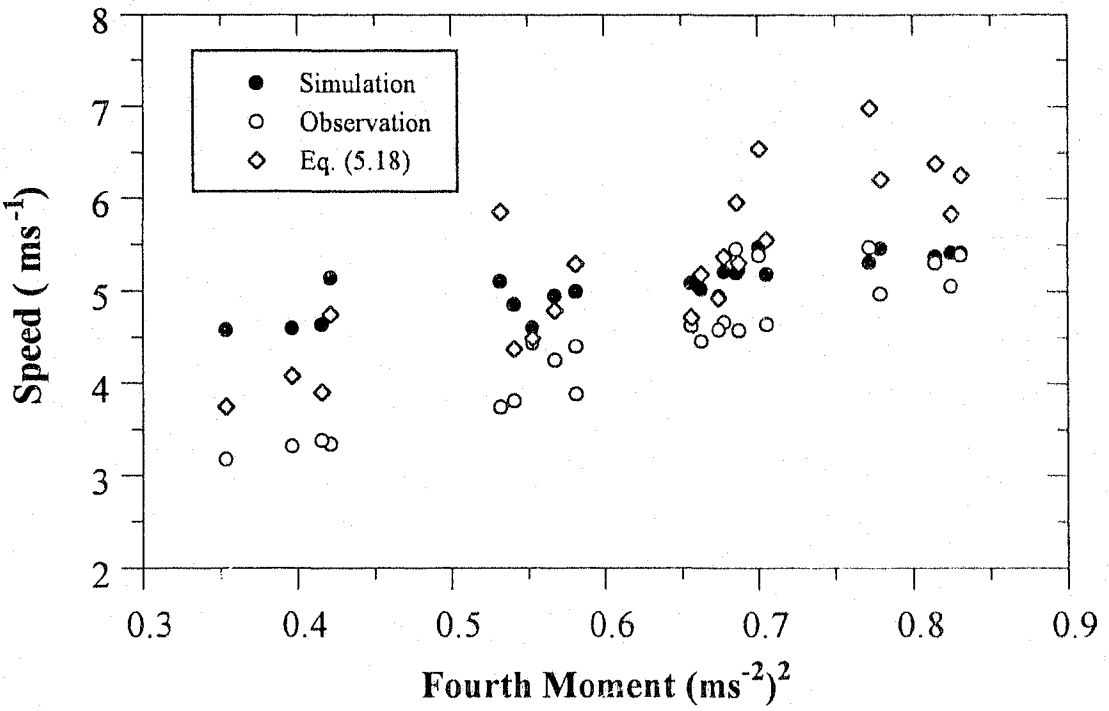

Figure 6.7: Comparison between the event speeds determined from the simulation (filled circles) and from the acoustical observation (open circles). Also shown is the speed predicted using Eq. (5.18) (diamonds).

$\bar{c}_{br}$ (defined in Eq. (5.18)) is also plotted for comparison. It can be seen that Eq. (5.18) predicts higher speeds than the model outputs at high m_4 values ($>$ 0.75) and lower speeds at low m_4 values ($<$ 0.5). In the intermediate range, Eq. (5.18) agrees with the model output. One possible explanation is that the use of the acceleration spectrum as a weighting function to find c_{br} in Eq. (5.18) is not appropriate. Alternative weighting is needed which weighs less on larger scales and more on smaller scales. A more comprehensive model is required to give better prediction of the mean scale of breaking from the wave spectrum.

Event Directivity

The distribution of direction of event velocity corresponding to Fig. 6.6a is shown in Fig. 6.8a. It is seen that the model distribution is far more concentrated than the observed distribution in Fig. 6.8b (replotted from Fig. 5.11c), apparently due to the complexity of the open ocean environment. The mean direction of event velocity is also given in Table 6.1. Comparing with Table 5.1, it is found that the mean direction from the model is very close to that predicted by Eq. (5.20). Referring to Table 5.2, the model direction is seen to agree with the observed direction for many of these datasets. However, the model direction can sometimes be significantly different from the event direction. In such a case, it is found that the observed direction is much closer to the wind direction. As explained in Chapter 5, wind action may play a role in this case.

Event Duration

The model duration distribution corresponding to Fig. 6.6a is shown in Fig. 6.9a, whereas the observed distribution in Fig. 5.12c is replotted in Fig. 6.9b. Both distributions show a decreasing trend as the duration increases. However, the model distribution is concentrated below duration of 0.8 s, and shows a much steeper slope than the observed distribution. On the contrary, the observed distribution spans a much wider range of duration, from 0.5 s up to 5.0 s.

The mean model duration in Fig. 6.5b is replotted against m_4 in Fig. 6.10, together with the acoustic duration from Fig 5.13b. It is observed that the acoustic duration is 3-4 times larger than the model duration. This will be discussed below.

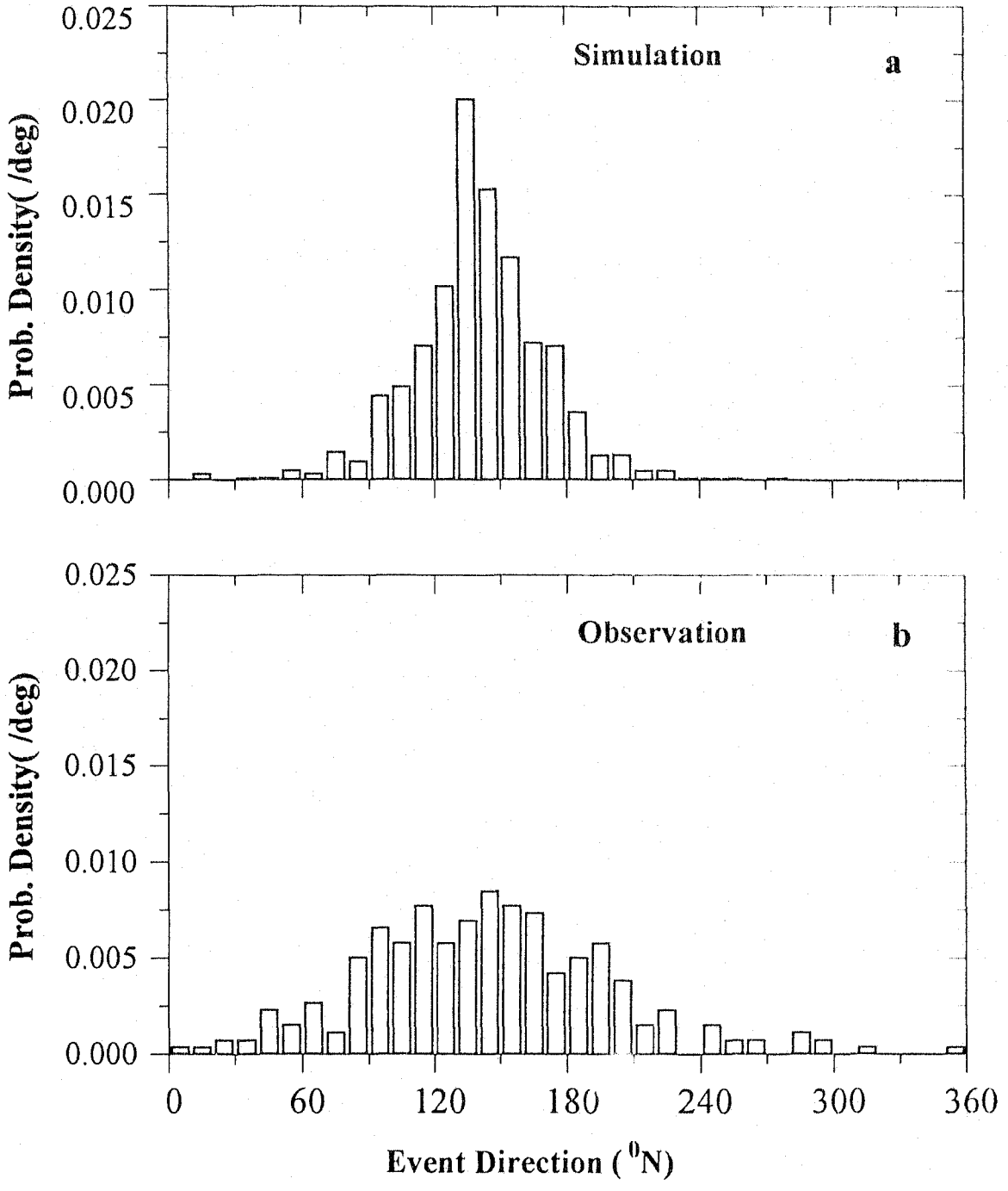

Figure 6.8: Distribution of the direction of event velocity. (a) From the simulation; (b) From the acoustical observation, based on dataset 14 in the table.

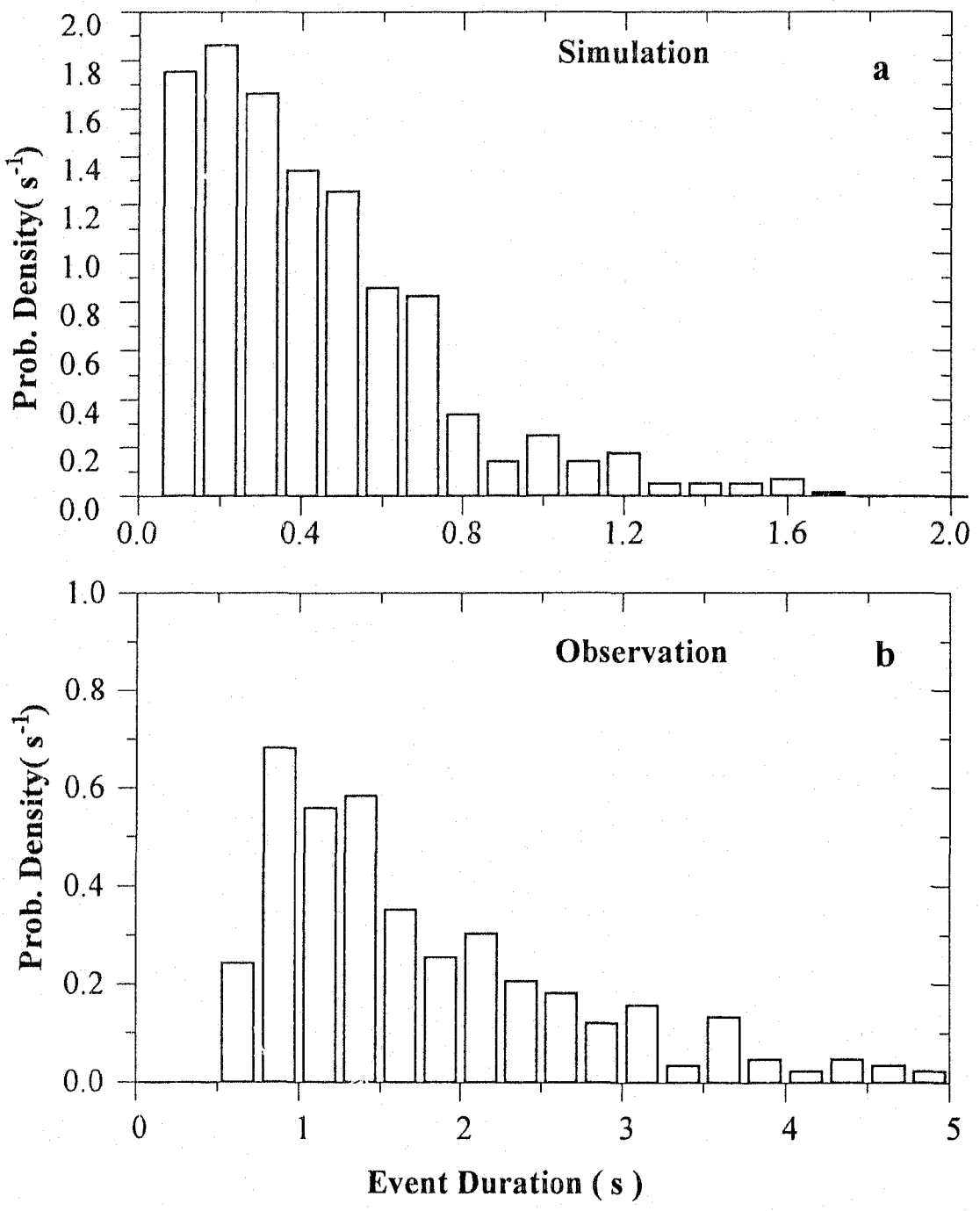

Figure 6.9: Distribution of event duration. (a) From the simulation, corresponding to Fig. 6.6a; (b) From the observation, corresponding to Fig. 6.6b.

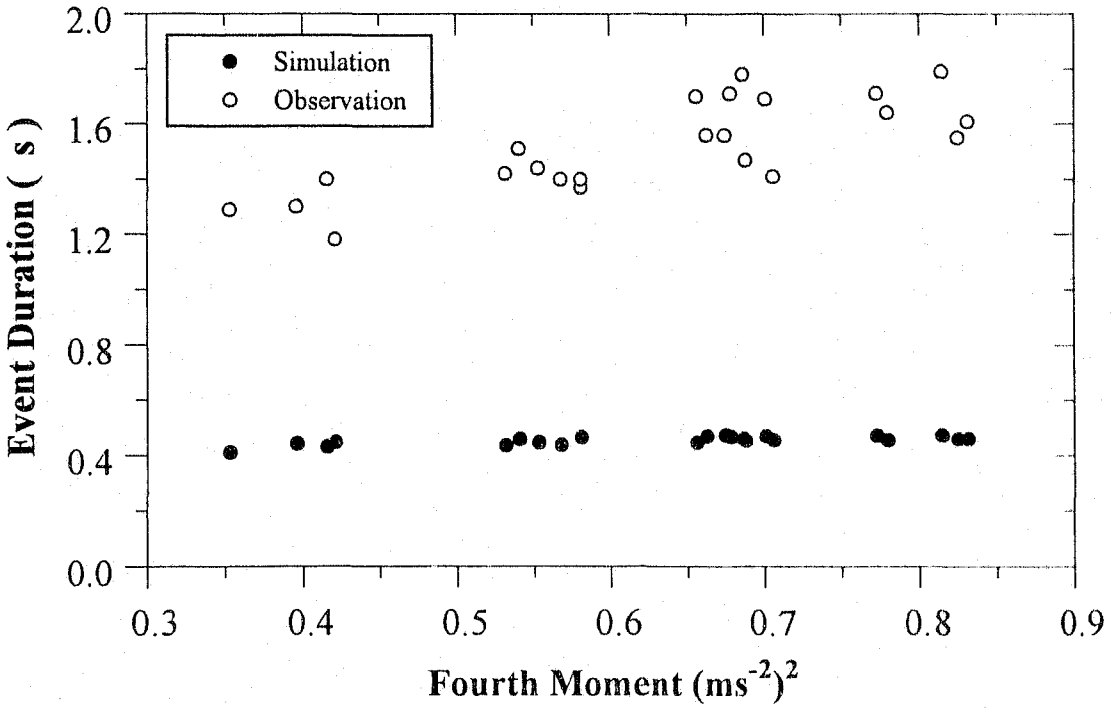

Figure 6.10: Dependence of breaking duration on m_4 from the model (filled circles, replotted from Fig. 6.5b), together with the acoustic duration (open circles, replotted from Fig. 5.13b).

Normalization

As discussed in Chapter 5, the mean event speed represents the mean scale of breaking. Therefore, the mean period and wavelength of breaking waves were derived from the mean speed using the dispersive relation, and used to normalize the mean event duration and downwind length, as shown in Figs. 6.11a and b. Both the normalized duration and downwind length decrease with the scale of breaking. These dependences are consistent with the observations shown in Figs. 6.11c-d, although the magnitudes are very different. It can also be seen that the scatter in the model results is comparable to the observations. This suggests that breaking wave statistics in the case of three-dimensional waves do not appear to have a statistically robust dependence on one or two parameters: it would possibly require knowledge of the entire directional wave spectrum to describe the statistics.

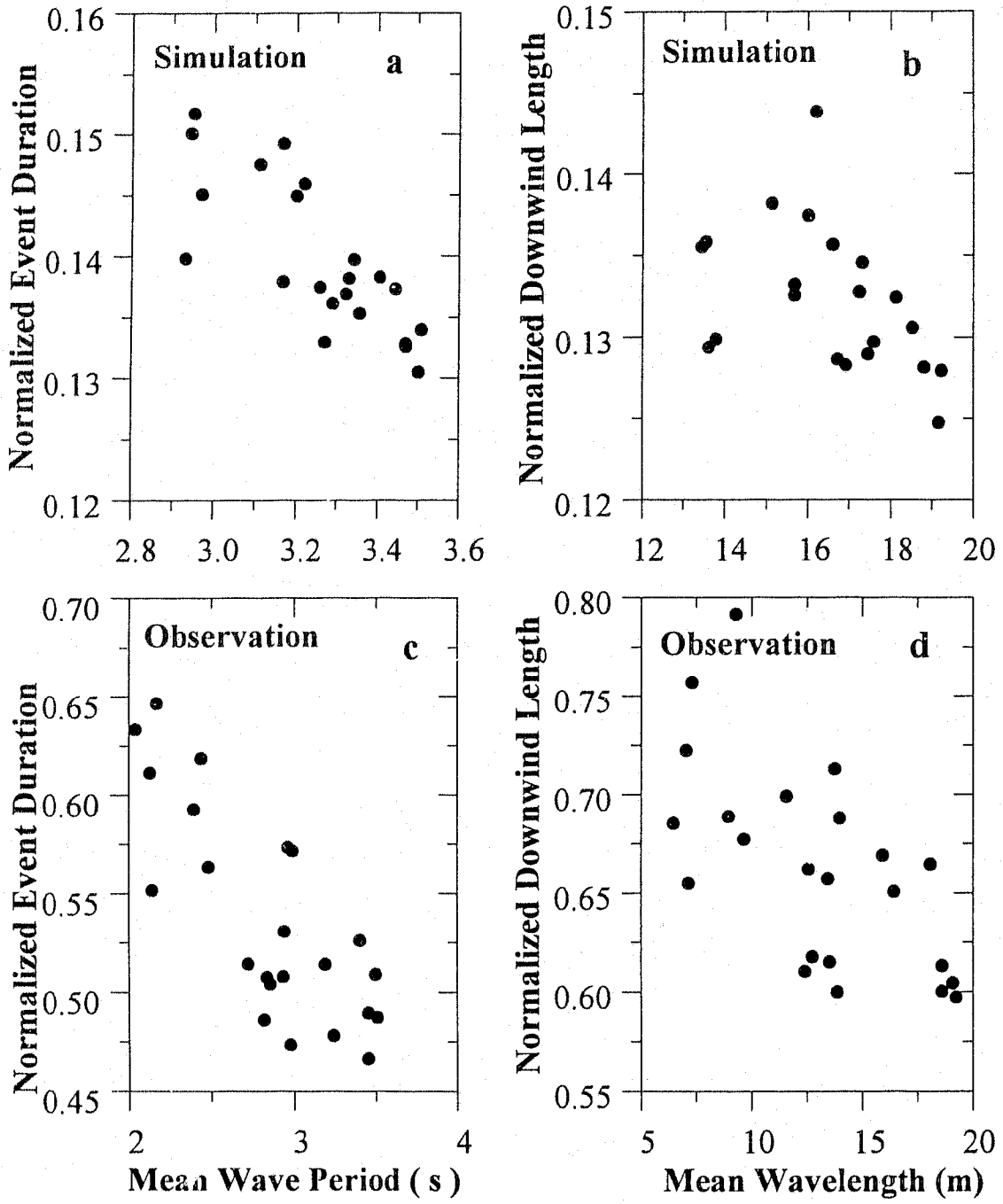

Figure 6.11: Normalized duration (a) and downwind length (b) versus the corresponding normalizing factors, i.e., mean wave period and wavelength. (c) and (d) are the acoustically observed normalized duration and downwind length (replotted from Fig. 5.17b and c).

The normalized model duration in Fig. 6.11a is only of order 0.12-0.16 for these datasets. Laboratory work by Hwang et al. (1989) shows that the normalized duration is in the range of 0.03-0.08. Referring to Fig. 6.11c, the acoustic duration is about one half of the wave period. It is therefore observed from both the numerical and laboratory experiment that although the process associated with breaking threshold variables is highly transient compared to the wave period, its consequences (sound or visible whitecaps) persist for a much longer period.

6.5 Summary

In this chapter, we have described an approach for synthesizing the surface wave field, and applied this approach to evaluate breaking wave statistics. From the simulation work, we found that

1. The breaking threshold determined by comparing the observed event density with the model density, is in the range of 0.17 to 0.26 which is significantly smaller than the theorectical value (0.388), and increases with m_4. The increasing trend is probably caused by the low sensitivity of the directional wave spectrum measurement at higher frequencies.

2. The dependence of whitecap coverage on a_{rms} from the simulation does not appear to fit the Snyder and Kennedy model, when the breaking threshold is chosen on the basis of the observation. However, the fit is better with a fixed choice of the threshold. This suggests that the Snyder and Kennedy model could still be used to approximate whitecap coverage derived from a two dimensional numerical model.

3. The travel speed of events determined from the model is close to the acoustically observed speed, although the comparison is subject to the limit of the directional wave spectra at higher frequencies. It is possible that the mean event velocity could also be calculated by some analytical form such as Eq.

(5.18) and Eq. (5.20).

4. The modelled breaking threshold variable lasts for a shorter (1/3 - 1/4) period than the consequence of breaking, i.e., the sound radiated by breaking waves. This must be taken into account in modelling breaking waves and making comparison with any type of passive acoustic observations.

In general, the model produces many characteristics of breaking waves that are consistent with our acoustical observations. The consistency in the distribution of event speed as well as the mean event speed, is particularly obvious and indicates that the model correctly identifies the mean velocity scale of breaking. The dependences of the normalized event duration and downwind length on the scale of breaking are also consistent with the observation. Discrepancies between the observed and model statistics also exist however. The most apparent is the magnitude of event duration. This emphasizes the importance of distingushing the wave breaking process itself and the various physical consequences resulting from it. The observed direction of travel of breaking waves deviates from the direction derived from the model, and sometimes shows a dependence on the wind direction, implying the relevance of wind action. The choice of the breaking threshold based on the acoustical data and the model outputs varies from one dataset to another. This would imply either the importance of nonlinearities or the inadequacy of a linear model with a single threshold.

There are apparently improvements that can be made to the model and may help narrow these discrepancies. For example, wind action and nonlinearities and swell should also be included. In particular, an improved linear representation of surface waves that includes weak nonlinearities has been developed by Creamer et al. (1989), and can be readily incorporated into the present computational framework. This work is presently underway. Incorporation of this approach into our model may lead to a better choice of the breaking threshold and therefore more certain prediction of breaking wave statistics.

Summary and Recommendations

Summary

The work described above has been motivated by the importance of breaking surface waves in wave dissipation and air-sea interaction. It has included the development of a novel passive acoustical approach for measurement of breaking waves, and the interpretation of the observations obtained by means of this technique to deepen our understanding of the wave breaking process.

The difficulties in measuring breaking surface waves have forced one to exploit remote-sensing techniques, including passive acoustics. The acoustical instrument used in this work contains an array of four broadband hydrophones, which tracks individual breaking waves using wave-generated sound, and thus allows measurement of both spatial and temporal characteristics of wave breaking.

The signal processing scheme for tracking breaking waves is based on the Generalized Cross Correlation method (Knapp and Carter, 1976). It requires computation of a series of cross correlations which constitute an image, and involves enhancement of the correlation image and event identification from the image with a pattern recognition approach. This scheme has been designed for automatic processing of a large amount of data. Data analysis based on the scheme has also been accelerated with the aid of a high-speed data processing system.

This scheme is however limited by two factors. One is environmental noise that always exists in any type of measurement, whereas the other is the finite source dimension problem which arose during the correlation analysis. These two factors

have led to the problem of incomplete measurement, and motivated the development of statistical models for necessary corrections. Because of the limited prior information about the statistics associated with the wave breaking process, and for the simplicity of theoretical analysis, these models have been based on some simplified but reasonable physical assumptions. As our understanding of wave breaking improves, the models can be placed on a more realistic and solid basis.

The experimental results obtained during the SWAPP experiment have been the first to provide both spatial and temporal statistics of breaking surface waves in the open ocean. These statistics, including breaking event density, travel velocity, lifetime, and spacing, have been obtained under a variety of environmental conditions. Empirical relations of the results with the environmental conditions have also been derived. Comparison between the breaking wave statistics and the simultaneously measured directional wave spectra suggests that wave breaking occurs at a mean scale appreciably smaller than (45-75%) the scale associated with the dominant wind wave component in the spectrum. There is also some evidence that the direction of travel of breaking waves tends to be aligned with the wind direction when the wind direction deviates from the wave direction, implying the importance both of wind action and of the history of wind and waves. There is however no clear correlation between the directions of swell and breaking waves.

Our observation also provides an estimate of breaking wave density which shows a decreasing trend with increasing wind due to the increase of the breaking scale. It is hoped that these results will provide input to a comprehensive wave dissipation model presently being developed by Banner (personal communication).

We have attempted to relate these results to the simultaneously measured directional wave spectra with the Monte-Carlo approach, due to lack of analytical tools. It is found that there is good similarity between the acoustically observed distribution of breaking event velocity and the numerically simulated distribution using a linear model with a single threshold. This suggests that such a model is capable of predicting the correct velocity scale of breaking. The model is however unable

to choose the breaking threshold confidently, due to the limits of linearity. It is also found that the breaking threshold variable (vertical acceleration) exceeding the selected threshold last for a far (3-4 times) shorter period than the sound generated by wave breaking.

The sound radiated by individual breaking waves not only allows tracking of these waves but also provides information about the structure of the breaking events and the sound generation mechanism by breaking. The coherence structure of radiated sound reveals the spatial anisotropy of the source dimension. A low frequency (200-500 Hz) component in the power spectrum can be well accounted for by the collective bubble oscillation hypothesis. Statistical analysis of the acoustic source intensity of breaking waves shows a generally increasing dependence on the breaking scale. The source intensity distribution appears to be exponential and supports a laboratory observation that the acoustic power radiated by a breaking wave is proportional to the energy dissipated by breaking (Melville et al., 1988; Loewen and Melville, 1991a). These results imply that surface wave dissipation could be remotely measured using ambient sound.

In summary, we have successfully developed a passive acoustical technique for measurement of breaking surface waves. By using this technique, we have been able to determine the spatial and temporal statistics of breaking waves and probe their acoustical radiation properties. These observations will provide input for modelling wave dissipation and thus contribute to the understanding of the physics of wave breaking.

Recommendations

Although this work has yielded interesting and important results on wave breaking, there are however a number of limitations that hinder further interpretation and exploration of the data. One apparent limitation of the present approach is the difficulty of resolving a finite dimension source due to the simplicity of the four-

hydrophone array. It is a rather challenging task both to locate finite dimension sources and to determine their dimension. This problem must however be solved if passive acoustical measurements of breaking waves are to be improved. Use of subarrays to replace omnidirectional hydrophones in the cross-correlator (Ferguson, 1989) provides one possible solution. This approach is a direct extension of Knapp and Carter's method, and its theory has been well established. The instrument would require only modest modifications. Time frequency analysis (wavelet transform) (Weiss and Young, 1992) offers a new tool for tackling this problem, but is mathematically more complicated. In pursuit of this target, a higher resolution array is presently being developed for passive acoustical imaging of breaking waves.

The sound generated by individual breaking waves is an immediate subject to follow on the basis of the present dataset. The preliminary analysis in the thesis shows limited correlation of the acoustic source intensity of breaking waves with the breaking scale and appears to support a linear relation between radiated acoustic power and energy dissipation due to breaking. It is therefore possible to make an estimate of energy dissipation by breaking from the measurements of the acoustic source intensity and the linear relation, and to compare the estimate with other measurements, or indirect estimates based on models, of wave dissipation. This will at least test the feasibility of using ambient sound to measure wave energy dissipation. The low frequency component in the sound radiated by a breaking wave is consistent with collective bubble oscillations and related to the amount of air injected by the breaking wave. It is also desirable to extend the study by simultaneously measuring acoustic radiation and entrained air fraction due to breaking to determine any correlation between them.

The results of the numerical simulation emphasize the importance of nonlinearities associated with wave breaking. The nonlinear model developed by Creamer et al. (1989) has essentially been implemented on the computer for generating sea surface. This has yet to be further developed to compute the Lagrangian acceleration. Once the acceleration is computed, the clustering-tracking algorithm described

in the thesis can readily be applied to the model outputs to obtain breaking wave statistics. This is expected to improve the simulation results.

It has been suggested that wave breaking is primarily associated with wave groups (Donelan et al., 1972), and that the breaking of small scale waves would be enhanced by swell (Phillips and Banner, 1974). Our observations probably contain breaking waves associated both with wave groups and swell. It is therefore desirable to separate these two scales of breaking. On the one hand, we can examine whether larger breaking waves show groupiness consistent with their scale. On the other hand, given a directional wave spectrum and a point measurement of wave height (available from the accelerometer and pressure sensor on the instrument), it is possible to determine whether there is any preference of breaking at the swell crest and at what scale the enhanced breaking occurs if there is any.

Higher frequency (8 kHz) ambient sound has been observed by Zedel and Farmer (1992) and shows modulations by surface waves. They attribute this phenomenon to small wave breaking induced by long-short wave interaction, or alternatively to variations in wind stress over the long waves. They also notice that the modulations, although present at all frequencies of ambient sound, are larger at higher frequencies. It is therefore speculated that the reduced modulations at lower frequencies result from the presence of discrete sources which are associated with larger scale breaking waves and radiate more low frequency acoustic power. With the present approach, it is possible to investigate the role played by larger discrete sources and smaller continuous sources in ambient sound generation.

Finally, passive acoustical measurements of breaking waves can be combined with active acoustical measurements of bubble distributions and other near-surface processes such as Langmuir Circulation, and also with other non-acoustic sensors, to determine the role played by wave breaking in air-sea interaction processes.

Bibliography

[1] Agrawal, Y. C., E. A. Terray, M. A. Donelan, P. A. Hwang, A. J. Williams III, W. M. Drennan, K. K. Kahma and S. A. Kitaigorodskii, 1988: Enhanced Dissipation of Kinetic Energy beneath Surface Waves. *Nature.* Vol 359, pp219-220.

[2] Arase, T., and E. M. Arase, 1968: Deep-sea Ambient Noise Statistics. *J. Acoust. Soc. Am.* 44(6), pp1679-1684.

[3] Banner, M. L. and D. H. Cato, 1988: Physical Mechanism of Noise Generation by Breaking Waves – A Laboratory Study. in *Natural Mechanisms of Surface-Generated Noise in the Ocean.* Ed. B. R. Kerman, Kluwer Academic Publishers, pp429-436.

[4] Banner, M. L. and O. M. Phillips, 1974: On Small-Scale Breaking Waves. *J. Fluid Mech.* 65, pp647-657.

[5] Bendat, J. S. and A. G. Piersol, 1986: *Random Data: Analysis and Measurement Procedures.* 2nd edition, John Wiley & Sons, Inc., p273.

[6] Bendat, J. S. and A. G. Piersol, 1980: *Engineering Applications of Correlation and Spectral Analysis.* John Wiley & Sons, Inc., pp166-167.

[7] Bortkovskii, R. S. 1987: Air-sea Exchange of Heat and Moisture During Storms. Ed. E. D. Monahan, D. Reidel Publishing Company.

[8] Bow, S-T, 1984: *Pattern Recognition: Application to Large Data-Set Problems.* Marcel Dekker, Inc.

[9] Carter, G. C., A. H. Nuttall, and P. G. Cable, 1973: The Smoothed Coherence Transform. *Proc. IEEE*(lett.) vol. 61, pp1497-1498.

[10] Clay, C. S., and H. Medwin, 1977: *Acoustical Oceanography: Principles and Applications.* John Wiley & Sons, Inc.

[11] Cox, H., 1973: Spatial Correlation in Arbitrary Noise Fields with Application to Ambient Sea Noise. *J. Acoust. Soc. Am.* 54(5), pp1289-1301.

[12] Creamer, D. B., F. Henyey, R. Schult, and J. Wright, 1989: Improved Linear Representation of Ocean Surface Waves. *J. Fluid Mech.* 265, pp135-161.

[13] Cron, B. F., and C. H. Sherman, 1962: Spatial-correlation functions of various noise models. *J. Acoust. Soc. Am.* 34, pp1732-1736.

[14] Crowther, P. A. and A. Hansla, 1990: The Lifetimes, Velocities, and Probable Origin of Sonic and Ultrasonic Noise Sources on the Sea Surface. in *Natural Physical Sources of Underwater Sound.* B. Kerman, Ed. Kluwer Academic Publishers.

[15] Ding, L. and D. M. Farmer, 1992a: A Signal Processing Scheme for Passive Acoustical Mapping of Breaking Surface Waves. *J. Atmos. Oceanic Technol,* Vol. 9, No. 4, pp484-494.

[16] Ding, L. and D. M. Farmer, 1992b: On the Acoustical Intensity of Breaking Waves. *Proc. Acoustics Week in Canada.* October, Vancouver. *Canadian Acoustics.* Vol. 20, No. 3, pp65-66.

[17] Ding, L. and D. M. Farmer, 1992c: Acoustical Intensity Statistics of Breaking Waves. *Proc. 14th International Conference on Acoustics. B5-7.* September, Beijing.

[18] Donelan, M. A., 1992: Air-Sea Interaction. In *The Sea: Ocean Engineering Science*. 9A. Eds. B. Le Mehaute and D. M. Hanes. J. Wiley & Sons Inc., New York. pp239-292.

[19] Donelan, M., M. S. Longuet-Higgins, and J. S. Turner, 1972: Periodicity in Whitecaps. *Nature* Vol 239, pp449-451.

[20] Ewing, J. A., M. S. Longuet-Higgins, and M. A. Srokosz, 1987: Measurements of the Vertical Acceleration in Wind Waves. *J. Phys. Oceanogr.* 17, pp3-11.

[21] Farmer, D. M. and L. Ding, 1992: Coherent Acoustical Radiation from Breaking Waves. *J. Acoust. Soc. Am.* 92(1), pp397-402.

[22] Farmer, D. M., R. C. Teichrob, C. J. Elder, and D. G. Sieberg, 1990: Novel Acoustical Instrumentation for the Study of Ocean Surface Processes. in *Oceans'90*, Washington, D.C., September, pp11-17.

[23] Farmer, D. M. and S. Vagle, 1989: Waveguide propagation of Ambient Sound in the Ocean-Surface Bubble Layer. *J. Acoust. Soc. Am.* 86, pp1897-1908.

[24] Farmer, D. M and S. Vagle, 1988: On the Determination of Breaking Surface Wave Distribution. *J. Geophys. Res.* 93(C4), pp3591-3600.

[25] Ferguson, B. G., 1989: Improved Time-Delay Estimates of Underwater Acoustic Signals Using Beamforming and Prefiltering Techniques. *IEEE J. Oceanic Engineering*, vol. OE-14, July, pp238-244.

[26] Guo, Y. P., 1987: Sound Generation in the Ocean by Breaking Surface Waves. *J. Fluid Mech.* 181, pp329-347.

[27] Hassab, J. C. and R. E. Boucher, 1979: Optimum Estimation of Time Delay by a Generalized Correlator.*IEEE Trans. Acoust. Speech, Signal Processing* vol ASSP-27, August, pp373-380.

[28] Henderson, T. L., 1985: Matched Beam Theory for Unambiguous Broadband Direction Finding. *J. Acoust. Soc. Am.* 78, pp563-574.

[29] Holthuijsen, L. H. and T. H. C. Herbers, 1986: Statistics of Breaking Waves Observed as Whitecaps in the Open Sea. *J. Phys. Oceanogr.* 16, pp290-297.

[30] Hwang, P. A., D. Xu,and J. Wu, 1989: Breaking of Wind-Generated Waves: Measurement and Characteristics. *J. Fluid Mech.* 202, pp177-200.

[31] Jessup, A. T., W. K. Melville and W. C. Keller, 1991: Breaking Waves Affecting Microwave Backscatter 2. Dependence on Wind and Wave Conditions. *J. Geophys. Res.* 96(C11), pp20561-20569.

[32] Katsaros, K. B. and S. S. Atakturk, 1991: Dependence of Wave Breaking Statistics on Wind Stress and Wave Development. *Proc. International Union of Theoretical and Applied Mechanics.* July, Australia.

[33] Kennedy, R. M., 1992: Sea Surface Dipole Sound Source Dependence on Wave Breaking Variables. *J. Acoust. Soc. Am.* 91(4), pp1974-1982.

[34] Kennedy, R. M. and R. L. Snyder, 1983: On the Formation of Whitecaps by a Threshold Mechanism. Part II Monte Carlo Experiments.*J. Phys. Oceanogr.* 13, pp1493-1504.

[35] Kerman, B. R., 1984: Underwater Sound Generated by Breaking Waves. *J. Acoust. Soc. Am.* 75, pp149-165.

[36] Knapp, C. H. and G. C. Carter, 1976: The Generalized Correlation Method for Estimation of Time Delay. *IEEE Trans. Acoust. Speech, Signal Processing* vol ASSP-24, August, pp320-327.

[37] Knudsen, V.O., R. S. Alford, and J. M. Emling, 1948: Underwater Ambient Noise. *J. Mar. Res.* 7, pp410-429.

[38] Lamarre, E. and W. K. Melville, 1992: Void Fraction Measurements in Bubble Plumes Generated by 2-D and 3-D Breaking Waves. (abstract). *J. Acoust. Soc. Am.* 91(4), Part 2, p2427.

[39] Lamarre, E. and W. K. Melville, 1991: Air Entrainment and Dissipation in Breaking Waves. *Nature,* Vol 351, pp469-472.

[40] Loewen, M. R. and W. K. Melville, 1992: Measurements of the Low Frequency Sound Produced by 2-D and 3-D Breaking Waves. (abstract). *J. Acoust. Soc. Am.* 91(4), Part 2, p2323.

[41] Loewen, M. R. and W. K. Melville, 1991a: Microwave Backscatter and Acoustic Radiation from Breaking Waves. *J. Fluid Mech.* 224, pp601-623.

[42] Loewen, M. R. and W. K. Melville, 1991b: A model of the Sound Generated by Breaking Waves. *J. Acoust. Soc. Am.* 90(4), pp2075-2080.

[43] Longuet-Higgins, M. S., 1990: Bubble Noise Spectra. *J. Acoust. Soc. Am.* 87, pp652-661.

[44] Longuet-Higgins, M. S., 1989: Monopole Emission of Sound by Asymmetric Bubble Oscillations. Part 1. Normal Modes & Part 2. An Initial-Value Problem *J. Fluid Mech.* 201, pp525-565.

[45] Longuet-Higgins, M. S., 1988: Mechanisms of Wave Breaking in Deep Water. in *Natural Mechanisms of Surface-Generated Noise in the Ocean.* Ed. B. R. Kerman, Kluwer Academic Publishers, pp1-30.

[46] Longuet-Higgins, M. S., 1985: Acceleration in Steep Gravity Waves. *J. Phys. Oceanogr.* 15, pp1570-1579.

[47] Longuet-Higgins, M. S., 1980: On the Distribution of the Heights of Sea Waves: Some Effects of Nonlinearity and Finite Band Width. *J. Geophys. Res.* 85(C3), pp1519-1523.

[48] Longuet-Higgins, M. S., 1963: The Generation of Capillary Waves by Steep Gravity Waves. *J. Fluid Mech.* 16, pp138-159.

[49] Longuet-Higgins, M. S., 1957: The Statistical Analysis of A Random, Moving Surface. *Philos. Trans. Roy. Soc. London. Ser.* A, 249, pp321-387.

[50] Longuet-Higgins, M. S. and N. D. Smith, 1983: Measurments of Breaking Waves by a Surface Jump Meter. *J. Geophys. Res.* 88(C14), pp9823-9831.

[51] Longuet-Higgins, M. S., and M. J. H. Fox, 1977: Theory of the Almost-Highest Wave: the inner solution. *J. Fluid Mech.* 80, pp721-741.

[52] Lu, N. Q. and A. Prosperetti, 1990: Underwater Noise Emissions from Bubble Clouds. *IEEE J. Oceanic Engineering,* vol. OE-15, October, pp275-281.

[53] Medwin. H. and A. C. Daniel, 1990: Acoustical Measurements of Bubble Production by Spilling Breakers. *J. Acoust. Soc. Am.* 88, pp408-412.

[54] Medwin. H. and M. M. Beaky, 1989: Bubble Sources of the Knudsen Sea Noise Spectra. *J. Acoust. Soc. Am.* 86, pp1124-1130.

[55] Melville, W. K., M. R. Loewen, F. C. Felizardo, A. T. Jessup, and M. J. Buckingham, 1988: The Acoustic and Microwave signatures of Breaking Waves. *Nature.* Vol 336, pp54-56.

[56] Melville, W. K. and R. J. Rapp, 1985: Momentum Flux in Breaking Waves. *Nature.* Vol 317, pp514-516.

[57] Mitsuyasu, H., 1985: A Note on the Momentum Transfer from Wind to Waves. *J. Geophys. Res.* 90(C2), pp3343-3345.

[58] Monahan, E. C. and I. G. O'Muirheartaigh, 1986: Whitecaps and the Passive Remote Sensing of the Ocean Surface. *Int. J. Remote Sensing.* Vol. 7, No. 5, pp627-642.

[59] Ochi, M. K. and C-H Tsai, 1983: Prediction of Occurrence of Breaking Waves in Deep Water. *J. Phys. Oceanogr.* 13, pp2008-2019.

[60] Papoulis, A., 1984: *Probability, Random Variables and Stochastic Processes.* Second edition. McGraw-Hill Book Company.

[61] Phillips, O. M., 1988: Equilibrium Range of Characteristics of Breaking Waves. in *Natural Mechanisms of Surface-Generated Noise in the Ocean.* Ed. B. R. Kerman, Kluwer Academic Publishers, pp31-38.

[62] Phillips, O. M., 1985: Spectral and Statistical Properties of the Equilibrium Range in Wind-Generated Gravity Waves. *J. Fluid Mech.* 156, pp505-531.

[63] Phillips, O. M., 1977: *The Dynamics of the Upper Ocean.* 2nd Edn. Cambridge University Press.

[64] Phillips, O. M. and M. J. Banner, 1974: Wave Breaking in the Presence of Wind Drift and Swell. *J. Fluid Mech.* 66, pp625-640.

[65] Preisendorfer, R. W., 1988: *Principal Component Analysis in Meteorology and Oceanography.* Elsevier Scientific Publishing Company.

[66] Prosperetti, A., 1988: Bubble-Related Ambient Noise in the Ocean. *J. Acoust. Soc. Am.* 84, pp1042-1054.

[67] Prosperetti, A. and N.Q. Lu, 1988. Cavitation and Bubble Bursting as Sources of Oceanic Ambient Noise *J. Acoust. Soc. Am.* 84, pp1037-1041

[68] Pumphrey, H. C. and J. E. Ffowcs Williams, 1990: Bubbles as Sources of Ambient Noise. *IEEE J. Oceanic Engineering,* Vol. OE-15, October, pp268-274.

[69] Rapp, R. J. and W. K. Melville, 1990: Laboratory Measurements of Deep-Water Breaking Waves. *Philos. Trans. Roy. Soc. London. Ser.* A, 331, pp735-800.

[70] Ross, D., 1976: *Mechanics of Underwater Noise.* Pergamon Press.

[71] Scharf, L. L., 1991: *Statistical Signal Processing.* Addison-Wesley Publishing Company.

[72] Shang, E.C. and V.C. Anderson, 1986: Surface-Generated Noise under Low Wind Speed at Kilohertz Frequencies. *J. Acoust. Soc. Am.* 79, pp964-971.

[73] Smith, S. D. and E. P. Jones, 1985: Evidence for Wind-dumping of Air-Sea Gas Exchange Based on Direct Measurments of CO_2 Fluxes. *J. Geophys. Res.* 90(C1), pp869-875.

[74] Snyder, R. L. and R. M. Kennedy, 1983: On the Formation of Whitecaps by a Threshold Mechanism. Part I: Basic Formulation. *J. Phys. Oceanogr.* 13, pp1482-1492.

[75] Snyder, R.L., L. Smith, and R. M. Kennedy, 1983: On the Formation of Whitecaps by a Threshold Mechanism. Part III: Field Experiment and Comparison with Theory. *J. Phys. Oceanogr.* 13, pp1505-1518.

[76] Srokosz, M. A., 1986: On the Probability of Wave breaking in Deep Water. *J. Phys. Oceanogr.* 16, pp382-385.

[77] Thorpe, S. A., 1992: Bubble Clouds and the Dynamics of the Upper Ocean. *Q. J. R. Meteorol. Soc.* 118, pp1-22.

[78] Thorpe, S.A. 1982: On the Clouds of Bubbles Formed by Breaking Waves in Deep Water and Their Role in Air-Sea Gas Transfer. *Phil Trans. Roy. Soc. London* A 304, pp155-210.

[79] Thorpe, S. A. and A. J. Hall, 1983: The Characteristics of Breaking Waves, Bubble Clouds, and Near-Surface Currents Observed Using Side Scan Sonar. *Cont. Shelf Res.* Vol. 1, No.4, pp353-384.

[80] Thorpe, S. A. and P. N. Humpheries, 1980: Bubbles and Breaking Waves. *Nature* Vol 283, pp463-465.

[81] Updegraff, G. E. and V. C. Anderson, 1991a: An Instrument for the *in situ* Measurement of Sea Surface Noise from a Depth of 1 m under Low Wind Conditions. *J. Acoust. Soc. Am.* 89, pp2253-2263.

[82] Updegraff, G. E. and V. C. Anderson, 1991b: Bubble Noise and Wavelet Spills Recorded 1 m below the Ocean Surface. *J. Acoust. Soc. Am.* 89, pp2264-2279.

[83] Urick, J. R., 1983: *Principles of Underwater Sound.* 3rd edition, McGraw-Hill Book Company.

[84] Vagle, S., W. Large, and D. M. Farmer, 1990: An Evaluation of the WOTAN Technique of Inferring Oceanic Winds from Underwater Ambient Sound. *J. Atmos. Oceanic Technol,* Vol. 7, No. 4, pp576-595.

[85] Weiss, L. G. and R. K. Young, 1992: Wideband Spatial Processing with Wavelet Transforms. *Proc. Sixth Signal Processing Workshop on Statistical Signal & Array Processing.* October, Victoria.

[86] Weissman, M. A., S. S. Atakturk, and K. B. Katsaros, 1984: Detection of Breaking Events in a Wind-Generated Wave Field. *J. Phys. Oceanogr.* 14, pp1608-1619.

[87] Wenz, G. M., 1972: Review of Underwater Acoustics Research: Noise. *J. Acoust. Soc. Am.* 51(3), pp1010-1924.

[88] Wenz, G. M., 1962: Acoustic Ambient Noise in the Ocean: Spectra and Sources. *J. Acoust. Soc. Am.* 34, pp1936-1956.

[89] Wu, J., 1992: Individual characteristics of Whitecaps and Volumetric Description of Bubbles. *IEEE J. Oceanic Engineering,* Vol. OE-17, January, pp150-158.

[90] Wu, J., 1979: Oceanic Whitecaps and Sea State. *J. Phys. Oceanogr.* 9, pp1064-1068.

[91] Xu, D-L., P. A. Hwang, and J. Wu, 1986: Breaking of Wind-Generated Waves. *J. Phys. Oceanogr.* 16, pp2172-2178.

[92] Yoon, S. W., L. A. Crum, A. Prosperetti, and N. Q. Lu, 1991: An Investigation of the Collective Oscillations of a Bubble Cloud. *J Acoust. Soc. Am.* 89, pp700-706.

[93] Zedel, L. and D. Farmer, 1992: Surface Wave Period Modulations in Near Surface Ambient Sound. *J. Geophys. Res.* To appear.

Appendix A

Hydrophone Channel Calibration

The broadband ambient sound recording system is shown in Fig. A.1. The frequency response of the system is flat for $f > 100$ Hz, and starts to drop from $f = 100$ Hz. The power spectral analysis performed in Chapter 4 includes correction for the reduced response, for frequencies down to 44 Hz. Due to the limit of the system at frequencies below 100 Hz, the power spectral analysis for $f < 100$ Hz may not be accurate; the results are only reliable for $f \geq 100$ Hz. The conversion from sound pressure to the PCM number can be expressed as

$$SL_{pcm} = SL_{press} + HS + G_{preamp} + G_A + G_B, \tag{A.1}$$

where

$$\begin{aligned} HS &= -175.5 \text{ dB (ref: } \mu Pa/V) \text{—Hydrophone sensitivity} \\ G_{preamp} &= 39.8 \text{ dB —Gain of preamplifier} \\ G_A &= 35 \text{ dB —Gain of amplifier} \\ G_B &= ?? \text{ dB —Gain of Mutiplexer-PCM} \end{aligned}$$

Unfortunately, G_B is not available. We therefore used the empirical relation between wind speed and sound level established by Vagle et al. (1990), to estimate G_B.

Vagle et al. give the following relation:

$$p_0 = Vs + b, \tag{A.2}$$

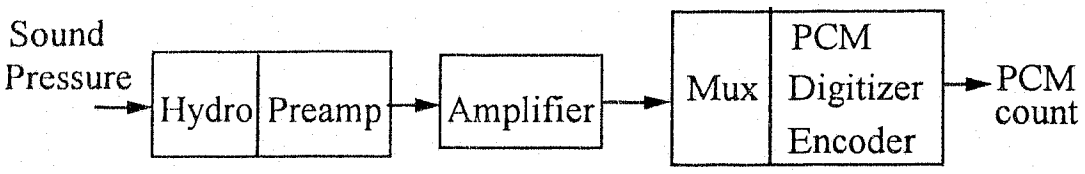

Figure A.1: Broadband ambient sound recording system

where V is wind speed in ms^{-1}, $s = 52.87$, and $b = -80.94$. This formula gives sound spectrum level (SSL) p_0 at 8 kHz. We choose dataset 14 in Table 5.1 which was obtained in a steady sea state. The corresponding wind speed is 13 ms^{-1}, for which,

$$SSL_0(8kHz) = 20\log_{10} p_0 = 55.65 \text{ dB (ref: } \mu Pa^2 Hz^{-1}).$$

SSLs at other frequencies can be calculated using

$$SSL(f) = SSL_0 - Q\log_{10}(f_0/f) \tag{A.3}$$

where $f_0 = 8$ kHz and $Q = -19$ dB/decade. From Eq. (A.3), we find that for wind speed of 13 ms^{-1}, $SSL(4kHz) = 61.37$ dB.

We calculated the SSL at 4 kHz from dataset 14 (averaged over 30 min), and substituted the result and $SSL(4kHz) = 61.37$ dB into Eq. (A.1). The estimated G_B was found to be 56.09 dB. Then Eq. (A.1) becomes

$$SL_{press} = SL_{pcm} + 44.61 \text{ dB}. \tag{A.4}$$

Eq. (A.4) was used to obtain the SSL time series and the acoustic source level of breaking waves in Chapters 3 and 4. Note that the resulting sound level only provides a rough estimate and serves as a reference. The whole system should be well calibrated in future experiments.

Appendix B

Generation of Coherent Random Signals

Theoretical models in signal processing and communication often assume Gaussian random noise. It is often desirable to synthesize Gaussian noise to test new algorithms and analyze their performances. The Monte Carlo approach that evaluates numerically complex physical and engineering problems involves synthesis of random fields or time series, as described in Chapter 6.

Recent developments of powerful digital computers and the Fast Fourier Transform (FFT) have made digital synthesis techniques very efficient. Synthesis of Gaussian random wave fields with a prescribed spectrum has been described in Chapter 6. There seem to be few discussions on the generation of correlated Gaussian noise. One approach for generating correlated noise is to filter a first noise sequence to obtain a second one. Here we describe an alternative algorithm that synthesizes two correlated Gaussian random sequences. Their power spectra and coherence satisfy prescribed forms. The algarithm is conceptually similar to the previous technique for generating a single sequence, but requires some transformation in the frequency domain. This work was motivated by the need to simulate surface-generated ambient noise in the ocean (Cron and Sherman, 1962) as discussed in Chapter 4.

B.1 Generation of One Sequence

Consider a real time sequence $x(n)$ and its Discrete Fourier Transform (DFT)

$$X(k) = \sum_{n=0}^{N-1} x(n) W_N^{-nk}. \tag{B.1}$$

The digital Power Spectral Density (PSD) is given by

$$S_x(k) = \frac{1}{N} E(|X(k)|^2). \tag{B.2}$$

$X(k)$ can be chosen to be

$$X(k) = (g_1(k) + j \cdot g_2(k)) \sqrt{\frac{N}{2} S_x(k)}, \tag{B.3}$$

where $g_1(k)$ and $g_2(k)$ are independent Gaussian random variables with $\mu = 0$ and $\sigma = 1$. $x(n)$ is then generated by the inverse DFT, that is,

$$x(n) = \frac{1}{N} \sum_{k=0}^{N-1} X(k) W_N^{nk}, \tag{B.4}$$

where $X^*(k) = X(N-k)$ so that $x(n)$ is real. Eq. (B.4) can easily be implemented using an FFT, but results in a periodic sequence with period of N, which imposes a practical limit on the length of the sequence that can be generated.

B.2 Generation of Two Coherent Sequences

Now consider two Gaussian sequences, $x_1(n)$ and $x_2(n)$, generated by $X_1(k)$ and $X_2(k)$ respectively. Assume that $x_1(n)$ and $x_2(n)$ are independent and have the same power spectrum, that is, $S_{x_1} = S_{x_2} = S_x$. Form a vector

$$\mathbf{X}(k) = [X_1(k)\ X_2(k)]^H.$$

The covariance maxtrix of $\mathbf{X}$ is then given by

$$\mathbf{R}_x = E(\mathbf{X}(k)\mathbf{X}^H(k)) = \begin{bmatrix} S_{x_1}(k) & 0 \\ 0 & S_{x_2}(k) \end{bmatrix} = S_x(k)\mathbf{I},$$

where $S_x = E(|X(k)|^2)$ and $\mathbf{I}$ is the identity matrix.

Our purpose is to generate another two sequences whose power spectra and coherence satisfy prescribed forms. In order to do so, we use the following transformation

$$\mathbf{Y}(k) = [Y_1(k)\ Y_2(k)]^H = \mathbf{B}^H\mathbf{X}(k).$$

The covariance matrix of $\mathbf{Y}$ is then found to be

$$\mathbf{R}_y = E(\mathbf{Y}(k)\mathbf{Y}^H(k)) = \begin{bmatrix} S_{y_1}(k) & C_{12}(k) \\ C_{12}^*(k) & S_{y_2}(k) \end{bmatrix} = S_x(k)\mathbf{B}^H\mathbf{B},$$

where $S_{y_1}(k)$ and $S_{y_2}(k)$ are the power spectra of $y_1(n)$ and $y_2(n)$ respectively and

$$C_{12}(k) = E(Y_1(k)Y_2^*(k)).$$

Such factorisation of $\mathbf{R}_y$ into the product is not unique, and a variety of algorithms can be used to determine $\mathbf{B}$. We choose the Cholesky method (Scharf, 1991) to obtain

$$\mathbf{B} = \begin{bmatrix} b_{11} & b_{12} \\ 0 & b_{22} \end{bmatrix},$$

where

$$\begin{aligned} b_{11} &= 1 \\ b_{12} &= \sqrt{\frac{S_{y_2}}{S_{y_1}}}\gamma_{12} \\ b_{22} &= \sqrt{\frac{S_{y_2}}{S_{y_1}}(1-|\gamma_{12}|^2)}, \end{aligned} \tag{B.5}$$

and

$$\gamma_{12}(k) = \frac{C_{12}(k)}{\sqrt{S_{y_1}(k)S_{y_2}(k)}}$$

is the complex coherence function of $y_1(n)$ and $y_2(n)$. As a result, we have

$$\begin{aligned} Y_1(k) &= X_1(k) \\ Y_2(k) &= \sqrt{\frac{S_{y_2}}{S_{y_1}}}(\gamma_{12}^*X_1(k) + \sqrt{1-|\gamma_{12}|^2}X_2(k)). \end{aligned} \tag{B.6}$$

In the derivation of Eq. (B.5), we have chosen $S_{y_1}(k)$ to be $S_x(k)$. That is, the first sequence, $y_1(n)$, can be generated from $S_{y_1}(k)$ using the approach described in the preceding section. Then the second sequence $y_2(n)$ is generated using the Fourier components defined in Eq. (B.6) when $S_{y_2}(k)$ and $\gamma_{12}(k)$ are also given. Note that $X_1(k)$ and $X_2(k)$ are given by Eq. (B.3) with the same $S_x(k)$ but different random sequences $g_1(k)$ and $g_2(k)$.

Appendix C

Principal Component Analysis

Principal Component Analysis (PCA) has widely been used in meteorology and oceanography. Detailed discussion of PCA can be found in the literature (e. g. Preisendorfer, 1988). Here we just briefly describe PCA in the bivariate case as applied in Chapter 4.

Consider a bivariate dataset $\{x(n), y(n)$: n=1, ..., N $\}$. This dataset is generally scattered, but we attempt to find the underlying relation. $x(n)$ and $y(n)$ can have different physical dimensions, and in this case, the data should be standardized for the convenience of analysis. That is,

$$u(n) = \frac{x(n) - \bar{x}}{\sqrt{S_{xx}}}, \qquad v(n) = \frac{y(n) - y}{\sqrt{S_{yy}}}$$

where

$$\bar{x} = \frac{1}{N}\sum_{n=1}^{N} x(n), \qquad y = \frac{1}{N}\sum_{n=1}^{N} y(n),$$

$$S_{xx} = \frac{1}{N-1}\sum_{n=1}^{N}[x(n) - \bar{x}]^2, \qquad S_{yy} = \frac{1}{N-1}\sum_{n=1}^{N}[y(n) - y]^2.$$

PCA starts from analysis of the scatter matrix of the given bivariate dataset, defined as

$$\mathbf{S} = \begin{bmatrix} C_{uu} & C_{uv} \\ C_{uv} & C_{vv} \end{bmatrix},$$

where

$$
\begin{aligned}
C_{uu} &= \frac{1}{N-1}\sum_{n=1}^{N} u^2(n) = 1, \\
C_{uv} &= \frac{1}{N-1}\sum_{n=1}^{N} u(n)v(n) = \gamma_{xy} \quad \text{correlation coefficient of } x \text{ and } y, \\
C_{vv} &= \frac{1}{N-1}\sum_{n=1}^{N} v^2(n) = 1.
\end{aligned}
$$

The two eigenvalues of **S** are therefore given by

$$\lambda_{1,2} = 1 \pm \gamma_{xy}. \tag{C.1}$$

The corresponding eigenvectors are in the directions of

$$\theta_1 = 45^0, \qquad \theta_2 = 135^0.$$

These directions are also referred to as the principal directions, in which $x(n)$ and $y(n)$ have the following relations:

$$y = \bar{y} \pm \sqrt{\frac{S_{yy}}{S_{xx}}}(x - \bar{x}), \tag{C.2}$$

where

$$y = \bar{y} + \sqrt{\frac{S_{yy}}{S_{xx}}}(x - \bar{x})$$

corresponds to the larger eigenvalue ($\lambda_1 = 1 + \gamma_{xy}$) and is used to represent the underlying relation between $x(n)$ and $y(n)$. This approach works better than linear regression in the case of relatively scattered data.

Appendix D

Distribution of the Difference of Two Random Variables with the Exponential Distribution

Consider two independent random variables x and y, each of which follows the exponential distribution:

$$\begin{aligned} f_x(x) &= \alpha e^{\alpha x} \quad x > 0 \\ f_y(y) &= \beta e^{\beta y} \quad y > 0. \end{aligned} \tag{D.1}$$

The distribution of the difference, $z = x - y$, is therefore given by

$$f_z(z) = \int_{-\infty}^{\infty} f_x(z+y) f_y(y) dy \tag{D.2}$$

which integrates to

$$f_z(z) = \begin{cases} \alpha\beta/(\alpha+\beta) e^{-\alpha z} & z \geq 0 \\ \alpha\beta/(\alpha+\beta) e^{\beta z} & z < 0 \end{cases}.$$

If $\alpha = \beta$, then

$$f_z(z) = \frac{1}{2} \alpha e^{-\alpha |z|}. \tag{D.3}$$

The conditional probability distribution of z given $z \geq 0$ is given by

$$f_z(z|z \geq 0) = \frac{f_z(z)}{F_z(\infty) - F_z(0)} \quad z \geq 0,$$

(see Papoulis, 1984, p80) which is found to be (assuming $\alpha = \beta$)

$$f_z(z|z \geq 0) = 2f_z(z) = \alpha e^{-\alpha z} \quad z \geq 0.$$

Therefore we conclude that the distribution of the magnitude of the difference of two independent random variables with the exponential distribution is also exponential.

Appendix E

Statistical Error Analysis

There are three basic breaking wave statistics in Chapter 5, that is, event density, speed and duration. Event density is obtained over some observation period and area. The result is just one sample and thus statistical error analysis cannot proceed. Downwind dimension, although dependent on event speed and duration, is treated as an independent statistic, since the correlation between event speed and duration is unknown. Therefore only the statistical errors of mean speed, mean duration, and mean downwind dimension, will be analysed here. The other statistics depend explicitly on the three statistics, and their statistical errors can always be derived from the present analysis.

Table E.1 gives the number of events and standard deviation for event speed, duration, downwind dimension. The confidence interval for a large number of samples can approximately be derived from the t-distribution (Bendat and Piersol, 1986). That is, the (1-α)% confidence interval is given by

$$[\bar{x} - \frac{st_{n;\alpha/2}}{\sqrt{N}} \leq \mu_x \geq \bar{x} + \frac{st_{n;\alpha/2}}{\sqrt{N}}],$$

where $n = N - 1$ is the degree of freedom for the t-distribution, N the number of samples, s the standard deviation, $\bar{x}$ the estimated mean, μ_x the true mean, and

$$\text{Prob}\{t_n > t_{n;\alpha/2}\} = \alpha/2.$$

The 90% confidence interval for these statistics is also included in Table E.1.

Data set #	N_1	N_2	S_V ms^{-1}	S_D s	S_L m	δ_V ms^{-1}	δ_D s	δ_L m
1	288	370	2.47	1.19	8.55	0.48	0.20	1.66
2	234	327	2.96	1.28	10.35	0.64	0.23	2.23
3	288	357	6.42	1.67	24.65	1.25	0.29	4.79
4	324	425	3.44	1.25	10.76	0.63	0.20	1.97
5	315	397	3.72	1.12	12.49	0.69	0.19	2.32
6	399	528	3.32	0.89	8.03	0.55	0.13	1.33
7	377	459	3.54	1.14	13.20	0.60	0.18	2.24
8	378	487	3.90	0.98	9.38	0.66	0.15	1.59
9	520	679	4.01	0.93	8.99	0.58	0.12	1.30
10	489	646	3.87	0.87	9.83	0.58	0.11	1.47
11	227	282	2.68	0.80	6.27	0.59	0.16	1.37
12	253	320	4.57	1.25	15.20	0.95	0.23	3.16
13	220	301	3.81	1.49	16.07	0.85	0.28	3.58
14	259	338	3.32	1.17	11.70	0.68	0.21	2.40
15	118	255	2.98	0.92	8.07	0.91	0.19	2.46
16	294	380	3.03	0.84	7.11	0.58	0.14	1.37
17	526	697	3.75	0.95	7.45	0.54	0.12	1.07
18	354	450	2.03	0.92	5.82	0.36	0.14	1.02
19	181	230	2.11	0.96	5.96	0.52	0.21	1.46
20	590	713	2.40	0.72	4.56	0.33	0.09	0.62
21	417	496	1.80	0.64	3.14	0.29	0.09	0.51
22	546	653	1.98	0.89	5.77	0.28	0.11	0.81
23	469	590	1.83	0.79	4.39	0.28	0.11	0.67

Table E.1: Statistical error analysis. S_V, S_D, and S_L are the standard deviation for event speed, duration, and downwind dimension; δ_V, δ_D, δ_L are the 90% confidence interval for event speed, duration, and downwind dimension; N_1 is the number of samples for event speed and downwind dimension; N_2 is for event duration.

Appendix F

Clustering Algorithm

Identification of breaking regions in the surface wave field is a procedure of clustering. Although many algorithms of the kind have been developed, most of them are heuristic and directed to specific problems. One of the simplest clustering algorithms for the case of an unknown cluster number is Batchelor and Wilkin's algorithm (Bow, 1984), sometimes known as the maximin distance algorithm. A description of the algorithm is as follows:

Step 1. Set arbitrarily the first point as the first cluster center.

Step 2. Determine which point is farthest away from this point, and assign the farthest point as the second cluster center.

Step 3. Calculate the distance from each remaining point to each cluster center. For each point, determine which cluster center is closer and record the distance from the point to the closer center.

Step 4. Determine the maximum of all the distances recorded in the previous step.

Step 5. Determine if the maximum distance is sufficient to assign the point associated with the maximum distance as a new cluster center. If it is, this point becomes a new cluster center. Otherwise, the algorithm terminates.

Step 6. Repeat steps 3 to 5 until the criterion for establishing a new cluster fails to be met.

The criterion used by this algorithm for establishing a new cluster is somewhat arbitrary. For a point to be classified as a new center, its distance from the farthest existing cluster center has to be an appreciable fraction of the typical distance between the existing clusters. The choice of this threshold greatly influences the performance of the algorithm. If this value is too low, a situation occasionally arises in which the algorithm fails to terminate, resulting in all the points being identified as individual clusters. If the value is too high, the algorithm may fail to separate close clusters. Through trial and error, a value of one quarter of the average distance between existing clusters was found to produce reasonable results.

This algorithm works effectively for the data that do not appear in tight groups, if the threshold is appropriately chosen. However, in the case where clusters are closely spaced in groups, the algorithm is unable to resolve these groups; it treats all the clusters in one group as one single cluster. Since the cluster center is defined at the weighted geometric center of the individual points in the cluster, if one of the subclusters disappears subsequently, the geometric center would shift appreciably, resulting in uncertainty in tracking individual events.

Reduction of the termination threshold sometimes helps solve this problem. This however leads, in addition to possible failure of termination, to another problem: a threshold that works for one frame may not work for others. For the same series of frames, it is necessary to keep the same threshold for statistical analysis. For this reason, such an approach is not suitable for clustering our data. We have therefore decided to modify the original algorithm to make it more effective on the wave data.

Modifications

The modification involves recursive clustering of subgroups and determination of the maximum size of a cluster. Data are first grouped with a loose termination threshold into a number of subgroups. Each subgroup is then subdivided with the

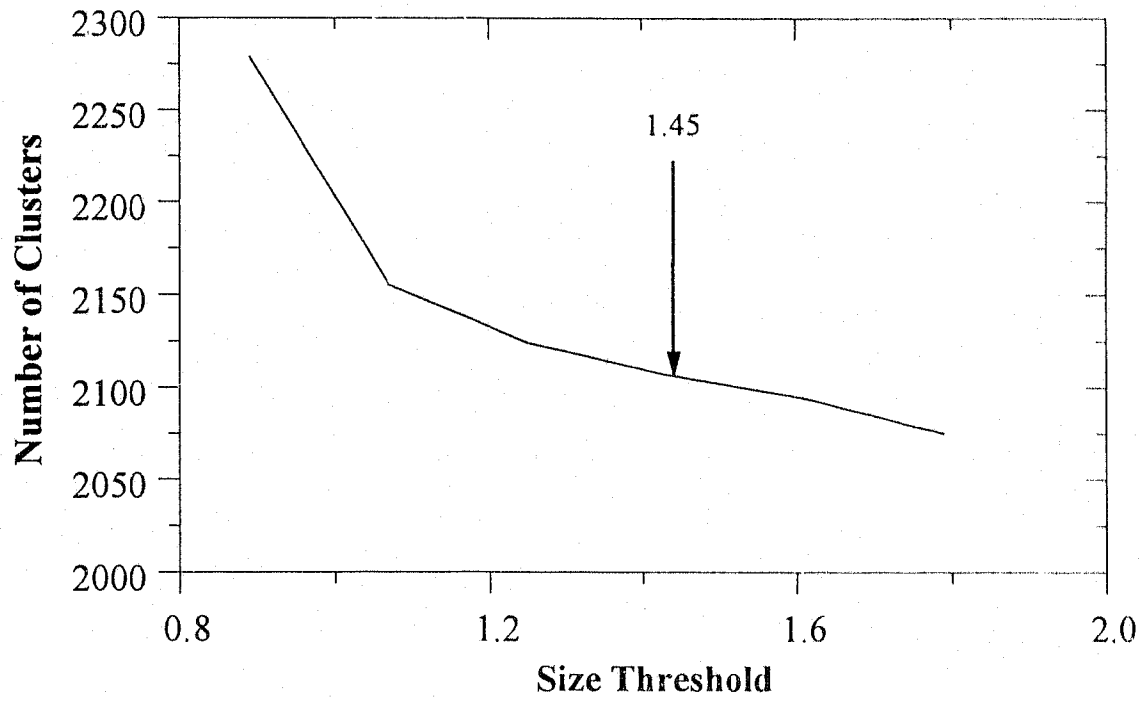

Figure F.1: Selection of the size threshold for determining a single cluster. The horizontal axis is the ratio of the maximum distance in a cluster to the theoretical distance. The vertical axis is the total number of clusters in a series of frames. The arrow indicates the selected threshold.

same algorithm into smaller and smaller groups, until each of these smaller groups is determined to contain only one cluster. A cluster is considered to be single if the distance between the most distant points in this cluster is comparable to the size of a tightest cluster (no gaps) with the same number of points.

The size of the tightest cluster is determined as follows. Consider a rectangular cluster with $n_1 \times n_2$ points equally spaced in the cluster. Such a cluster is tightest with no gap inside (except for the finite spatial resolution). The maximum distance within the cluster is therefore

$$D = \sqrt{(n_1 - 1)^2 + (n_2 - 1)^2} \cdot ds$$

where ds is the spatial resolution. From previous observations of whitecaps (Bortkovskii,

1987), the length is twice the width, that is,

$$(n_2 - 1)ds = 2(n_1 - 1)ds,$$

and therefore for large n_1 and n_2, $D = \sqrt{2.5M}ds$ with $M = n_1 n_2$ being the total number of points in the cluster.

The algorithm compares the maximum distance between two points in a cluster to D. If the ratio is below a threshold, then the cluster is considered to be single. The choice of this size threshold is important. Figure F.1 shows the total number of clusters in a series of frames against the threshold. It is seen that the number starts to be stable when the threshold is above 1.25. The optimal choice in this case would be 1.45 based on the argument given in Chapter 5. This criterion breaks down when there is only one point in the cluster. In this case, the cluster is treated as random noise and discarded.

The termination threshold used in this algorithm is chosen to be relatively high to allow for subsequent recursion. It was found that for a given maximum size threshold, the number of clusters starts being invariant to the choice of the termination threshold when this threshold is above 0.5 times the average distance between existing clusters. Therefore, a value of 0.8 was chosen for this threshold.

Comment

The recursive version of the algorithm correctly identifies clusters in the data in the vast majority of cases. The results are relatively independent of the termination threshold for subgroups, since the program continues until a group of points are determined to represent a single cluster. This modified algorithm also runs faster than the original one. The reason for the improvement in speed, particularly in the case of a large number of clusters, is that calculations of the distance between points and existing clusters increase dramatically with the number of clusters. Compared with the old algorithm, the recursive one, by breaking the data into small groups, limits the number of clusters in any given group to a small fraction of the total.

Therefore, each group requires appreciably fewer calculations of the distance, and as a result, the total number of calculations is significantly smaller than that required by the original algorithm (a factor of 25%).

Since the original algorithm does not require the additional size threshold, it is simpler and more objective, and should be applied when the data do not appear in tight groups. However, when there are closely spaced clusters, the algorithm is unable to resolve them. In this case, the recursive version should be applied.